



Ministério da
**Ciência, Tecnologia
e Inovação**



sid.inpe.br/mtc-m19/2011/08.11.13.08-TDI

NUMERICAL SIMULATION OF MEMS-BASED COLD GAS MICRONOZZLE FLOWS

Israel Borges Sebastião

Master Thesis at Post Graduation Course applied in Engineering and Space
Technology/Combustion and Propulsion, advised by Dr. Wilson Fernando
Nogueira dos Santos, approved in September 15, 2011.

URL of the original document:

<<http://urlib.net/8JMKD3MGP7W/3A8PU95>>

INPE
São José dos Campos
2011

PUBLISHED BY:

Instituto Nacional de Pesquisas Espaciais - INPE

Gabinete do Diretor (GB)

Serviço de Informação e Documentação (SID)

Caixa Postal 515 - CEP 12.245-970

São José dos Campos - SP - Brasil

Tel.:(012) 3208-6923/6921

Fax: (012) 3208-6919

E-mail: pubtc@sid.inpe.br

BOARD OF PUBLISHING AND PRESERVATION OF INPE INTELLECTUAL PRODUCTION (RE/DIR-204):**Chairperson:**

Dr. Gerald Jean Francis Banon - Coordenação Observação da Terra (OBT)

Members:

Dr^a Inez Staciarini Batista - Coordenação Ciências Espaciais e Atmosféricas (CEA)

Dr^a Maria do Carmo de Andrade Nono - Conselho de Pós-Graduação

Dr^a Regina Célia dos Santos Alvalá - Centro de Ciência do Sistema Terrestre (CST)

Marciana Leite Ribeiro - Serviço de Informação e Documentação (SID)

Dr. Ralf Gielow - Centro de Previsão de Tempo e Estudos Climáticos (CPT)

Dr. Wilson Yamaguti - Coordenação Engenharia e Tecnologia Espacial (ETE)

Dr. Horácio Hideki Yanasse - Centro de Tecnologias Especiais (CTE)

DIGITAL LIBRARY:

Dr. Gerald Jean Francis Banon - Coordenação de Observação da Terra (OBT)

Marciana Leite Ribeiro - Serviço de Informação e Documentação (SID)

Deicy Farabello - Centro de Previsão de Tempo e Estudos Climáticos (CPT)

DOCUMENT REVIEW:

Marciana Leite Ribeiro - Serviço de Informação e Documentação (SID)

Yolanda Ribeiro da Silva Souza - Serviço de Informação e Documentação (SID)

ELECTRONIC EDITING:

Vivéca Sant´Ana Lemos - Serviço de Informação e Documentação (SID)



Ministério da
**Ciência, Tecnologia
e Inovação**



sid.inpe.br/mtc-m19/2011/08.11.13.08-TDI

NUMERICAL SIMULATION OF MEMS-BASED COLD GAS MICRONOZZLE FLOWS

Israel Borges Sebastião

Master Thesis at Post Graduation Course applied in Engineering and Space
Technology/Combustion and Propulsion, advised by Dr. Wilson Fernando
Nogueira dos Santos, approved in September 15, 2011.

URL of the original document:

<<http://urlib.net/8JMKD3MGP7W/3A8PU95>>

INPE
São José dos Campos
2011

Cataloging in Publication Data

Sebastião, Israel Borges.
Se21n Numerical simulation of MEMS-based cold gas micronozzle
flows / Israel Borges Sebastião. – São José dos Campos : INPE,
2011.

xxx+204 p. ; (sid.inpe.br/mtc-m19/2011/08.11.13.08-TDI)

Master Thesis (Master Thesis in Engineering and Space Tech-
nology/Combustion and Propulsion) – Instituto Nacional de
Pesquisas Espaciais, São José dos Campos, 2011.

Advisers : Dr. Wilson Fernando Nogueira dos Santos.

1. Direct Simulation Monte Carlo (DSMC)
2. Rarefied flow.
3. Microelectromechanical Systems (MEMS).
4. Micronozzle.
5. Supersonic flow. I.Título.

CDU 621.313.53


Copyright © 2011 do MCT/INPE. Nenhuma parte desta publicação pode ser reproduzida, armazenada em um sistema de recuperação, ou transmitida sob qualquer forma ou por qualquer meio, eletrônico, mecânico, fotográfico, reprográfico, de microfilmagem ou outros, sem a permissão escrita do INPE, com exceção de qualquer material fornecido especificamente com o propósito de ser entrado e executado num sistema computacional, para o uso exclusivo do leitor da obra.

Copyright © 2011 by MCT/INPE. No part of this publication may be reproduced, stored in a retrieval system, or transmitted in any form or by any means, electronic, mechanical, photocopying, recording, microfilming, or otherwise, without written permission from INPE, with the exception of any material supplied specifically for the purpose of being entered and executed on a computer system, for exclusive use of the reader of the work.

Aprovado (a) pela Banca Examinadora
em cumprimento ao requisito exigido para
obtenção do Título de Mestre em

Engenharia e Tecnologia
Espaciais/Combustão e Propulsão

Dr. Wilson Fernando Nogueira dos
Santos



Presidente / Orientador(a) / INPE / Cachoeira Paulista - SP

Dr. Jerônimo dos Santos Travelho



Membro da Banca / INPE / São José dos Campos - SP

Dr. Leonardo Santos de Brito Alves



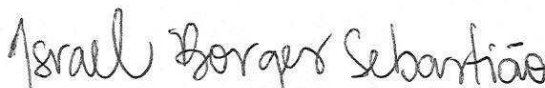
Convidado(a) / IME / Rio de Janeiro - RJ

Este trabalho foi aprovado por:

() maioria simples

unanimidade

Aluno (a): Israel Borges Sebastião



São José dos Campos, 15 de setembro de 2011

*“Dignity consists not in possessing honors, but in the consciousness
that we deserve them.”*

ARISTOTLE

To my family, masters and friends...

ACKNOWLEDGEMENTS

I would like to express my sincere gratitude to my advisor, Dr. Wilson F. N. Santos, for his sincerity, guidance, support and patient during my studies. Certainly, his lessons and humility transcended my expectations.

I thank my all professors and the INPE/LCP graduate program that provided me opportunities to advance my knowledge.

I thank my committee members for their valuable comments and suggestions on this work.

I owe a special thank to Dr. Jeronimo S. Travelho whose his encouragement and integrity have been decisive in my academic and personal life.

I would also like to thank the financial support provided by CNPq (Conselho Nacional de Desenvolvimento Científico e Tecnológico) under Grant No. 580249/2008-5.

Finally, I am most grateful to my family, in special to my parents, whose always taught me that wisdom can overcome all barriers.

ABSTRACT

The recent tendency in the design of space systems has aligned to reduce the life cycle cost of space programs by means of a reduction in the complexity of satellite missions. In this context, one of the possible options is reducing the mass of the whole system. Therefore, concepts of micropropulsion based on microtechnologies have been developed in order to attend the requirements of future space missions. The current state of semiconductor technology based on silicon has allowed the manufacturing process of small scale systems, called as MEMS (MicroElectroMechanical Systems). Among the many MEMS applications are the microunits of low thrust, where micronozzles are present. According to the relevant literature, the most studies investigated the micronozzle performance for different length scales and flow conditions. However, these investigations have not focused on the influence of the surface curvature on the micronozzle flow structure. In macronozzles, it is known that discontinuities on the surface affect the system performance due to the arising of shock waves inside the device. Thus, in order to obtain further insight into the physics of micronozzle flows, a numerical simulation of a rarefied flow in a convergent-divergent micronozzle array with rectangular cross-section is investigated by using the Direct Simulation Monte Carlo (DSMC) method. By considering a convex-concave divergent surface, the impact of different divergent shapes on the two-dimensional flowfield structure, aerodynamic surface quantities and micronozzle performance are explored by changing the surface slope and radius of curvature at the inflection point. In order to decouple other geometric influences, the ratio between exit and throat areas as well as the divergent exit angle were kept the same for all cases. Moreover, the inlet-outlet boundary conditions are based on pre-defined pressure values. The computational results pointed out a small impact on the macroscopic properties due to variations in the slope and curvature of the divergent surface. The symmetric assumptions employed in this account resulted in a recirculation region in the external flow. The simulations also showed that thermodynamic nonequilibrium takes place in the entire divergent flow, in special, at the nozzle lip. By concerning to the aerodynamic surface quantities, simulations indicated that the thermal and mechanical loads that take place along the divergent surface are highly dependent on the smoothness of the surface along the inflection point. Finally, this study also revealed that the geometric shape of the divergent surface does not perform significant influence on the specific impulse. Anyway, the presence of the divergent surface provided a specific impulse that is almost two times higher than that one obtained by a micronozzle with only the convergent part operating in the same conditions.

SIMULAÇÃO NUMÉRICA DO ESCOAMENTO DE GÁS FRIO EM MICROBOCAIS BASEADOS EM MEMS

RESUMO

A atual tendência no projeto de sistemas espaciais tem caminhado no sentido de se reduzir o custo do ciclo de vida dos programas através da redução da complexidade das missões dos satélites. Nesse contexto, umas das opções diz respeito à redução da massa total do sistema. Desse modo, conceitos de micropropulsão baseados em microtecnologias têm sido desenvolvidos a fim de se atender as exigências das futuras missões espaciais. O atual estágio da tecnologia de semicondutores à base de silício tem permitido a fabricação de sistemas de pequena escala, denominados por MEMS (MicroElectroMechanical Systems). Dentre as várias aplicações dos MEMS encontram-se os micropropulsores de baixo empuxo, onde os microbocais estão presentes. De acordo com a literatura relevante, a maioria dos estudos investigou o desempenho dos microbocais para diferentes escalas e condições de contorno. Entretanto, essas investigações não focaram na influência da curvatura da superfície na estrutura do escoamento em microbocais. É sabido que, em macrobocais, descontinuidades na curvatura alteram o desempenho dos bocais devido ao surgimento de ondas de choque no interior do dispositivo. Assim, com o intuito de adquirir uma compreensão mais profunda da física presente no escoamento em microbocais, a simulação numérica de um escoamento rarefeito num microbocal do tipo convergente-divergente é realizada através do Método de Simulação Direta de Monte Carlo (DSMC). Tal dispositivo é considerado como parte de uma matriz de microbocais. Considerando ainda uma superfície divergente do tipo convexa-côncava, os impactos de diferentes perfis dessa superfície na estrutura do escoamento, quantidades aerodinâmicas da superfície e desempenho do microbocal são explorados alterando-se a inclinação e o raio de curvatura da superfície no ponto de inflexão. Com o propósito de se desacoplar outros efeitos geométricos, a razão entre as áreas da garganta e de saída assim como o ângulo de divergência na saída são mantidos os mesmos para todos os casos. Além disso, as condições de entrada e saída são baseadas em valores pré-definidos de pressão. Os resultados computacionais apontaram um pequeno impacto nas propriedades macroscópicas devido às variações na inclinação e curvatura da superfície divergente. As hipóteses de simetria adotadas neste trabalho resultaram numa região de recirculação no escoamento externo. As simulações ainda mostraram que o não-equilíbrio termodinâmico ocorre em todo escoamento divergente, em especial, no lábio do bocal. No que diz respeito às quantidades aerodinâmicas, as simulações indicaram que as cargas térmicas e mecânicas que agem ao longo da superfície divergente dependem fortemente da inclinação da superfície próximo ao ponto de inflexão. Finalmente, este estudo ainda revelou que a forma geométrica da superfície divergente não desempenhou uma influência significativa no impulso específico. De qualquer modo, a presença da superfície divergente forneceu um impulso específico que é cerca de duas vezes maior que aquele obtido para um microbocal apenas com a parte convergente operando nas mesmas condições.

LIST OF FIGURES

	<u>Pág.</u>
1.1 Examples of small satellites: (a) SwissCube was launched in 2009 (1 kg and operating) and (b) SACI1 was launched in 1999 (60 kg and nonoperating).	2
1.2 (a) Concept of a constellation communication system and (b) two nanosatellites just after ejection from Space Shuttle.	3
1.3 Micronozzle examples: (a) 34 μm throat and area ratio of 7:1;(b) 90 μm throat and area ratio of 6.2:1.	4
1.4 A typical convergent-divergent nozzle configuration.	6
1.5 Flow regime limits in terms of the local Knudsen number.	8
1.6 Overall Knudsen range for typical MEMS and NEMS (Nanoelectromechanical Systems) applications under standard conditions.	8
1.7 Scanning Electron Microscope (SEM) images of surface roughness in MEMS: (a) longitudinal patterns, (b) zoomed region and (c) transversal patterns.	9
1.8 Comparison of micronozzle arrangements: single versus array pattern. . .	13
1.9 Schematic drawing of the micronozzle divergent section.	14
2.1 Flow classification in terms of dimensionless parameters.	20
2.2 Flow modeling classification.	21
2.3 The Knudsen number limits on the mathematical models and flow regimes.	26
3.1 Typical DSMC flowchart.	34
3.2 Planar representation of a binary collision in the laboratory frame. . . .	36
3.3 Trajectories of the molecules in the center of mass frame.	39
3.4 Interaction of the reduced mass particle with a fixed scattering center. . .	40
3.5 Direct and inverse collisions in the reduced mass frame of reference. . . .	41
3.6 (a) Actual collision between two hard spheres and (b) the representation of the same collision by a sphere of influence and a punctual molecule. . .	42
3.7 Geometric information of the collision on the plane Υ : (a) Intersection between the undisturbed trajectory and σ_T and (b) the representation of the differential area, within σ_T , near the intersection point.	42
3.8 (a) Typical intermolecular potential fields and (b) the contrast between the molecular paths of the Sutherland model and a nonattractive model.	44

3.9	Thermal speed and thermal velocity x -component Maxwellian distributions.	56
3.10	Schematic view of a two-dimensional domain composed of four orthogonal inflow boundaries.	57
3.11	Normalized number flux to a surface element in terms of q	58
3.12	Propagation of a weak pressure wave (a) in the laboratory frame and (b) in the frame moving with the wave.	59
3.13	Schematic view of the variables required in the pressure boundary conditions.	61
3.14	Schematic drawing of the (a) Maxwell and the (b) CLL reflection models.	64
4.1	(a) Isometric view of a micronozzle array and (b) its two-dimensional representation on the indicated plane.	67
4.2	(a) Schematic view of the computational grid for the entire micronozzle array and (b) the simulated regions.	68
4.3	Geometry definition of the computational domain.	69
4.4	Geometric differences between group A (top), B (middle) and C (bottom) cases.	73
4.5	Schematic view of computational domain and boundary conditions.	76
5.1	Influence of varying the number of cells in the x (left column) and y (right column) directions on the skin friction (top), pressure (middle) and heat transfer (bottom) coefficients.	86
5.2	Influence of varying the number of cells in the x (left column) and y (right column) directions on the pressure distribution for section $X = -1.8$ (top), $X_{Ld} = 0.0$ (middle) and $X_{Ld} = 1.0$ (bottom).	87
5.3	Influence of varying the reference time step (left column) and the number of simulated molecules (right column) on the skin friction (top), pressure (middle) and heat transfer (bottom) coefficients.	90
5.4	Influence of varying the reference time step (left column) and the number of simulated molecules (right column) on the pressure distribution for section $X = -1.8$ (top), $X_{Ld} = 0.0$ (middle) and $X_{Ld} = 1.0$ (bottom).	91
5.5	Influence of varying the number of samples on the aerodynamic properties (left column) and pressure distribution (right column).	92
5.6	Geometry definition of the computational domain for the validation case.	94
5.7	Schematic view of computational domain and boundary conditions for the validation case.	94

5.8	Mach number (top), pressure (middle) and translational temperature (bottom) distributions along the centerline ($Y = 0.0$) for different back pressures p_b	96
5.9	Comparisons of experimental results versus numerical results for the mass flow rate (top), and average pressure along upstream (middle) and downstream (bottom) cross-sections.	97
5.10	Comparison of the present DSMC solution versus NS and isentropic solutions for the Mach number distribution along the centerline.	98
6.1	Mach number (M) profiles along the micronozzle for group A cases. . . .	101
6.2	Mach number (M) profiles along the micronozzle for group B cases. . . .	102
6.3	Mach number (M) profiles along the micronozzle for group C cases. . . .	103
6.4	Streamline distribution for group A cases.	109
6.5	Streamline distribution for group B cases.	110
6.6	Streamline distribution for group C cases.	111
6.7	Mach number (M) distribution along the micronozzle for group A cases.	112
6.8	Mach number (M) distribution along the micronozzle for group B cases.	113
6.9	Mach number (M) distribution along the micronozzle for group C cases.	114
6.10	Mach number (M) distribution along the micronozzle for cases A1 (top), B1 (middle) and C1 (bottom), where dashed lines are normal to the divergent surface.	115
6.11	Density ratio (ρ/ρ_{in}) profiles along the micronozzle for group A cases. . .	119
6.12	Density ratio (ρ/ρ_{in}) profiles along the micronozzle for group B cases. . .	120
6.13	Density ratio (ρ/ρ_{in}) profiles along the micronozzle for group C cases. . .	121
6.14	Density ratio (ρ/ρ_{in}) distribution along the micronozzle for group A cases.	122
6.15	Density ratio (ρ/ρ_{in}) distribution along the micronozzle for group B cases.	123
6.16	Density ratio (ρ/ρ_{in}) distribution along the micronozzle for group C cases.	124
6.17	Schematic view of the pressure and temperature gradients near the convex (left) and concave (right) divergent surfaces in present account. . . .	126
6.18	Qualitative flow structure illustrating the main physical mechanisms observed in the present simulations.	127
6.19	Pressure ratio (p/p_{in}) profiles along the micronozzle for group A cases. .	130
6.20	Pressure ratio (p/p_{in}) profiles along the micronozzle for group B cases. .	131
6.21	Pressure ratio (p/p_{in}) profiles along the micronozzle for group C cases. .	132
6.22	Pressure ratio (p/p_{in}) distribution along the micronozzle for group A cases.	133
6.23	Pressure ratio (p/p_{in}) distribution along the micronozzle for group B cases.	134
6.24	Pressure ratio (p/p_{in}) distribution along the micronozzle for group C cases.	135

6.25	Translational temperature ratio (T_T/T_{in}) profiles along the micronozzle for group A cases.	141
6.26	Translational temperature ratio (T_T/T_{in}) profiles along the micronozzle for group B cases.	142
6.27	Translational temperature ratio (T_T/T_{in}) profiles along the micronozzle for group B cases.	143
6.28	Temperature ratio (T/T_{in}) profiles along the micronozzle for case A1. . .	144
6.29	Temperature ratio (T/T_{in}) profiles along the micronozzle for case B1. . .	145
6.30	Temperature ratio (T/T_{in}) profiles along the micronozzle for case C1. . .	146
6.31	Translational temperature ratio (T_T/T_{in}) distribution along the micronozzle for group A cases.	147
6.32	Translational temperature ratio (T_T/T_{in}) distribution along the micronozzle for group B cases.	148
6.33	Translational temperature ratio (T_T/T_{in}) distribution along the micronozzle for group C cases.	149
6.34	Knudsen number (Kn) profiles along the micronozzle for the case A1. . .	153
6.35	Knudsen number (Kn) profiles along the micronozzle for the case B1. . .	154
6.36	Knudsen number (Kn) profiles along the micronozzle for the case C1. . .	155
6.37	Knudsen number (Kn) distribution along the micronozzle for group A cases.	156
6.38	Knudsen number (Kn) distribution along the micronozzle for group B cases.	157
6.39	Knudsen number (Kn) distribution along the micronozzle for group C cases.	158
6.40	Dimensionless number flux (N_f) distribution along the internal micronozzle surface for group A (top), B (middle) and C (bottom) cases.	161
6.41	Pressure coefficient (C_p) distribution along the internal micronozzle surface for group A (top), B (middle) and C (bottom) cases.	163
6.42	Skin friction coefficient (C_f) distribution along the internal micronozzle surface for group A (top), B (middle) and C (bottom) cases.	167
6.43	Distribution of the normalized viscous stress tensor component ($-\tau_{xy}/p_{din}$) along the micronozzle for group A cases.	168
6.44	Distribution of the normalized viscous stress tensor component ($-\tau_{xy}/p_{din}$) along the micronozzle for group B cases.	169
6.45	Distribution of the normalized viscous stress tensor component ($-\tau_{xy}/p_{din}$) along the micronozzle for group C cases.	170

6.46	Heat transfer coefficient (C_h) distribution along the internal micronozzle surface for group A (top), B (middle) and C (bottom) cases.	174
6.47	Total, incident and reflected parcels of the heat transfer coefficient (C_h) along the internal micronozzle surface for cases A1 (top), B1 (middle) and C1 (bottom).	175
6.48	Total, translational, rotational and vibrational contributions of the heat transfer coefficient (C_h) along the internal micronozzle surface for cases A1 (top), B1 (middle) and C1 (bottom).	176
6.49	Normalized specific impulse (\hat{I}_{sp}) at different X_{Ld} stations for group A (top), B (middle) and C (bottom) cases.	179

LIST OF TABLES

	<u>Pág.</u>
1.1 Satellite classification.	2
1.2 Proposed geometric configurations for the micronozzle divergent surface.	15
3.1 Molecular parameters for different models.	48
4.1 Geometric configurations at the inflection point.	71
4.2 Common geometric definitions.	71
4.3 Additional geometric definitions.	72
4.4 Physical properties of the working fluid.	75
4.5 Flow conditions.	77
5.1 Cell distribution – direction x versus y – applied in the verification process.	85
5.2 Additional geometric definitions for the validation case.	94
6.1 Common throat section data.	178

LIST OF ABBREVIATIONS

AEB	–	Agência Espacial Brasileira
BBGKY	–	Bogolyubov-Born-Green-Kirkwood-Yvon
CFD	–	Computational Fluid Dynamics
CL	–	Cercignani-Lampis
CLL	–	Cercignani-Lampis-Lord
CVD	–	Chemical Vapor Deposition
DAC	–	DSMC Analysis Code
DOFs	–	Degree of Freedom
DSMC	–	Direct Simulation Monte Carlo
ESA	–	European Space Agency
GHS	–	Generalized Hard Sphere
GSS	–	Generalized Soft Sphere
HS	–	Hard Sphere
IP	–	Information Preservation
IPL	–	Inverse Power Law
LB	–	Larsen-Borgnakke
MEMS	–	Microelectromechanical Systems
MD	–	Molecular Dynamics
MGL	–	Monotonic Lagrangian Grid
MTT	–	Multiple Translational Temperature
MPI	–	Message Passing Interface
NASA	–	National Aeronautics and Space Administration
NC	–	Null Collision
NEMS	–	Nanoelectromechanical Systems
NS	–	Navier-Stokes
NTC	–	No Time Counter
OpenMP	–	Open Multi-Processing
PDSC	–	Parallel Three-Dimensional DSMC Code
PNAE	–	Programa Nacional de Atividades Espaciais
PVD	–	Physical Vapor Deposition
RTMC	–	Relaxation Time Monte Carlo
SHO	–	Simple Harmonic Oscillator
SMILE	–	Statistical Modeling In Low-Density Environment
SWPM	–	Stochastic Weighted Particle Method
TC	–	Time Counter
UHO	–	Unharmonic Oscillator
VHS	–	Variable Hard Sphere
VSS	–	Variable Soft Sphere

LIST OF SYMBOLS

a	– sound speed
\mathbf{a}	– acceleration vector
A	– area
A, B, C	– constant or particular values
b	– miss-distance impact parameter
c	– molecular speed
\mathbf{c}	– molecular velocity vector
\mathbf{c}_0	– macroscopic stream vector
C_f	– skin friction coefficient (Equation 6.23)
C_h	– heat transfer coefficient (Equation 6.28)
C_p	– pressure coefficient (Equation 6.21)
d	– molecular diameter
D_H	– hydraulic diameter
e	– specific energy of a molecule
\mathbf{e}	– unit normal vector
E_t	– translational energy
f	– velocity distribution function; fraction of molecules reflected diffusively; a function; friction coefficient
f_0	– Maxwellian or equilibrium velocity distribution function
F	– force
\mathbf{F}	– force vector
F_t	– thrust force
F_N	– scaling factor, i.e., the number of real molecules represented by one simulated molecule
h	– a half size; specific enthalpy
i, j, k	– Cartesian components; particular values
I_{sp}	– specific impulse
k	– Boltzmann constant, $k = 1.380658 \times 10^{-23}$ J/K
Kn	– Knudsen number
L	– characteristic length
m	– molecular mass
m_r	– reduced mass
M	– Mach number
n	– number density; an exponent
N	– a number; number of simulated molecules per cell
N_{coll}	– number of collision pairs per cell over Δt
N_f	– dimensionless number flux (Equation 6.20)
\dot{N}	– number flux

\dot{N}_i	–	inward number flux
\hat{N}_i	–	normalized inward number flux
N_S	–	total number of samples
p	–	pressure; normal momentum component
P_{coll}	–	probability of a particular collision
P_i	–	probability of the mode i to be adjusted
q	–	energy flux
Q	–	a function that relates f to a macroscopic quantity
r	–	a distance; molecular radius
\mathbf{r}	–	position vector
r_c	–	radius of curvature
R	–	a radius in the micronozzle geometry
Re	–	Reynolds number
R_f	–	a random fraction between 0 and 1
s	–	speed ratio; refers to an isentropic process
S	–	size scaling factor
S/V	–	surface-to-volume ratio
t	–	time
T	–	thermodynamic temperature; a temperature
u, v, w	–	velocity component in the x -, y - and z -directions, respectively
V	–	macroscopic or stream flow speed
V_c	–	cell volume
x, y, z	–	Cartesian axes in the physical space
X	–	dimensionless length (x/h_t)
X_{Ld}	–	dimensionless length (x/L_d)
Y	–	dimensionless height (y/h_t)
Z	–	relaxation collision number

Greek

α	–	exponent in the VSS model; accommodation coefficient
α_g, β_g	–	micronozzle geometric parameters
α_r	–	internal energy accommodation coefficient
β	–	reciprocal of the most probable molecular speed in an equilibrium gas
γ	–	specific heat ratio
Γ	–	gamma function
δ	–	mean molecular separation; viscous layer thickness
δ_{mcs}	–	mean collision separation
δt	–	time increment
Δt	–	time step

ε	– azimuthal impact parameter; perturbation parameter; molecular energy
ζ	– number of degrees of freedom
η	– exponent in the Inverse Power Law model; streamline normal direction
θ	– an angle
Θ	– an angle; characteristic temperature
κ	– constant in the Inverse Power Law model
λ	– molecular mean free path
Λ	– Larsen-Borganakke inelastic fraction
μ	– viscosity coefficient
ν	– collision frequency; Prandtl-Meyer angle
ξ	– streamline tangential direction
ρ	– density
σ	– collision cross-section
$\sigma d\Omega$	– differential collision cross-section
σ_t	– tangential momentum accommodation coefficient
σ_T	– total collision cross-section
τ	– relaxation time; tangential momentum component
τ_c	– mean collision time
τ_w	– shear stress at the surface
v	– relative speed exponent in the VHS model, $v = \omega - 1/2$
Υ	– a plane
ϕ	– a macroscopic quantity; potential field
χ	– deflection angle
Ψ	– specific impulse efficiency; a function
ω	– viscosity index

Subscripts

A,B,C,D	– particular values
b	– buffer or external section value
c	– convergent section value; a particular computational cell
$coll$	– refers to molecular collisions
d	– divergent section value
e	– exit section value
i	– a particular molecular mode; incident value
$ideal$	– ideal (isentropic) conditions
in	– inlet value
m	– center of mass value; most probable value
max	– maximum value
min	– minimum value

<i>n</i>	–	normal component
<i>O</i>	–	based on or related to overall values
<i>p,q,s</i>	–	particular molecular species
<i>r</i>	–	relative; reflected value
<i>real</i>	–	real conditions
<i>ref</i>	–	reference values
<i>R</i>	–	based on or related to the rotational modes
<i>t</i>	–	throat section value; tangential component
<i>T</i>	–	based on or related to the translational modes
<i>V</i>	–	based on or related to the vibrational modes
<i>w</i>	–	surface value
<i>0</i>	–	stagnation value
<i>0,1,2,3</i>	–	particular values

Superscripts

*	–	post collision values
'	–	thermal or peculiar component; a second value
~	–	center of mass frame
-	–	average value
^	–	normalized value
<i>Cont</i>	–	value employed in the continuum approach
<i>DSMC</i>	–	value employed in the DSMC method

CONTENTS

	<u>Pág.</u>
1 INTRODUCTION	1
1.1 Motivation	1
1.2 Micronozzle Flow Regimes and Features	5
1.3 Previous Work	10
1.4 Purpose of the Present Work	13
2 FLUID FLOW PHYSICAL ASPECTS	17
2.1 Microflow General Issues	17
2.2 Flow Classification	18
2.3 Flow Modeling	21
3 DIRECT SIMULATION MONTE CARLO METHOD	29
3.1 Overview	29
3.2 DSMC Methodology	33
3.3 Binary Elastic Collisions	36
3.3.1 Scattering	36
3.3.2 Cross Section	41
3.4 Molecular Model	43
3.5 Collision Sampling Schemes	49
3.6 Inelastic Collisions	52
3.7 Boundary Conditions	54
3.7.1 Inflow Boundaries	55
3.7.2 Gas-Surface Interaction Model	62
4 COMPUTATIONAL PROCEDURE	67
4.1 Micronozzle Geometry Definition	67
4.2 Physical Models and Working Fluid	74
4.3 Flow Conditions	76
5 VERIFICATION AND VALIDATION PROCESSES	79
5.1 DSMC Requirements	79
5.2 Grid Generation	82

5.3	Adaptive and Optimization Procedures	83
5.4	Verification Test Case	83
5.4.1	Spatial Discretization Effects	84
5.4.2	Time Discretization Effects	88
5.4.3	Particle Number Effects	88
5.4.4	Sample Number Effects	89
5.5	Validation Test Case	93
6	COMPUTATIONAL RESULTS	99
6.1	Flowfield Structure	99
6.1.1	Mach Number Field	99
6.1.2	Density Field	116
6.1.3	Pressure Field	125
6.1.4	Temperature Field	136
6.1.5	Knudsen Field	150
6.2	Aerodynamic Surface Properties	159
6.2.1	Dimensionless Number Flux	159
6.2.2	Pressure Coefficient	162
6.2.3	Skin Friction Coefficient	164
6.2.4	Heat Transfer Coefficient	171
6.3	Micronozzle Performance	177
6.3.1	Specific Impulse	177
7	CONCLUSIONS	181
7.1	Concluding Remarks	181
7.2	Future Work	182
	REFERENCES	185

1 INTRODUCTION

1.1 Motivation

The national initiatives in the space area have gained a new impulse with the National Program for Space Activities (PNAE¹). According to [Brazilian Space Agency \(2005\)](#), the PNAE aims to encourage the country to develop and to apply space technologies in order to solve national problems for benefit of the Brazilian society. Among the several actions and space activities, the PNAE identifies as indispensable the enhancement of knowledge in strategic technologies as well as the transference of them to the industrial area. In the space platform area, there is high priority about technologies necessary to increase the performance and to attain the mission requirements, e.g., the attitude² control, sensors and space actuators, besides micro- and nanotechnologies that will allow drastic reductions in mass, volume and consumption of ground and in-orbit equipments.

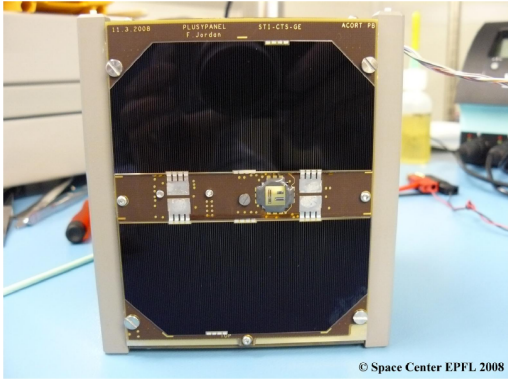
The recent tendency in the design of space systems has aligned to reduce life cycle cost of the space programs through a reduction in the complexity of the satellite missions. In this sense, one of the possible options is reducing the mass of the whole system. The mass reduction will be possible only by means of a system miniaturization, i.e., a reduction in the satellite scale or in part of it. This concept of small space devices is embodied in the slogan “*Faster, Better, Smaller and Cheaper*” ([CUIEL, 2004](#)), which has been the new directive of commercial companies, universities and space research agencies such as NASA (National Aeronautics and Space Administration) and ESA (European Space Agency). Based on this philosophy, the space sector has focused on the development of a new space system generation called microsattellites ([MARGOTTINI, 2007](#)). Figure 1.1 presents some examples of small satellites.

Nowadays, a brief classification of satellites ([KONECNY, 2004](#)) has been adopted based on their wet mass, i.e., the initial total satellite mass including fuel. Table 1.1 presents this classification. Within this classification, the term “*Small Satellites*” is applied to all space vehicles whose in-orbit mass is less than 500 kg.

The use of microsattellites has several advantages, e.g., small mass and volume, low

¹Portuguese acronym for the National Program for Space Activities - *Programa Nacional de Atividades Espaciais*.

²To provide torque in order to keep the space vehicle pointed in the desired direction.



(a)



(b)

Figure 1.1 - Examples of small satellites: (a) SwissCube was launched in 2009 (1 kg and operating) and (b) SACI1 was launched in 1999 (60 kg and nonoperating). SOURCE: (a) Shea (2009) and (b) Sucessos e Insucessos do Programa Espacial Brasileiro (2009).

Table 1.1 - Satellite classification.

Group Name	Wet Mass (kg)
Large satellite	> 1000
Medium satellite	500 to 1000
Minisatellite	100 to 500
Microsatellite	10 to 100
Nanosatellite	1 to 10
Picosatellite	0.1 to 1
Femtosatellite	< 0.1

power consumption, large scale fabrication, short development time and high system integration degree. In general, microsatellites demand small launch vehicles or can also be launched as piggyback of another primary payload³. Moreover, the same platform may be used for different payloads and the design of the missions can be based on spacecraft constellations⁴ (MOSER et al., 1999; NERI, 1999), as depicted in Figure 1.2.

³In space exploration, the payload is the carrying capacity of the spacecraft, e.g., scientific instruments or experiments.

⁴A mission configuration of multiple small satellites working together or in formation. Some designs require a larger “mother” satellite communication with ground controllers.

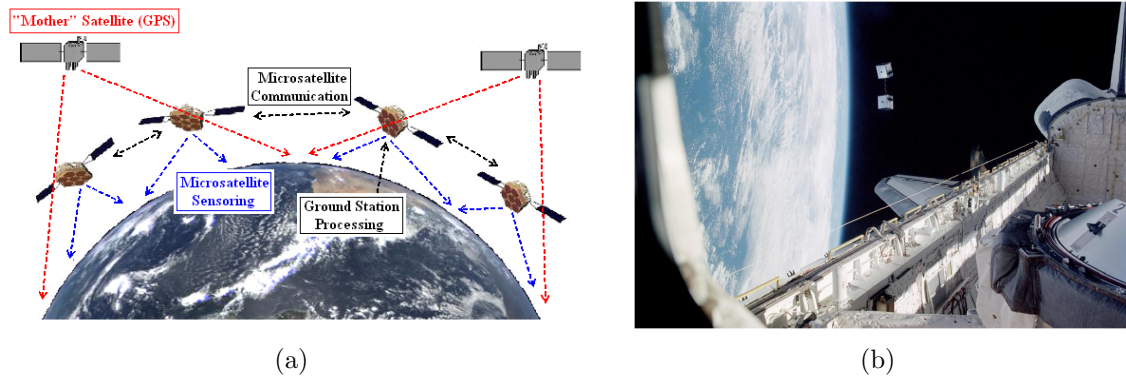


Figure 1.2 - (a) Concept of a constellation communication system and (b) two nanosatellites just after ejection from Space Shuttle.
 SOURCE: (a) Adapted from Moser et al. (1999) and (b) Shea (2009).

On the other hand, the microsatellite disadvantages, among others, may be listed as: (i) high mission risks due to the fact that microsatellites are recent technologies with questionable reliability; (ii) short spacecraft life time; and (iii) reduced mission applicability since usually a microsatellite contains only one instrument, for instance, a camera or an antenna. However, in general, all these characteristics lead to lower overall mission costs and have been a new inspiration source for the scientific community. For instance, the Surrey University claims that 95% of performance of large satellites can be reached by using small satellites for only 5% of the cost or 70% of performance at 1% of the cost (KONECNY, 2004).

In the period from 1980 to 1999, a total of 238 minisatellites and 249 microsatellites were launched around all the globe in order to attend different costumers: commercial (37.1%), military (35.1%), government (17.3%), university (5.4%) and amateur (5.1%). The use of these satellites was distributed in the following areas: communications (69.2%), science (14.4%), technology demonstration (11.0%), military (2.3%) and earth observation (1.4%) (KONECNY, 2004). The reason for the communication sector to leadership is the investment return: for each 200 million dollars invested in a constellation of small communication satellites, it is estimated a profit of 1 billion dollars within an average time of 5 years (NERI, 1999).

In general, the main components and aspects required for development and operation of a microsatellite can be summarized in the launch vehicle, choice of orbit, attitude and orbit controls, sensors, power, data readout and ground station pro-

cessing. In this way, concepts of micropropulsion based on microtechnologies have been developed in order to meet the requirements of future space missions (HITT et al., 2001; KOHLER et al., 2002; MANZONI, 2000; ROSSI et al., 2001; ZAKIROV et al., 2001). Small scale satellites need propulsive systems of small thrust, for orbital maintenance and maneuvers⁵ in order to provide a slender attitude control of the vehicles and to correct their trajectories, which may suffer disturbances due to solar radiation pressure and/or drag present in the space navigation.

The propulsive system of these microsatellites normally provides a thrust of the order of μN and mN (microNewtons and miliNewtons). The thrust in such systems is usually obtained by a gas or a mixture of gases expanding through a convergent-divergent micronozzle. Figure 1.3 illustrates two examples of micronozzles (BAYT, 1999; HITT et al., 2001) that are applied in micropropulsion systems. These microthrusters can be applied individually or as array patterns to small satellite propulsive systems.

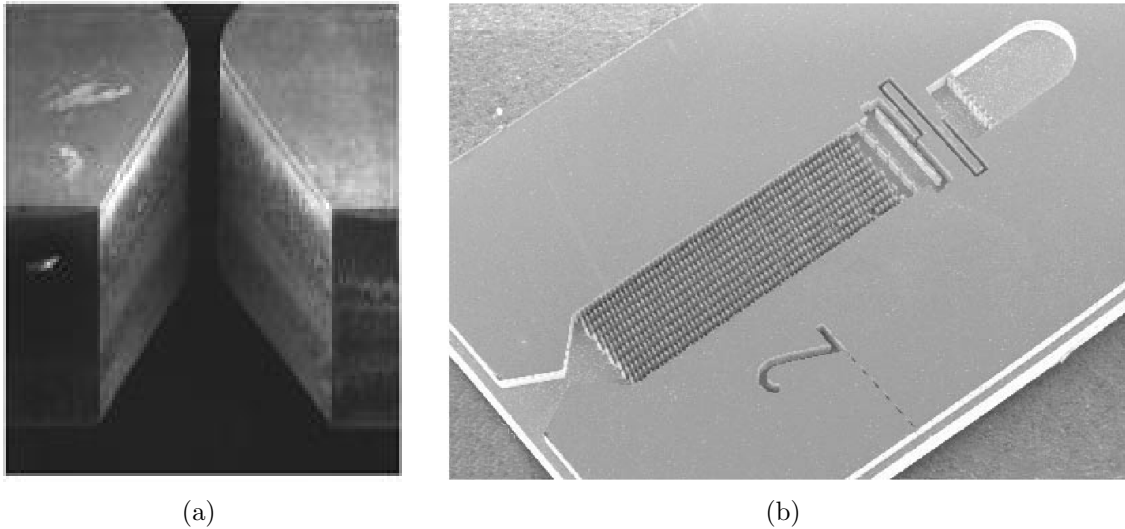


Figure 1.3 - Micronozzle examples: (a) $34\ \mu\text{m}$ throat and area ratio of 7:1;(b) $90\ \mu\text{m}$ throat and area ratio of 6.2:1.

SOURCE: (a) Bayt (1999) and (b) Hitt et al. (2001).

In this scenario, the aforementioned trending on microsatellites emphasizes the importance of the micronozzle flow understanding in the performance improvement of

⁵To keep the space vehicle in the desired mission orbit or to move it to another desired orbit.

micropropulsive systems. Since the physical processes present in microflows may be quite different from conventional macroflows, the knowledge about the flow structure in microscale is primordial in the design of these devices.

1.2 Micronozzle Flow Regimes and Features

The current state of semiconductor technology based on silicon has allowed the application of silicon plates in the manufacturing process of microscale devices. This manufacturing technique has been applied in the development of small scale systems, called as MEMS (**M**icro**E**lectro**M**echanical **S**ystems) (BEEBY et al., 2004; MALUF; WILLIAMS, 2000; VARADAN et al., 2003) and several others microdevices (EPSTEIN et al., 1997). Among the many MEMS applications are the microunits of low thrust (BAYT, 1999; JANSON et al., 1999; KETSDEVER, 2003), where micronozzles are present.

In a micronozzle flow the thermodynamic fluid properties and velocity experiences different orders of magnitude. Figure 1.4 shows a typical convergent-divergent nozzle configuration. In the inlet chamber, the pressure must be higher than its ambient value to allow a downstream flow. In this situation, even in microchambers, the flow is usually within the continuum flow regime that assumes the gas as a continuous medium without concerning about microscopic events. In this case, such a concept is reasonable since the local intermolecular collision frequency is so large that the gas and its interaction with solid surfaces⁶ can be described by means of the molecular average (macroscopic) behavior. Therefore, individual molecular processes can be neglected. In the continuum flow regime, a macroscopic approach is applied and the flow is described by spatial and temporal variations of the primary properties, e.g., pressure, density, temperature and velocity.

As the gas flows through the convergent part, it is expanded, i.e., the pressure decreases and the velocity increases. In this part, the flow remains subsonic up to the throat neighborhood, which is a transonic region. Finally, in the divergent part, the gas flow is basically supersonic and a strong expansion process drastically reduces pressure as it approaches the exit section. In this sense, near the exit section, the molecular mean free path⁷ is usually of the same order of micronozzle characteristic dimensions, e.g., the throat size. As a result, intermolecular and molecule-surface

⁶Hereafter refereed also as only surface, wall or body.

⁷The average distance traveled by the molecules between the intermolecular collisions.

collisions occur with similar frequency and then both process have equal importance. Under such conditions, from a molecular point of view, the flow is within the transitional flow regime. In this context, it is worthwhile to mention that somewhere between convergent and divergent micronozzle parts the gas flow presents different behavior, specially near the surfaces, since the flow regime changes from continuum to transitional. These phenomena are the velocity slip and the temperature jump, which characterize a different regime called as slip flow.

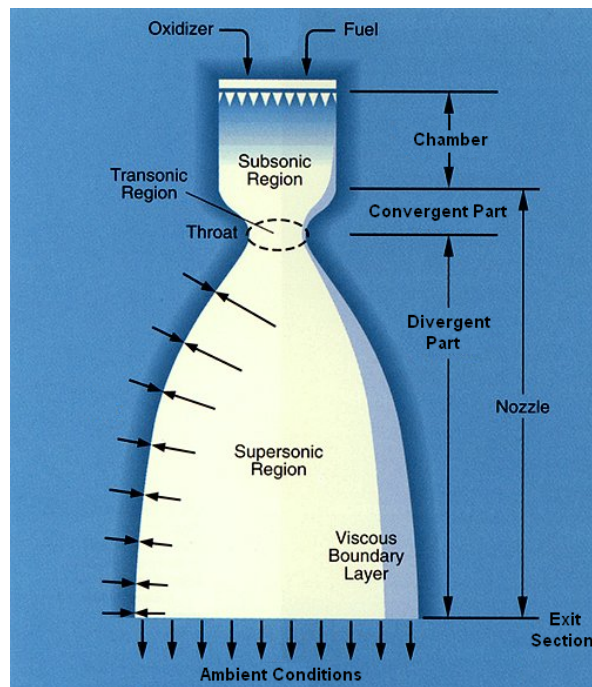


Figure 1.4 - A typical convergent-divergent nozzle configuration.
SOURCE: O’Leary and Beck (1992).

Meanwhile, if for some reason the mean free path becomes much larger than the characteristic dimension, the molecules reflected from a surface perform intermolecular collisions only far away from this wall. In such a case, the oncoming molecules do not suffer significant influence by the wall presence. In this fashion, since the molecule-surface collision frequency is much higher than the intermolecular collision frequency, the former prevails. This situation is called collisionless or free molecular flow regime. According to the present discussion, it is important to note that micronozzles operate covering different flow regimes.

In order to define quantitative limits for each flow regime, the degree of rarefaction of a flow is expressed in terms of the Knudsen number Kn defined by,

$$Kn = \frac{\lambda}{L} \quad (1.1)$$

where λ and L are the molecular mean free path and a characteristic length of the flow, respectively. According to the hard sphere model, the mean free path in an equilibrium gas with molecular diameter d and number density n – molecules per unit of volume – is:

$$\lambda = \frac{1}{\sqrt{2} n \pi d^2} \quad (1.2)$$

Since the mean free path is inversely proportional to the number density, and consequently to the pressure, it is easy to observe that the rarefaction degree is not fully defined only by the pressure condition. In the same way, it is misleading to support that all microflows present a high Knudsen number. At first, one might be tempted to select the characteristic length scale as some overall flow dimension in order to determine an overall Knudsen number. However, a better description is possible if a local Knudsen number is defined with L as the gradient length scale of a macroscopic quantity ϕ :

$$L = \frac{\phi}{|\nabla\phi|} \quad (1.3)$$

where ϕ may represent the local velocity, density, pressure or temperature. This equation shows that small values of L can be obtained by strong gradients in the flow. Consequently, the local Knudsen number is defined by the ratio of the local λ to the local L . Therefore, it is evident that in a steady state flow Kn may change spatially and also according to the macroscopic property considered.

As $Kn \rightarrow 0$, the flow is within the continuum flow regime, since rarefaction effects are not present. In the opposite limit, as $Kn \rightarrow \infty$, the flow is defined by the free molecular flow regime. The flow regime limits are depicted in Figure 1.5 in terms of the local Knudsen number.

The cold gas propulsive system is one of the most basic technologies applied in micronozzles to attitude control. In this system, micronozzle devices operate over a range of stagnation pressures that may vary from 0.1 to 6 atm, depending on the mission requirements. Nevertheless, the exit pressure normally attains near-vacuum conditions, as expected for satellite applications.

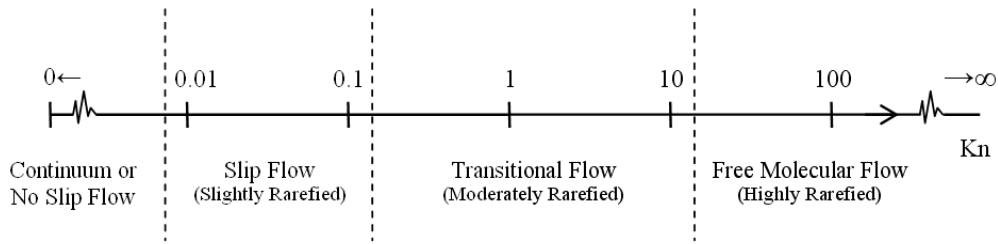


Figure 1.5 - Flow regime limits in terms of the local Knudsen number.

For illustration purposes, in a micronozzle air flow operating under the stagnation conditions of 300 K and 1 atm, the mean free path in the inlet chamber is 0.5423 nm. Assuming a consistent exit pressure of 0.01 atm, the mean free path increases to approximately 54.23 nm in the exit section. As a result, the overall Knudsen numbers in the chamber and at the exit section are approximately 0.0027 and 0.27, respectively, based on a throat size equal to 20 μm . Consequently, in such a circumstance, to describe the whole micronozzle flow as a continuum phenomenon may lead to inaccurate results. In order to overcome errors in flow prediction, the molecular processes must be taken into account. Figure 1.6 emphasizes the present example.

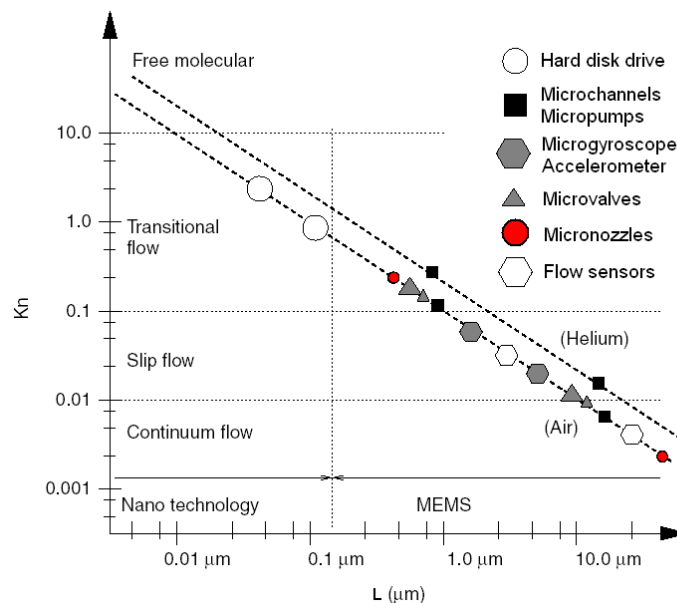


Figure 1.6 - Overall Knudsen range for typical MEMS and NEMS (Nanoelectromechanical Systems) applications under standard conditions.

SOURCE: Adapted from Beskok (2006).

Many particularities make a MEMS-based micronozzle gas flow different from a conventional macroscale convergent-divergent nozzle, i.e., a macronozzle. For instance: (i) in general the micronozzle geometry is not axisymmetric as the macronozzle geometry; (ii) usually, micronozzles have rectangular cross-sections due to their specific manufacturing processes; (iii) a reduction in the nozzle dimensions increases the influence of viscous effects on the flow, since the Reynolds number (Re) becomes small; (iv) due to a high relative roughness (Figure 1.7), the surface finishing has a significant influence on the flow structure; (v) the heat transfer can be excessively high if the wall temperature is much lower than the stagnation temperature; and (vi) the head losses due to slip flow processes may perform a significant impact.

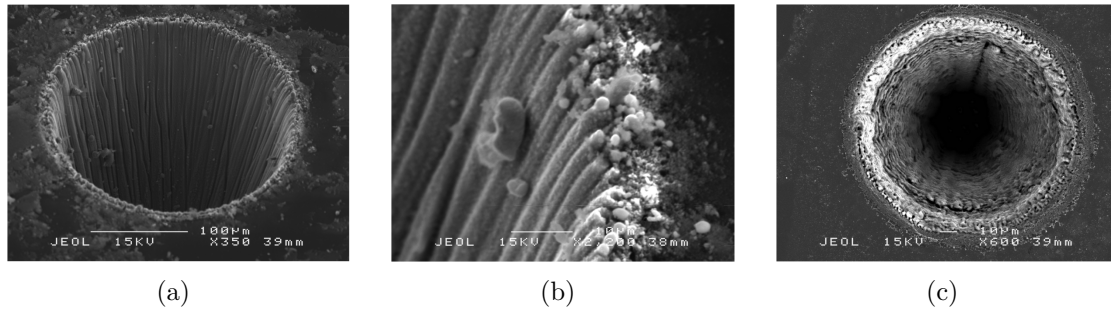


Figure 1.7 - Scanning Electron Microscope (SEM) images of surface roughness in MEMS: (a) longitudinal patterns, (b) zoomed region and (c) transversal patterns. SOURCE: Torre et al. (2010).

Moreover, when the size scale of a mechanical system changes, the influence of each present physical phenomenon may be modified. For example, if all characteristic dimensions in a system are reduced from meters to millimeters, it corresponds to a reduction in the size scale of 1 to 1000, i.e., a size scaling factor S of $1/1000$. Therefore, the characteristic length, height and width are reduced by a scale of 1 to 1000. On the other hand, the volume is reduced by $(1/1000)^3$, that is, S^3 . In this sense, the force due to the surface tension is scaled by S^1 , the electrostatic force by S^2 and the gravitational force by S^4 , i.e., the gravitational force is reduced by $S^4 = (1/1000)^4 = 1/1.000.000.000.000$, i.e., by a factor of one trillion (TRIMMER; STROUD, 2006). Consequently, changes in the dimensions of a physical system result in changes of the forces applied on this system. For this reason, the flow structure present in micronozzles is expected to be different from the one observed in macronozzles.

1.3 Previous Work

Microelectromechanical systems have been considered as an emerging technology with significant potential for future growth (HO; TAI, 1998; HO; TAI, 1996; O'CONNOR, 1992). Microactuators, microrefrigerators, microgenerators, micropumps, and micronozzles, examples of miniaturized devices, have become important because of their applications to medical and engineering problems (GAD-EL-HAK, 1999; KARNI-ADAKIS et al., 2005; SEN et al., 1996; TITOV et al., 2007). In spite of the growing number of successful applications of MEMS in scientific and engineering devices, nowadays there is only a minimum level of understanding related to the fluid dynamics and heat transfer processes in fluidic MEMS.

According to the current literature, several experimental and numerical studies related to macro- and micronozzles have been performed in order to investigate the influence of certain physical processes on the behavior of such devices. These studies have focused on, among other aspects, the micronozzle performance (BAYT et al., 1997; BAYT; BREUER, 2001a; BAYT; BREUER, 2001b; LIU et al., 2006), Reynolds number influence (KETSDEVER et al., 2005), effects of 2D versus 3D micronozzle geometries (ALEXEENKO et al., 2002a; ALEXEENKO et al., 2002c; MENZIES et al., 2002), behavior of continuum versus high rarefaction regimes (LIU et al., 2006; MO et al., 2006; TITOV et al., 2005; XIE, 2007), gas-surface interaction effects (BUONI et al., 2001; YANG; WEI, 2006), temperature influence (ALEXEENKO et al., 2002b; ALEXEENKO et al., 2005; JONES; MATTICK, 2003; WANG; LI, 2004a), geometric effects (CHEN et al., 2005; CHOUDHURI et al., 2001; HAO et al., 2005) and performance of propulsive systems with micronozzles arranged in array patterns (HORISAWA et al., 2009). For the purpose of this review, only some relevant studies are described below.

Based on a continuum approach, Sivells (1955) proposed a method to design two-dimensional supersonic nozzles with continuous surface curvature, e.g., De Laval nozzle (SHAPIRO, 1954). By assuming an ideal fluid flow, this method estimates the nozzle length. Then, by correcting this assumption, the nozzle profile is obtained by taking into account the effects of the boundary layer growth. The aim of these results was to supply data for practical configuration of wind tunnels with flexible plates, which were adjusted by discrete points. Then, in order to improve the accuracy of this matching, the method required even a continuous third derivative⁸ through the

⁸The radius of curvature of a function depends on the second derivative of this same function. In this sense, the rate of change of this curvature depends on the third derivative.

inflection point in the divergent part.

Also based on a continuum approach, [Back et al. \(1965\)](#) and [Manson et al. \(1980\)](#) performed experiments with macronozzles of conical and rectangular cross-section, respectively. Both studies showed that the surface radius of curvature at the throat must be at least twice the throat size in order to maximize the mass flux efficiency, i.e., to maximize the discharge coefficient. Thereby, they observed that the transonic region is influenced by the throat radius of curvature.

[Epstein et al. \(1997\)](#) sketched the state of the art related to thermal microsystems, e.g., gas microturbines and bipropellant microengines. They described several advantages provided by the use of MEMS. Finally, they emphasized key points to apply this technology, e.g., the magnitude of the forces involved, characteristic times in chemical reactions, thermal and mechanical properties of the raw materials and limitations in the manufacturing processes.

[Bayt and Breuer \(2001a\)](#) have fabricated a micronozzle integrated with a heat exchanger, i.e., a microresistojet. Silicon was used to fabricate both structural and electrical items, such a scheme simplified the integration of the devices. They observed that the increase in the flow energy due to heat exchange reduced the mass flow required for a same level of thrust. In short, such an energy exchange contributed to save fuel.

The performance of a micronozzle was also studied by [Bayt and Breuer \(2001b\)](#). The efficiency was experimentally evaluated by the discharge coefficient, thrust, specific impulse I_{sp} and impulse efficiency Ψ , defined by the Equation 1.4. The displacement and momentum thickness were also calculated numerically for several Reynolds numbers. In this situation, the aim was to estimate the influence of the viscous effects, which reduce the effective exit area. Then, it was suggested to maximize the ratio between the micronozzle transversal dimension (depth) to the micronozzle exit dimension in order to reduce the influence of the boundary layer developed on the plane surfaces, i.e., the not contoured surfaces.

$$\Psi = \frac{I_{sp_{real}}}{I_{sp_{ideal}}} \quad (1.4)$$

[Hitt et al. \(2001\)](#) have described the progress of some space agencies in the design of micropropulsive systems. They mentioned briefly advantages and disadvantages of

different propellants for such systems. Moreover, they presented characteristics and constructive data of a MEMS-based micropropulsive system via catalyzed hydrogen peroxide decomposition.

Alexeenko et al. (2002a) have studied numerically the performance of axisymmetric and three-dimensional micronozzles with rectangular cross-section by using continuum and kinetic approaches. Effects of the gas-surface interactions on the flow structure were investigated by a statistical model. The simulations showed that the distribution of the macroscopic properties is highly dependent on the dimensionality of the micronozzle flow simulation. Moreover, the impact of the gas-surface interactions on thrust level was investigated for axisymmetric, two- and three-dimensional micronozzles. For the conditions examined, they observed that the gas-surface interactions present in the three-dimensional case reduce the thrust level by approximately 5% and 20% in comparison to the axisymmetric and two-dimensional cases, respectively. Therefore, the prediction of three-dimensional micronozzle flows by using a two-dimensional approach may lead to significant errors. Finally, three-dimensional numerical results obtained for $Re \approx 200$ showed good agreement with experimental data.

Titov et al. (2008) have simulated a three-dimensional micronozzle flow with stagnation pressure of the order of 5 atm and Reynolds numbers varying from 200 to 2000. In such a level of pressure, the standard statistical methods commonly applied to describe microflows become inefficient due to the excessive computational cost. On the other hand, the continuum approach is not adequate to predict flows with the high rarefaction conditions observed in the micronozzle exit. Hence, in order to overcome the difficulties due to different spatial scales and the high viscous effects present in the flow, they proposed a modified statistical method based on the kinetic approach. However, the level of agreement between numerical and experimental results varied with the geometry and boundary conditions of the micronozzle.

Recently, Horisawa et al. (2009) performed numerical studies in micronozzles with rectangular cross-sections. The behavior was investigated for two conditions, single and array patterns, as demonstrated in Figure 1.8. Simulations for a single micronozzle showed good agreement with experimental data. Finally, the numerical results for the array fashion demonstrated a representative increase in the system performance as well as considerable changes on the external flow structure.

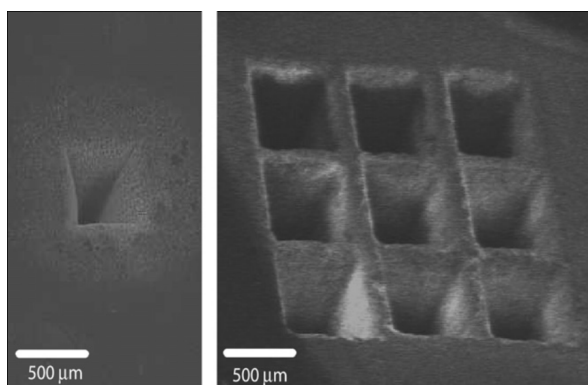


Figure 1.8 - Comparison of micronozzle arrangements: single versus array pattern.
SOURCE: Horisawa et al. (2009).

1.4 Purpose of the Present Work

According to the relevant literature, most studies have investigated the micronozzle performance for different length scales and flow conditions. However, these investigations have not focused on the influence of the surface curvature on the micronozzle flow structure. In macronozzles, it is known that discontinuities on the surface affect the system performance due to the arising of shock waves inside the devices. Furthermore, it has been observed that the Mach number distribution along the centerline is related to the wall curvature (FROST; LIEPMAN, 1952; RAO, 1961; SIVELLS, 1955).

From a geometric point of view, the divergent micronozzle part can be divided into two regions: a convex region from the throat to the inflection point, where the nozzle surface is gradually curved away from the symmetry plane, and a concave region from the inflection point to the nozzle lip, where the surface is curved back until it is nearly parallel to the symmetry plane. The Figure 1.9 shows a schematic drawing of the micronozzle divergent part.

In this fashion, the present study aims to investigate the effect of the slope and curvature of the divergent surface on the flow structure, aerodynamic properties as well as on the micronozzle performance. The flow structure is understood as the distribution of the primary properties, e.g., velocity, density, pressure and temperature, in the whole flowfield. The aerodynamic properties are defined as the heat flux to and the normal and tangential forces acting on the surface. Such properties are usually expressed in terms of heat transfer, pressure and skin friction coefficients,

respectively. Finally, the micronozzle performance is expressed by the thrust and/or the specific impulse.

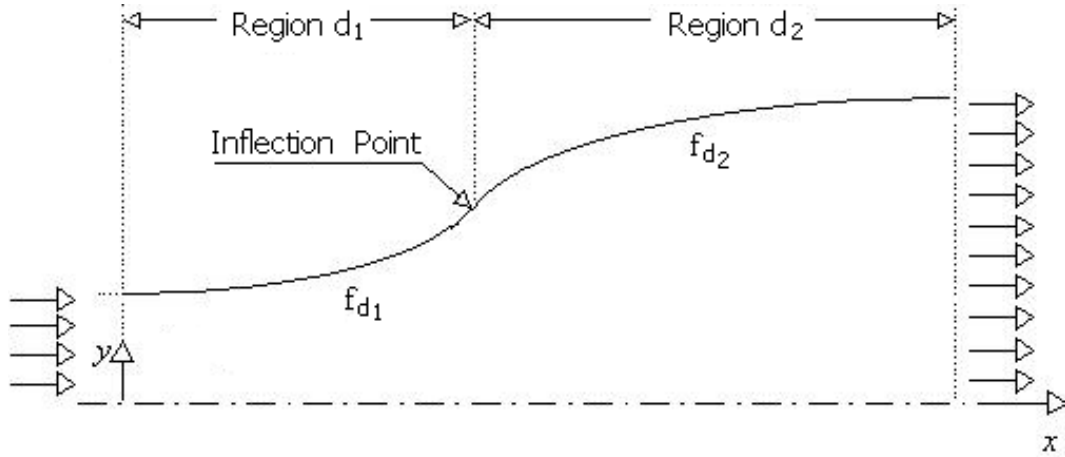


Figure 1.9 - Schematic drawing of the micronozzle divergent section.

Two functions f_{d_1} and f_{d_2} are defined to represent the surface shape in the regions d_1 and d_2 , respectively. In this connection, f'_{d_1} and f'_{d_2} (first derivative of f_{d_1} and f_{d_2}) represent a local slope for the respective surface. Similarly, f''_{d_1} and f''_{d_2} (second derivatives) are related to the local radius of curvature. Therefore, the goal of this study is objectively to provide a comprehensive description of the micronozzle flow by considering different situations at the inflection point, as defined in Table 1.2.

In order to obtain further insight into the physics of micronozzle flows, a numerical simulation of a rarefied flow in a convergent-divergent micronozzle, with rectangular cross-section, is performed in the present work. Such a device is considered as part of a micronozzle array. The inlet and outlet boundary conditions are based on pre-defined values of pressure. In general, the performance of propulsive systems is highly dependent on the aerodynamic design of the divergent nozzle portion. In this scenario, for a defined area ratio, the influence of different divergent shapes on the flowfield structure is investigated by employing the Direct Simulation Monte Carlo (DSMC) method. Such an information has primordial importance in the design and development of micronozzles, which can be implemented in small satellite propulsive systems.

The remainder of the present dissertation is discussed in detail into six more chapters.

Table 1.2 - Proposed geometric configurations for the micronozzle divergent surface.

Case		Condition at the Inflection Point		
Group	Number	f_{d_2}/f_{d_1}	f'_{d_2}/f'_{d_1}	$ f''_{d_2} / f''_{d_1} $
A	1			1
	2	1	1	>1
	3			<1
B	1			1
	2	1	>1	>1
	3			<1
C	1			1
	2	1	<1	>1
	3			<1

In order to guide the reader, an overview of each chapter is provided as following.

Chapter 2: Initially, historical data about MEMS is provided in this chapter. Afterwards, it is discussed physical aspects that classify a microflow and then the concepts of different flow models are introduced.

Chapter 3: A detailed description of the appropriate DSMC method is presented in this chapter. Particular attention is paid on the DSMC methodology, elastic and inelastic collisions, molecular models, collision sampling and boundary conditions.

Chapter 4: The geometric definitions, boundary conditions as well as all important assumptions adopted in the computational procedures are pointed out in this chapter.

Chapter 5: This chapter is devoted to outline the verification and validation processes of the DSMC code employed in the present simulations. The verification procedure is applied to one of the cases proposed in this dissertation. On the other hand, the validation process is applied to a test case defined by a convergent-divergent micronozzle that has experimental and numerical results.

Chapter 6: The major features of the numerical solutions obtained in the simulations are presented and discussed in this chapter. These results are ex-

pressed in terms of the primary properties, aerodynamic coefficients and normalized specific impulse.

Chapter 7: The last chapter outlines the main results and conclusions drawn in this research. Finally, further investigations are proposed as future work in order to clarify open question that should be included on the present dissertation.

2 FLUID FLOW PHYSICAL ASPECTS

2.1 Microflow General Issues

The early studies on rarefied gas flows were developed at the beginning of the last century. At that time, experimental researches were performed on the mass flow rate of a gas in tiny tubes (KNUDSEN, 1909) and on the drag of small spheres in the air (KNUDSEN; WEBER, 1911; MILLIKAN, 1911; MILLIKAN, 1923), i.e., low speed microscale flows. Later, due to the requirements of the aerospace exploration, the studies on rarefied gas flows focused on hypersonic flows around bodies. Finally, at the end of the last century, the interest in microflows returned. However, after a century, the motivation in microflow research has changed from a basic science issue to engineering and scientific applications with high potential for worldwide market. According to Gad-el-Hak (2006b), the global funding for micro- and nanotechnologies have quintupled from 1997 to 2002, and in 2004 the nanotechnology investments exceeded US\$ 3.5 billion. For the next decade, it is estimated that micro- and nanotechnology markets will represent around US\$ 820 billion per year in the worldwide economy.

The MEMS technology is moving faster than a complete comprehension of the microscale phenomena. In this sense, the recent interest in MEMS technology demands a better understanding of the physical processes present in microscale devices. The challenges present in microflow studies are related to high rarefaction effects, viscous dissipation, compressibility, molecular processes and thermal creep¹, among others. In MEMS, for instance in micronozzles, the gas density may change several orders of magnitude. Therefore, the complexity required to model such flows increases due to the presence of different flow regimes.

From the experimental branch in MEMS, several questions have been pointed out when its results cannot be predicted or explained by conventional continuum approach. Besides, many MEMS concepts cannot be appropriately tested because of the lack of facilities capable of measuring very small values of the physical quantities. The current spatial sensor resolutions are not sufficient to describe completely a microflow. Spatial resolutions smaller than 100 μm are normally obtained by more expensive and complex systems. In short, under laboratory conditions it is a difficult

¹Thermal creep is a microscale phenomenon that can cause pressure variations along microtubes with tangential temperature gradients.

and expensive task to carry out reliable microflow researches. In order to overcome these difficulties, some appropriate analytical and numerical methods may be employed to solve microflow problems, which are typically within the transitional flow regime. The correct choice of a specific method or model will depend on the rarefaction degree, complexity and characteristics of the flow.

2.2 Flow Classification

The flow is usually characterized by an amount of dimensionless parameters, in which each one of them has its own physical meaning. In the case of MEMS, without significant heat exchange between the gas flow and the solid surfaces, e.g., the cold gas micronozzles, the main parameters are the Mach number M , the Reynolds number Re , and the Knudsen number Kn .

The Mach number is expressed by the ratio of the local macroscopic flow speed V to the local sound speed a . The sound speed is the speed at which a small pressure disturbance, in a wave form, propagates through a compressible medium. According to the conservation equations, for a steady and isentropic process, the wave propagation phenomenon depends on the local rate of change of the pressure p with respect to the density ρ . If the medium is assumed as a calorically perfect gas, the sound speed can be expressed in terms of the thermodynamic temperature T , i.e., in terms of the translational and internal molecular excitation. Therefore, from a continuum point of view, the disturbance propagates due to the elastic nature of the fluid. In contrast, from a molecular point of view, the disturbance is propagated by random intermolecular collisions that perform momentum exchange. The present discussion is summarized by Equation 2.1, where γ is the ratio of specific heats, k is the constant of Boltzmann and m is the molecular mass.

$$M = \frac{V}{a} = \frac{V}{\sqrt{(\partial p / \partial \rho)_s}} = \frac{V}{\sqrt{\gamma k T / m}} \quad (2.1)$$

The Mach number physical meaning can be understood as a dynamic measure between the inertial and compressibility forces, or also as a measure of the directed motion of the molecules compared to the random thermal motion of the molecules. It is worthwhile to observe that the square of the Mach number, called Cauchy number, is related to the ratio of the kinetic energy to the thermal energy. As a result, at very small Mach numbers, the flow speed is considerably smaller than the sound speed and hence the inertial forces are not capable to perform a significant density

variation. In such a case, the compressibility effects are negligible and the flow may be considered as incompressible ($\Delta\rho = 0$). Generally, a flow is considered as compressible if the local fractional change in density is too large to be ignored, namely, $\Delta\rho/\rho \geq 0.05$. Moreover, the typical cutoff Mach number separating incompressible and compressible isothermal flows is $M = 0.3$. Under such a Mach number value, it can be mathematically proved that pressure change errors provided by assuming a constant density are around 3% (SAAD, 1993). It must be emphasized that a small Mach number is a sufficient criterion for incompressibility only in the absence of other physical process, such as an intense heat transfer, which can cause strong density changes. Finally, the Mach number also classifies the flow regime in terms of the fluid flow energy. As a rule of thumb, for $M < 1.0$ the flow is subsonic, $M = 1.0$ the flow is sonic, $0.8 < M < 1.4$ the flow is transonic, $1.0 < M < 5.0$ the flow is supersonic and for $M > 5.0$ the flow is hypersonic.

The Reynolds number Re is the dimensionless parameter that classifies the flow as either laminar or turbulent. This number is a measure of the ratio between the inertial and viscous forces present in the flow. The laminar flow occurs for small Re values. In a limit case with $Re \ll 1$, the viscous forces are predominant in the flow problem and then the inertial effects may be neglected. In a laminar flow, adjacent fluid layers move smoothly towards each other in the streamwise direction. On the other hand, if $Re \gg 1$, the inertial forces overcome the viscous forces. As a result, flow disturbances may not be damped effectively by the viscous forces. This process may develop random eddies and a complex flow behavior. Such a regime is called by turbulent flow. Depending on the flow, a transitional regime may develop. It is important to note that this transitional regime – laminar to turbulent – has a different physical meaning in comparison to the transitional flow regime in the rarefied context. Additionally, another possible classification according to the viscosity influence is expressed in terms of viscous and inviscid flows. Equation 2.2 defines the Reynolds number, where L is a characteristic length in the flow and μ is the dynamic viscosity.

$$Re = \frac{\rho V L}{\mu} \quad (2.2)$$

As aforementioned, the Knudsen number definition in Equation 1.1 establishes it as the ratio of the mean free path to a characteristic length in the flow. As briefly discussed in the Section 1.2, the Knudsen number describes the rarefaction degree of a flow, and according to the local value of Kn the flow can present different

physical behaviors. Depending on this dimensionless parameter, the flow regime may be basically classified as continuum, slip, transitional or free molecular. Thus, based on the Knudsen number, it is possible to define the appropriate approach to model the problem. Figure 2.1 summarizes schematically the present flow classification in terms of the Knudsen, Reynolds and Mach numbers.

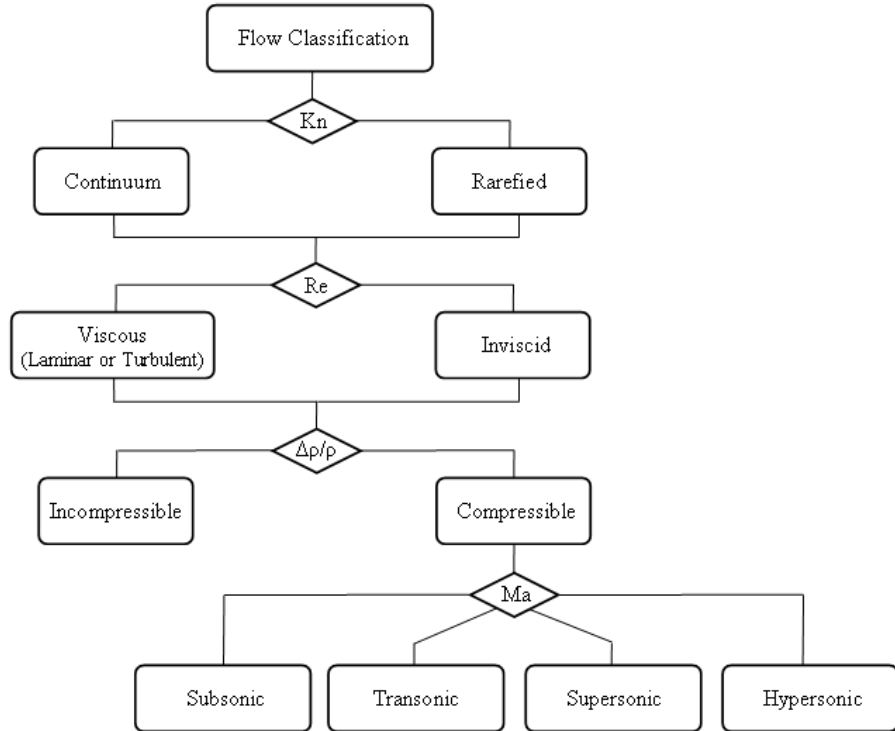


Figure 2.1 - Flow classification in terms of dimensionless parameters.

Another very important information characterized by the Kn value is the degree of thermodynamic equilibrium in a flow. In order to predict the failure of the thermodynamic equilibrium and continuum assumptions, several breakdown parameters were proposed (BIRD, 1970; BIRD, 1980; BIRD, 2002; BOYD, 1995; GEORGE; BOYD, 1999; WANG; BOYD, 2003). Since the failure of these assumptions is related to viscosity and heat transfer, the breakdown parameter is essentially dependent on the local Knudsen numbers based on velocity, density and temperature. Roughly speaking, a large breakdown parameter indicates a large nonequilibrium degree. In general, the assumption of thermodynamic equilibrium in a flow with a local $Kn=0.05$ provides errors of approximately 5% (BOYD, 2002). Some physical explanations for such errors are that, under high rarefaction degree, the intermolecular collision frequency

is not sufficient to ensure a local isotropic phase space of velocities. In addition, the number of molecules per unit volume within infinitesimal fluid elements, used in continuum descriptions, may differ considerably from the average.

2.3 Flow Modeling

In the fluid mechanics field, the fluid can be modeled based on two points of view: (1) as the matter is really composed, a molecular arrangement, or (2) as a continuum medium where the matter is assumed continuously and infinitely divisible. The first method, called as microscopic or molecular model, describes the fluid as consisting of molecules whose motion is governed by the laws of dynamics. The molecular treatment can be performed by two schemes: (i) the deterministic or (ii) the probabilistic. On the other hand, the continuum model describes the flow in terms of temporal and spatial changes of the macroscopic properties. Under specific assumptions, this approach employs the conservation of mass, momentum and energy to provide a set of nonlinear partial equations that govern the flow. In Figure 2.2, a general fluid modeling chart is depicted. The relation between these models is discussed in the following.

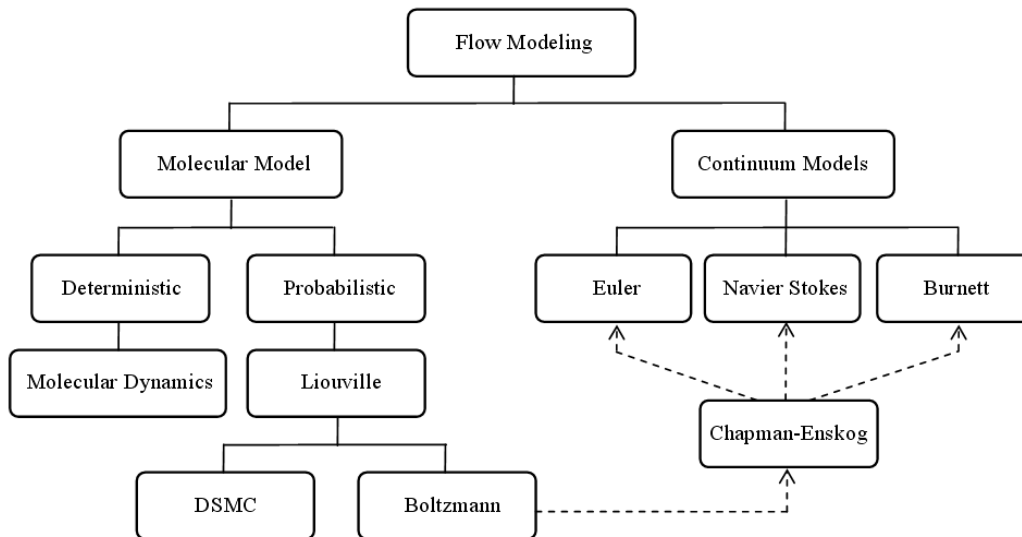


Figure 2.2 - Flow modeling classification.
SOURCE: Adapted from Gad-el-Hak (2006a).

In the continuum model, the molecular nature of the fluid is not considered. For

meaningful results, the local macroscopic quantities, e.g., velocity, density, pressure or temperature, are defined as averages over fluid elements that must be sufficiently small when compared with the smallest significant macroscopic length in the flow but sufficiently large to contain a representative number of molecules. These requirements allow the use of differential and integral calculus to describe the flow and to assure that the statistical fluctuation level in the assumption of a local average process is small. Probably due to the analytical resources, this model is more familiar than the molecular approach to most fluid dynamicists.

In such a continuum treatment, the fluid properties are the dependent variables while the spatial coordinates and time are the independent ones. However, only the conceptual equations for the conservation of mass, momentum and energy do not form a closed set of equations. Consequently, some additional relations between the unknown functions must be assumed to establish a closed system. In the continuum approach, this situation is overcome by assuming constitutive relations for the fluid nature. For instance, when the flow is in thermodynamic equilibrium or near to it, i.e., under a very small Kn condition, the shear stress is assumed linearly proportional to the strain rate (a Newtonian fluid) as well as the heat flux linearly proportional to the temperature gradient (Fourier's Law). Based on the former constitutive relation, the well known Navier-Stokes equations for linear momentum conservation are obtained. Nevertheless, within the expression *Navier-Stokes equations* the conservation equation of mass and energy are commonly included.

In the limit of zero Knudsen number, the transport phenomena that occur by molecular processes may be neglected by assuming an inviscid and nonconducting fluid. Therefore, the transport terms in Navier-Stokes equations vanishes. In such a case, one defines the Euler equations that, for an incompressible flow, can be further integrated along a streamline to result in the Bernoulli equation. The last formulation provides a straight relation between pressure and velocity.

When the flow deviates from thermodynamic equilibrium, e.g., in the transitional flow regime, the constitutive relations used to derive the Navier-Stokes equations must be updated to take into account rarefaction and nonlinear effects. Consequently, additional high-order nonlinear terms are required in the stress tensor and heat flux vector. In this connection, each extra term represents an order of departure from the thermal equilibrium. The second-order approximation of these transport terms yields the Burnett equations (BURNETT, 1935), whose interest has grown

over the years in despite of the many analytical and numerical difficulties associated with these equations (CHAPMAN; COWLING, 1970; FISCKO; CHAPMAN, 1988; ZHONG, 1991; WELDER *et al.*, 1993; COMEAUX *et al.*, 1995; BALAKRISHNAN; AGARWAL, 1996). Since Burnett equations contain derivatives higher than second-order, additional boundary conditions are required to determine an unique solution, and then such a result can be dependent on the selected boundary values (LEE, 1994). Moreover, the conventional Burnett equations may violate the Second Law of Thermodynamics at high Knudsen numbers (COMEAUX *et al.*, 1995). Finally, Agarwal (2006) presented an overview of Burnett equations and its variations in addition to results of numerical simulations for hypersonic and microdevice flows.

Continuum treatment should be applied as long as the flow does not deviate significantly from thermal equilibrium. As the nonequilibrium degree increases, deriving the required constitutive relations becomes an increasingly complex and time consuming mathematical and numerical enterprise. In this scenario, the alternative is to invoke a molecular-based model, which recognizes the fluid structure as a myriad of discrete particles² and ideally determines position, velocity and thermal state of every particle at all times. Since there is a representative number of particles within the smallest significant fluid volume, the local macroscopic quantities can be obtained by averaging processes from the discrete molecular information.

In molecular models, the microscopic processes performed by particles, for instance, motion, collision, energy exchange, are described by laws of classical or quantum mechanics. The main deterministic molecular treatment, called Molecular Dynamics (MD) method (ALDER; WAINWRIGHT, 1957; ALDER; WAINWRIGHT, 1958), considers the motion and molecular interactions deterministically, although it does use probabilistic procedures for the initial molecular positions and states. After the motion, collisions are considered if different molecule volumes overlap one another. The MD method is more suitable to study liquids or dense gases near the critical point. Due to the high computational requirement, such an approach should be employed when continuum or molecular statistical methods are inadequate.

From a classical point of view, a flow can be completely described by determining the coordinates, velocities and internal state of each molecule at a particular time. However, even in a small fluid portion, the number of molecules is so large that indi-

²The expression particles, in the present context, may represent molecules, atoms, ions and electrons.

vidual treatment (e.g., by Newton's laws) would be impossible. Therefore, in order to specify the molecular information, a statistical approach must be employed. This description is expressed in terms of distribution functions, namely, $f = f(\mathbf{r}, \mathbf{c}, t)$. Such a function provides the number of molecules within a particular infinitesimal range of time t , position \mathbf{r} and thermal state³, i.e., within an infinitesimal element of the phase space⁴.

As presented in Equation 2.3, the Boltzmann equation describes the time evolution of the velocity distribution function for a single system of particles. This is an integro-differential conservation equation for f and represents a fundamental formulation in kinetic theory.

$$\left(\frac{\partial}{\partial t} + \mathbf{c} \cdot \frac{\partial}{\partial \mathbf{r}} + \mathbf{a} \cdot \frac{\partial}{\partial \mathbf{c}} \right) f(\mathbf{r}, \mathbf{c}, t) = \left(\frac{\partial f}{\partial t} \right)_{coll} \quad (2.3)$$

Basically, it states that the rate of change of the number of molecules in a fixed phase space element may be caused by the following process: (i) the convection of molecules across the physical space volume element due to the molecular motion; (ii) the change of the velocity class of the molecules – molecules that cross the velocity space element – as a result of an external force \mathbf{F} per mass m unity, namely, $\mathbf{a} = \mathbf{F}/m$; and (iii) the depletion and replenishment of molecules within the velocity space elements due to intermolecular interactions. The latter process is described by a nonlinear integral, called collision integral, which is the major source of mathematical difficulties.

In such an equation, the velocity distribution function is the unique dependent variable. However, the independent variables increase according to the number of physical variables on which the thermal state depends. As aforementioned, in a monatomic gas flow, these variables are the time, three spatial coordinates and three molecular velocity components, i.e., seven independent variables in a six-dimensional phase space. In order to construct a specific solution to the Boltzmann equation, all physical process, initial and boundary conditions, must be specified in terms of their relations with the velocity distribution function. Finally, when the local velocity distribution function $f(\mathbf{c})$ of a given flow is known, the macroscopic quantities concerned in fluid dynamics can be computed by finding moments of the probability

³Here, it is assumed a monatomic gas whose thermal state is uniquely defined by the translational mode, i.e., by the molecular velocity vector \mathbf{c} .

⁴Similarly the continuum mathematical treatment, the range of variables considered in such an element must be sufficiently small, so that the range of the distribution function within this element is small. Therefore, this element may be referred as a point in the phase space.

distribution function f/n . These values are obtained by multiplying f/n by a certain function of the molecular velocity, $Q = Q(\mathbf{c})$, and then taking the integral over the appropriate velocity space.

In the Boltzmann equation derivation, a number of important assumption are made: (i) the fluid must be a dilute gas⁵ so that only binary collisions are considered; (ii) the effects of external forces on the collision process are small in comparison to the intermolecular forces acting between these particles; (iii) the molecular chaos, i.e., at any position and time the velocities of two different particles are uncorrelated; and (iv) the distribution function is essentially constant along a distance comparable to the molecular diameter d and over a time comparable to the duration of a collision (KOGAN, 1969; VINCENTI; KRUGER, 1965). Additionally, some arguments, e.g., the *inverse collisions*⁶, must be established to facilitate the handling of the collision integral. Basically, this argument allows to express the post-collision velocities in terms of the initial velocity parameters.

The Boltzmann equation is formally defined through the derivation from the Liouville equation. The latter describes the motion of a gas, consisting of a sufficiently large number N of particles, in a $6N$ -dimensional phase space, where $3N$ particle coordinates and $3N$ velocity components are expressed. By applying repeated integration of the Liouville equation, a hierarchy (a sequence) of relations, called BBGKY equations (Bogolyubov-Born-Green-Kirkwood-Yvon) (KOGAN, 1969) are obtained. In essence, such general equations may take into account triple and multiple collisions, and then hold important principles for the description of dense gases.

The conservation equations of mass, momentum and energy can be established by applying the moment of the Boltzmann equation, the so-called moment equations or equations of transfer. For a gas flow in complete equilibrium, i.e., with all zero gradients ($Kn \rightarrow 0$), the velocity distribution function holds everywhere the Maxwellian form f_0 . Similarly, if a specific region in the flow holds sufficiently small gradients, it is still reasonable to consider a local equilibrium. Based on these two assumptions, the

⁵When the mean molecular spacing δ is large compared with the effective molecular diameter d , namely $\delta/d \gg 1$. In such a case, only a minor fraction of the space occupied by the gas holds a molecule. Then, molecules will travel, in most time, without influence of other molecules. For example, for air under standard conditions, the relation of microscopic distances results in $\lambda : \delta : d \approx 170 : 10 : 1$.

⁶By definition, the inverse of a given (original) collision is a collision that have (i) initial velocities equal to the post-velocities of the original collision and (ii) the same direction of the line center (VINCENTI; KRUGER, 1965). See also Section 3.3.1.

Euler and Navier-Stokes equations can be obtained by employing the moment equations, respectively. An alternative approach is embodied in the Chapman-Enskog theory for the transport terms. In this case, the Boltzmann equation is solved by assuming the velocity distribution function f as a small perturbation of the equilibrium condition, as follows in Equation 2.4.

$$f = f^{(0)} + \varepsilon f^{(1)} + \varepsilon^2 f^{(2)} + \dots \quad (2.4)$$

In this equation, the term $f^{(0)}$ represents the Maxwellian distribution f_0 , ε is a parameter that provides a measure of the Knudsen number, i.e., $\varepsilon = \varepsilon(Kn)$, $\varepsilon f^{(1)}$ is the first-order correction term of f , $\varepsilon^2 f^{(2)}$ is the second-order correction term and so on. Since in a perturbation technique the higher order term is a correction of the lower one, particular attention should be paid to the fact that such an approach is valid only for small values of Kn , that is, for small departures from the equilibrium state. Finally, the approximations of zeroth order ($f = f_0$), first-order ($f = f^{(0)} + \varepsilon f^{(1)}$) and second-order ($f = f^{(0)} + \varepsilon f^{(1)} + \varepsilon^2 f^{(2)}$) yield the constitutive relations defined in the Euler, Navier-Stokes and Burnett equations, respectively. Figure 2.3 presents the limits of typical mathematical formulations expressed in terms of the local Knudsen number.

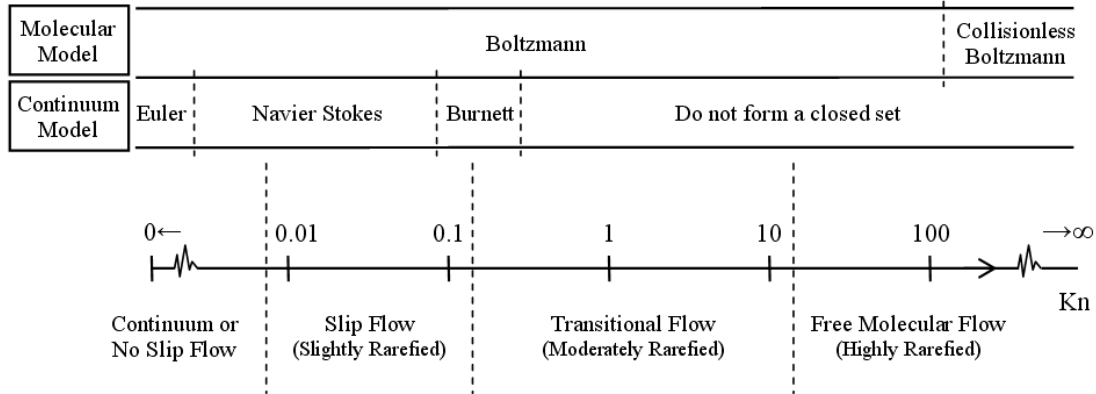


Figure 2.3 - The Knudsen number limits on the mathematical models and flow regimes.

At this point it is clear that, at least for small Knudsen numbers, the molecular statistical approach is able to match with the continuum models. However, due to mathematical difficulties, analytical solutions of the Boltzmann equation are possible only for a restrict range of simple flow cases. In this connection, in spite of this *ana-*

lytical classification, the final results of the Boltzmann equation generally depend on numerical calculations, and exact solutions are even more rare. In order to overcome these limitations, instead of pursuing analytical solutions to such a complex mathematical model, numerical methods attempt to reproduce the flow physics by direct simulation. Since such direct simulation methods share with considerable rigor the most physical basis and assumptions used in Boltzmann equation, they can be considered a *solution* of this equation. In this context, from a molecular approach, the following numerical methods may be employed for (i) direct solution: direct Boltzmann CFD (Computational Fluid Dynamics) (NORDSIECK; HYCKS, 1967; YEN, 1970; TAN et al., 1989), integral method (KOGAN, 1969), discrete velocity method (BROADWELL, 1964; GATINOL, 1970); or for (ii) direct simulation (of the flow physics): test particle Monte Carlo (HAVILAND; LAVIN, 1962; HAVILAND, 1965; KOGAN, 1969), lattice Boltzmann (AGARWAL; YUN, 2006; CHEN; DOOLEN, 1998) and direct simulation Monte Carlo (DSMC) (BIRD, 1976; BIRD, 1994).

Finally, for the purpose of the present work, only the DSMC method will be explained in the following.

3 DIRECT SIMULATION MONTE CARLO METHOD

3.1 Overview

The Direct Simulation Monte Carlo¹ (DSMC) method is a particle direct simulation technique based on the kinetic theory of gases. This method was first proposed and applied by Bird (1963) to investigate homogeneous gas relaxation and shock wave structure (BIRD, 1965) problems. Subsequently, this method was improved to study complex multidimensional problems in the fields of gas dynamics and physical-chemistry (BIRD, 1976; BIRD, 1994). Currently, several reviews of DSMC method are available (BIRD, 1978; BIRD, 1998; BIRD, 2001; CHENG, 1993; CHENG; EMMANUEL, 1995; MUNTZ, 1989; ORAN et al., 1998; PRASANTH; KAKKASSERY, 2006).

In essence, both DSMC and Boltzmann equation are based on the same physical basis. They are subject to the same limitations, namely, the assumption of molecular chaos and the restriction to dilute gases. In the treatment of molecular interactions, both approaches demand the introduction of physical models. However, as DSMC deals with particles individually, the implementation of realistic models into direct simulation environment is easier than their development by mathematical formulation. The key difference between DSMC and Boltzmann equation solver is that the former method does not depend on the existence of inverse collisions (BIRD, 1994). As a result, the applicability of this method have now gone beyond the range of validity of the Boltzmann equation.

The DSMC method has become the most common computational technique for modeling complex transitional flows of engineering interest. This method can be applied to a wide range of rarefied flows within regimes that neither Navier-Stokes nor collisionless Boltzmann² equations are appropriate. In the past 50 years, DSMC results have been validated through comparisons with analytical and experimental data in excellent agreement (BIRD, 1990; HARVEY, 1986; HARVEY; GALLIS, 2000; HARVEY; GALLIS, 2003; HOLDEN; WADHAMS, 2003; PHAM-VAN-DIEP; MUNTZ, 1989). In spite of the early DSMC applications were performed on hypersonic and high altitude problems, the recent studies on rarefied flows are beyond the aerospace sci-

¹According to Hammersley and Handscomb (1964), Monte Carlo methods comprise that branch of experimental mathematics that concerns with experiments on random numbers.

²Collisionless Boltzmann equation is a particular case of the original formulation. When the Knudsen number tends to infinity the intermolecular interactions can be neglected. As a result, the collision integral drops out the equation, providing tremendous simplifications (NARASHIMA, 1962).

ence. Among other applications are the aforementioned microscale gas flows and the design and processing of materials, e.g., low-pressure simulations on CVD (Chemical Vapor Deposition) and PVD (Physical Vapor Deposition) processes.

The present direct simulation method takes advantage of the fact that physical processes are described by the behavior of individual molecules instead of using distribution functions. Such an approach provides, without considerable changes in the basic procedures, the following advantages: simple treatment of complex geometries; easy extension of one-dimensional problems to two- and three-dimensional ones; the existence, uniqueness, convergence and stability issues are irrelevant because of the physical basis of the method; possibility for parallel computing; and applicability of different suitable models to treat surface and intermolecular interactions, including models that concern with internal degrees of freedom and chemical reactions. In this context, many complex physical phenomena can be studied with DSMC, for instance, mixture of chemical species, relaxation of internal energy modes, chemical reactions, such as dissociation and recombination, ionization, radiation, multiple collisions and gas-surface interactions such as absorption, surface reactions and desorption.

In order to reduce computational cost, the idea of this particle simulation method is to restrict the number of simulated particles to a manageable level since it is impossible to simulate all real molecules in a flow. In this sense, the DSMC method models real gas flows as a collection of simulated particles of correct physical size where each simulated particle represents a specific number of real molecules. Each particle holds its own position, velocity components and internal states that are stored and modified with time as these particles move or interact with each other or physical boundaries within the computational domain.

Subject to the hypothesis of dilute gas, the key principle of the DSMC method is to split, for a given interval of time, the continuous process of molecular motion and interactions into two subsequent stages: free molecular movement and molecular collision relaxation. Molecules are moved deterministically over distances appropriate to their velocities and the chosen discrete time step, while collisions have a statistical treatment. A computational grid of cells is applied to represent the physical domain to be studied. These cells are employed to simulate collisions and to sample the local microscopic quantities. In the collision procedure, only interactions between particles located within the same cell are allowed at a given time step. Since molecular chaos is assumed, the changes in the distribution function are supposed to be small

within the cell. As a result, the relative distance between particles is not taken into account when they collide.

In this scenario, the method requires a cell size smaller than the local mean free path, namely $\lambda/3$, in order to avoid a nonphysical transfer of momentum and energy. This requirement is even more severe in the direction of strong gradients. Additionally, the cell size must assure that changes of the flow quantities within every cell are small in order to provide a suitable resolution in the average process. For these different reasons, the sampling and collision grids could be different and sometimes a coarse sampling grid can be used³.

Another primary requirement in DSMC is related to the time discretization. As mentioned, the particle motion and intermolecular collisions are decoupled over discrete time steps that can represent the real time. In order to be consistent with this uncoupling, the time step must be everywhere smaller than the local mean collision time. Another requirement is related to the mean residence time⁴, which must be smaller than the time step. This condition aims to avoid that particles cross more than one cell during a given time step. In this fashion, they will not be able to move without the possibility of collisions. The infringement of such a requirement causes a *smearing* of the macroscopic properties, providing nonphysical results.

An additional DSMC requirement concerns to the minimum number of simulated particles per cell. As noted before, this method employs a cell scheme for the sampling of microscopic properties and for the collision procedures. In this way, N should be large enough to avoid statistical fluctuations in the sampling process. Since the collision rate depends on the number N of simulated particles within the cell, then it is desirable to have N as large as possible. In this manner, the collision rate would be more realistic, and the mean collision separation⁵ δ_{mcs} would be reduced, which minimizes the smearing of gradients. On the other hand, as N increases, the number of possible collision pairs selected for the collision process becomes excessive. In such a way, it is desirable to have N as small as possible in order to reduce the computational cost. This conflict can be overcome by introducing the subcell scheme

³For instance, in a given region of the flow with both very small λ and macroscopic gradients.

⁴The mean time that particles take to cross a given cell. Evidently, this time depends on the local molecular velocities and cell sizes.

⁵The mean distance between particles involved in a collision event. Since particle positions are ignored, this distance and cell size may have the same order. Hence, one of the criteria for consistent DSMC results is that $\delta_{mcs}/\lambda \ll 1$ everywhere.

(BIRD, 1987) that consists in subdividing the collision cell into a set of subcells for the selection of collision pairs. This implementation improves the results and method consistency because it assures that collisions occur only with neighboring particles. Moreover, this technique minimizes the nonconservation of angular momentum in each collision (MEIBURG, 1986), although the total angular momentum within a cell is almost conserved if cell size requirements are met (BIRD, 1987; NAMBU et al., 1988). Finally, subject to these requirements, research study results have shown that each cell must contain around 20 to 30 particles (SHU et al., 2005).

At this point, it is clear that DSMC simulations provide improved results as time step and cell size tends to zero as well as the number of simulated particles tends to infinity. However, excessive number of simulated particles or temporal and spatial discretization should be avoided in order to attain a high DSMC performance.

In direct simulations, the initial and boundary conditions are expressed in terms of the individual molecular behavior instead of distribution functions. Initially, an arbitrary state of the flow, such as vacuum or uniform equilibrium, is set. At the inlet boundaries, the state of entering molecules is specified according to the correspondent local macroscopic state. As molecules interact with solid boundaries an appropriate treatment is employed. Consequently, from an initial configuration, the flow develops with time in a natural manner instead from an artificial iteration process based on initial and final estimations of the flowfield.

The present method employs an explicit time marching technique and, essentially, its results are always nonstationary. In order to study unsteady flows, an ensemble⁶ of independent simulations may be computed and averaged to establish final results. Results for steady problems correspond to a unique unsteady problem sampled for sufficiently large times to obtain an acceptable statistical accuracy.

Currently, different of the continuum CFD branch, there are only a few numerical packages that employ the fundamental schemes of DSMC. In general, these implementations differ mainly in the collision selection procedures, interaction physical models and grid strategies. Among these packages, the most used are: DS2V/3V (BIRD, 2005), DAC (DSMC Analysis Code) (LEBEAU, 1999), SMILE (Statistical Modeling In Low-Density Environment) (IVANOV et al., 1998), MONACO (DIETRICH; BOYD, 1996), IP (Information Preservation) method (SHEN, 2000), DSMC with

⁶A suitable group of similar systems (replicas).

MLG (Monotonic Lagrangian Grid) (CYBYK *et al.*, 1995), PDSC (Parallel Three-Dimensional DSMC Code) (WU *et al.*, 2005), and SWPM (Stochastic Weighted Particle Method) (RAJASANOW; WAGNER, 1996).

3.2 DSMC Methodology

The primary numerical procedures employed by the DSMC method are depicted in the flowchart presented in Figure 3.1. In each time step iteration, the DSMC algorithm may be conveniently composed of four subsequent and independent steps: (i) move the simulated particles and treat boundary interactions; (ii) index the particles, (iii) sort the particles and simulate collisions and (iv) sample and average particles information.

The computational domain is initialized as vacuum or an uniform gas flow in thermodynamic equilibrium. Such an initial state may be based on the freestream conditions of the physical space. Velocity, density, pressure, temperature and internal energy of the gas entering in the computational domain, over each time step, are specified in terms of known boundary conditions. The velocity of simulated particles is defined as a linear combination of the thermal velocity and the stream velocity. The boundary conditions that correspond to the desirable flow are imposed at the beginning of time counting so that steady flows are obtained after sufficient time evolution. Finally, steady results are provided by averaging processes of the information sampled after the steady state is achieved.

After defining position, velocity and internal state of all simulated particles, these particles are moved over distances corresponding to their velocity components and the current time step. Consequently, the new position of the particles must be determined. Such an information can be obtained in different ways. For Cartesian computational domains, the new position and cell are rapidly identified by the tracking scheme proposed by Bird (1994). For computational domains with structured and unstructured grid, several particle tracking schemes are presented in the literature (DIETRICH, 1990; LAUX, 1997). For more complex computational grids, such as hexahedral or tetrahedral types, others schemes can be employed to determine the particle position (CHEN, 1997; MACPHERSON *et al.*, 2009; NANCE *et al.*, 1997; WILMOTH *et al.*, 1996).

Once the particle position is known, appropriate actions are applied if the particle

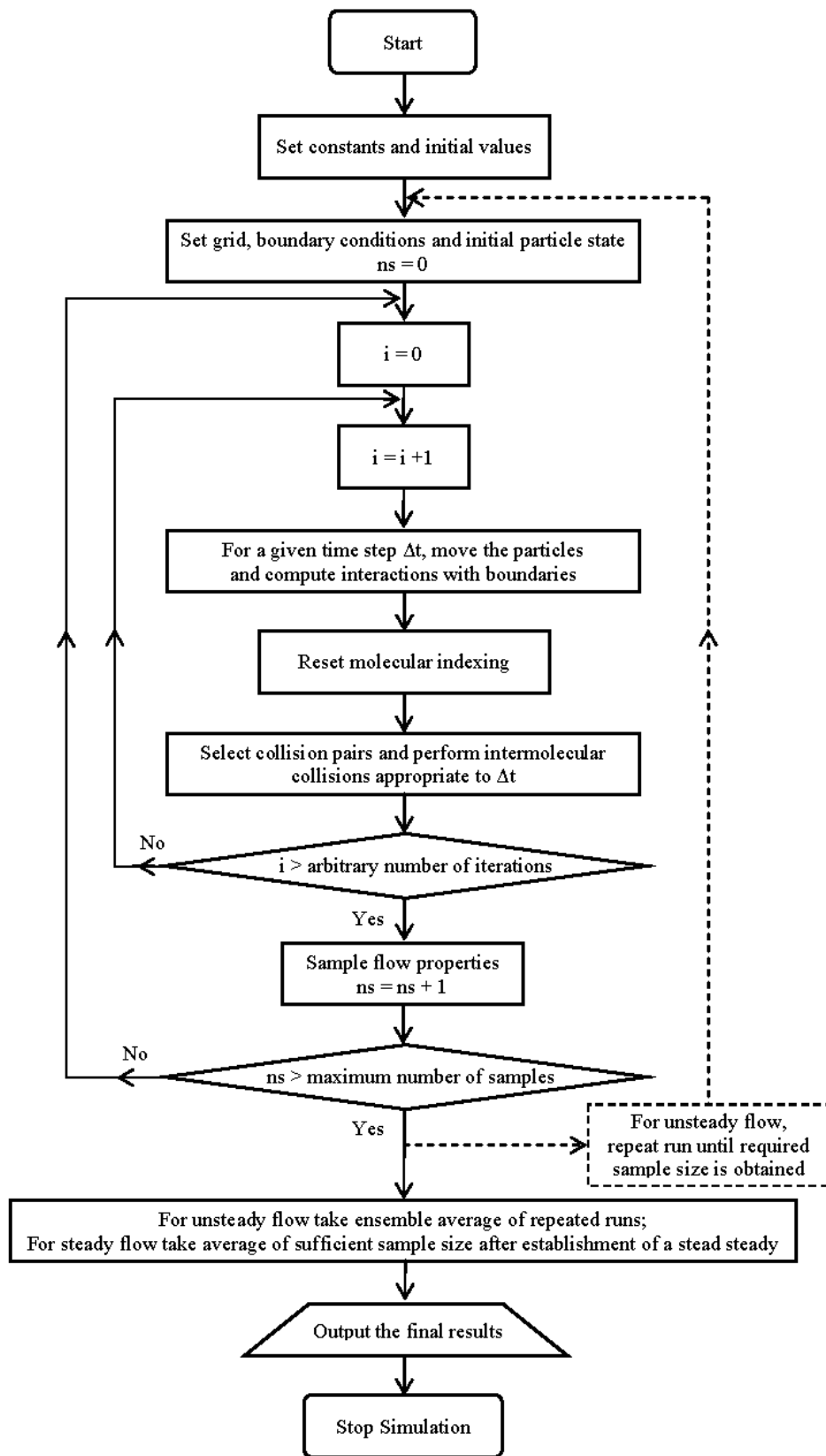


Figure 3.1 - Typical DSMC flowchart.

interacts with a solid boundary, plane of symmetry or external flow boundary. Particles that leave the computational domain are removed from the simulated flow. Then, based on freestream macroscopic information, new particles are introduced into the simulation through the external boundaries of the computational domain. Molecule-surface collisions are commonly treated as specular, diffuse or a combination of these types. Furthermore, more sophisticated surface chemistry models, e.g., absorption, surface reactions and desorption can also be employed (BERGEMANN, 1995; SIMMONS; LORD, 1997).

At this stage, the particles must be indexed in a convenient manner. In general, such a sorting is related to the particle position. This procedure is used for two subsequent steps: calculate intermolecular collisions and obtain particles information samples. For the selection of collision pairs and the calculation of intermolecular collisions, each cell is defined in an index scheme so that all molecules within this cell can be located by a reference list. An efficient index scheme was proposed by Bird (1976) in the original DSMC algorithm.

Once the molecules are indexed, the next step is the computation of intermolecular collisions. Such interactions are treated statistically whereas the particles are moved deterministically. Different schemes for simulating collision rates have been developed and applied in DSMC method. These schemes infer, in a given time step, the correct number of representative collisions from pairs of molecules selected randomly within each cell. Such a calculation is a key point to ensure a consistent flow simulation. Among these schemes, it can be pointed out the *Time Counter* (TC) method (BIRD, 1976), the *Nambu* method (NAMBU, 1986), the *Majorant Frequency* method (IVANOV; ROGAZINSKII, 1988), the *No Time Counter* (NTC) method (BIRD, 1989), the *Null Collision* (NC) method (KOURA; MATSUMOTO, 1991), the *Randomly Sampled Frequency* (RSF) method (FAN; SHEN, 1992) and the *generalized NTC* method (ABE, 1993). The NTC method has been widely employed in DSMC simulations in recent years.

The collision procedure is generally performed within individual cells. In this sense, the time step, the cell volume and the number of molecules per cell are fundamental parameters to determine the number of probable collision pairs. These pairs are randomly selected and they are also subjected to the requirement that the mean collision separation between them must be a small fraction of the mean free path. Such a requirement is imposed by selecting collision pairs randomly, but preferably,

from the same subcell or from the neighboring ones. Then, selected collision pairs are accepted or not based on a probabilistic strategy. Once a particular collision event is accepted, a molecular model is employed to assure linear momentum and energy conservation for the post-collision state.

Finally, the primary steps are concluded by applying the sampling process of the microscopic information in each cell. These data are averaged in an appropriate manner in order to provide the local macroscopic properties, such as velocity, density, pressure and temperature. In short, the DSMC method calculates the macroscopic properties based on averages of the microscopic information.

3.3 Binary Elastic Collisions

3.3.1 Scattering

In dilute gases, the molecules perform a continuous motion and occupy only a small fraction of the available space. In this sense, ternary collisions (three body collisions) are very rare events. A rough estimative shows that the probability for such an interactions to occur in a gas is about $(d/\delta)^3$ (SHEN, 2000). As a result, for dilute gases ($\delta/d \gg 1$), e.g., for air under ambient conditions, which provides $\delta/d \approx 8$, this probability is less than 0.3%. Therefore, the binary collisions are overwhelmingly more likely. An elastic collision is defined as one in which there is no interchange between translational and internal energies. Then, the momentum and energy conservation equations are employed with geometric parameters to describe a collision mathematically, i.e., post-collision velocities are determined from pre-collision information.

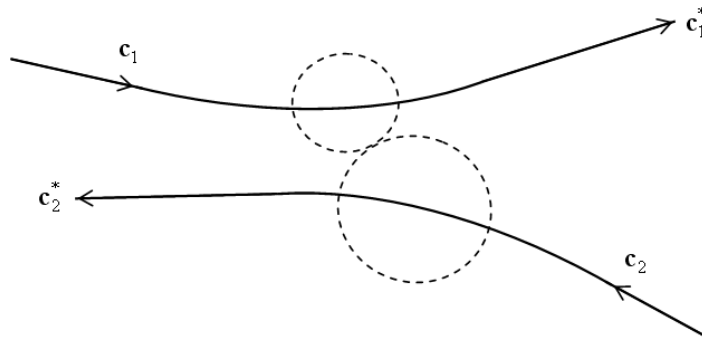


Figure 3.2 - Planar representation of a binary collision in the laboratory frame.

Given two monatomic molecules in a binary collision, their pre-collision velocities in the laboratory frame of reference may be denoted by \mathbf{c}_1 and \mathbf{c}_2 as illustrated in Figure 3.2. If the physical properties and trajectories of these molecules are known, the post-collision velocities \mathbf{c}_1^* and \mathbf{c}_2^* can be determined. Hence, the linear momentum and energy conservation equations for two molecules of mass m_1 and m_2 yield:

$$m_1\mathbf{c}_1 + m_2\mathbf{c}_2 = m_1\mathbf{c}_1^* + m_2\mathbf{c}_2^* = (m_1 + m_2)\mathbf{c}_m \quad (3.1)$$

$$m_1c_1^2 + m_2c_2^2 = m_1c_1^{*2} + m_2c_2^{*2} \quad (3.2)$$

where it is introduced the center of mass velocity \mathbf{c}_m of the present pair of molecules.

$$\mathbf{c}_m = \frac{m_1\mathbf{c}_1 + m_2\mathbf{c}_2}{m_1 + m_2} = \frac{m_1\mathbf{c}_1^* + m_2\mathbf{c}_2^*}{m_1 + m_2} \quad (3.3)$$

According to Equation 3.3 the center of mass velocity is not changed by the collision process because of the linear momentum conservation. Moreover, the relative pre- and post-collision velocities between the molecules can be written as:

$$\mathbf{c}_r = \mathbf{c}_1 - \mathbf{c}_2 \quad (3.4a)$$

$$\mathbf{c}_r^* = \mathbf{c}_1^* - \mathbf{c}_2^* \quad (3.4b)$$

By combining Equations 3.1 and 3.4, the pre-collision velocities $\tilde{\mathbf{c}}_1$ and $\tilde{\mathbf{c}}_2$ relative to the center of mass can be obtained, and the same procedure is valid for the post-collision velocities $\tilde{\mathbf{c}}_1^*$ and $\tilde{\mathbf{c}}_2^*$ as follows.

$$\tilde{\mathbf{c}}_1 = \mathbf{c}_1 - \mathbf{c}_m = \frac{m_2}{m_1 + m_2}\mathbf{c}_r \quad (3.5a)$$

$$\tilde{\mathbf{c}}_2 = \mathbf{c}_2 - \mathbf{c}_m = -\frac{m_1}{m_1 + m_2}\mathbf{c}_r \quad (3.5b)$$

$$\tilde{\mathbf{c}}_1^* = \mathbf{c}_1^* - \mathbf{c}_m = \frac{m_2}{m_1 + m_2}\mathbf{c}_r^* \quad (3.6a)$$

$$\tilde{\mathbf{c}}_2^* = \mathbf{c}_2^* - \mathbf{c}_m = -\frac{m_1}{m_1 + m_2}\mathbf{c}_r^* \quad (3.6b)$$

From Equation 3.5, it can be observed that in the center of mass reference frame the pre-collision velocities of the two molecules are antiparallel, and hence their

trajectories will lie in the same plane. Additionally, it is assumed that molecules are centers of force, i.e., the force between them acts only between their centers. As a result, throughout the collision, the intermolecular force and trajectories remain in the same plane that was previously determined by the pre-collision velocities. Equation 3.6 shows that the post-collision velocities are also antiparallel in the center of mass frame. Therefore, in such a frame the collision is completely planar.

The energy conservation equation, Equation 3.2, can be rewritten by using Equations 3.5, 3.6 and the definition of reduced mass m_r .

$$m_1 c_1^2 + m_2 c_2^2 = (m_1 + m_2) c_m^2 + m_r c_r^2 \quad (3.7a)$$

$$m_1 c_1^{*2} + m_2 c_2^{*2} = (m_1 + m_2) c_m^2 + m_r c_r^{*2} \quad (3.7b)$$

where

$$m_r = \frac{m_1 m_2}{m_1 + m_2} \quad (3.8)$$

Thus, the total kinetic energy in the laboratory frame is equal to the kinetic energy of the total mass moving with the center of mass speed plus the kinetic energy of a molecule of mass m_r moving with the relative speed. Moreover, from the energy conservation, Equation 3.2, and Equation 3.7, it can be observed that the magnitude of the relative velocity remains the same throughout the collision, i.e.,

$$c_r = c_r^* \quad (3.9)$$

By using Equation 3.9 and the fact that pre- and post-collision velocities are antiparallel in the center of mass frame of reference, the conservation of angular momentum in such a frame ($c_r b = c_r^* b^*$) only requires that the impact parameter b^7 , i.e., the projected distance between the pre-collision velocities, remains unchanged after the collision. The representation of the collision in the center of mass frame is depicted in Figure 3.3.

At this point, the conservation equations of linear momentum, angular momentum and energy have been employed (five equations). However, the present challenge is to determine the post-collision velocities of the two molecules (six scalar unknowns), which requires another equation. Since \mathbf{c}_m , \mathbf{c}_r and b can be obtained from the pre-

⁷It can also be called as *miss-distance*, i.e., the distance of the closest approach of the undisturbed trajectories of the two molecules in the center of mass frame.

collision information, the determination of the post-collision velocities in the center of mass frame reduces to the calculation of the deflection angle χ . This angle indicates the direction change of the relative velocity vector.

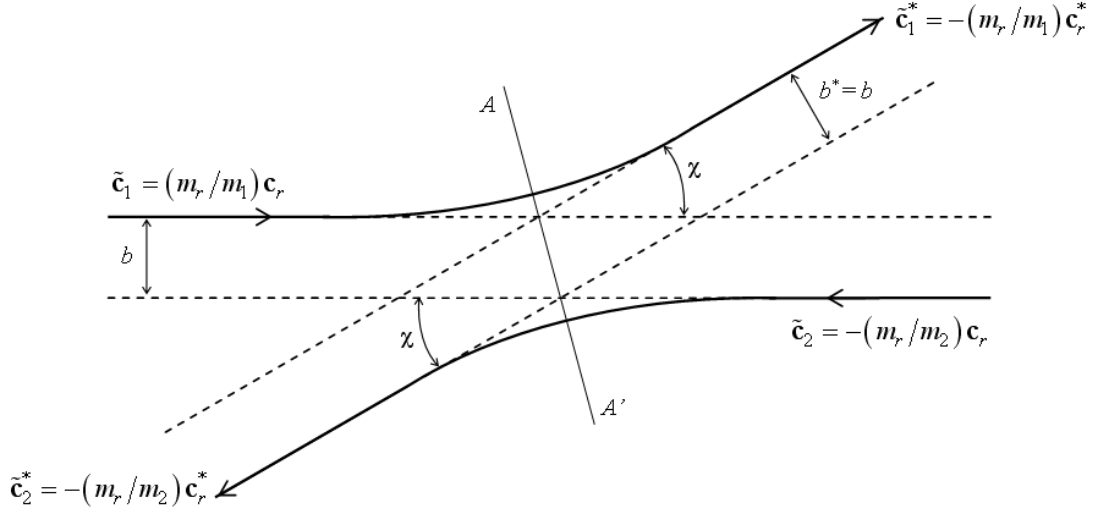


Figure 3.3 - Trajectories of the molecules in the center of mass frame.

As assumed earlier, the molecules are centers of force spherically symmetric. In this scenario, by introducing \mathbf{F} as the force between the two molecules involved in the collision, and \mathbf{r}_1 and \mathbf{r}_2 as their position vector, the motion equations for these molecules are given by:

$$m_1 \ddot{\mathbf{r}}_1 = \mathbf{F} \quad (3.10a)$$

$$m_2 \ddot{\mathbf{r}}_2 = -\mathbf{F} \quad (3.10b)$$

If Equation 3.10a is multiplied by m_2 and Equation 3.10b by m_1 , such dynamic relations can also be rewritten as:

$$m_1 m_2 (\ddot{\mathbf{r}}_1 - \ddot{\mathbf{r}}_2) = (m_1 + m_2) \mathbf{F}$$

Now, the relative velocity is denoted as $\mathbf{c}_r = \dot{\mathbf{r}}_1 - \dot{\mathbf{r}}_2 = \dot{\mathbf{r}}$ and the reduced mass definition is again employed to yield:

$$m_r \ddot{\mathbf{r}} = \mathbf{F} \quad (3.11)$$

Therefore, the relative motion of the two molecules in the laboratory frame of reference is equivalent to the motion of a molecule of mass m_r relative to a fixed center of force (Figure 3.4). Such a force depends only on the distance r from the fixed center and is commonly expressed in terms of a potential field $\phi(r)$. Since $F = -d\phi/dr$, for a given intermolecular potential field and pre-collision information, Equation 3.11 can be solved for the value of χ . In other words, this equation is coupled with the five aforementioned conservation equations in order to form a closed set.

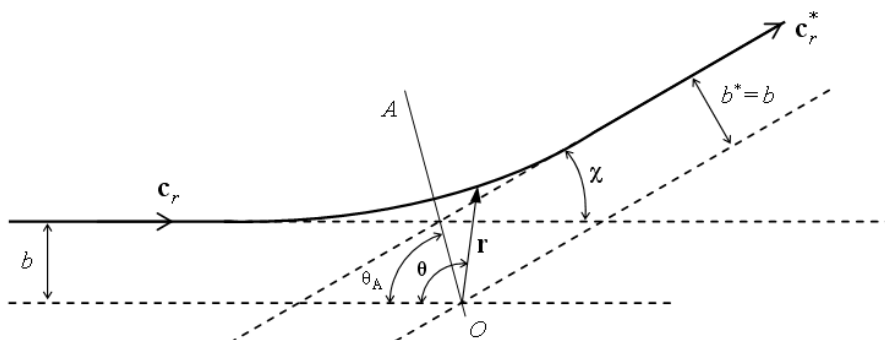


Figure 3.4 - Interaction of the reduced mass particle with a fixed scattering center.

Once the value of χ is determined, the angle ε between the collision plane and some reference plane can be obtained by purely geometric reasoning. In this sense, the post-collision velocities expressed previously in the collision plane and in the center of mass frame of reference can be rewritten in terms of the laboratory frame of reference (SHEN, 2000).

Herein, the transformation from the laboratory to the center of mass frame of reference reduces the three-dimensional trajectories into two-dimensional ones in the collision plane. Such new trajectories are symmetrical about the apse line AA' , due to the antiparallel velocities. A further transformation from the center of mass to the reduced mass frame of reference reduces the two trajectories to one that remains symmetrical about the new apse line, which passes through the scattering center O . Another consequence of this symmetry can be observed if a given collision between molecules of pre-collision velocity \mathbf{c}_1^* and \mathbf{c}_2^* , and impact parameter b is performed in the center of mass frame. As indicated in Figure 3.5, such an event results in post-collision velocities \mathbf{c}_1 and \mathbf{c}_2 and is called as the inverse ($\mathbf{c}_1^*, \mathbf{c}_2^* \rightarrow \mathbf{c}_1, \mathbf{c}_2$) of the original collision ($\mathbf{c}_1, \mathbf{c}_2 \rightarrow \mathbf{c}_1^*, \mathbf{c}_2^*$).

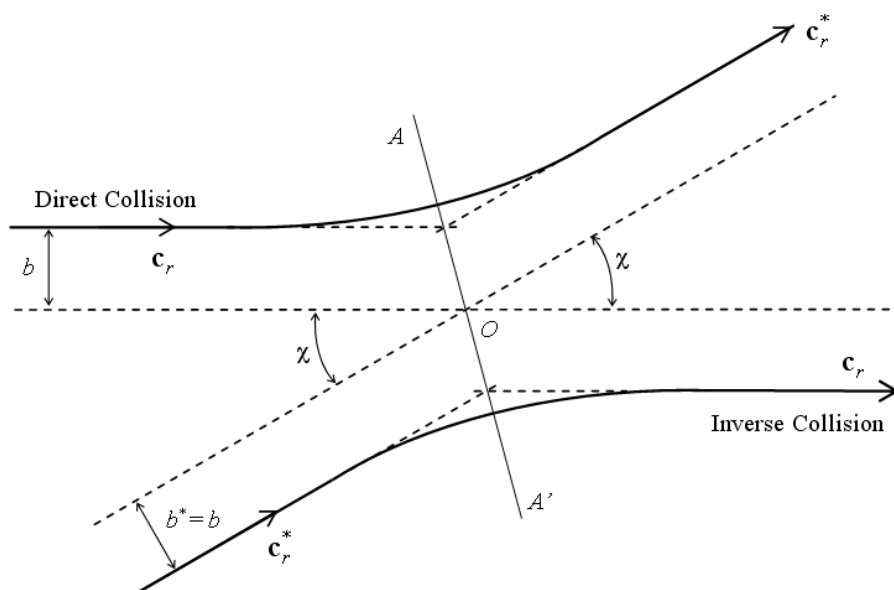


Figure 3.5 - Direct and inverse collisions in the reduced mass frame of reference.

3.3.2 Cross Section

At this point it is worthwhile to introduce the concept of a cross-section. A hard elastic sphere of diameter d provides an oversimplified but useful model of a molecule. From Figure 3.6(a), it is clear that two molecules of diameter d_1 and d_2 collide if their trajectories are such that the distance between their centers decreases to d_{12} , where $d_{12} = (d_1 + d_2)/2$. On the other hand, as shown in Figure 3.6(b), one molecule can be represented by a *sphere of influence* of radius d_{12} , while all other molecules are represented only by their centers. In this scenario, a collision occurs when the undisturbed trajectory (center) of a molecule overlaps the sphere of influence. In the reduced mass frame, such an event can be represented in a plane Υ normal to \mathbf{c}_r that crosses the center of this virtual sphere. In this case, the total collision cross-section σ_T is the area contained in this plane as indicated in Figure 3.7(a).

As previously discussed, the intermolecular potential field $\phi(r)$ and two impact parameters – b and ε – related to the geometric information of the collision must be specified in order to determine the post-collision velocities. A primary role of the intermolecular potential is to establish, for a given \mathbf{c}_r , a relationship between b and the deflection angle χ , i.e., $\chi = \chi(\mathbf{c}_r, b)$. Since these angle and pre-collision velocities are known, the post-collision velocities can be completely described.

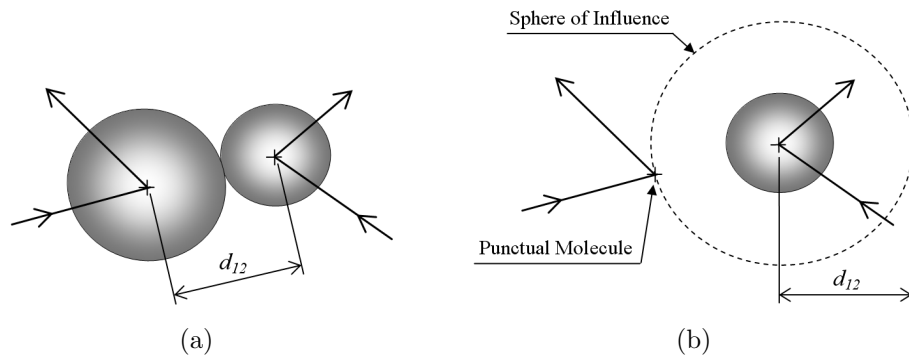


Figure 3.6 - (a) Actual collision between two hard spheres and (b) the representation of the same collision by a sphere of influence and a punctual molecule.

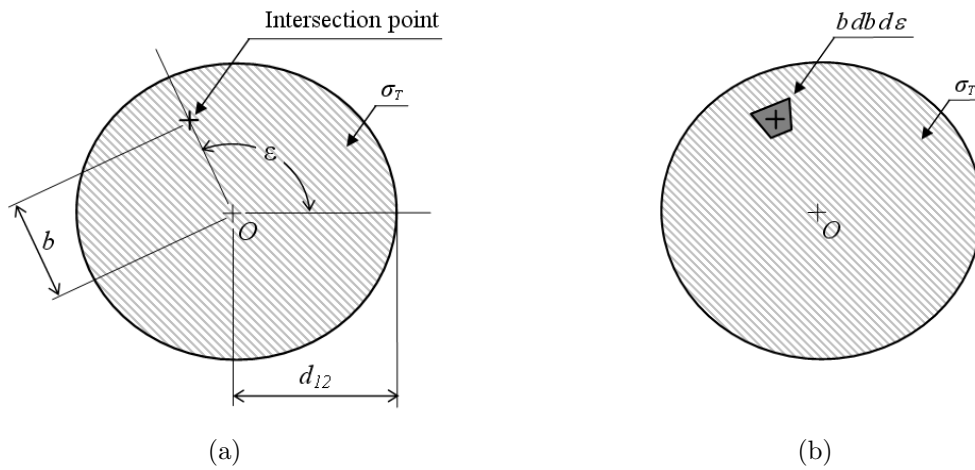


Figure 3.7 - Geometric information of the collision on the plane Υ : (a) Intersection between the undisturbed trajectory and σ_T and (b) the representation of the differential area, within σ_T , near the intersection point.

A general form to express such a relationship is set in terms of the differential collision cross-section $\sigma d\Omega$. First, as illustrated in Figure 3.4, a given collision that is performed in the fixed scattering center O with \mathbf{c}_r must be considered. In such a collision, the undisturbed trajectory of the particle of mass m_r crosses the total collision cross-section. Without loss of generality, this intersection occurs through the differential area $b db d\epsilon$ pointed out in Figure 3.6(b). Then, roughly speaking, $\sigma d\Omega$ indicates that the molecules crossing this differential area would be scattered within a range $d\chi$ and $d\epsilon$ near to \mathbf{c}_r^* . For a detailed geometric explanation, additional literature is available (BIRD, 1994; SHEN, 2000; VINCENZI; KRUGER, 1965).

By performing an appropriate integration of $\sigma d\Omega$, the total collision cross-section σ_T can be set. In essence, this variable is required to determine if a collision occurs or not. Moreover, σ_T is primordial to establish fundamental data in the molecular modeling, e.g., the collision frequency, the mean free path and the transport coefficients. Nevertheless, σ depends on the relationship between b and χ . Such a relation is based only on the intermolecular force \mathbf{F} that models the collision. As a consequence, σ_T depends on the potential field $\phi(r)$ employed.

The most simplified molecular model is that one introduced in Figure 3.6. In this model the molecules are assumed as rigid and nonattractive spheres that perform elastic collisions, behaving as billiard balls. Hence, this approach considers a collision between molecules of species p and q , whose effective⁸ diameters are d_p and d_q , respectively. Therefore, the requirement for a collision is that the distance between their centers decreases to $(d_p + d_q)/2$. Consequently, the total collision cross-section is given by:

$$\sigma_{T_{pq}} = \pi \frac{(d_p + d_q)^2}{4} = \pi d_{pq}^2 \quad (3.12)$$

where

$$d_{pq} = \frac{(d_p + d_q)}{2} \quad (3.13)$$

With this result, the mean collision rate ν_{pq} for molecules of specie q with molecules of specie p can be obtained according to Equation 3.14. This value is the reciprocal of the mean collision time, and it is also called collision frequency:

$$\nu_{pq} = n_q \overline{\sigma_{T_{pq}} c_{r_{pq}}} \quad (3.14)$$

where, n_q represents the number density of specie q , i.e., the number of molecules of specie q per unit of volume. Moreover, for a constant total collision cross-section, the latter equation can be rewritten as:

$$\nu_{pq} = \pi d_{pq}^2 n_q \overline{c_{r_{pq}}} \quad (3.15)$$

3.4 Molecular Model

The molecular behavior in the collision process depends on the choice of the intermolecular force field. In general, such a field is assumed to be spherically symmetric,

⁸In general, for attractive molecular models the effective diameter is somewhat larger than the geometric diameter. Then, a molecule is influenced by the other one before they perform contact.

so that the force between molecules is a function only of the distance r between their centers. Features of different typical intermolecular force fields are depicted in Figure 3.8 for molecules with diameter d . The real representation shows that molecules interact with a weak attractive force at large distances. As r decreases this force becomes somewhat larger. However, for short distances the force is strongly repulsive and the electronic molecular orbits may overlap. At the condition $F = 0$, the molecular kinetic energy does not allow the particles to remain in equilibrium at the corresponding distance.

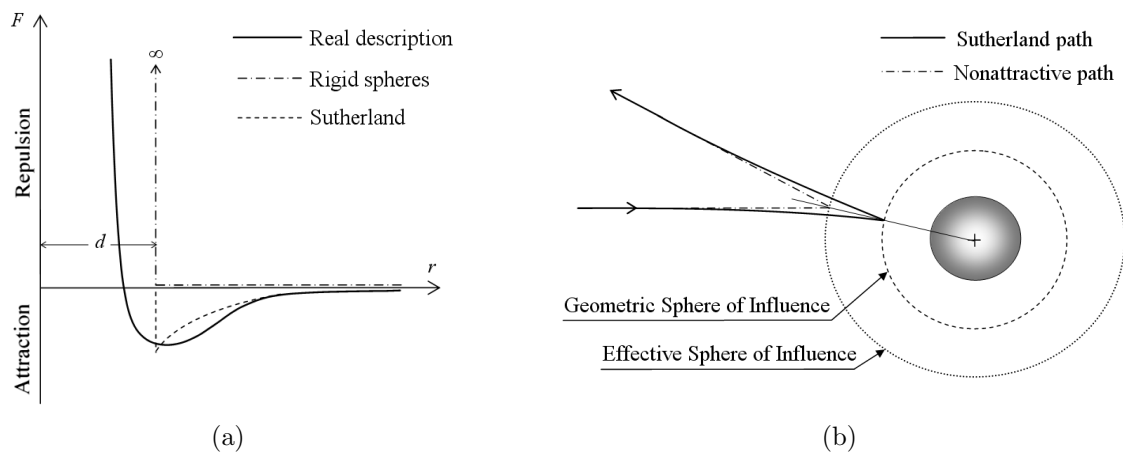


Figure 3.8 - (a) Typical intermolecular potential fields and (b) the contrast between the molecular paths of the Sutherland model and a nonattractive model.
SOURCE: Adapted from Vincenti and Kruger (1965).

Since the real description is complex, it is clear from Figure 3.8(a) that molecular models, e.g., the Sutherland or the hard elastic sphere, employ some degree of approximation. In this way, a suitable model is often chosen, and the simplest of these takes into account only for the repulsive component. A model may be defined as suitable for a particular application if it provides sufficient data agreement between experiment and theory.

The inverse power law (IPL) model is a flexible molecular model to describe typical nonionized hypersonic flows. In such a scheme, the intermolecular repulsive force field may be modeled according to Equation 3.16, where r is the distance between molecule centers in the collision and κ and η are known constants. Combinations of

these last two parameters provide different quantitative behaviors in the collision.

$$F = \frac{\kappa}{r^\eta} \quad (3.16)$$

A special case of the inverse power law model is the well-known Maxwell model, which is obtained by setting $\eta = 5$. Despite some physical limitations, the Maxwell model (Maxwellian molecule) is widely applied in analytical descriptions. Another important simplification of the IPL model correspond to the aforementioned hard sphere (HS) model that is obtained by setting $\eta \rightarrow \infty$ for r greater than d_{12} . Since problems of engineering interest involve the simulation of billions or trillions of collisions, then a simple and efficient model should be considered. In this scenario, the HS model is the simplest alternative.

In the hard sphere model, the total cross-section is constant for simple gases⁹. The deflection angle χ is uniformly distributed between 0 and π , i.e., the scattering is isotropic in the center of mass frame of reference. However, such a scattering law is unrealistic. Another disadvantage of the HS model is that σ_T does not take into account the dependency with relative translational energy ($E_t = m_r c_r^2/2$) of the molecules. For realistic collisions, σ_T decreases as the translational energy involved in the collision increases.

In the HS model, since σ_T is constant and independent of the translational energy, the deflection angle χ depends only on the geometry of the collision. Such an angle is given by Equation 3.17. Since molecular chaos is assumed, all values for the impact parameter b are equally likely and hence the reason for the isotropic scattering is clear.

$$\chi = 2 \cos^{-1}(b/d) \quad (3.17)$$

When the intermolecular force field is given by the inverse power law described by Equation 3.16, the Chapman-Enskog theory provides a straight relation between the viscosity coefficient μ and the gas temperature according to:

$$\mu \propto T^\omega \quad (3.18)$$

⁹A gas composed of a single chemical specie, where all molecules are assumed to have the same structure.

where the powers are dependent on the free parameter η as following,

$$\omega = \frac{1}{2} + v = \frac{1}{2} \left(\frac{\eta + 3}{\eta - 1} \right), \quad v = \frac{2}{\eta - 1} \quad (3.19)$$

By using Equation 3.19, the dependence of the total collision cross-section σ_T , based on the IPL model, can be established as:

$$\sigma_T \propto E_t^{-v} \propto c_r^{-2v} \quad (3.20)$$

A fundamental difference between the molecular models may be expressed in the dependence of the transport coefficients on temperature. According to Equation 3.18, the viscosity coefficient is proportional to temperature raised to a constant power. For this reason, ω is sometimes called as viscosity index. Equation 3.19 also shows that in both HS and Maxwell models, the value of ω is equal to 0.5 and 1, respectively. Such simplified models can be regarded as theoretical limiting cases for the behavior of real gases, since for the majority of real gases ω is within 0.6 and 0.9.

In order to overcome this unrealistic behavior, alternative molecular models based on hard spheres have been proposed. These models have proven successful in reproducing the macroscopic behavior of gases with a feasible computational efficiency. Prasanth and Kakkassery (2008) published a brief review about molecular models for DSMC simulations. The first alternative scheme was the variable hard sphere (VHS) model introduced by Bird (1981). In this model, similar to hard spheres, molecules perform an isotropic scattering, i.e., all directions (χ) are equally likely for c_r^* in the center of mass reference frame. On the other hand, the total collision cross-section σ_T , or the effective molecular diameter d , is proportional to a certain inverse power of the relative speed c_r in the same sense that presented by Equation 3.20. The VHS model has been widely employed in DSMC simulations. In despite of its unrealistic scattering, the VHS model is indicated for many engineering applications. This occurs because, for such applications, it has been observed that the influence of the effective total collision cross-section is overwhelmingly more important than that of the scattering law.

Based on the realistic dependence of the total collision cross-section on E_t , expressed in Equation 3.20, the VHS model employs an effective molecular diameter d dependent on c_r , in addition to the classical scattering law of the HS model. In this context, the VHS model can be summarized by the following relations, with the

subscript $_{ref}$ indicating reference values,

$$\frac{\sigma_T}{\sigma_{T_{ref}}} = \left(\frac{d}{d_{ref}} \right)^2 = \left(\frac{E_t}{E_{t_{ref}}} \right)^{-v} = \left(\frac{c_r}{c_{r_{ref}}} \right)^{-2v} \quad (3.21)$$

Then, for a given known $\sigma_{T_{ref}}$, the VHS model establishes the effective total collision cross-section σ_T . Roughly speaking, instead of a direct definition of σ_T , such a model determines this variable as a correction of $\sigma_{T_{ref}}$, based on the physical reasoning described in Equation 3.21, so that:

$$\sigma_T = \pi d^2 = \sigma_{T_{ref}} \left(\frac{c_r}{c_{r_{ref}}} \right)^{-2v} = \sigma_{T_{ref}} c_{r_{ref}}^{(2\omega-1)} / c_r^{(2\omega-1)} \quad (3.22)$$

At this point, the relations between effective and reference values are required to determine the total effective collision cross-section. Obviously, such relations must be consistent with each other. Thereby, Bird (1994) defined d_{ref} in the VHS model as:

$$\pi d_{ref}^2 = \sigma_{T_{ref}} c_{r_{ref}}^{(2\omega-1)} / \overline{c_r^{(2\omega-1)}} \quad (3.23)$$

Here, $\overline{c_r^{(2\omega-1)}}$ represents a mean value obtained by assuming an equilibrium gas. From classical kinetic theory, the following expression can be written as:

$$\overline{c_r^j} = \frac{2}{\pi^{1/2}} \Gamma \left[\frac{(j+3)}{2} \right] \left(\frac{2kT}{m_r} \right)^{j/2} \quad (3.24)$$

Thus,

$$\overline{c_r^{(2\omega-1)}} = \frac{(2kT/m_r)^{(\omega-1/2)}}{\Gamma(5/2 - \omega)} \quad (3.25)$$

As a result, by combining Equations 3.22, 3.23 and 3.25 the relation between effective and relative diameters at a relative speed c_r , in the VHS model, is given by:

$$\left(\frac{d}{d_{ref}} \right)^2 = \frac{[2kT / (m_r c_r^2)]^{(\omega-1/2)}}{\Gamma(5/2 - \omega)} \quad (3.26)$$

Finally, the DSMC method computes the effective total collision cross-section σ_T , for each selected collision, using Equation 3.27.

$$\sigma_T = \sigma_{T_{ref}} \left(\frac{d}{d_{ref}} \right)^2 = \sigma_{T_{ref}} \frac{[2kT / (m_r c_r^2)]^{(\omega-1/2)}}{\Gamma(5/2 - \omega)} \quad (3.27)$$

In this numerical procedure d_{ref} , T_{ref} and ω are treated as known and tabulated

constant values. Then, $\sigma_{T_{ref}}$ can be set similar to Equation 3.12, where the reference diameter is applied to provide $\sigma_{T_{ref}} = \pi d_{ref}^2$. Additionally, Bird (1994) showed that the present formulation is independent of the selected value for d_{ref} and does not require an equilibrium gas.

The main advantage of the VHS model is the realistic physical reasoning employed. It leads to a viscosity coefficient proportional to powers of the order of 0.75, similar to real gases. Moreover, the finite cross-section of the VHS model allows the definition of a mean free path (BIRD, 1994) and viscosity coefficient (BIRD, 1983) that match the real gas behavior, as presented in Equations 3.28 and 3.29. On the other hand, the use of a simplified isotropic scattering law provides unrealistic values for the diffusion coefficients. Thus, for gas mixture flows with diffusion performing an essential role, the use of the HS or VHS model must be re-evaluated.

$$\lambda = \left[2^{1/2} \pi d_{ref}^2 n (T_{ref}/T)^{(\omega-1/2)} \right]^{-1} \quad (3.28)$$

$$\mu = \frac{(15m/8) (\pi kT/m)^{1/2}}{\pi d_{ref}^2 (2-v)^v \Gamma(4-v)} \quad (3.29)$$

For reference purposes, the parameters defined in Equation 3.19 are tabulated in Table 3.1 for Maxwell, VHS and HS models.

Table 3.1 - Molecular parameters for different models.

Model	η	ω	ν
Maxwell	5	1.00	0.50
VHS	9	0.75	0.25
HS	∞	0.50	0

In order to improve the VHS model, Koura and Matsumoto (1991) have introduced the variable soft sphere (VSS) model (KOURA; MATSUMOTO, 1992). This molecular model computes σ_T in the same way as the VHS model, but with an anisotropic scattering law. According to Equation 3.30, an additional parameter α , which depends on the relative energy in the collision, is employed to determine the deflection angle. Since $\alpha > 1$ for real gases, this deflection angle is less than the one provided by HS and VHS models. Such a behavior is the reason for the name variable *soft*

sphere model.

$$\chi = 2 \cos^{-1} [(b/d)^{1/\alpha}] \quad (3.30)$$

The implementation of this model in DSMC simulations is more complex than the implementation of the VHS model. However, the VSS model yields improved values for the diffusion coefficients.

Hassan and Hash (1993) introduced the generalized hard sphere (GHS) model. This molecular model takes into account both repulsive and attractive forces in the collision. The scattering law is the same as that in HS and VHS model. Since the GHS model is able to reproduce attractive interactions, it is appropriate to simulate low temperature flows, where the attractive portion in the collision plays fundamental role (HASH et al., 1994; KUNC et al., 1995).

Later, Fan (2002) developed the so-called generalized soft sphere (GSS) model. This generalization employs the same dependence of σ_T on E_t adopted in the GHS model, which reproduces an attractive-repulsive potential. However, its scattering law is the same as that described by the VSS model. In addition, the transport coefficients obtained by the GSS model provide a good agreement with experimental results for a large range of temperatures.

3.5 Collision Sampling Schemes

One of the key ideas in DSMC computations is to decouple molecular motion and collisions over a consistent time step. Thereby, a realistic transport of the microscopic quantities, which is performed by intermolecular collisions, requires the establishment of a correct collision frequency within each cell. In such a procedure, the appropriate collision pairs are probabilistically determined for each cell. As aforementioned in Section 3.2, there are different DSMC schemes to compute the collision rates. These schemes achieve higher computational performance than the molecular dynamics method because they do not take into account the relative position of colliding particles within a cell. For the purpose of the present work, only the time counter (TC) and the no time counter (NTC) methods are described here.

The numerical procedures employed to calculate the local collision rate and to define the collision pairs can be based on the cell information. However, the choice of the collision pairs is preferably performed within the subcells that compose the respective cell. In this context, the number N of simulated particles in the cell, the

cell volume V_c , and the time step Δt are fundamental data. From the kinetic theory of gases, it can be shown that the number N_{coll} of collision pairs, which must be simulated in a cell over the time step Δt , is given by the following equation,

$$N_{coll} = \frac{1}{2}N\nu\Delta t = \frac{1}{2}Nn\overline{\sigma_T c_r} \Delta t \quad (3.31)$$

According to Equation 3.31, in order to determine N_{coll} , it is necessary to compute the mean value $\overline{\sigma_T c_r}$ for each time step Δt . For such a calculation, the product between σ_T and c_r must be evaluated for all possible collision pairs. Called *direct* or *Kac* method, this numerical procedure would have a computational time proportional to N^2 . Moreover, within a given cell or in most cases within a subcell, a possible colliding pair of particles is randomly chosen. Then, a selection rule is applied to determine if this pair is accepted for the collision procedure. Thus, the last two steps are repeated until N_{coll} selected pairs per cell is reached.

In order to obtain a computational time proportional to N , Bird (1976) introduced the time counter (TC) method. In such a technique, an initial value for the maximum product between σ_T and c_r is set for each cell, which is indicated by $(\sigma_T c_r)_{max}$. This value is required in the selection rule of such a method. The other steps can be described by the following sequence:

- 1) Within a given cell or subcell, a pair of particles is randomly chosen.
- 2) For this pair, the product between σ_T and c_r is computed.
- 3) If such a particular value of $\sigma_T c_r$ is greater than $(\sigma_T c_r)_{max}$, the maximum value is upgraded for this cell.
- 4) The probability P_{coll} of collision between these particles is given by:

$$P_{coll} = \frac{\sigma_T c_r}{(\sigma_T c_r)_{max}} \quad (3.32)$$

Then, if $P_{coll} > R_f$, the pair is selected for the collision procedure, where R_f is a random number between 0 and 1. On the other hand, if $P_{coll} < R_f$, the product $(\sigma_T c_r)_{max}$ restores its last value and a new pair is randomly chosen, i.e., the sequence returns to the step 1. This acceptance-rejection method for the selection of pairs over a Δt is explained in detail by Bird (1994).

- 5) If the pair is accepted for collision, by setting $N_{coll} = 1$ in Equation 3.31, the cell time is advanced by an increment δt given by:

$$\delta t = \frac{2}{N n \sigma_{TC_r}} \quad (3.33)$$

- 6) The sequence (1-5) is repeated while $\delta t_1 + \delta t_2 + \delta t_3 + \dots \leq \Delta t$. Where the subscripts (1,2,3...) indicate different accepted collision pairs over the current time step Δt .

Despite reproducing the correct nonequilibrium collision rate with an optimal computational performance, this technique can lead to some problems under extreme nonequilibrium conditions, such as in strong shock waves. From a physical point of view, the collision distribution over Δt can become nonhomogeneous. The acceptance of low probability collisions, i.e., pairs with a small value of σ_{TC_r} , results in large δt values. Consequently, the time increment sum can exceed Δt by unacceptable amounts. From a computational aspect, as reported by [Baganoff and McDonald \(1990\)](#), the total number of simulated collisions may be very different from one cell to another. Besides, this number is unknown until time step Δt is reached. Such a situation makes the numerical vectorization of the collision procedure a difficult task.

Later, [Bird \(1989\)](#) introduced the no time counter (NTC) method to overcome the difficulties observed in the TC procedures. Both NTC and TC methods have the same selection rule for the collision pair, which is based on the acceptance-rejection method. Nevertheless, in the NTC method the maximum number N_{coll} of collisions to be selected, over Δt in a given cell, is set before the selection of the pairs. Hence, in this new scheme, the time count idea is replaced by an explicit dependence of N_{coll} on the time step Δt . In other words, N_{coll} does not depend on the choice of pairs or particular values of σ_{TC_r} . In the NTC method, this number of collisions is expressed by:

$$N_{coll} = \frac{1}{2} \frac{N \bar{N} F_N(\sigma_{TC_r})_{max} \Delta t}{V_c} \quad (3.34)$$

where \bar{N} is the time or ensemble average value of N and F_N indicates the number of real particles represented for each simulated particle within the respective cell. Similarly to Equation 3.31, it is worthwhile to observe that $\bar{N} F_N / V_c$ is equal to the local number density n . Furthermore, it is clear that in this scheme the computational

time is also proportional to N . Additional information about the NTC method can be found in the literature (BIRD, 1994; SHEN, 2000).

3.6 Inelastic Collisions

High-temperature and rarefied environments are typically found in hypersonic and microscale flows, respectively. Under such conditions the flow structure is often characterized by thermal and/or chemical nonequilibrium. A flow in thermal nonequilibrium is one whose temperatures associated with the translational, rotational and vibrational internal modes of energy are unequal, i.e., these modes do not share a common distribution of energies. The nonequilibrium can also be characterized by a flow with an anisotropic velocity space. Moreover, most flows observed in engineering applications are composed not only of monatomic molecules, as those discussed in previous sections, but also of diatomic and/or polyatomic molecules. In this scenario, the DSMC simulations require phenomenological molecular models that reproduce the macroscopic behavior of these real flows, while providing an acceptable computational performance.

A flow out of thermodynamic equilibrium relaxes towards the equilibrium state by successive molecular interactions, which promote energy exchange between translational and internal modes. In this context, phenomenological models that simulate inelastic collisions must allow the definition of the necessary number of rotational (ζ_R) and vibrational (ζ_V) degrees of freedom (DOFs). Additionally, a particular model must satisfy the principle of detailed balancing (or reciprocity). This principle means that in an equilibrium gas there must exist exact energy equipartition between the translational and internal modes, and the distribution function of this quantities must hold a Maxwellian form.

In the available literature, there are different suitable models that deal with rotational (BOYD, 1989), vibrational (BERGEMANN; BOYD, 1992), chemical (CARLSON; BIRD, 1995) and electronic (BOYD et al., 1995) modes. In general, such models are spherically symmetric. Another common feature between most of them is the use of the Larsen-Borgnakke (LB) model (BORGNAKKE; LARSEN, 1975). The LB implementation into the DSMC simulations is widely employed. This model is based on the principles of kinetic theory and statistical mechanics. The LB model was developed originally to treat the energy transfer between translational and rotational modes. Notwithstanding, it was extended to vibration-translation energy transfer.

The main assumptions of the classical LB model are listed in the following:

- i) The post-collision internal and relative translational energies are sampled according to the local equilibrium (Maxwellian) distribution functions;
- ii) For a particular internal energy mode i (rotational or vibrational), *on average*, the fraction Λ_i of the intermolecular collisions is considered as inelastic while the remaining fraction $(1 - \Lambda_i)$ is treated as elastic;
- iii) The spectrums of rotational and vibrational energies are continuous.

It is worthwhile to point out that only the fraction Λ_i out of the total collisions leads to thermal relaxation of the energy mode i . Such a relaxation rate can be expressed in terms of the relaxation collision number Z_i . This value can be interpreted as the average number of collisions required for a particular internal mode to reach the equilibrium state. Once Z_i is determined by experiments or analysis, the probability P_i of the internal energy mode i to be adjusted in a given collision can be written by Equation 3.35. Then, this result is applied to an acceptance-rejection method in order to determine if the respective internal energy must or not be changed.

$$P_i = \Lambda_i = \frac{1}{Z_i} \quad (3.35)$$

Constant values of the rotational and vibrational relaxation collision number, e.g., $Z_R = 5$ and $Z_V = 50$, have been widely employed in the DSMC computations until the 1990s. For engineering problems, this assumption provides reasonable results. Nowadays, more realistic relaxation collision numbers, based on temperature- or energy-dependence, can also be used for the rotational (BOYD, 1990a; BOYD, 1990c; BOYD, 1990b) or vibrational (BOYD, 1989; BOYD, 1991; HASH; HASSAN, 1992) modes. At this point, it is important to mention that the relaxation collision number Z_i employed in the DSMC context (Equation 3.35) is different from the relaxation collision number Z_i^{Cont} predicted by the continuum approach. By employing continuum techniques that use conservation equations to describe the evolution of the internal energies, the Jeans-Landau-Teller (JEANS, 1916; LANDAU; TELLER, 1936) equation provides,

$$Z_i^{Cont} = \frac{\tau_i}{\tau_c} \quad (3.36)$$

where τ_i is the relaxation time for the internal mode i , and τ_c is the mean collision time that refers to the translational mode. The latter characteristic time is equal to

the reciprocal of the collision rate, i.e., $\tau_c = 1/\nu$. According to Lumpkin et al. (1991), differences between Z_i and Z_i^{Cont} are assigned to the energy transfer procedures employed by the DSMC implementation of the LB model. In this fashion, the relation between the continuum and particle (DSMC) relaxation collision numbers can be written as:

$$Z_R = \left(\frac{\zeta_T}{\zeta_T + \zeta_R} \right) Z_R^{Cont} \quad (3.37)$$

$$Z_V = \left(\frac{\zeta_T}{\zeta_T + \zeta_R + \zeta_V} \right) Z_V^{Cont} \quad (3.38)$$

The Larsen-Borgnakke model can be applied to the internal modes by employing either a classical (continuum) or quantum (discrete) approach. For the rotational mode, quantum effects are usually important in flows with very low temperatures, where the rotational degrees of freedom might not be fully excited. In spite of this fact, the use of a continuum spectrum of rotational energy provides sufficient accuracy for high-temperature flows. In addition, discrete rotational models for DSMC computations are limited to diatomic molecules. Then, for simulations with polyatomic molecules a continuum approach must be used. On the other hand, the discrete behavior of the vibrational internal modes is poorly approximated by a continuum distribution. In real molecules, the vibration energy spectrum is characterized by large gaps between the neighboring energy levels. As a result, a quantum procedure to set the vibrational energy provides a more realistic modeling of such process. In the quantum scheme, the definition of the number of effective vibrational DOFs can be based either on a simple harmonic oscillator (SHO) or an unharmonic oscillator (UHO) model. As reported by Bird (1994), DSMC results showed that unharmonic effects have a bigger impact on dissociation rates than on the overall vibrational energy. In such a literature, a detailed explanation of both the continuum and quantum (SHO and UHO) procedures for vibrational mode can be found. In this context, a concise review about inelastic collision models is presented by Ivanov et al. (1998). A discussion on inelastic collision models more complex than those concerned in the LB model is beyond the scope of the present work.

3.7 Boundary Conditions

In gas dynamic problems there are basically two types of boundary conditions: (i) those ones specified by the freestream¹⁰ macroscopic properties, and (ii) those ones

¹⁰An undisturbed flow that holds thermodynamic equilibrium.

defined by the physical behavior of a solid surface that interacts with the particles. In the molecular-discrete approach, the first boundary type deals with the inlet and outlet of molecules through a given surface. The main idea of the inlet procedure is to define the flux and thermal state of the molecules that are moving into the simulated domain. The outlet procedure simply consists in removing the molecules that leave the domain. Obviously, both procedures must be consistent with the desired flow simulation. The second boundary type treats the gas-surface interactions, which can modify the thermal state of the impinging molecules and promote heat and momentum exchange between gas and surface. The influence of the gas-surface interaction model plays an important role on rarefied gas flows. Such an influence is even more significant in microscale flows, where viscous effects near the surface are one of the more important physical mechanisms. In this context, the main features of the boundary conditions employed in the present work are discussed next.

3.7.1 Inflow Boundaries

The microscopic state of each simulated particle that enters in the computational domain is determined according to an equilibrium gas flow with pre-defined stream velocity \mathbf{c}_0 , whose components in the Cartesian frame of reference are u_0 , v_0 and w_0 . At this point, a trivial but very important concept about the molecular velocity \mathbf{c} is pointed out in Equation 3.39. This expression shows that the velocity of each molecule is composed of a linear combination of a macroscopic velocity¹¹ \mathbf{c}_0 and a peculiar velocity¹² \mathbf{c}' . It is also worthwhile to mention that $\bar{\mathbf{c}} = \mathbf{c}_0$, since the random motion of a molecule provides $\bar{\mathbf{c}'} = 0$.

$$\mathbf{c} = \mathbf{c}_0 + \mathbf{c}' \quad (3.39)$$

Based on the kinetic theory, for each inlet particle, the definition of the translation and internal energies depends on the thermodynamic temperature of the inlet gas flow.

Since \mathbf{c}_0 is known *a priori*, the definition of \mathbf{c} for each particle is determined by obtaining randomly a particular component of \mathbf{c}' from the Maxwellian velocity distribution f_0 , which is expressed by Equation 3.40. Herein, $d\mathbf{c}'$ stands for a volume element in the velocity space. By assuming an isotropic velocity space, Figure 3.9

¹¹Sometimes called as stream or mean velocity.

¹²Sometimes called as thermal or random velocity

presents a normalized Maxwellian distribution for the thermal speed (c') and for a thermal velocity component (u'). The Maxwellian distributions do not depend on the molecular model employed.

$$\frac{f_0}{n} d\mathbf{c}' = \frac{\beta^3}{\pi^{3/2}} \exp[-\beta^2 c'^2] d\mathbf{c}' = \frac{\beta^3}{\pi^{3/2}} \exp[-\beta^2 (u'^2 + v'^2 + w'^2)] du' dv' dw' \quad (3.40)$$

where,

$$c'_m = \sqrt{\frac{2kT}{m}} = \frac{1}{\beta} \quad (3.41)$$

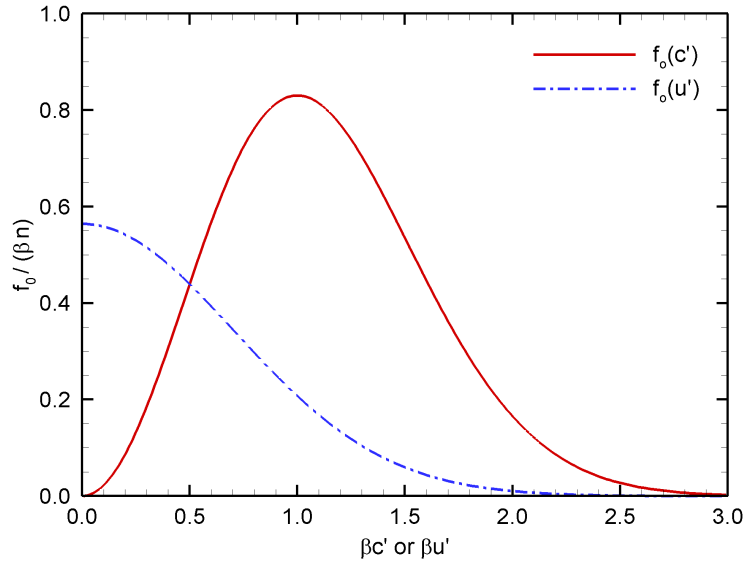


Figure 3.9 - Thermal speed and thermal velocity x -component Maxwellian distributions.

In addition to the thermal state definition for each inlet particle, it is necessary to determine the inward number flux \dot{N}_i of these particles across the surface elements of a given boundary. Such a task is analytically solved by assuming an equilibrium distribution function for the inflow gas. For an inward gas flow with a known stream velocity \mathbf{c}_0 , temperature T , and number density n , the kinetic theory of gases provides:

$$\dot{N}_i = n \frac{c'_m}{2\sqrt{\pi}} \left\{ \exp(-q^2) + q\sqrt{\pi} [1 + \text{erf}(q)] \right\} \quad (3.42)$$

where

$$q = s \cos \theta \quad (3.43)$$

and

$$s = \frac{c_0}{c'_m} = c_0\beta \quad (3.44)$$

In Equations 3.42, 3.43 and 3.44, “erf” denotes the error function, s is the molecular speed ratio¹³, and θ is the angle between \mathbf{c}_0 and the unit vector \mathbf{e} normal to the surface element, as depicted in Figure 3.10 for different cases.

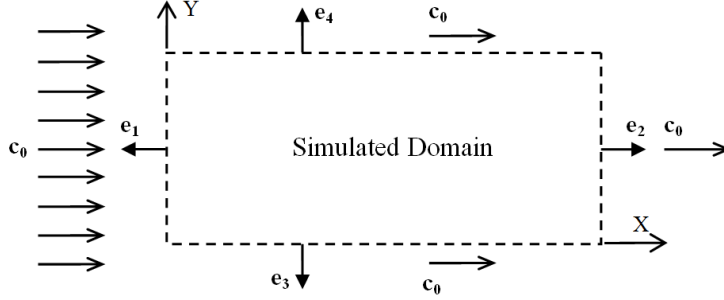


Figure 3.10 - Schematic view of a two-dimensional domain composed of four orthogonal inflow boundaries.

In Figure 3.10, a stream gas flow parallel to the axis X crosses the simulated domain. As a result, due to the random molecular motion, particles can enter in the domain through all boundaries. In the present scheme, the value of θ is different for each boundary, namely, $\theta_1 = \pi$, $\theta_2 = 0$ and $\theta_3 = \theta_4 = \pi/2$. As shown in Figure 3.11, the dimensionless inward number flux, $\hat{N}_i = \beta \dot{N}_i/n$, presents interesting features when plotted as a function of q . If the upstream boundary (1) experiences a hypersonic flow ($q \rightarrow \infty$) this equation yields $\hat{N}_i \rightarrow q$. On the other hand, if a hypersonic flow crosses the downstream boundary (2), i.e., $q \rightarrow -\infty$, the number of molecules that enter in the computational domain by this boundary can be neglected since $\hat{N}_i \rightarrow 0$. It is worthwhile to observe that these particles move in the opposite direction of the macroscopic velocity. Such a phenomenon is called thermal backflow, and is typically neglected in most numerical simulations when $q \leq -3$.

In the conventional DSMC computations for super- or hypersonic external gas flows, Equation 3.42 is employed in an explicit manner to calculate \dot{N}_i since c_0 , T and n are known. As mentioned, for hypersonic downstream boundaries a “vacuum” condition is generally imposed. In this way, no molecules enter the simulated domain from

¹³Sometimes defined as the molecular Mach number.

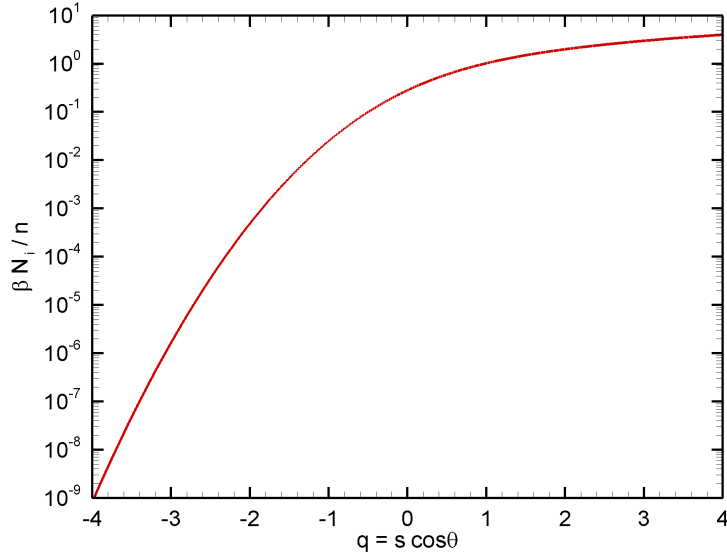


Figure 3.11 - Normalized number flux to a surface element in terms of q .

external regions. Since the inlet particle boundaries are based on freestream equilibrium conditions such boundaries are required to be far away from the disturbed flow regions. Moreover, in low speed microflow experiments, because of technical limitations, the boundary conditions that can be directly obtained are pressure and temperature instead of velocity and number density. Therefore, from an experimental point of view, the use of pressure boundary conditions is more realistic than the velocity boundary conditions used in hypersonic external flows. In addition, for microflows, \mathbf{c}' is generally of the same order of \mathbf{c}_0 , therefore, neglecting the inward molecular flux in a given boundary may lead to inappropriate results.

Previous studies have proposed different methods to treat pressure boundary conditions for subsonic flows. In short, at a particular temperature, these methods impose an inlet stream velocity that reproduces a given pre-defined pressure in the boundary vicinity. Ikegawa and Kobayashi (1990) proposed a method based on the particle flux conservation and employed ideal gas relations. Nance et al. (1998) used a similar treatment for each cell in the upstream boundary. Wu et al. (2001) employed a particle-based method at both upstream and downstream boundaries. In order to improved such a scheme, Liou and Fang (2000) proposed an alternative method where the local inlet boundary information was obtained by extrapolation from upstream boundary adjacent cell values, while the downstream treatment was based on concepts of the one-dimensional characteristic theory. Wang and Li (2004b) im-

plemented an implicit method based on the characteristic theory for both upstream and downstream boundaries. Recently, Yang et al. (2010) have suggested the use of this same scheme, but applying a particular velocity for the inlet velocity calculation instead of the sound speed.

In the present study, the method proposed by Wang and Li (2004b) is employed. However, in contrast with the original formulation, the present implementation uses the translational temperature T_T in regions with no thermal equilibrium instead of the overall temperature T_O for the calculations. Such a modification is based on the fact that disturbances are propagated according to the translational movement that is related with T_T . As will be shown in the next chapters, this improvement provides results in excellent agreement with experimental and numerical data. The main concepts of the present pressure boundary conditions are discussed in the following.

The one-dimensional characteristic theory provides relations between the physical properties of a gas that is disturbed by a finite (nonlinear) wave (ANDERSON, 1990). However, in a limiting case, if such a wave is infinitely weak and the disturbance process is steady, one-dimensional and isentropic, this wave can be treated as a sound wave. In this scenario, the analysis of both an acoustic wave and a finite wave provide the same relations. First, as presented in Figure 3.12(a), is considered a compressible ideal gas of pressure p , density ρ , and enthalpy h at rest in a duct of uniform cross-section area A . If the piston on the left side induces a steady velocity of magnitude du to the right side, then an infinitesimal weak wave is generated with velocity a . As a consequence, this disturbance performs infinitesimal changes on the undisturbed gas. By changing the reference frame such that it moves with the wave, the problem is reduced to a steady flow as shown in Figure 3.12(b).

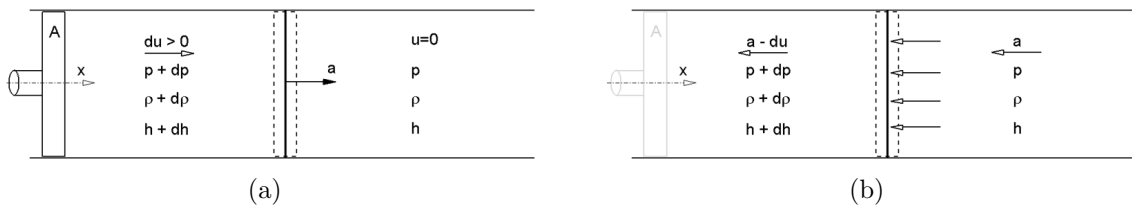


Figure 3.12 - Propagation of a weak pressure wave (a) in the laboratory frame and (b) in the frame moving with the wave.

In this scenario, the mass and momentum conservation equations can be applied across the infinitesimal sound wave depicted in Figure 3.12(b) to yield:

$$\begin{aligned}\rho A a &= (\rho + d\rho) A (a - du) \\ \rho du &= a d\rho\end{aligned}\tag{3.45}$$

and

$$\begin{aligned}pA - (p + dp) A &= \rho A a [(a - du) - a] \\ dp &= \rho a du\end{aligned}\tag{3.46}$$

Equations 3.45 and 3.46 can be combined to provide the propagation velocity a of the sound wave, where the subscript s means an isentropic process.

$$a = \sqrt{\left(\frac{dp}{d\rho}\right)_s}\tag{3.47}$$

Finally, by using Equations 3.45 and 3.47 the following relation can be written for a forward-running wave¹⁴.

$$du = +\frac{dp}{a\rho}\tag{3.48}$$

If the piston is displaced to the left side, an analogous analysis can be developed for the case of a backward-running wave¹⁵. Therefore, the resulting equation is

$$du = -\frac{dp}{a\rho}\tag{3.49}$$

By rewriting Equations 3.47, 3.48, 3.49 in terms of finite differences, in addition to the ideal gas law based on the translational temperature T_T , a set of equations can be constructed for the cells adjacent to the boundaries. For illustration purposes, the two-dimensional channel showed in Figure 3.13 is considered, where the bracketed variables are known and the remaining variables must be determined. The subscripts j and k denote a particular cell adjacent to the upstream and downstream boundaries, respectively. Similarly, the subscripts in and b indicate a local region that is external to the simulated domain and adjacent to the cell j and k , respectively.

¹⁴When the wave and the disturbed gas move in the same direction.

¹⁵When the wave and the disturbed gas move in the opposite direction.

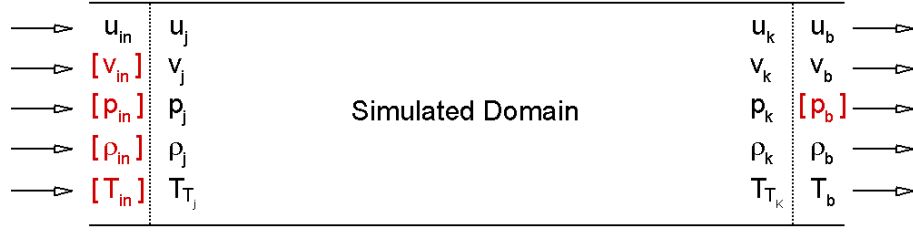


Figure 3.13 - Schematic view of the variables required in the pressure boundary conditions.

Since the unknown variables in Figure 3.13 depend on the flow behavior inside the channel, an iterative numerical procedure is required to determine these values. Based on the aforementioned equations and the known variables that are constant, the main sequence of calculations used in the upstream boundary is:

$$a_j = \sqrt{\gamma_j k T_{T_j} / m_j} \quad (3.50)$$

$$(u_{in})_j = u_j + \frac{p_{in} - p_j}{a_j \rho_j} \quad (3.51)$$

$$(v_{in})_j = v_{in} \quad (3.52)$$

$$n_{in} = \frac{p_{in}}{k T_{in}} \quad (3.53)$$

For the downstream boundary, similar approach is applied. The resulting set of equations is given by:

$$a_k = \sqrt{\gamma_k k T_{T_k} / m_k} \quad (3.54)$$

$$(u_b)_k = u_k + \frac{p_k - p_b}{a_k \rho_k} \quad (3.55)$$

$$(v_b)_k = v_k \quad (3.56)$$

$$(n_b)_k = \frac{\rho_k}{m_k} \quad (3.57)$$

$$(T_b)_k = \frac{p_b}{(\rho_b)_k k} \quad (3.58)$$

The calculated quantities u , v , n and T_b are then applied in Equation 3.42 to determine the number flux through the boundary elements. By using this procedure, the inlet and outlet boundary conditions are updated up to reach the desired pressure within the cells j and k . This implicit boundary treatment successfully leads the problem to steady state and matches the correct downstream pressure and overall mass balance. However, due to the statistical scatter of the DSMC method, this pro-

cedure provides inappropriate results for extremely low speed flows. In these cases, the Information Preservation (IP) method (SHEN, 2000) can be an alternative technique. Moreover, under extreme nonequilibrium situations, i.e., $Kn \gg 1$, the present pressure boundary conditions may fail since the ideal gas law is not adequate for such cases.

3.7.2 Gas-Surface Interaction Model

Since most engineering problems in rarefied gas flows involve gas-surface interaction phenomena, a suitable boundary condition is required in order to obtain reliable results from numerical simulations. The common gas-surface interaction models at molecular level are: (1) specular, (2) diffuse, and (3) some combination of these.

In a specular reflection, molecules are reflected like a perfectly elastic sphere with reversal of the normal velocity component and no change on the parallel components and energy. In such a process the particles can only transfer normal momentum to the surface. As a result, heat transfer and friction on the wall can not exist in the specular model. Due to these properties, the specular reflection is usually employed as a plane or axis of symmetry. On the other hand, in a diffuse reflection, molecules are reflected equally in all directions, i.e., with an isotropic scattering, usually with a complete thermal accommodation. Such an accommodation means that the molecule reaches thermal equilibrium with the surface temperature during the collision. The final velocity of the molecules is randomly assigned according to a half-range Maxwellian distribution determined by the surface temperature.

Originally, the combination of diffuse reflection with specular reflection is called Maxwell model (MAXWELL, 1879). In essence, this model assumes that a fraction f of the incident molecules would adhere to the surface long enough to come to thermal equilibrium with the surface and would be reflected diffusely in a completely accommodating fashion according to a Maxwellian distribution corresponding to the surface temperature. The remaining fraction $(1 - f)$ is assumed to reflect specularly from the surface.

The Maxwell model was followed by the introduction of coefficients that describe the degree of accommodation of the incident normal momentum, tangential momentum and kinetic energy to those of the surface. In other words, these accommodation coefficients may be considered as parameters that indicate the ability of incident

molecules to adjust themselves, from a thermodynamic point of view, to the body surface during the time that they are in contact. The traditional definition (SCHAFF; CHAMBRE, 1958) for these coefficients is usually expressed as being:

$$\alpha_n = \frac{p_i - p_r}{p_i - p_w} \quad (3.59a)$$

$$\sigma_t = \frac{\tau_i - \tau_r}{\tau_i - \tau_w} \quad (3.59b)$$

$$\alpha_r = \frac{e_i - e_r}{e_i - e_w} \quad (3.59c)$$

where p , τ and e refer to the momentum flux acting normal and tangential to the surface, and the energy flux to the surface, respectively. The subscripts i and r stand for the incident and reflected components, and w refers to the component that would be produced by a diffuse reflection at the surface temperature.

Data from many experiments show that molecules reflected from solid surfaces present lobular distributions under high vacuum conditions and are poorly represented by the Maxwell model. However, this model is widely used because it satisfies the principle of detailed balance or reciprocity. Detailed balance means that at equilibrium every molecular process and its inverse process must be individually balanced. A phenomenological model that satisfies detailed balance and has demonstrated improvement over the Maxwell model was proposed by Cercignani and Lampis (1971). The Cercignani-Lampis (CL) model is based on the definition of the coefficients α_n and α_t that represent the accommodation coefficients for the kinetic energy associated with the normal and tangential components of velocity, respectively.

The CL model provides a continuous spectrum of behavior from specular reflection at one end to diffuse reflection with complete energy accommodation at the other end, and produces physically realistic distributions of direction and energy for the re-emitted molecules. Lord (1991a) demonstrated that the CL model is suitable for the DSMC method, and described how to incorporate it into the DSMC procedures. The DSMC method with Lord's implementation is referred as the Cercignani-Lampis-Lord (CLL) model. Figure 3.14 displays a schematic comparison of the Maxwell reflection model and the CLL reflection model. The CL model has also been extended for covering diffuse scattering with partial energy accommodation of the vibrational modes for diatomic molecules modeled as simple harmonic oscillators (LORD, 1991b)

and as unharmonic oscillators (LORD, 1995).

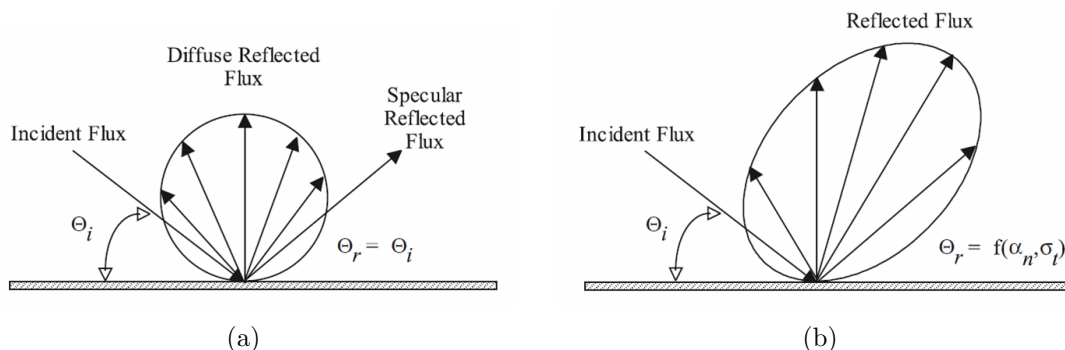


Figure 3.14 - Schematic drawing of the (a) Maxwell and the (b) CLL reflection models. SOURCE: Santos (2007)

The CLL model is derived by assuming that there is no coupling between the normal and tangential momentum components. The two adjustable parameters appearing in the CLL model, α_n and σ_t , are related to the translational energy normal component and momentum tangential component, respectively. Nevertheless, in the implementation of the CLL model in the DSMC method, Bird (1994) has shown that it is equivalent to specifying the normal α_n and tangential α_t components of the translation energy by assuming that σ_t lies between 0 and 1. The accommodation coefficient σ_t can also be considered as the fraction of molecules reflected diffusively. It is also important to mention that in the CLL model the accommodation coefficient of internal energy α_r is allowed to be independent of the translational accommodations.

Accommodation coefficients depend on the fluid, surface material and surface roughness. Previous studies determined σ_t experimentally to be within 0.2 and 0.8, where the lower limit corresponds to exceptionally smooth surfaces while the upper limit is typical in most practical surfaces. For instance, Arkilic (1997), by performing experimental measurements in microchannel flows, reported $\sigma_t = 0.80$ for nitrogen, argon, and carbon dioxide in contact with a silicon crystal. Such a value is somewhat different from the typical value assumed in macroflows ($\sigma_t = 1$). In general, this departure is significant when simulations of viscous effects on the microdevice performance are required. Additional information about the impact of incomplete accommodation in external-hypersonic and internal-microscale rarefied gas flows can

be found in recent literature (SANTOS, 2007; SEBASTIÃO; SANTOS, 2010a; SEBASTIÃO; SANTOS, 2010b).

4 COMPUTATIONAL PROCEDURE

4.1 Micronozzle Geometry Definition

As mentioned in Section 1.4, the purpose of this work is to investigate the influence of geometric aspects of the divergent nozzle part on the flow structure, aerodynamic properties and performance of such a device. Herein, the divergent part is composed of convex and concave surfaces linked by an inflection point, as previously shown in Figure 1.9. Hence, different aerodynamic configurations are modeled by changing the slope and curvature of these surfaces at the inflection point.

The geometry definition is also based on the fact that the micronozzles generally have rectangular cross-sections, and are employed in micronozzle layers or arrays (HORI-SAWA *et al.*, 2009; ZHAN *et al.*, 2004). Figure 4.1(a) presents a typical array pattern of convergent-divergent micronozzles. By focusing on the plane that crosses this array, Figure 4.1(b) reveals three similar profiles side by side, which are indicated by their centerlines.

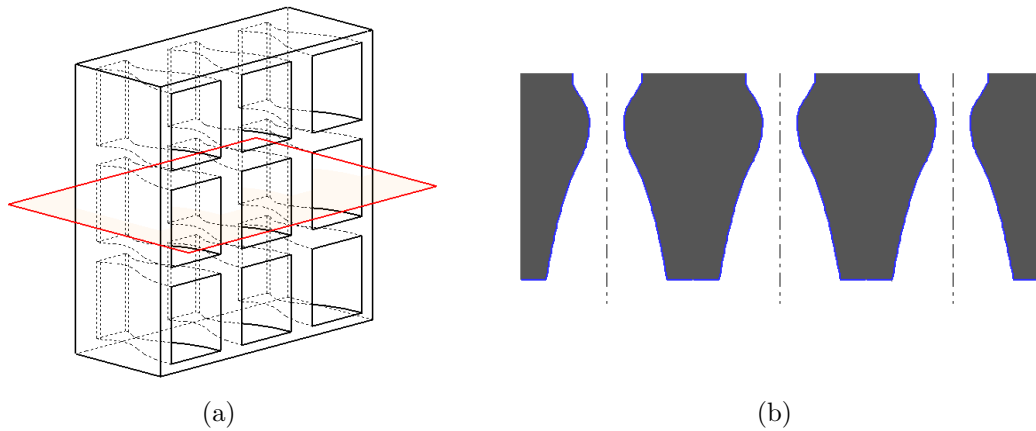


Figure 4.1 - (a) Isometric view of a micronozzle array and (b) its two-dimensional representation on the indicated plane.

Obviously, in order to perform DSMC simulations in this microdevice, a spatial discretization must be applied in the flow region. As reported by Ivanov *et al.* (1999), neglecting the plume region in micronozzle flows, i.e., simulating only the internal flow, provides over-predicted results. With the external flow modeled, streamlines in the plume diverge from the nozzle centerline to a far greater extent than those

observed in the simulations that end at the exit section. By considering the plume, near the nozzle lip, the abrupt expansion causes a much lower pressure along the wall as well as the divergence losses results in less thrust. These effects are simulated by including a buffer – external – region as depicted in Figure 4.2(a). Such a grid holds particular symmetry between each nozzle and also along their centerlines. Therefore, it is assumed that the study of a two-dimensional flow in the present micronozzle array can be predicted by simulating only the regions pointed out in Figure 4.2(b) with appropriate boundary conditions. Such a simplification yields a tremendous computational saving.

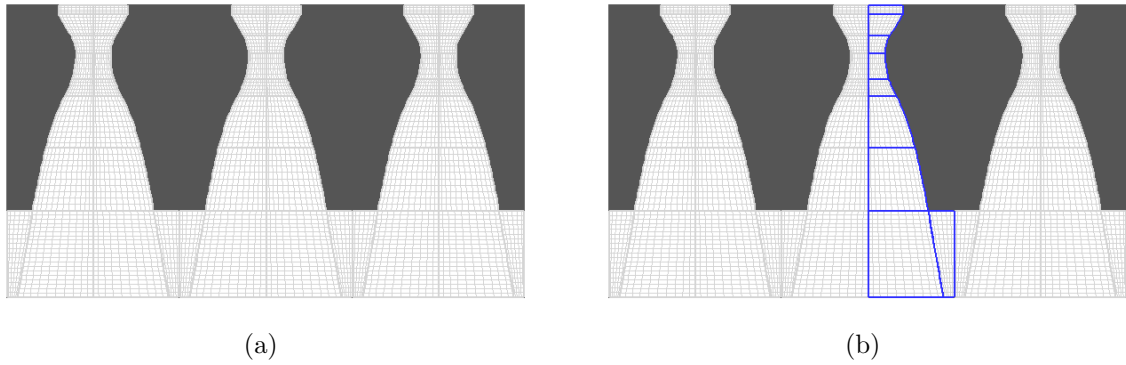


Figure 4.2 - (a) Schematic view of the computational grid for the entire micronozzle array and (b) the simulated regions.

Additionally, it is also important to remark that the results obtained by the present two-dimensional approach should be consistent as long as the neglected micronozzle transversal dimension is much greater than the micronozzle throat and exit widths. In this situation, the current two-dimensional simulations can be considered a cross-section from the three-dimensional case extracted far enough from the flat wall, making its presence negligible.

In order to allow a flexible grid for cell clustering, the flowfield is divided into an arbitrary number of regions, e.g., the nine regions showed in Figure 4.3. In this scenario, region 1 represents the inlet chamber, regions 2-3 the convergent part, regions 4-7 the divergent part, and regions 8-9 the buffer zone. Due to the symmetry assumptions, dimensions indicated by h mean a half size while the lengths are indicated by L . The subscripts in , c , t , d , e and b refer to the inlet, convergent, throat, divergent, exit and buffer sections, respectively.

In this geometry, the convergent part is composed of a surface inclined by a half angle θ_c that is tangent to a round shape of constant radius R_c . In analogous fashion, the convex surface of the divergent part is described by a round shape of constant radius R_d with slope θ_d at the inflection point. On the other hand, the concave surface is described by a power-law shape that depends on a particular exponent n , and constants A and B . As geometric constrains, at the exit section ($x = L_d$), the concave surface must provide an exit divergent angle θ_e and a half exit size h_e that are pre-defined for all cases. Finally, the buffer zone dimensions, h_b and L_b , are completely independent of the internal micronozzle design.

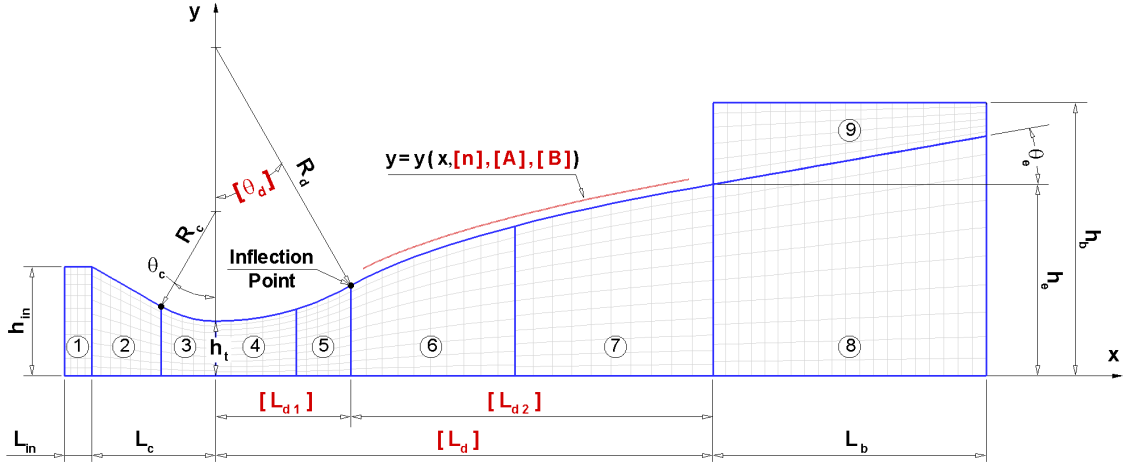


Figure 4.3 - Geometry definition of the computational domain.

Based on these arbitrary considerations, the functions f_{d_1} and f_{d_2} mentioned in Section 1.4 to describe the convex ($0 < x \leq L_{d_1}$) and concave ($L_{d_1} < x \leq L_d$) surfaces in the divergent part are defined according to Equations 4.1 and 4.2, respectively. Therefore, y'_{d_1} and y'_{d_2} represent a local slope for each surface, and y''_{d_1} and y''_{d_2} are related to the local radius of curvature¹.

$$f_{d_1} = y_{d_1} = h_t + R_d - (R_d^2 - x^2)^{1/2} \quad (4.1)$$

$$f_{d_2} = y_{d_2} = A(x - B)^n \quad (4.2)$$

The geometric constrains applied to express the divergent shape in a mathematical

¹For a curve in the plane xy that can be written as $y = f(x)$, the radius of curvature r_c is given by: $r_c = [1 + (f')^2]^{3/2} / f''$ (KLAF, 1956).

form are listed below.

- 1) In the divergent surface, both the convex and concave functions must be equal at the inflection point;

$$y_{d_1}(L_{d_1}) = y_{d_2}(L_{d_1}) \quad (4.3)$$

- 2) At the inflection point, the ratio between the slope of the concave to the convex surface must be equal to the parameter α_g ;

$$\alpha_g = \frac{y'_{d_2}(L_{d_1})}{y'_{d_1}(L_{d_1})} \quad (4.4)$$

- 3) Similarly, the absolute value of the ratio between the second derivatives, which are related to the radius of curvature, must be equal to the parameter β_g at the inflection point;

$$\beta_g = \left| \frac{y''_{d_2}(L_{d_1})}{y''_{d_1}(L_{d_1})} \right| \quad (4.5)$$

- 4) At the exit section, the divergent shape must provide a given half size h_e ;

$$y_{d_2}(L_d) = h_e \quad (4.6)$$

- 5) At the exit section, the surface slope must be equal to a given angle θ_e ;

$$y'_{d_2}(L_d) = \tan \theta_e \quad (4.7)$$

In this stage, for given values of α_g and β_g in addition to the known (unbracketed) variables in Figure 4.3, the unknown (bracketed) variables can be determined by Equations 4.1-4.7. In other words, α_g and β_g are the geometric parameters that control the divergent shape. Moreover, with such a strategy, it is allowed to keep all known variables in Figure 4.3 with the same values and to obtain different geometric configurations by only combining the values α_g and β_g .

By employing the definitions of α_g and β_g , Table 1.2 can be rewritten with specific values that are in fact applied in the present study. These values are listed in Table 4.1.

In group A cases, both convex and concave surfaces have the same slope at the inflection point ($\alpha_g = 1.0$), which means a smooth transition in this vicinity. In contrast, the divergent surface is discontinuous in the other groups. For B and C groups, at the inflection point, the concave surface is abruptly turned away ($\alpha_g = 2.0$) and turned back ($\alpha_g = 0.5$) from the symmetry plane, respectively. Moreover, the condition for the radius of curvature is varied by changing β_g in all groups. Finally, in order to perform comparisons, the geometry A1 is arbitrarily selected as the reference case.

Table 4.1 - Geometric configurations at the inflection point.

Case		Condition at the Inflection Point		
Group	Number	y_{d2}/y_{d1}	α_g	β_g
A	1			1.0
	2	1.0	1.0	2.0
	3			0.5
B	1			1.0
	2	1.0	2.0	2.0
	3			0.5
C	1			1.0
	2	1.0	0.5	2.0
	3			0.5

Furthermore, Table 4.2 summarizes the arbitrary variables used in the geometry definition. These values are somewhat based in previous works (ALEXEENKO et al., 2005; BAYT; BREUER, 1998; HAO et al., 2005; LIU et al., 2006; PIEKOS; BREUER, 1996) and are normalized by the half throat size h_t , equal to $10\mu\text{m}$. In order to decouple the influence of these variables on the flowfield structure, they are kept with the same value for the all nine simulated cases. The convergent θ_c and the exit divergent θ_e angles are set as 30 and 10 degrees, respectively.

Table 4.2 - Common geometric definitions.

h_{in}/h_t	h_e/h_t	h_b/h_t	L_{in}/h_t	L_b/h_t	R_c/h_t	R_d/h_t
2.00	3.50	5.00	0.25	5.00	2.00	5.00

For illustration purposes, Figure 4.4 depicts the differences between the geometric configurations defined in Tables 4.1 and 4.2. These comparisons are made in terms of the groups – A,B and C – and for clarity only the uncommon geometries are shown. Furthermore, the region near the inflection point is zoomed in order to better illustrating the meaning of variables α_g and β_g . In this group of plots, the coordinates X and Y represent the lengths x and y normalized by the half throat size h_t , respectively.

Finally, for each case, the uncommon geometric data are listed in Table 4.3. Since the convex and concave surfaces are described by different functions and the parameter α_g can assume values different of unity, the angle θ_d of the convex ($x \rightarrow L_{d_1}^-$) and concave ($x \rightarrow L_{d_1}^+$) surfaces can also be different. Hence, the angles θ_{d_1} and θ_{d_2} are defined by Equations 4.8a and 4.8b, respectively.

$$\tan \theta_{d_1} = y'_{d_1} (L_{d_1}) \quad (4.8a)$$

$$\tan \theta_{d_2} = y'_{d_2} (L_{d_1}) \quad (4.8b)$$

Table 4.3 - Additional geometric definitions.

	L_{d_1}/h_t	L_d/h_t	L_{d_1}/L_d	θ_{d_1}	θ_{d_2}	n
Case A1	2.4687	9.0923	0.2715	29.587°	29.587°	0.3910
Case A2	3.0642	7.6375	0.4012	37.768°	37.768°	0.2659
Case A3	1.9766	10.3530	0.1909	23.286°	23.286°	0.5052
Case B1	1.2430	10.1960	0.1219	14.395°	27.173°	0.5088
Case B2	1.5924	9.3738	0.1699	18.571°	33.889°	0.4329
Case B3	0.9832	10.9760	0.0896	11.411°	21.923°	0.5831
Case C1	3.8764	6.0543	0.6403	50.830°	31.538°	0.1431
Case C2	4.1036	5.2035	0.7886	55.157°	35.688°	0.0711
Case C3	3.4945	7.4392	0.4697	44.339°	26.040°	0.2650

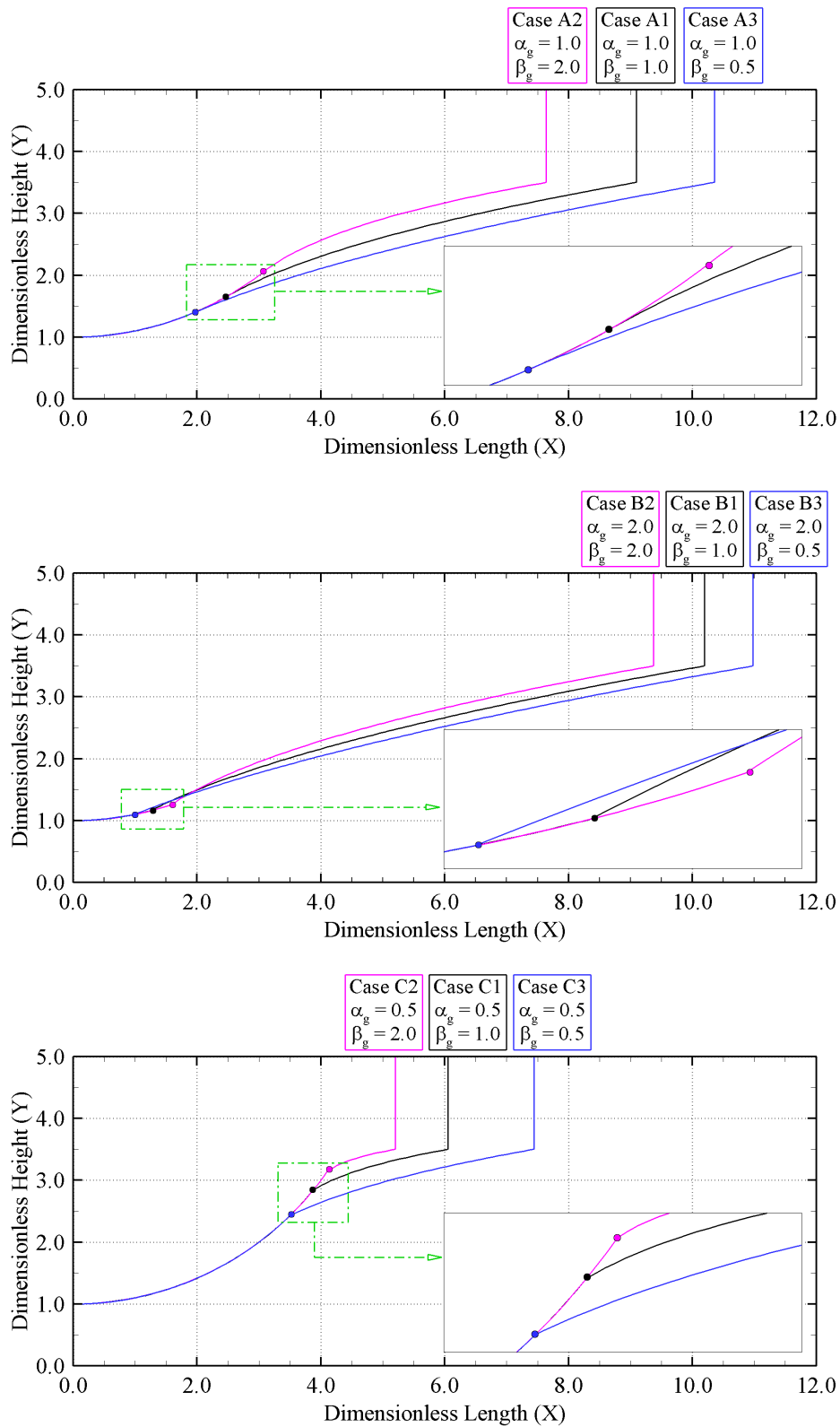


Figure 4.4 - Geometric differences between group A (top), B (middle) and C (bottom) cases.

4.2 Physical Models and Working Fluid

As discussed in Section 2.3, different methods can be applied to describe rarefied flows, each one with a particular degree of complexity. The Boltzmann equation expresses the fundamental physical principles present in most gas flows. However, due to mathematical difficulties, the solution for the Boltzmann equation is not feasible for a wide range of cases. In order to overcome these difficulties, the DSMC method has become a reliable computational technique for modeling complex transitional flows of engineering interest. Among others, typical problems include high altitude rocket plumes, MEMS, spacecraft propulsion, reentry vehicles, etc.

In the present work, the DSMC computational code employed is based on the same physical concepts described by Bird (1994). The molecular collision kinetics is modeled by the variable hard sphere (VHS) model (BIRD, 1981) and the no time counter (NTC) collision sampling technique (BIRD, 1989) described in Chapter 3. Energy exchange between kinetic and internal modes – vibration and rotation – is controlled by the phenomenological Borgnakke-Larsen (BL) statistical model (BORGNAKKE; LARSEN, 1975). Simulations are performed by considering a nonreacting gas model consisting of two chemical species, N_2 and O_2 .

For a given collision, the probability of an inelastic event is defined by the inverse of the relaxation collision number, which corresponds to the number of collisions, on average, for a molecule to undergo relaxation. The probability of an inelastic collision determines the rate at which energy is transferred between the translational and internal modes after a collision. In this sense, constant relaxation collision numbers of 5 and 50 are used for the calculations of rotation and vibration, respectively. In addition, the BL mechanism of translational-vibrational energy exchange is implemented in its quantum version by considering a simple harmonic oscillator (SHO) model.

The viscosity coefficient μ_{in} and the mean free path λ_{in} of the inlet gas flow are determined by considering the VHS model (BIRD, 1983) with viscosity indexes ω equal to 0.74 and 0.77 for N_2 and O_2 , respectively. Table 4.4 summarizes the main physical properties of the working fluid employed in this work.

As shown in Figure 4.3, the convergent part of the micronozzle is simulated in order to reproduce a correct velocity, pressure and temperature distributions in the throat

section. Additionally, a buffer zone is introduced to provide a more realistic pressure adjustment and to avoid any influence from the downstream boundary conditions on the region of interest, i.e., the divergent part. For cell clustering purposes, the simulated domain is divided into nine regions. The regions are further subdivided into computational cells, and cells are then subdivided into subcells. In this fashion, the cell provide a convenient reference sampling of the microscopic properties, while the collision partners are preferably selected from the same subcell for the establishment of the collision rate. Each cell has its own time step Δt and scaling factor F_N , which indicates the number of real molecules represented by a simulated molecule.

Table 4.4 - Physical properties of the working fluid.

Parameter	Value	Unit
Working fluid	N_2+O_2	
Molecular weight	28.96	kg/kmol
Molecular mass N_2	4.650×10^{-26}	kg
Molecular mass O_2	5.312×10^{-26}	kg
Molecular diameter N_2	4.110×10^{-10}	m
Molecular diameter O_2	4.010×10^{-10}	m
Molar fraction N_2	0.237	
Molar fraction O_2	0.763	
Viscosity index N_2	0.74	
Viscosity index O_2	0.77	
Degrees of freedom N_2	5 to 7	
Degrees of freedom O_2	5 to 7	

A schematic view of the computational domain is showed in Figure 4.5. According to this figure, the simulated domain is composed of six boundary types. The boundaries I and II represent the internal and external surfaces of the micronozzle, respectively. Diffuse reflection is the physical treatment applied to each molecule that interacts with these surfaces. Due to the symmetry assumptions discussed in Section 4.1, the boundaries III and IV are treated as symmetry planes, where there are no normal gradients. In such a model, the normal velocity component of the reflected molecules is reversed, while the parallel components remain unchanged. The sides V and VI represent the upstream and downstream inflow boundaries discussed in Subsection 3.7.1. As an initial conditional, the inlet velocity u_{in} is predicted analytically by assuming an one-dimensional, steady and isentropic compressible flow.

This value is determined in a such manner that sonic conditions are obtained in the throat region. Both the upstream and downstream boundary conditions are described in terms of pre-defined pressures values.

The grid generation procedures, the analysis of the time and spatial discretizations as well as the impact of the number of simulated molecules on the numerical results are discussed in the next chapter.

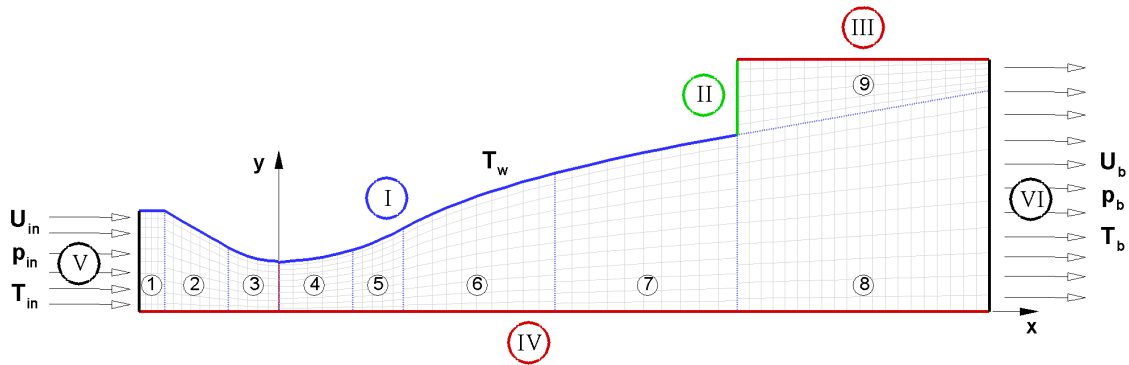


Figure 4.5 - Schematic view of computational domain and boundary conditions.

4.3 Flow Conditions

Based on Figures 4.3 and 4.5, the main geometric and flow parameters can be summarized as the expansion area ratio h_t/h_e , the exit divergent angle θ_e , the surface temperature T_w , the back pressure p_b , the pressure p_{in} and temperature T_{in} in the inlet boundary. According to the continuum approach, the expansion area ratio h_t/h_e and expansion pressure ratio p_{in}/p_b determine the mass flux across the nozzle. For the all investigated cases, the flow is choked near the throat. In this sense, the flow-field structure can be affected by geometry parameters and also compressibility and rarefaction effects, gas-surface interactions, surface temperature, etc. However, the two latter influences are beyond the focus of this work.

The present study is focused on the geometric influence of the divergent part on the flow structure. As listed in Table 4.1, this influence is studied by simulating different geometric configurations at the inflection point. The flow conditions employed are somewhat based on values that are commonly observed in practical applications and numerical simulations for cold gas propulsive systems (ALEXEENKO et al., 2002a;

BAYT; BREUER, 2001b; HAO et al., 2005; TITOV et al., 2008).

Table 4.5 presents the main properties of the inlet gas flow as well as the flow conditions in the external environment. The inlet pressure p_{in} is assumed equal to 100 kPa and the back pressure p_b equal to 5 kPa, which correspond to an expansion pressure ratio p_{in}/p_b equal to 20. The temperature of the inlet gas T_{in} and surfaces T_w are equal to 300 K.

By assuming the throat size ($2h_t$) as the characteristic dimension and taking the inlet mean free path λ_{in} , the overall Knudsen Kn_{in} and Reynolds Re_{in} numbers are approximately equal to 0.0027 and 150, respectively. It is worthwhile to observe that the thermodynamic properties change along the micronozzle. Then, based on the throat size and exit conditions, the overall Knudsen and Reynolds numbers are approximately 20 times greater and 10 times smaller than Kn_{in} and Re_{in} , respectively. Such a wide range of Knudsen values in addition to possible regions away from thermal equilibrium justify the molecular approach employed in the present study.

Table 4.5 - Flow conditions.

Parameter	Value	Unit
Inlet pressure (p_{in})	100	kPa
Back pressure (p_b)	5	kPa
Inlet temperature (T_{in})	300	K
Surface temperature (T_w)	300	K
Inlet density (ρ_{in})	1.161	kg/m ³
Inlet number density (n_{in})	2.414×10^{25}	m ⁻³
Inlet viscosity (μ_{in})	1.703×10^{-5}	Pa·s
Inlet mean free path (λ_{in})	5.423×10^{-8}	m
Inlet overall Knudsen (Kn_{in})	0.0027	
Inlet overall Reynolds (Re_{in})	150	

5 VERIFICATION AND VALIDATION PROCESSES

The application of a numerical method to solve practical problems requires a reliable way to estimate the accuracy of such solutions. In this scenario, before performing simulations in order to obtain particular results, it is necessary to submit such a numerical code to verification and validation processes (OBERKAMPF; TRUCANO, 2002). These processes estimate the reliability of the numerical method for a specific application. The verification stage evaluates whether the numerical procedures or equations are solved correctly. On the other hand, the validation stage examines if the problem is modeled correctly from a physical point of view. In the DSMC context, the verification is related to three main sources of errors: (i) spatial discretization, (ii) time discretization, and (iii) number of simulated particles per cell. For particular test cases, the validation strategy consists in comparing the results obtained by the present code with other results – numerical, analytical or experimental – available in the literature. In the next sections, the verification and validation processes applied in the present study will be discussed in detail.

5.1 DSMC Requirements

It is well known that the DSMC method has become a reliable and efficient kinetic approach to study rarefied gas flows with a significant degree of nonequilibrium. In such a method, a computational grid of cells is applied to represent the physical domain to be studied. These cells are employed to simulate collisions and sample local microscopic properties.

Most problems of engineering interest generally involve complex geometries with curved surfaces. As a result, a conventional Cartesian grid may be inappropriate to describe such flowfields. However, alternative schemes for grid generation demand additional computational cost besides sophisticated particle tracking procedures. In this way, the DSMC performance is highly dependent on the grid strategy employed.

In order to enhance the computational performance and allow a cell clustering according to local flow conditions, different grid schemes have been developed. In essence, there are two types of grid: (1) structured and (2) unstructured. The techniques for grid generation may also be classified as (i) algebraic methods, (ii) partial differential methods, or (iii) conformal mapping based on complex variables. Furthermore, the grid system may be categorized as (a) fixed or (b) adaptive. Evidently,

each strategy for grid generation provides particular advantages, e.g., high computational efficiency, variable cell sizes according to local flow gradients or the mean free path and so on. Additional detail for different grid schemes are presented by [Nance et al. \(1997\)](#) and [Wilmoth et al. \(1996\)](#).

In the DSMC context, two strategies for grid generation have been widely employed – unstructured body-fitted and sophisticated Cartesian grids – for different purposes. Among the many contributions, it is worthwhile to point out the body-fitted grid program proposed by [Wilmoth et al. \(1996\)](#), the transfinite interpolation method ([OLYNICK et al., 1989](#)), and the Cartesian grid codes with multi-level cells ([BIRD, 1990](#)) or with cell self adaptation ([RAULT, 1994](#)).

As aforementioned in Section 3.1, there are three fundamental requirements in DSMC method: (1) the cell size must be smaller than the local mean free path, (2) the time step must be smaller than the local mean collision time, and (3) the number of simulated molecules per cell must be high enough to avoid significant statistical fluctuations in the sampling process. The second requirement is related to a primary assumption employed in the DSMC method, where the molecular movement in a dilute gas can be decoupled from the intermolecular interactions if a sufficient small time step is used.

In order to correctly simulate intermolecular collisions, the cell sizes must be smaller than a third of the local mean free path. Such a requirement is even more important in the direction of strong gradients, e.g., in the direction normal to body surfaces or through shock waves. This is due to fact that in some regions, for instance near the surface, the cell size must be sufficiently small to reproduce the physical process in an accurate manner. If the cell sizes near the surface are excessively large, molecules far away from the surface can transfer momentum and energy to such a surface. This behavior may lead to inappropriate predictions of the aerodynamic forces on and heat flux to the body surface. In this scenario, the cell size must vary according to the local gradients and mean free path.

The selection of a time step smaller than the local mean collision time is required to allow a consistent uncoupling between the molecular movement and collisions. In addition, the time step must be small enough to avoid particles crossing more than one cell during a single time increment. As reported in Section 3.1, within each cell, this condition allows particles to collide each other performing a realistic transfer of

momentum and energy. Finally, simulation results are independent of the time step as long as the time step and cell size requirements are respected.

The number N of simulated particles per cell influences on different parameters – reproduction of a correct collision rate, mean separation distance, statistical fluctuations and computational efficiency – as discussed in Section 3.1. Moreover, the total number of simulated particles and cells are strongly related to the statistical correlations between these particles. A significant level of statistical dependence, or particle correlations, means that the molecular chaos hypothesis, which is a fundamental assumption in molecular approach, is no longer valid. Since the DSMC method employs a finite number of particles, the number of collision pairs per cell is also limited and the probability of repeated collisions¹, which is related to N , may be fairly high. Such a phenomenon is physically impossible and results in high statistical dependence of the results on N . A practical to estimate these errors is to vary the number of simulated particles and cells until the DSMC solution does not change any longer. More detailed investigations about statistical correlations can be found in the available literature (IVANOV et al., 1989; IVANOV; GIMELSHEIN, 2003; SHEVYRIN et al., 2005).

In order to efficiently simulate the flow physics using a statistical modeling, a minimum value of N is necessary. In general, 20 to 30 simulated particles per cell is an acceptable number for DSMC computations. Notwithstanding, the number density may vary several orders of magnitude within the flowfield. Hence, maintaining an uniform distribution of simulated particles may be a difficult task, i.e, setting N as a constant in the entire computational domain. As pointed out by Kannenberg and Boyd (2000), the number of simulated particles per cell varies inversely with the number density for two- and three-dimensional DSMC simulations. This counter-intuitive result means that high density regions contain a small number of simulated particles and vice-versa. Since the most physical processes occur in high density regions, e.g., collisions and reactions, it is primordial that N satisfies the minimum requirements in such regions. The large variations of N within the simulated domain can be overcome with a variable scaling factor F_N . This parameter indicates the number of real particles represented by a simulated one.

In this sense, since the computational domain is divided into cells, a different time step Δt and scaling factor F_N can be set for each cell. Employing a DSMC grid with

¹Subsequent collisions between the same pair of particles.

cell sizes, time steps and scaling factors, that vary according to the local gradients and mean free path, yields a significant reduction in the total number of simulated particles as well as an improved spatial resolution. As a result, the DSMC efficiency increases and the computational effort is balanced within the simulated domain. It is worthwhile to highlight that, although the time step and scaling factor vary across cells, the ratio $F_N/\Delta t$ must be the same for all domain. This requirement assures that the mass flux across the cell boundaries is conserved (OLYNICK et al., 1989).

Another important parameter in the DSMC method is related to the total number N_S of samples extracted from each cell. Since the macroscopic properties are obtained from averages, one measure of the quality of a DSMC solution is determined by the statistical scatter dependence on N_S . A given sample may be generated by simulating a large number of particles for a short period of time or a small number of particles for a large period of time. According to Bird (1976), both schemes provide the same results. As shown in Section 3.5 for the NTC scheme, the computational time is proportional to the number N of simulated particles per cell. In this way, it is preferable to use a minimum value of N because such a situation requires a smaller amount of computer memory, while the computational effort and statistical scatter remain the same (FALLAVOLLITA et al., 1993). The acceptable level of statistical scatter depends on the simulation purpose.

Finally, previous studies investigated the dependence of the DSMC numerical accuracy on the cell size (ALEXANDER et al., 1998; ALEXANDER et al., 2000), on the time step (GARCIA; WAGNER, 2000; HADJICONSTANTINO, 2000) as well as on the number of particles per cell (SHU et al., 2005). On the other side, the two main computational limitations in the DSMC method – run time and storage – were examined by Rieffel (1999) for rarefied gas flows.

5.2 Grid Generation

In the present investigation, the grid generation strategy is based on the same scheme presented by Bird (2006) in the DSMC code named as DSG2. In this scheme, the computational domain is divided into an arbitrary number of regions. Each region is composed of four sides, where two sides can be straight or curved and the other two sides must be straight, e.g., the nine regions in Figure 4.5. Then, along the boundaries of each region, points are distributed in a such manner that the number of points in the opposite sides is equal. These correspondent points are connected by

straight segments to form quadrilateral cells. The point clustering can be determined by different algebraic functions (HOFFMANN; CHIANG, 2000), what allow a higher point density in desired positions. Since this strategy is applied independently for each region, complex flowfield structures can be predicted according to the DSMC requirements in an efficient manner.

5.3 Adaptive and Optimization Procedures

The computational procedure employed for the grid adaptation is basically composed of the following steps:

- 1) A computational grid is generated based on the inlet and estimated outlet gas flow;
- 2) The scaling factor F_N and time step Δt values are defined for each cell according to the DSMC requirements and subject to the condition that $F_N/\Delta t$ has the same value in every cell;
- 3) The parameters – F_N and Δt – are iteratively modified as the flow evolves within the simulated domain until each cell contains, on average, the desired number of simulated particles;
- 4) For the entire flowfield, all DSMC requirements are verified. If within any cell these conditions are not satisfied, the grid adaptation procedure – steps 1, 2 and 3 – is restarted for a more appropriate spatial discretization.

In addition, the present DSMC algorithm is partially using the shared memory parallelization routines from OpenMP. All these improvements increase computational performance and attain the DSMC requirements.

5.4 Verification Test Case

As presented in Section 4.1, different aerodynamic configurations are modeled by changing the slope and radius of curvature at the inflection point of the divergent micronozzle part. For comparison purposes, a geometry with smooth divergent surface – case A1 – is defined as the reference case. Hence, the gas flow in the micronozzle with A1 geometry is the subject of the verification process. The flow properties and boundary conditions employed for such simulations are the same ones previously presented in detail in Chapter 4.

Based on the selected geometry, case A1, the simulated domain contains approximately a length of 165 μm . The inlet mean free path λ_{in} is equal to 5.423×10^{-8} m and the pressure ratio p_{in}/p_{out} is equal to 20. Under these conditions, a mean free path in the external flow of $20\lambda_{in}$ is expected. Moreover, the convergent-divergent geometry naturally changes the pressure levels, and consequently λ , inside the micronozzle. Thus, a grid based only on λ_{in} would need more than 3200 cells in the x -direction while a grid based only on the mean free path of the external flow would need about 160 cells in the same direction. As a result, it is clear that a grid with variable cell size in x - and y -directions is necessary.

Since the present work is focused on studying the divergent part of the micronozzle, the DSMC requirements in such a region must be rigorously respected. In order to attain these requirements, a computational grid with appropriate cell clustering is employed. The distribution of cells is tabulated in Table 5.1 for each one of the nine regions in Figure 4.5 that compose the computational domain. This grid contains 57,065 cells and is defined as the standard grid. Besides such a grid, alternative spatial discretizations, named as coarse and fine grids, are applied to investigate the influence of the grid resolution on the numerical results.

5.4.1 Spatial Discretization Effects

The impact of the grid resolution on the computational results plays an important role in the present work. An excessively coarse resolution can significantly reduce the accuracy in the prediction of aerodynamic forces on and heat flux to the body surface as well as in the flowfield distribution. In this fashion, the skin friction, pressure and heat transfer coefficients in addition to profiles of macroscopic quantities are used as representative parameters in the investigation of grid resolution effects.

These effects are investigated in order to determine the number of cells in each direction required to achieve grid independent solutions. Grid independence is examined by running the calculations with different number of cells in x - and y -directions compared to the standard grid. The effect of altering the cell size in the x -direction is analyzed for coarse and fine grids with, respectively, 50% less and 50% more cells with respect to the standard grid, while the number of cells in the y -direction is kept the same. In the x -direction, an intense cell clustering is applied in the inlet region in a such manner that cell size increases in downstream direction. Table 5.1 presents the number of cells employed in each computational region for coarse, standard and

fine grids.

Table 5.1 - Cell distribution – direction x versus y – applied in the verification process.

	Coarse (x)	Coarse (y)	Standard	Fine (x)	Fine (y)
Region 1	4×290	8×145	8×290	12×290	8×435
Region 2	17×265	35×132	35×265	52×290	35×397
Region 3	12×215	25×107	25×215	37×215	25×322
Region 4	17×215	35×107	35×215	52×215	35×322
Region 5	7×190	15×95	15×190	22×190	15×285
Region 6	19×190	38×95	38×190	57×190	38×285
Region 7	25×190	50×95	50×190	75×190	50×285
Region 8	25×190	50×95	50×190	75×190	50×285
Region 9	25×70	50×35	50×70	75×70	50×105
#Cells	28,090	28,485	57,065	85,155	85,550

The left column in Figure 5.1 depicts the influence of varying the number of cells in the x -direction on the skin friction C_f , pressure C_p and heat transfer C_h coefficients along the micronozzle internal surface. In such plots, the X -coordinate stands for the length x normalized by the half throat size h_t . In essence, as observed in Figure 5.1, the mentioned coefficients are not affected by altering the grid resolution in the x -direction.

In analogous fashion, an examination is made in the y -direction with a coarse and fine grids with, respectively, 50% less and 50% more cells than the standard grid, while the number of cells in the x -direction is kept the same. In the y -direction, cell clustering is used near solid surfaces where the gradients are usually more intense. According to the right column in Figure 5.1, the effect of changing the cell size in the y -direction on C_f , C_p and C_h is rather insensitive to the range of cell spacing considered.

The grid resolution impact on the flowfield structure is also analyzed by plotting profiles of macroscopic properties. Different velocity, pressure, temperatures and density profiles are calculated, although not shown, for this verification process. For brevity, only three pressure profiles – normalized by p_{in} – for cross-sections along the micronozzle are shown. This choice is based on the fact that pressure profiles presented the larger variations in comparison to other properties. Figure 5.2 illustrates these

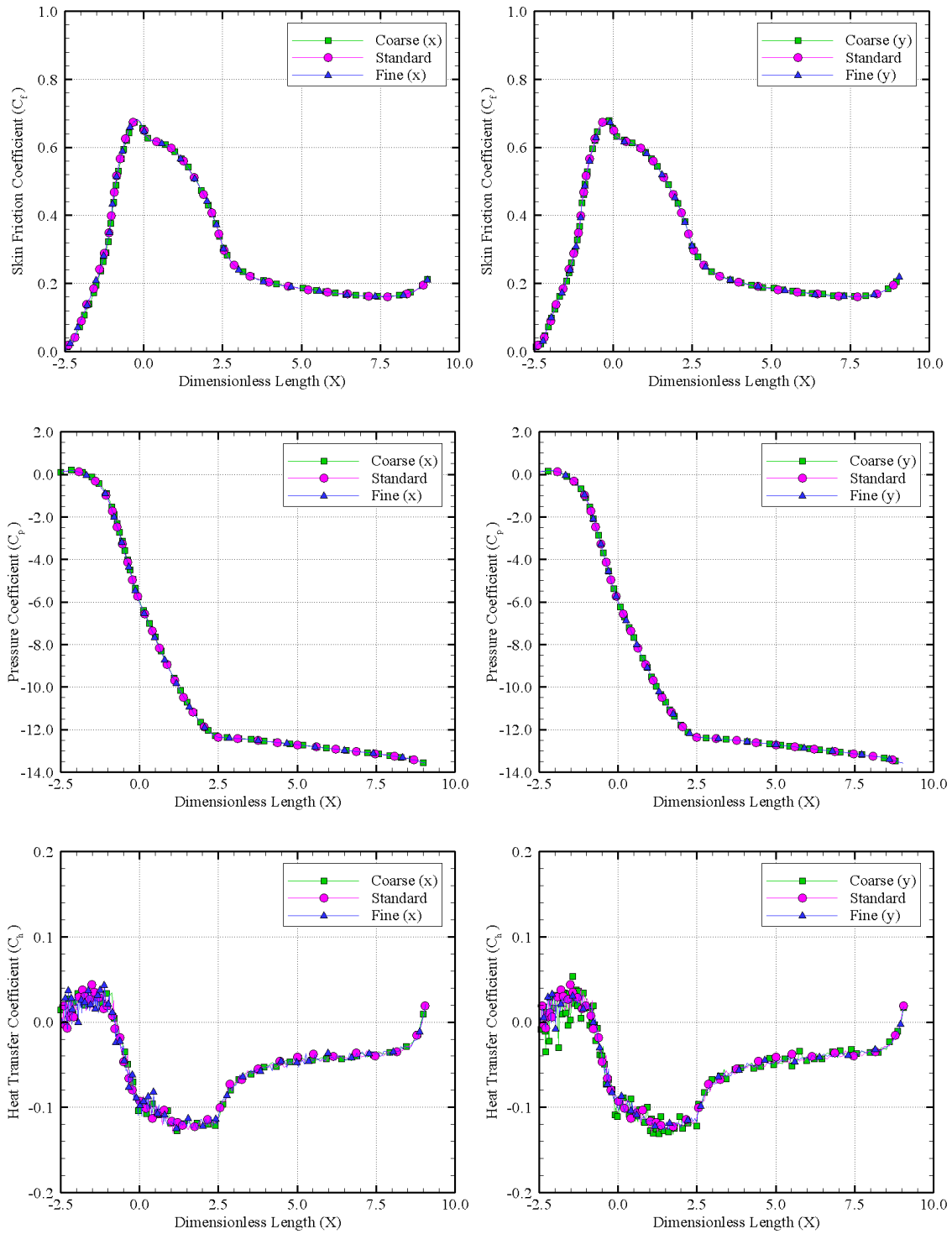


Figure 5.1 - Influence of varying the number of cells in the x (left column) and y (right column) directions on the skin friction (top), pressure (middle) and heat transfer (bottom) coefficients.

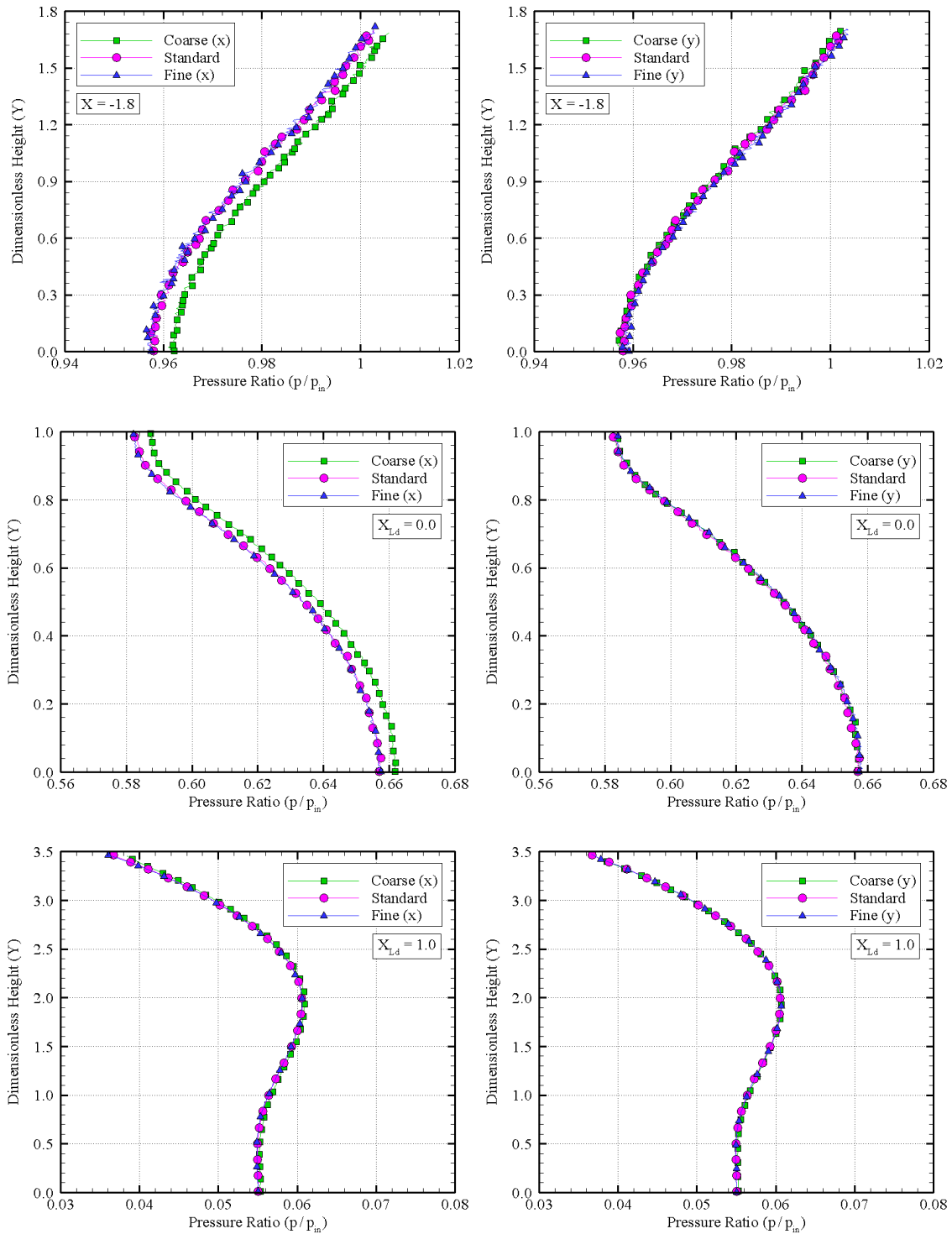


Figure 5.2 - Influence of varying the number of cells in the x (left column) and y (right column) directions on the pressure distribution for section $X = -1.8$ (top), $X_{Ld} = 0.0$ (middle) and $X_{Ld} = 1.0$ (bottom).

variations for convergent ($X = -1.8$), throat ($X_{Ld} = 0.0$) and exit ($X_{Ld} = 1.0$) sections, where X_{Ld} refers to the x -coordinate normalized by the length of the divergent region L_d (Figure 4.3).

Therefore, the results presented in Figures 5.1 and 5.2 indicate that the standard grid, with a total of 57,065 cells, is essentially grid converged according to a graphical profile analysis.

5.4.2 Time Discretization Effects

Similarly to the investigation of grid resolution effects, an examination of the time discretization is made. The present analysis is performed using the reference case with standard grid that originally employs a reference time step Δt_{ref} equal to $\Delta t_{min}/16$. The parameter Δt_{min} represents the minimum value between the mean collision time and the mean residence time (Section 5.1) computed within the entire simulated domain when steady state is achieved. Due to the adaptive procedures mentioned in Section 5.3, the local time step can be somewhat different from Δt_{ref} but still respecting the DSMC requirements. At this point, it is just important to keep in mind that the real mass flux across the cell boundaries is defined according to the reference time Δt_{ref} .

In this context, in order to quantify the impact of different reference time steps on the DSMC solution, two variations of the reference case with standard grid are investigated. In such new cases the parameter Δt_{ref} is set equal to $\Delta t_{min}/4$ and $\Delta t_{min}/64$. For the present conditions, the left column in Figures 5.3 and 5.4 illustrates that the solutions are essentially independent of the time step as long as $\Delta t_{ref} \leq \Delta t_{min}/16$. Thus, it is verified that a reference time step equal to $\Delta t_{min}/16$ attains the requirements for the reference case analyzed.

5.4.3 Particle Number Effects

Additional effort is dedicated to estimate the influence of the number of simulated particles on the solution. The standard grid examined in Subsections 5.4.1 and 5.4.2 corresponds to approximately 1,200,000 simulated particles when the steady state is achieved. By using this same grid, two other simulations are run with different number of particles. These new cases correspond to approximately 600,000 and 1,800,00 simulated particles within the computational domain. The effects of such variations on skin friction, pressure and heat transfer coefficients as well as on the pressure

ratio distribution are demonstrated in the right column of the Figures 5.3 and 5.4. Basically, these three cases presented the same results for the investigated properties. Hence, the standard grid with a total of 1,200,000 particles is considered sufficient for the computation of the flowfield and aerodynamic properties.

5.4.4 Sample Number Effects

As discussed in Section 5.1, the level of statistical scatter in a DSMC solution is strongly related to the total number N_S of samples extracted from each cell. Hence, for a particular problem, it is important to determine the value of N_S that provides an acceptable scatter. In the previous subsections, all simulations were performed with 200,000 samples per cell. In this sense, it is necessary to verify if this value is sufficient to yield a small fluctuation level. For this purpose, the reference case with a standard grid and approximately 1,200,00 simulated particles is run for 20,000 and 100,000 samples. Figure 5.5 reveals an excessive scatter for 20,000 samples while for 100,000 samples the results show a considerable improvement. When N_S is increased to 200,000, the statistical scatter is further reduced, but only by a small factor. Based on these results, N_S equal to 200,000 is a feasible value that can provide acceptable fluctuation level for the case investigated.

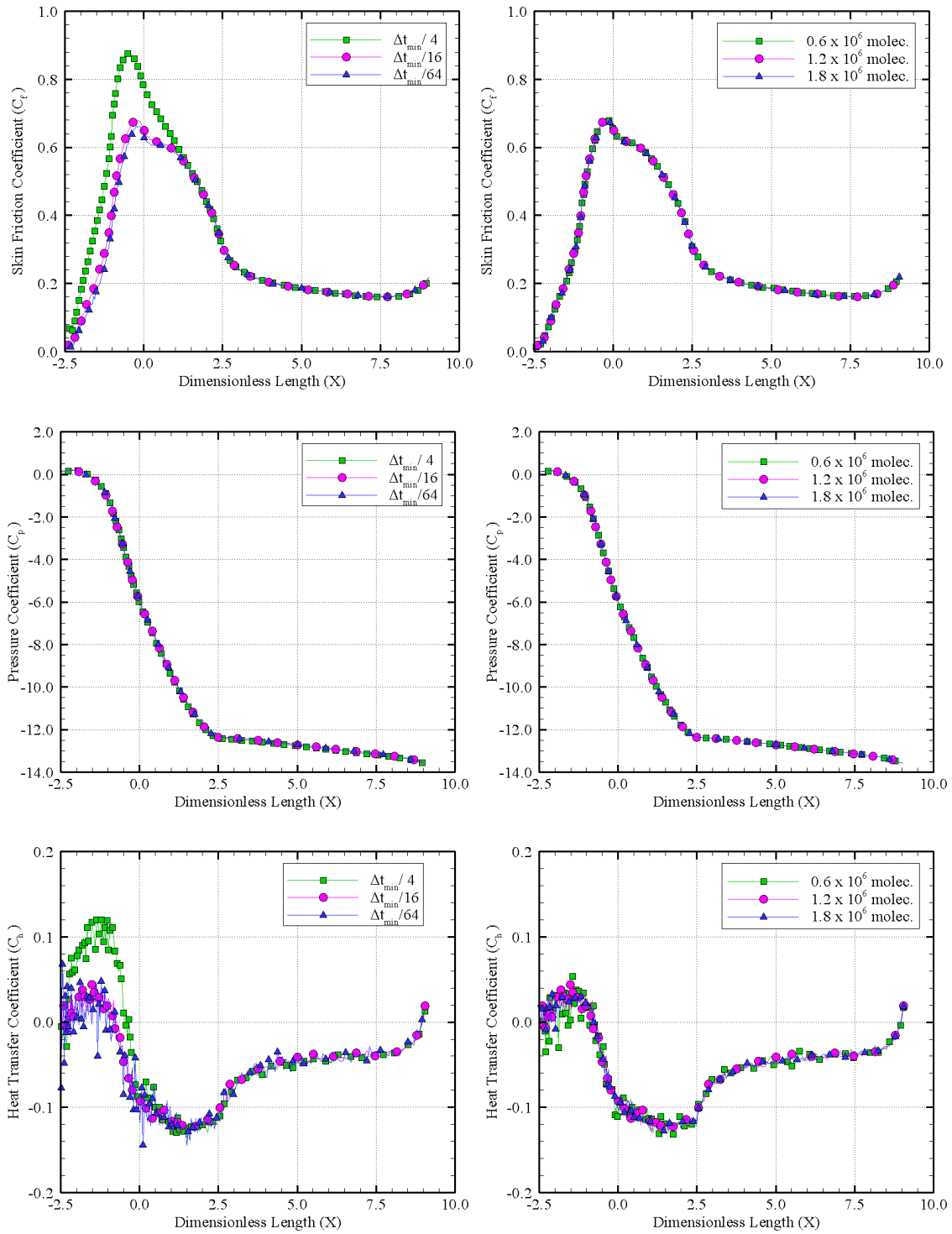


Figure 5.3 - Influence of varying the reference time step (left column) and the number of simulated molecules (right column) on the skin friction (top), pressure (middle) and heat transfer (bottom) coefficients.

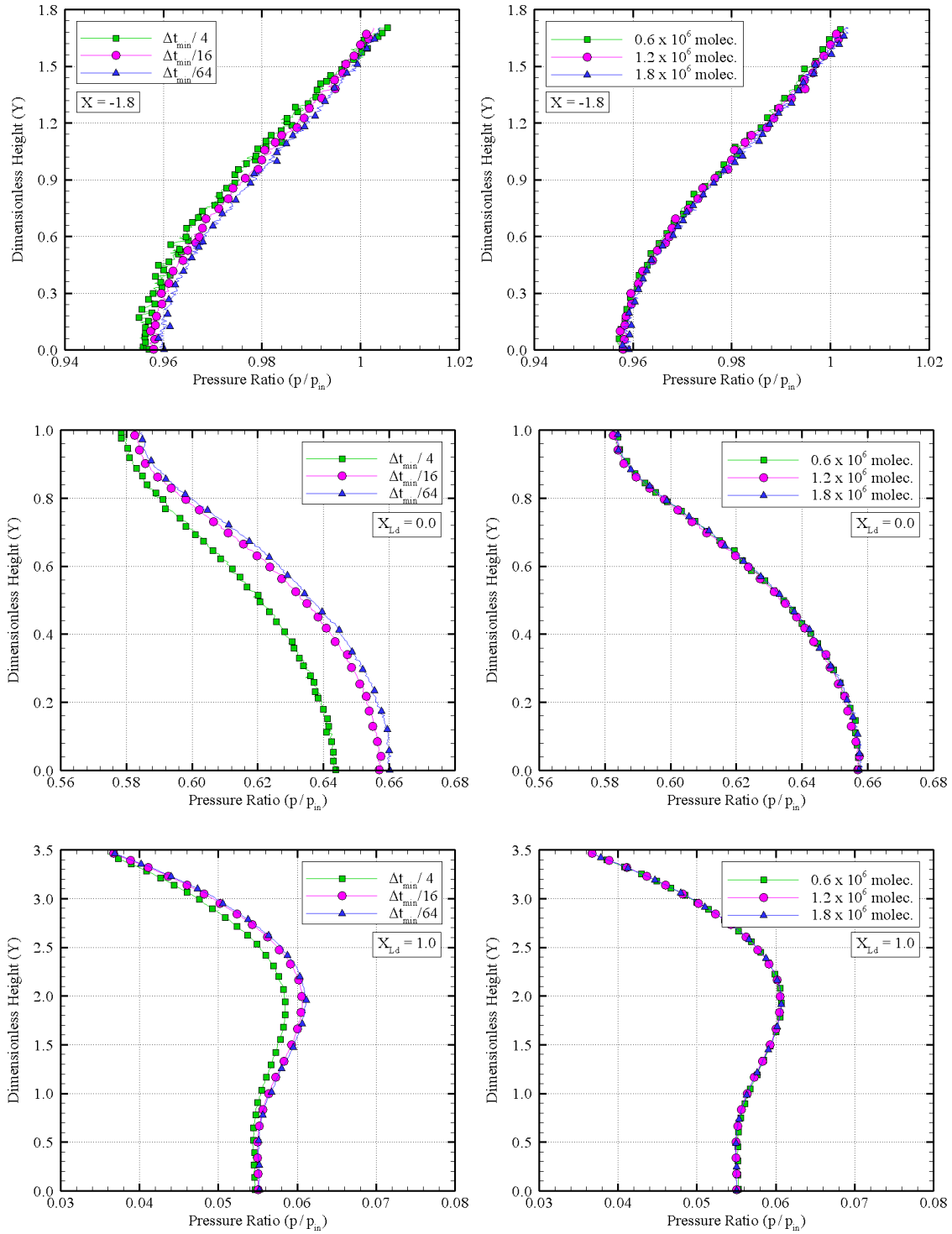


Figure 5.4 - Influence of varying the reference time step (left column) and the number of simulated molecules (right column) on the pressure distribution for section $X = -1.8$ (top), $X_{Ld} = 0.0$ (middle) and $X_{Ld} = 1.0$ (bottom).

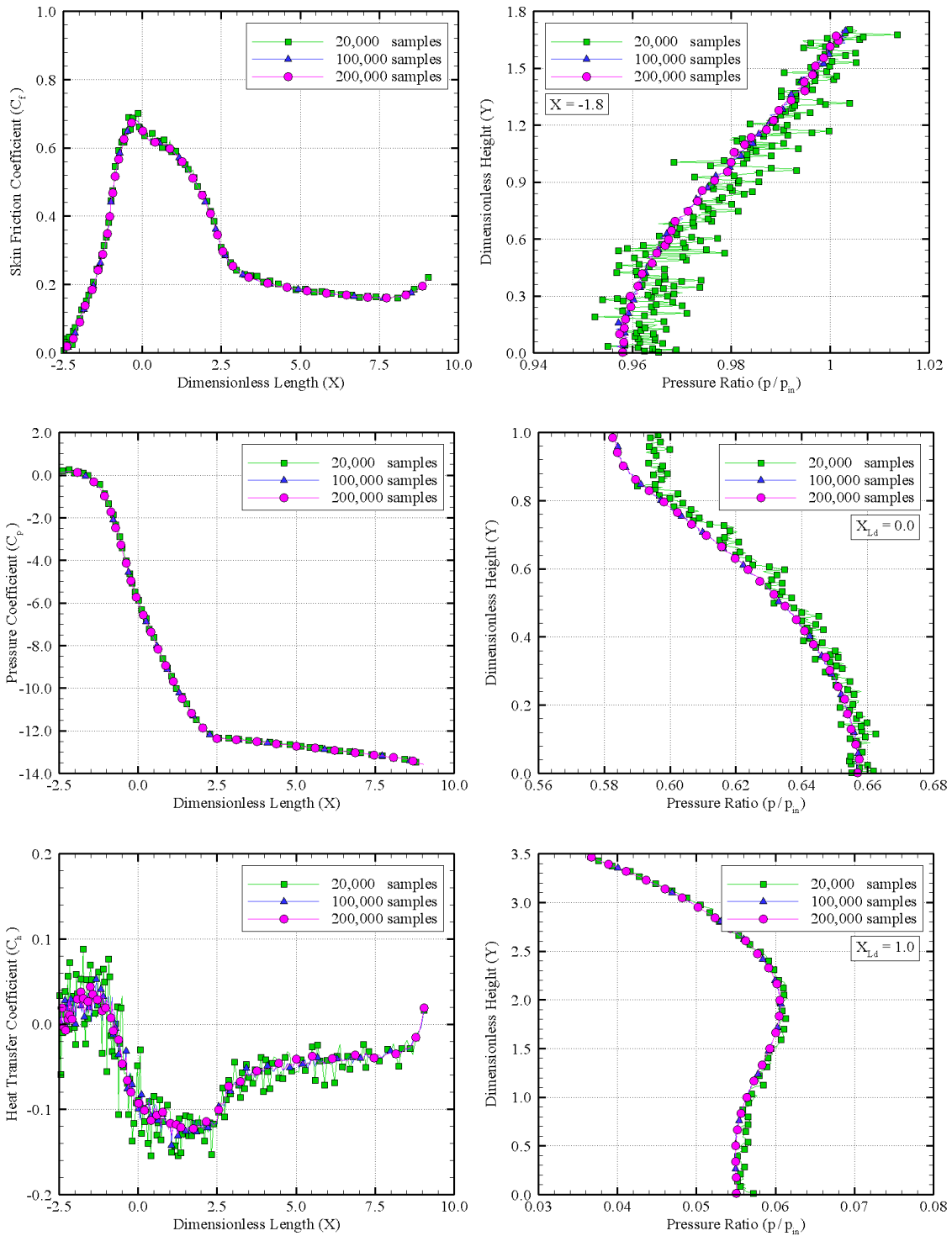


Figure 5.5 - Influence of varying the number of samples on the aerodynamic properties (left column) and pressure distribution (right column).

5.5 Validation Test Case

The main idea of this validation process is to examine if a particular internal gas microflow simulated is correctly modeled, from a physical point of view, by the present DSMC code. For such a purpose, this algorithm is employed to solve a test case that has experimental and/or alternative numerical solutions available in the literature. Then, these different solutions are compared in order to analyze possible deviations.

The test case used to validate the current DSMC implementation is based on the experimental-numerical study carried out by Hao et al. (2005). In their work, experiments on a micronozzle with rectangular cross-section were conducted to measure the mass flow rate and pressure distributions near the throat under different outlet pressures. Moreover, temperature and Mach number distributions along the centerline for various nozzle scales and outlet conditions were obtained numerically through the two-dimensional compressible Navier-Stokes (NS) equations with slip condition. Fortunately, these experimental results have been reproduced using different numerical methods, e.g., DSMC (LAN, 2009; XIE, 2007), NS equations with slip condition (HAO et al., 2005; SAN et al., 2009; XIE, 2007), argumented Burnett equations (SAN et al., 2009) and relaxation time Monte Carlo (RTMC) method with multiple translational temperature (MTT) model (LAN, 2009). Since the data and assumptions employed in each method are available in the literature, the subsequent discussions are limited only to necessary details.

In the experimental test case (HAO et al., 2005), the baseline configuration consisted of a micronozzle with half throat size h_t of 10 μm , expansion area ratio of 1/1.7 and depth of 120 μm . This microdevice was fabricated with silicon wafers and tested in a clean room. Air was the working fluid employed in the experiments such that its properties are essentially the same as presented in Table 4.4. In a similar fashion, except for the back pressure p_b that was varied for each test, the experimental flow conditions were exactly the same as those listed in Table 4.5, i.e., $p_{in} = 100$ kPa, $T_{in} = 300$ K, $T_w = 300$ K and so on.

The geometry definition and boundary conditions used in the present DSMC simulation are illustrated in Figures 5.6 and 5.7. Table 5.2 shows all dimensions normalized by the half throat size h_t . According to this data, the convergent θ_c and the exit divergent θ_e angles are equal to 25.6 and 4.2 degrees, respectively. Since

the experiments involved a single micronozzle, it is important to observe that the computational boundary III is treated as a downstream inflow boundary, while the other boundaries remain with the same treatment adopted in Section 4.2. Here, it is also worthwhile to remark that the solid surfaces – boundaries I and II – are treated as diffuse.

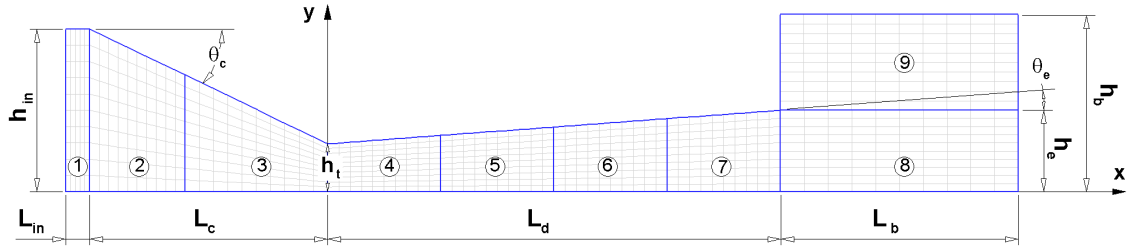


Figure 5.6 - Geometry definition of the computational domain for the validation case.

Table 5.2 - Additional geometric definitions for the validation case.

h_{in}/h_t	h_e/h_t	h_b/h_t	L_{in}/h_t	L_c/h_t	L_d/h_t	L_b/h_t
3.40	1.70	3.70	0.50	5.00	9.50	5.00

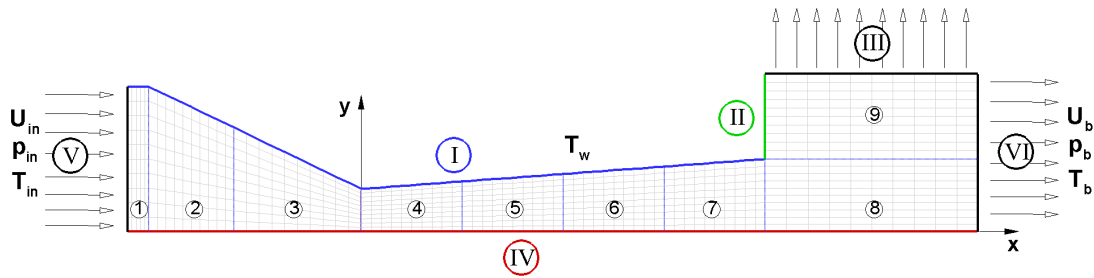


Figure 5.7 - Schematic view of computational domain and boundary conditions for the validation case.

In the present two-dimensional simulations, the same verification process (not shown) discussed in Section 5.4 is applied in order to define the grid resolution, time step, number of molecules and number of samples related to the DSMC requirements. The inlet pressure is kept at 100 kPa, while the back pressure p_b is set

equal to 10 kPa, 40 kPa, 70 kPa and 90 kPa, for each case. These four different values of back pressure are selected for comparisons with the aforementioned experimental results. For such cases, the results are expressed in different ways as illustrated in Figures 5.8, 5.9 and 5.10. In this set of plots, the X - and Y -coordinates stand for the lengths x and y normalized by the half throat size h_t , respectively.

In Figure 5.8, Mach, pressure and translational temperature distributions along the centerline are exhibited for different values of p_b . The more intense changes in these properties occur for p_b equal to 10 kPa and 40 kPa, which induces steady supersonic flows in the divergent part. The pressure distributions also reveal that the present pressure adjustment, discussed in Subsection 3.7.1, provides a satisfactory agreement with the pre-defined values, p_{in} and p_b , in the vicinity of the upstream and downstream boundaries, respectively. Small deviations of these values are observed only for p_b equal to 10 kPa. Such errors may be related to high rarefaction degree and nonequilibrium conditions near the downstream boundary, where the ideal gas assumption may be inappropriate. Nevertheless, since the external flow is supersonic, such departures are restricted to small distances and do not affect the region of interest, i.e., the divergent surface.

Turning next to Figure 5.9, the mass flow rate through the throat is described as a function of the pressure difference Δp , where $\Delta p = p_{in} - p_b$. The quasi-one-dimensional continuum isentropic solution (ANDERSON, 1990; SAAD, 1993; SHAPIRO, 1954) provides an analytical reference for the mass flow rate and Mach number distributions. As expected, the flow becomes choked for large pressure differences. In addition, due to viscous effects, the experimental and numerical results present a lower mass flow rate in comparison to those for the isentropic case. Besides the throat position ($X = 0.0$), the average pressure along upstream ($X = -1.8$) and downstream ($X = 2.2$) cross-sections are also shown.

Additionally, Figure 5.10 compares the Mach number distribution along the centerline with that obtained by NS and isentropic solutions. As observed, the Mach distribution is overpredicted by the isentropic solution in the divergent part, where the neglected viscous effects are more intense. The present DSMC solution extends to $X \approx 15.0$ due to the buffer zone, which was not considered in the other solutions.

The present solutions are compared with the experimental measurements and/or other numerical solutions. Assuming the uncertainty of the experimental data to

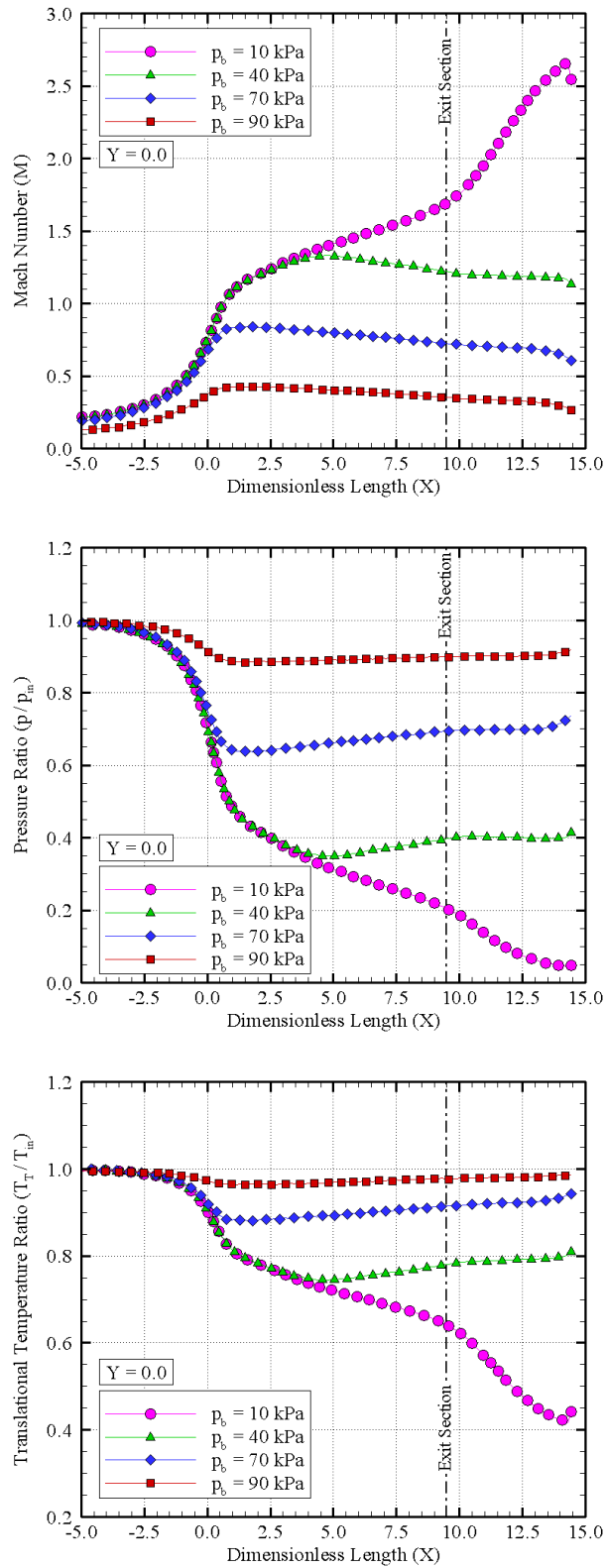


Figure 5.8 - Mach number (top), pressure (middle) and translational temperature (bottom) distributions along the centerline ($Y = 0.0$) for different back pressures p_b .

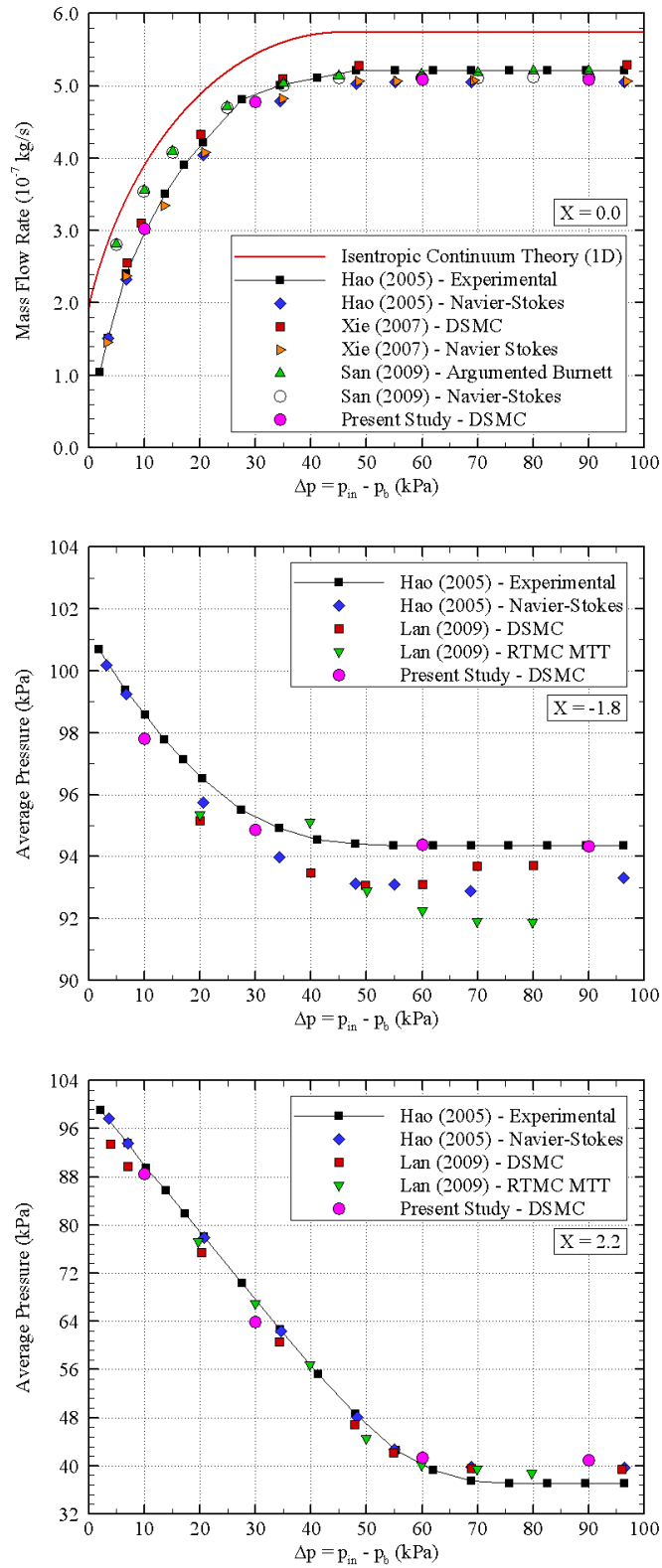


Figure 5.9 - Comparisons of experimental results versus numerical results for the mass flow rate (top), and average pressure along upstream (middle) and downstream (bottom) cross-sections.

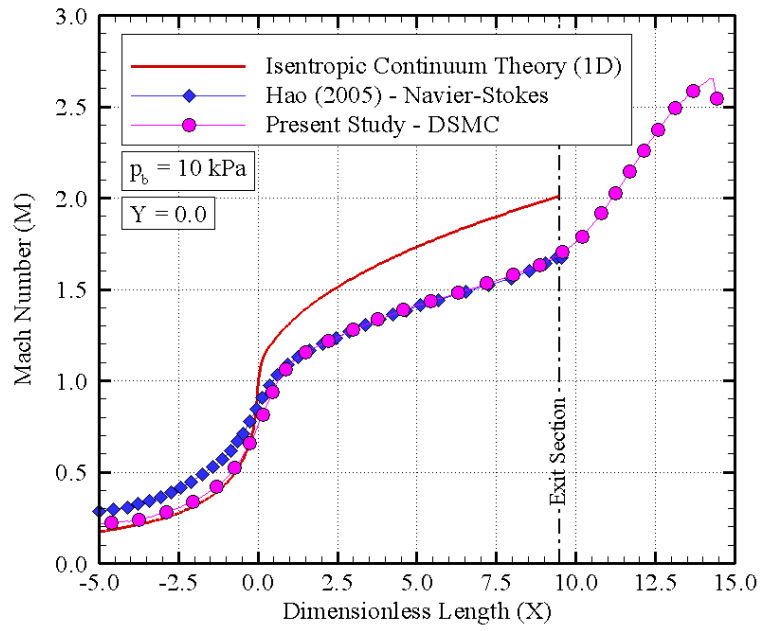


Figure 5.10 - Comparison of the present DSMC solution versus NS and isentropic solutions for the Mach number distribution along the centerline.

be approximately 3% (HAO et al., 2005), the results indicate, in general, a good agreement between different approaches. In this sense, for the analyzed test case, it is verified that the current DSMC code reproduces with sufficient accuracy, mainly in the divergent surface, the real physical behavior.

6 COMPUTATIONAL RESULTS

Since the present simulations are carried out over a wide range of conditions and properties, it proves worthwhile to summarize the main results. In this case, the purpose of this chapter is to discuss and compare influences on the flowfield structure, aerodynamic surface properties as well as micronozzle performance due to variations of the geometric parameters α_g and β_g , i.e., variations of the micronozzle divergent shape. As long as suitable, comparisons between typical rarefied and continuum behaviors are made.

6.1 Flowfield Structure

This section explores the primary macroscopic properties computed from the DSMC results. For the present account, properties of particular interest are velocity, density, pressure and temperature. In addition, in order to map nonequilibrium regions, the Knudsen number distribution is presented. Velocity and density are fundamental dynamic quantities that do not depend on the assumption of thermal equilibrium, such as pressure and temperature. Thus, for the same dynamic aspect, equilibrium or nonequilibrium thermodynamic features arise due to the thermal behavior of the gas. Hence, velocity – expressed in terms of the Mach number – and density are examined first, followed by pressure, temperature and Knudsen number distributions.

6.1.1 Mach Number Field

Due to the statistical nature of the DSMC method, the macroscopic properties are obtained from local averages of the microscopic quantities, i.e., averages within the computational cells. Therefore, the local stream macroscopic velocity vector is given by the following expression:

$$\mathbf{c}_0 = \frac{\overline{m\mathbf{c}}}{\overline{m}} = \frac{\sum_{j=1}^N m_j \mathbf{c}_j}{\sum_{j=1}^N m_j} \quad (6.1)$$

where m , and \mathbf{c} refer to the mass and molecular velocity vector, respectively, and N is the total number of simulated molecules computed within the respective cell during the simulation.

As aforementioned in Subsection 3.7.1, the molecular velocity is composed of a lin-

ear combination of the macroscopic and peculiar velocities, i.e., $\mathbf{c} = \mathbf{c}_0 + \mathbf{c}'$. Consequently, the mean molecular velocity $\bar{\mathbf{c}}$ is equal to \mathbf{c}_0 because the random molecular motion provides $\bar{\mathbf{c}'} = 0$.

In the present context, the Mach number M is defined by Equation 6.2, where V and a represent the local macroscopic and sound speeds, respectively. As presented in Equation 6.3, the local specific heat ratio γ is a function of the molecular degrees of freedom (VINCENTI; KRUGER, 1965). It is important to observe the translational temperature T_T is employed in the sound speed definition instead of the thermodynamic temperature. Such a choice is based on the fact that gas disturbances are propagated according to translational molecular movement, which is related to T_T . It will be shown in Subsection 6.1.4 that in nonequilibrium regions the translational and internal modes may be associated to different temperatures. Then, the definition of thermodynamic temperature, in essence, is not possible for such regions.

$$M = \frac{V}{a} = \frac{V}{\sqrt{\gamma k T_T / m}} \quad (6.2)$$

$$\gamma = \frac{\zeta_T + \zeta_R + \zeta_V + 2}{\zeta_T + \zeta_R + \zeta_V} \quad (6.3)$$

Mach number M profiles along the micronozzle are shown in Figures 6.1, 6.2 and 6.3 for group A, B and C cases, respectively. These profiles are presented for six different cross-sections between the throat and exit section. In all cases, the flow is choked near the throat section and hence there are no differences between the convergent profiles of such cases. In this set of pictures, X_{L_d} stands for the x -coordinate normalized by the length of the divergent region L_d , and Y refers to the y -coordinate normalized by the half throat size h_t . Therefore, for all cases, X_{L_d} equal to 0.0 and 1.0 represent throat and exit cross-sections, respectively. Among the other four intermediate X_{L_d} stations, there is one section that refers specifically to the inflection point x -coordinate ($x = L_{d_1}$) of a particular case. In these particular cross-sections, X_{L_d} is equal to L_{d_1}/L_d . Consequently, such stations vary according to the respective group (A, B and C). For example, in group A, X_{L_d} equal to 0.1909, 0.2715 and 0.4012 refers to the inflection point x -coordinate of cases A3, A1 and A2, respectively. Table 4.3 summarizes the L_{d_1}/L_d ratio for each case.

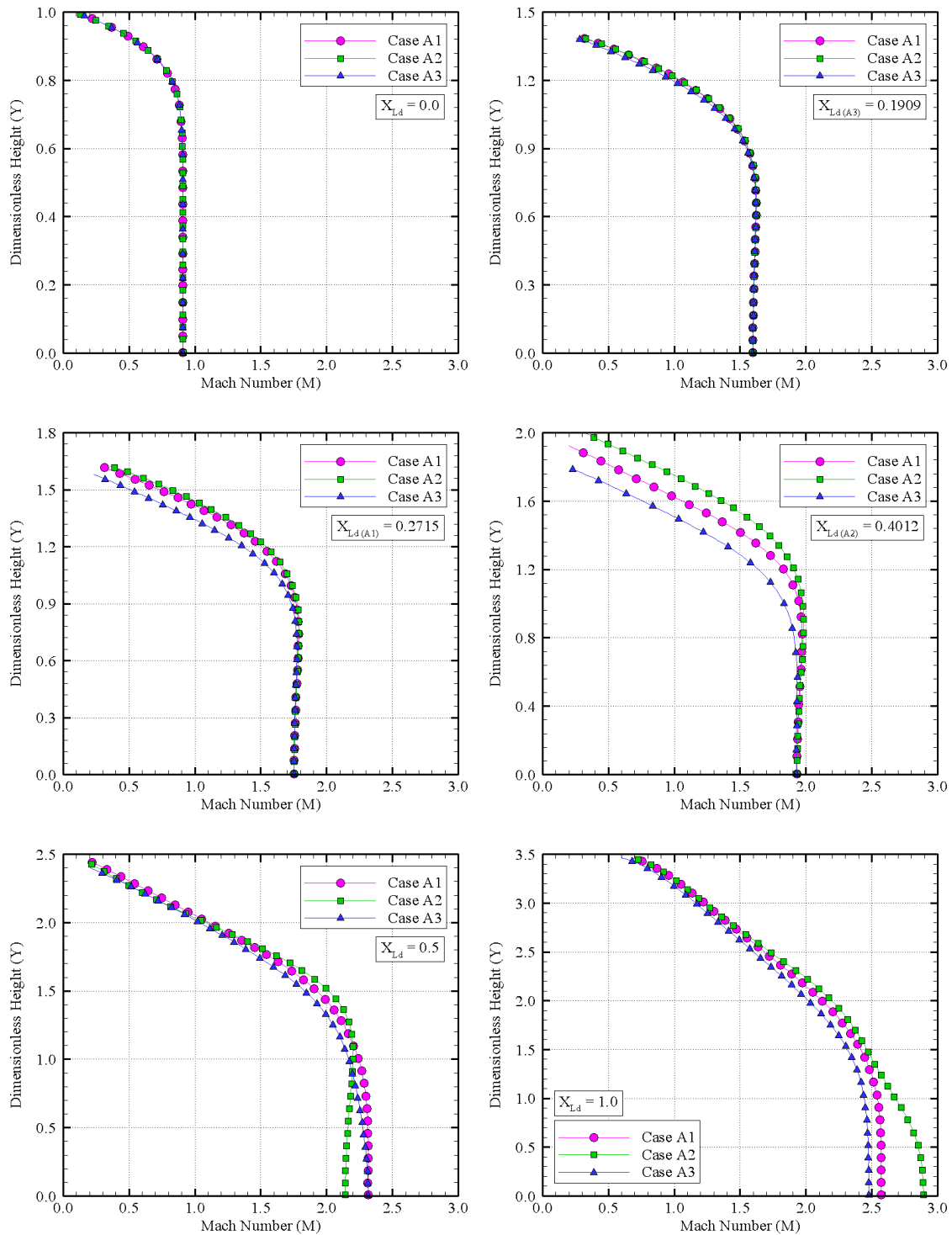


Figure 6.1 - Mach number (M) profiles along the micronozzle for group A cases.

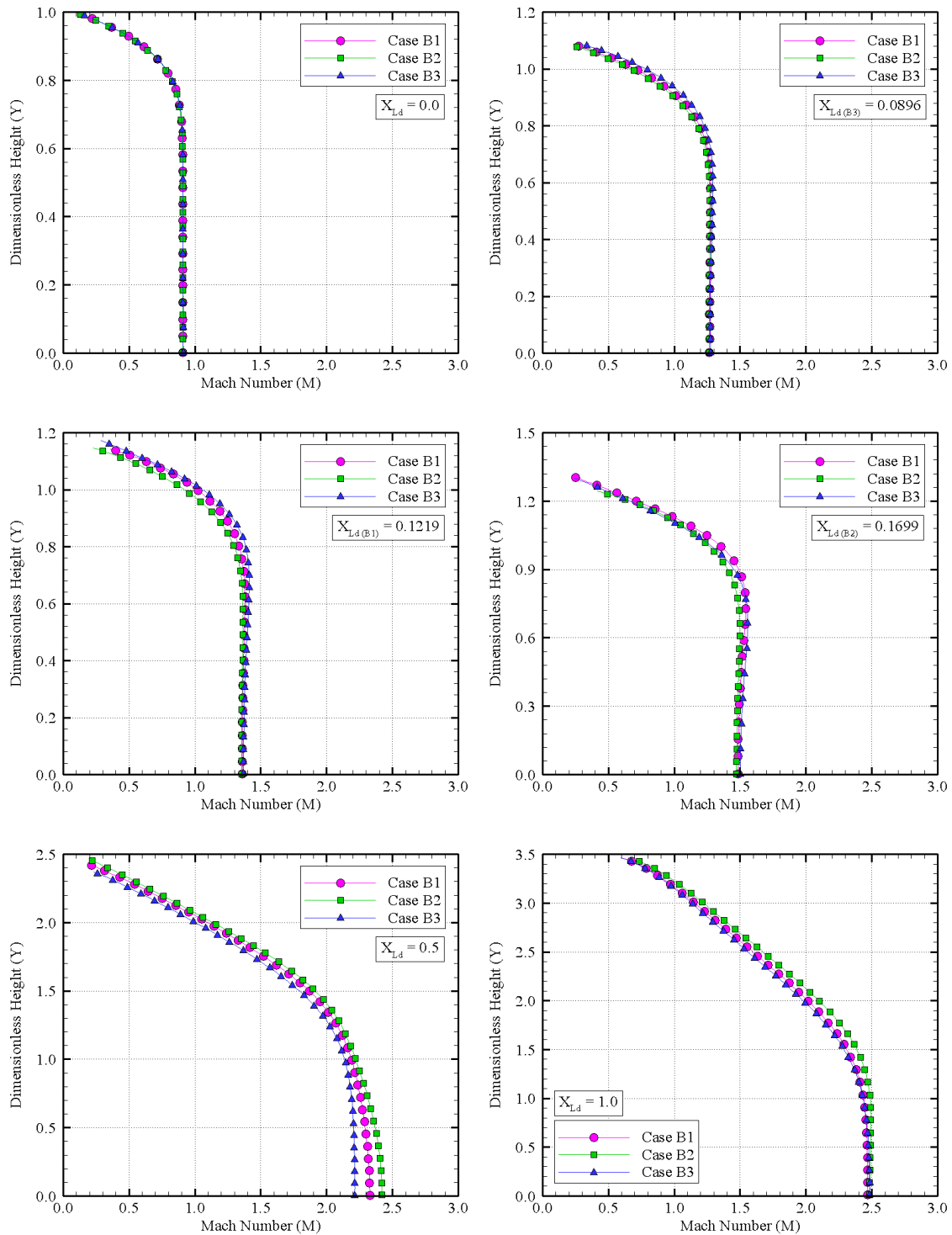


Figure 6.2 - Mach number (M) profiles along the micronozzle for group B cases.

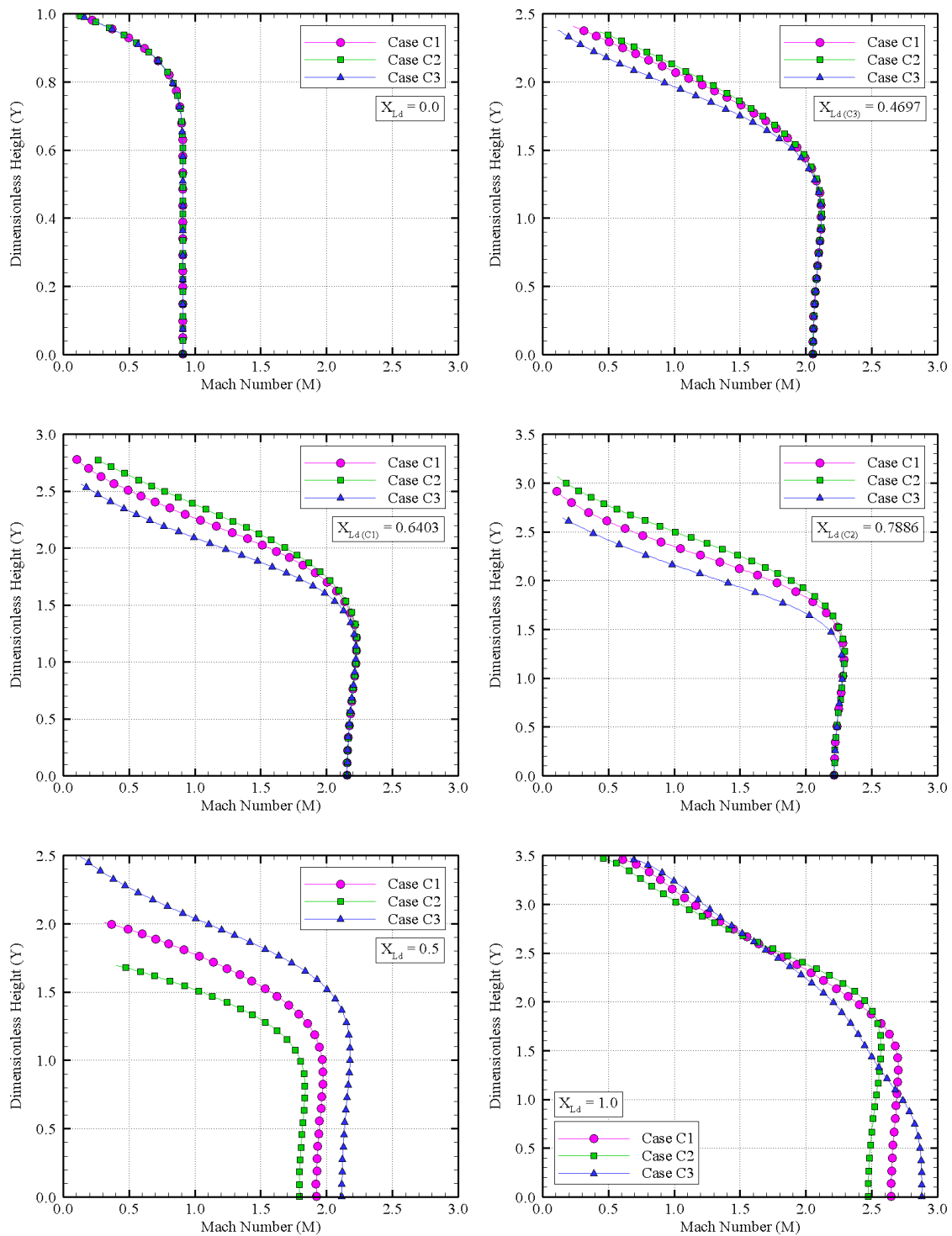


Figure 6.3 - Mach number (M) profiles along the micronozzle for group C cases.

According to Table 4.1, the surface slope is continuous along the inflection point ($\alpha_g = 1.0$) for group A cases, while such a slope is discontinuous in the other groups. As mentioned in Section 4.1, in groups B and C, the concave surface is abruptly turned away ($\alpha_g = 2.0$) and turned back ($\alpha_g = 0.5$) from the symmetry plane at the inflection point, respectively. In addition, based on cases A1, B1 and C1, the radius of curvature of the divergent surface is varied by changing the parameter β_g in each respective group.

Figure 6.1 implies that the Mach distribution is essentially uniform near the centerline for the six sections. Furthermore, due to viscous and rarefaction effects, these profiles demonstrate small, but nonzero, values of M near the surface. Since in its vicinity the stream velocity is parallel to the surface, it is reasonable to interpret these nonzero Mach numbers as an indication of velocity slip. Such a phenomenon is a classical feature in rarefied flows. By comparing the throat and exit sections, it is clear that the velocity slip increases along the downstream direction. Near the nozzle lip, the flow acceleration and the wall heat transfer reduce the local density. As a result, rarefaction and nonequilibrium become more significant, increasing the velocity slip.

As expected, the Mach number increases along the downstream direction as the cross-section area increases in the divergent section. For the present geometry, and based on the isentropic quasi-one-dimensional continuum approach (SHAPIRO, 1954), the centerline Mach number should be equal to 2.8 at the exit section. In contrast, the profiles show Mach values smaller than 2.8 at $X_{Ld} = 1.0$ and $Y = 0.0$. A possible reason for such results is the presence of irreversible processes – friction and heating – in the real flow. In the present profiles, the ratio between the Y range where the Mach distribution is nonuniform to the total Y range of a particular profile is an indication of the viscous layer influence. In general, the results show that such a ratio increases along the downstream direction. Therefore, based on this ratio, one can conclude that the thickness of the viscous layer increases along the divergent region.

Another important aspect noted is related to the Mach number distribution at the throat. According to the isentropic quasi-one-dimensional assumption, the flow properties are uniform along the entire cross-section and only vary in the flow direction. In this approach, the first sonic point is at the throat. In contrast, Figure 6.1 demonstrates a subsonic condition at $X_{Ld} = 0.0$. This different result is assigned to

the fact that microscale flows have high surface-to-volume (S/V) ratios. Hence, the viscous layer thickness is comparable to the cross-section height or depth. Basically, within such a layer, property distributions are nonuniform and irreversible processes, such as viscous dissipation, are intense. As a consequence, for the same boundary conditions, the quasi-one-dimensional and isentropic assumptions breakdown as the flow scale decreases.

Still referring to Figure 6.1, no qualitative influences are observed at the vicinity of the inflection point, i.e., for $0.1909 \leq X_{Ld} \leq 0.4012$. This is an indication that, at least for the investigated range of β_g , changes on the radius of curvature do not influence the local Mach profiles of the internal flow. The small quantitative differences in M observed between these cases are mainly caused by the fact that, for a same intermediate X_{Ld} station, each case provides a different cross-section area.

Turning to Figures 6.2 and 6.3, which display group B and C results, it is basically observed the same qualitative behaviors discussed for the group A. For the present conditions and ranges of α_g and β_g , these pictures indicate that even discontinuities on the divergent surface do not cause direct impact on the Mach distribution near the inflection point.

At this point, it is worthwhile to take an overview on the streamline traces in Figures 6.4, 6.5 and 6.6. A common and interesting characteristic on these plots is the recirculation region that is confined in the external surface. Similar behavior was founded by Wick (1953) for continuum sonic flows through abrupt changes on the cross-section area. It is important to remark that due to the constant boundary conditions employed in the present simulations this recirculation becomes a stable phenomenon after the flow reaches steady state. Careful analysis about the recirculation stability should be carried out by including periodic or nonperiodic disturbances on the boundary conditions. These disturbances may be related to pressure, temperature, velocity and so on. Meanwhile, such studies are beyond the present scope.

In general, the three geometric groups – A, B and C – have demonstrated the same streamline behavior. However, for case C2, it can be observed that the most streamlines are not deflected by the concave surface. Moreover, streamline traces show no flow separation due to the abrupt increasing of the surface slope as well as no shock waves due to the contraction of the supersonic flow at the inflection point. The high rarefaction degree and strong viscous effects near the inflection are

possible explanation for these counter-intuitive behaviors. The lack of intermolecular collisions leads to a degradation of strong gradient processes while the subsonic condition induced by friction attenuates the discontinuity impact on the flow near the inflection point.

In the initial design of nozzles operating in the continuum regime, the method of characteristics (SAAD, 1993; SHAPIRO, 1954) can be employed to describe unsteady or steady irrotational and isentropic multi-dimensional supersonic flows. In this method, the fluid is assumed as being a calorically perfect gas subject to continuous waves of small, but finite, amplitude. In order to respect these assumptions and to avoid flow separation or boundary layer effects, the turning angles θ_{d_1} and θ_{d_2} depicted in Figure 4.3 must be smaller than $\nu_e/2$, where ν_e is the Prandtl-Meyer angle of the exit flow. Assuming a continuum and isentropic flow for the present geometry and inlet-outlet conditions, the maximum value for the turning angle should be 22.87 degrees. Thus, according to Table 4.3 and the method of characteristics only case B3, whose maximum angle for the divergent surface is 21.92 degrees, should not present flow separation. In other words, for the present rarefied flows, the violation of the maximum divergent angle predicted by the method of characteristic does not result in flow separation.

Finally, in an effort to emphasize the main points of interest mentioned so far, Figures 6.7, 6.8 and 6.9 depict contour maps for the Mach number distribution in the entire simulated domain. In this family of plots, dimensionless X - and Y -coordinates refers to the length x and height y normalized by the half throat size h_t . Furthermore, the hollowed circle positioned on the divergent surface represents the inflection point. According to these plots, it is clear that the flow is essentially subsonic in the recirculation zone and along the entire internal surface. It is also interesting to note that the subsonic layer is generally thinner between the throat and the inflection point, but it becomes thicker from this point up to the nozzle lip vicinity. The sonic region starts near the throat, covers the internal surface and passes very near the nozzle lip. Focusing on the supersonic regions, some relation between the length of the divergent surface and the maximum Mach values of the external flow can also be noted. As the divergent length L_d is decreased, by changing the geometric parameters α_g and β_g , the external Mach number becomes slightly higher in comparison to the larger divergent lengths.

In the divergent and external regions, the pattern of the Mach isolines is highly

dependent on the viscous layer growth and on the heat transfer from the concave surface to the gas. As long as the slope of the convex surface at the inflection point θ_{d_1} increases, there is a tendency of the viscous layer growth does not occupy the centerline vicinity. As a result, within the quasi-inviscid core, the Mach number gradient is essentially parallel to the centerline, similar to the quasi-one-dimensional approach. Conversely, as θ_{d_1} decreases the viscous layer occupies most of the divergent part and hence the flow tends to be fully viscous. Despite the friction effects near the concave surface, Mach number isolines are parallel to the surface because in this region the temperature gradients are basically in the surface direction. The dashed lines in Figure 6.10 depict the normal surface direction for cases A1, B1 and C1. Based on these figures, the influence of the viscous effects and surface temperature on M can be estimated by recognizing regions where the Mach isolines are nearly perpendicular to the dashed lines. Thus, since $M \propto V/\sqrt{T}$, the Mach value decreases in the surface direction due to friction and heating effects that decreases V and increases T , respectively. Depending on the geometric and boundary conditions, different interactions between these effects can occur along the micronozzle. For this reason, different patterns of the Mach number distribution are observed in the present results.

Another possible explanation for the aforementioned relation between M and L_d may be the variation in the internal surface area. Roughly speaking, irreversible processes, e.g., friction and heating, are strongly dependent on the surface area. As L_d is increased, the internal surface area is also increased and the viscous and heating effects become more intense. Equations 6.4 and 6.5 are based on the continuum approach for generalized one-dimensional compressible flows (SHAPIRO, 1954). Assuming constant specific heat ratio, these equations describe the relative change on M^2 as a function of the relative changes in the cross-section area A , stagnation temperature T_0 and friction coefficient f along the micronozzle:

$$\frac{dM^2}{M^2} = -2\Psi \frac{dA}{A} + (1 + \gamma M^2) \Psi \frac{dT_0}{T_0} + \gamma M^2 \Psi \frac{4f dx}{D_H} \quad (6.4)$$

$$\Psi = \frac{1 + \frac{\gamma-1}{2} M^2}{1 - M^2} \quad (6.5)$$

where D_H is the local hydraulic diameter.

Since the present divergent flow is supersonic, $dA/A > 0$ and $M > 1$, it is clear that $\Psi < 0$. Therefore, according to Equation 6.4, the first term in the right hand

side contributes to a relative increase in M while the third term – friction influence – causes a decrease in the Mach value. The second term models the heat transfer between gas and solid surface. For the present account, the surface temperature T_w is generally greater than the gas temperature near the wall in the divergent section. As a result, the heat flux from this isothermal wall to the gas causes a positive change in the stagnation temperature T_0 . Consequently, based on Equation 6.4, such a heating produces a reduction in the Mach number.

In short, as L_d decreases, the reduction in surface internal area causes less intense friction and heating to the gas flow. For this reason, under the present conditions, the Mach number reduction should also be less significant. Hence, at least for the investigated micronozzles, the qualitative aspect of the Mach number matches quite well with the continuum theory. Finally, according to these results, it seems that the slope and radius of curvature of the divergent surface impacts on the overall Mach distribution. The reason for that is because both geometric parameters affect significantly the viscous layer growth as well as the internal surface area, which is related to friction and heating processes.

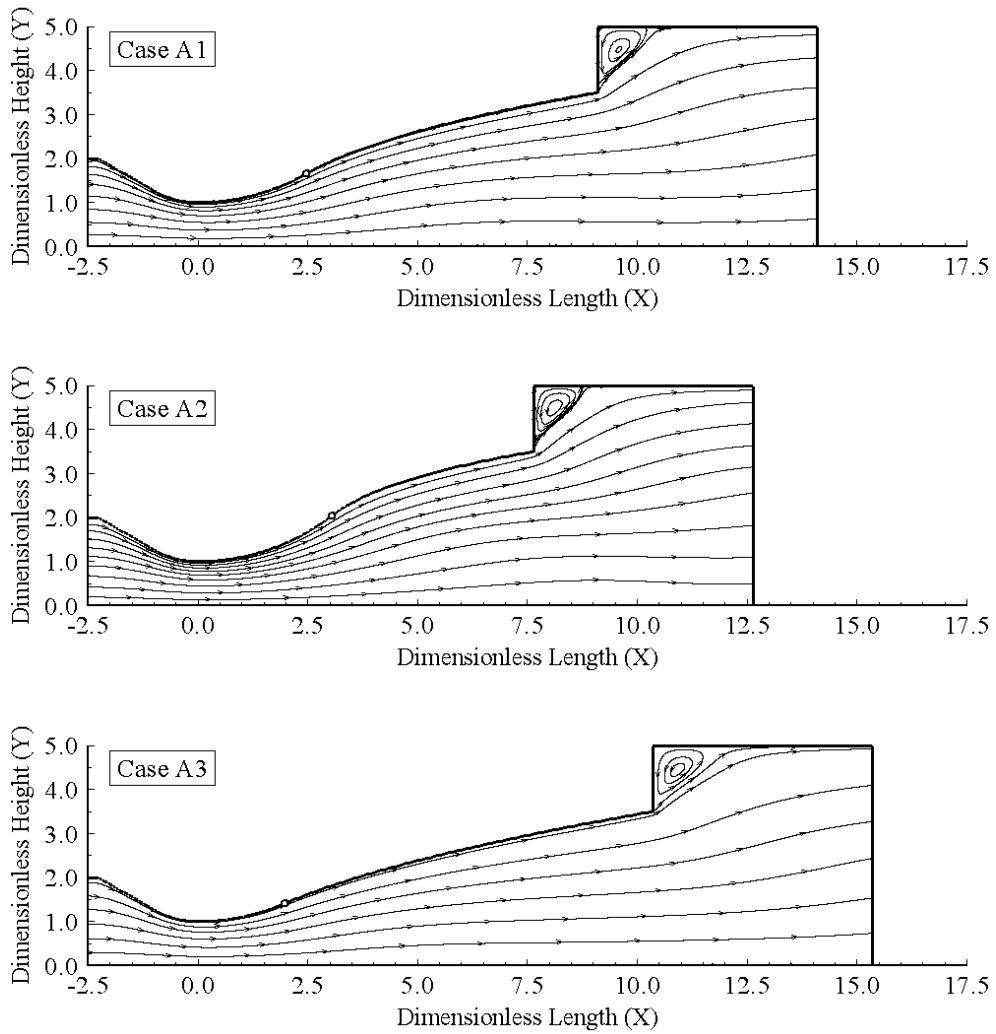


Figure 6.4 - Streamline distribution for group A cases.

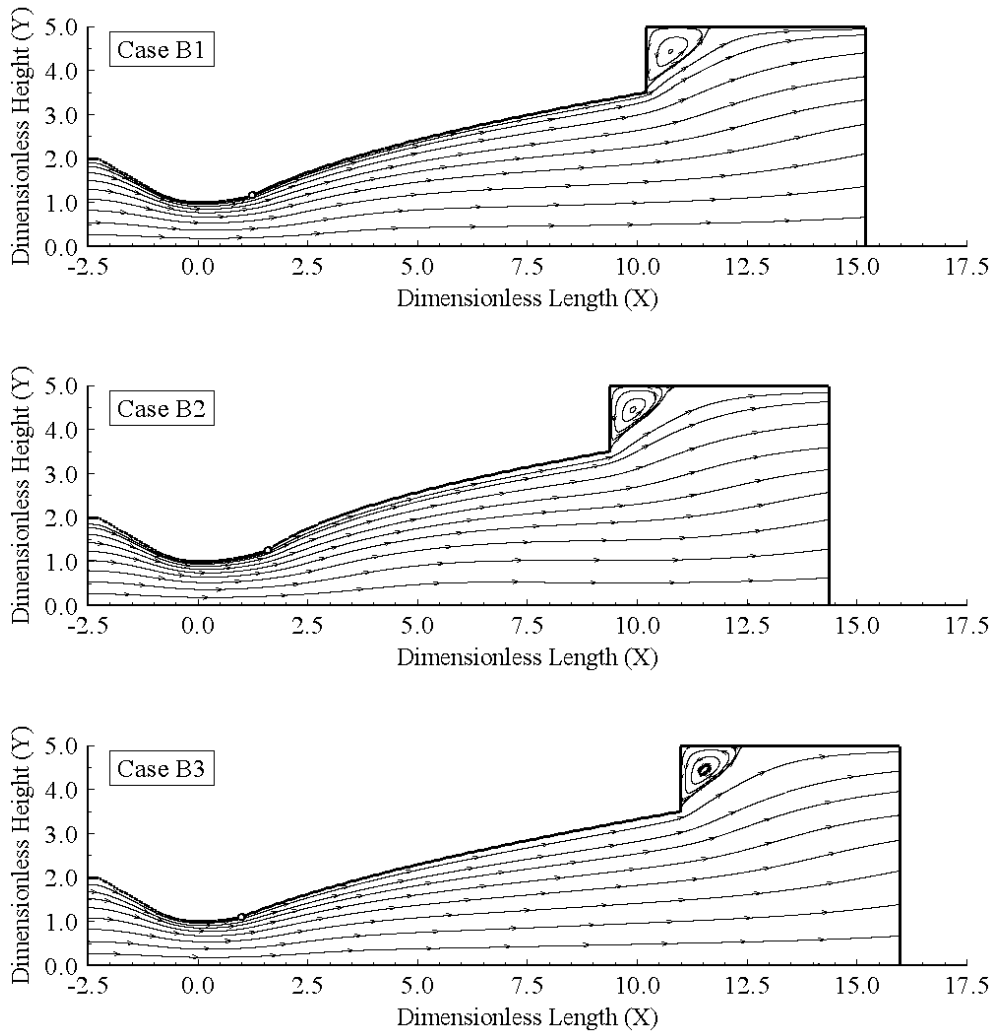


Figure 6.5 - Streamline distribution for group B cases.

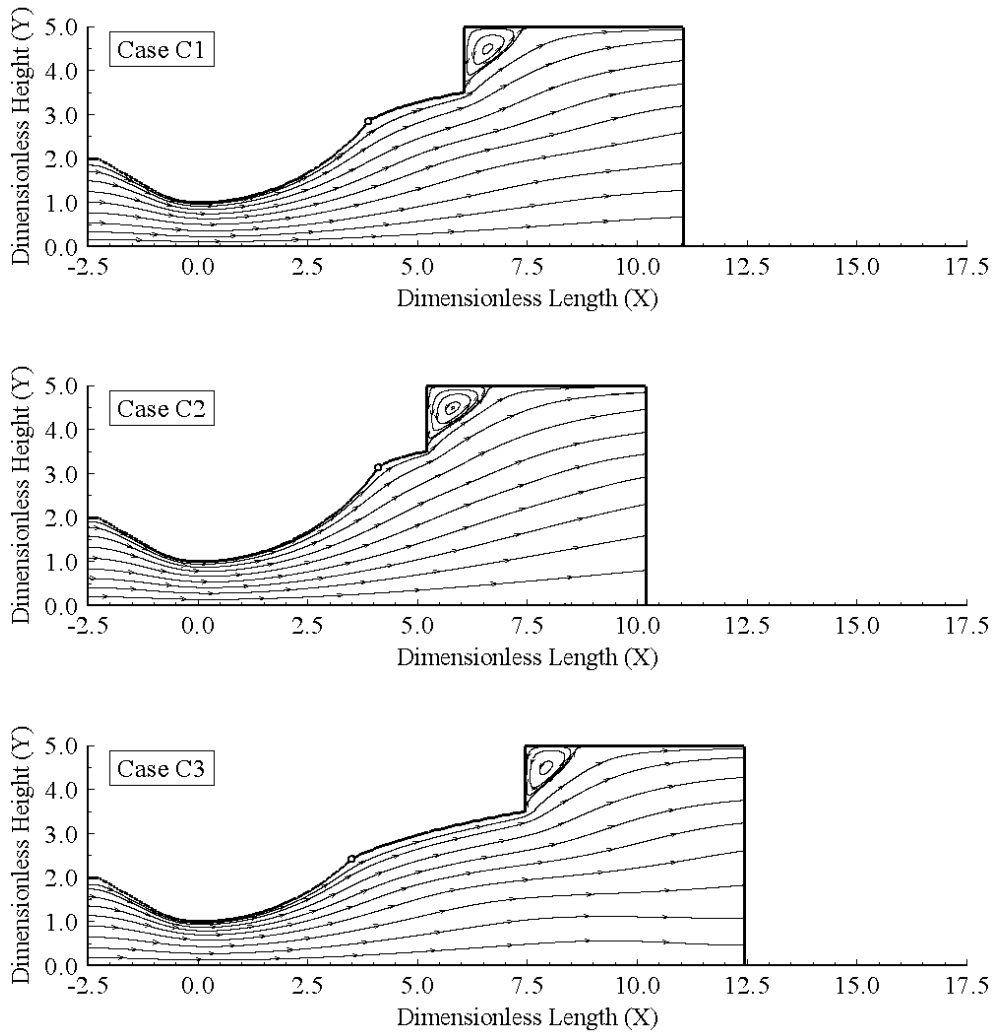


Figure 6.6 - Streamline distribution for group C cases.

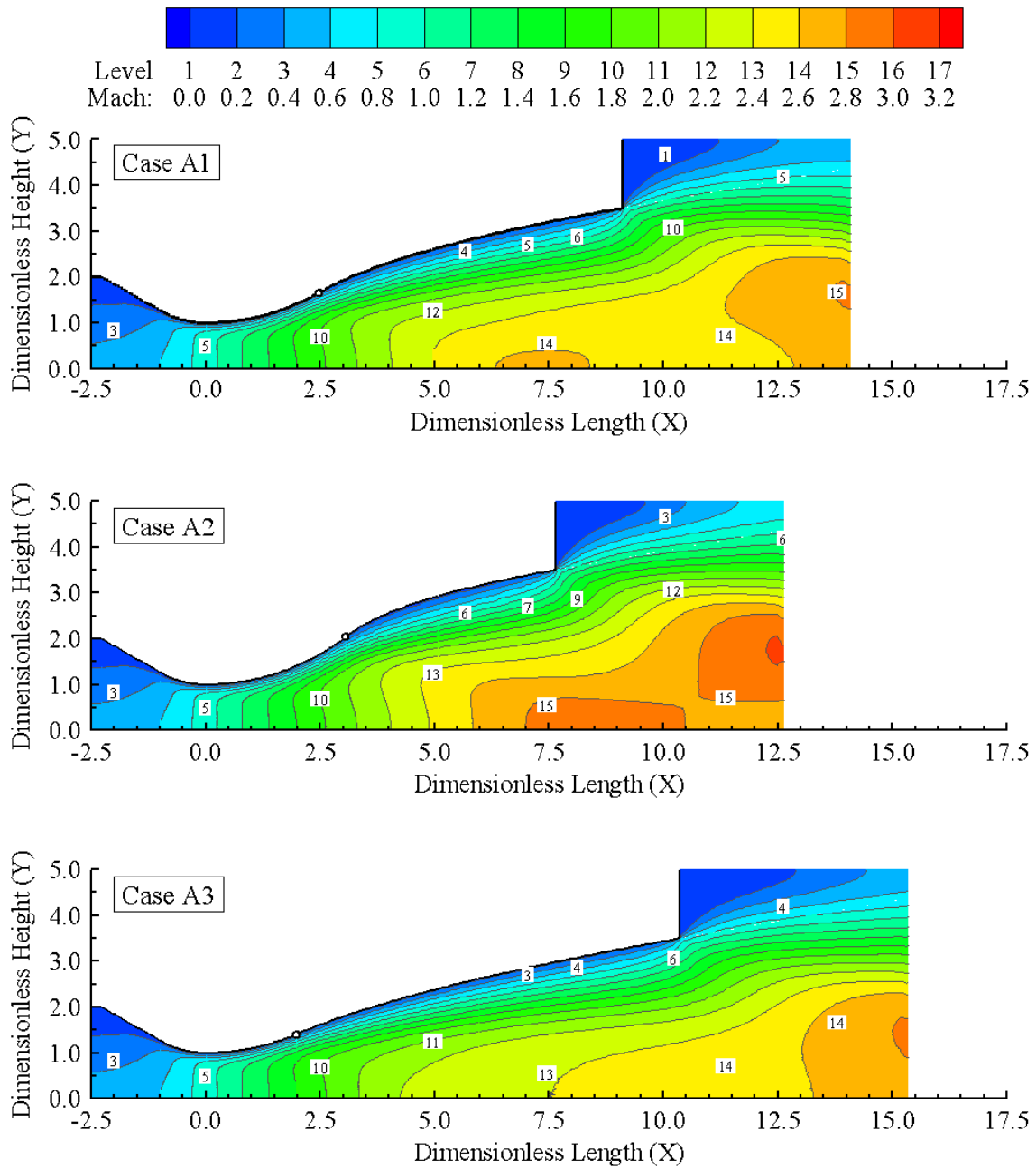


Figure 6.7 - Mach number (M) distribution along the micronozzle for group A cases.

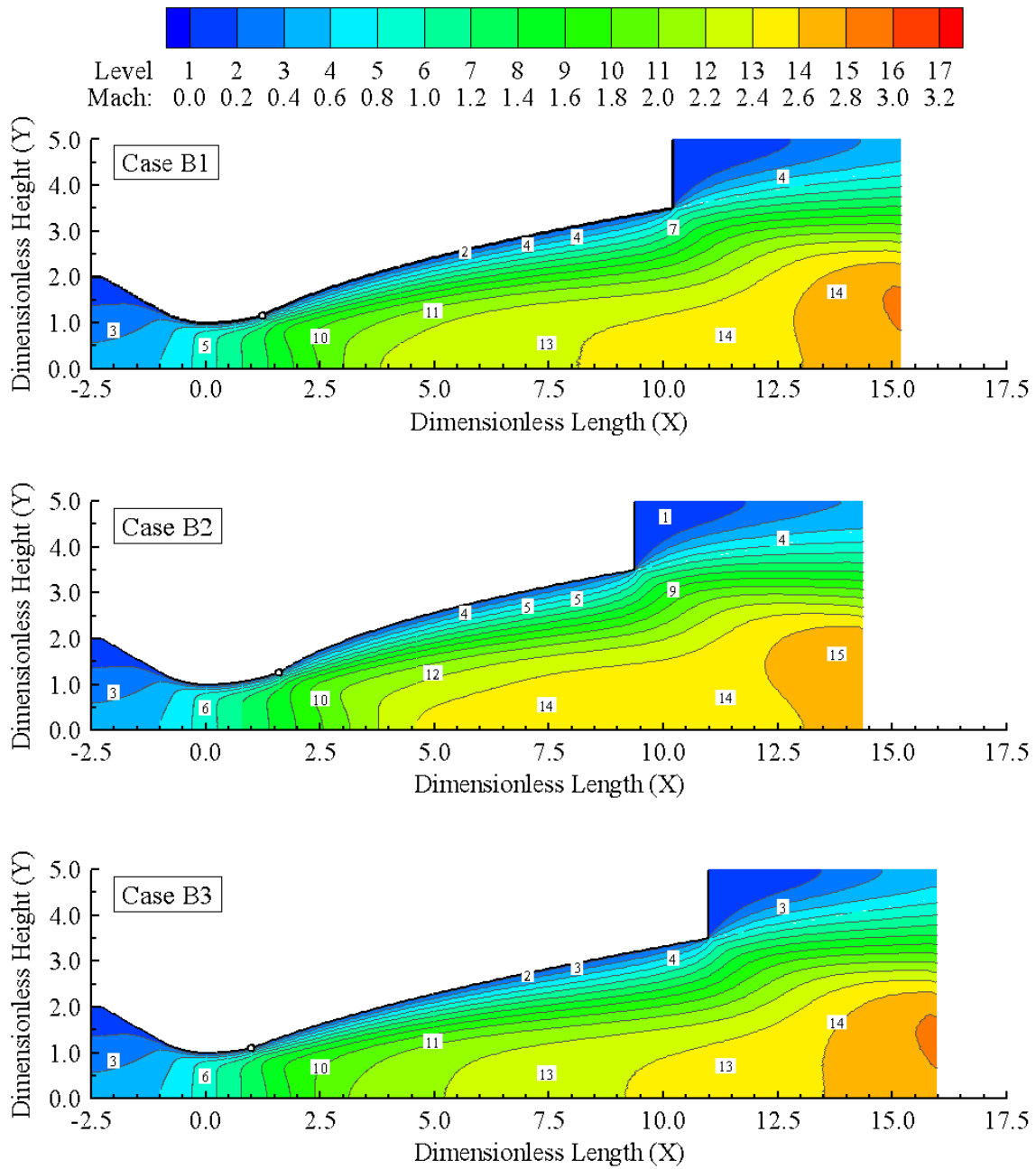


Figure 6.8 - Mach number (M) distribution along the micronozzle for group B cases.

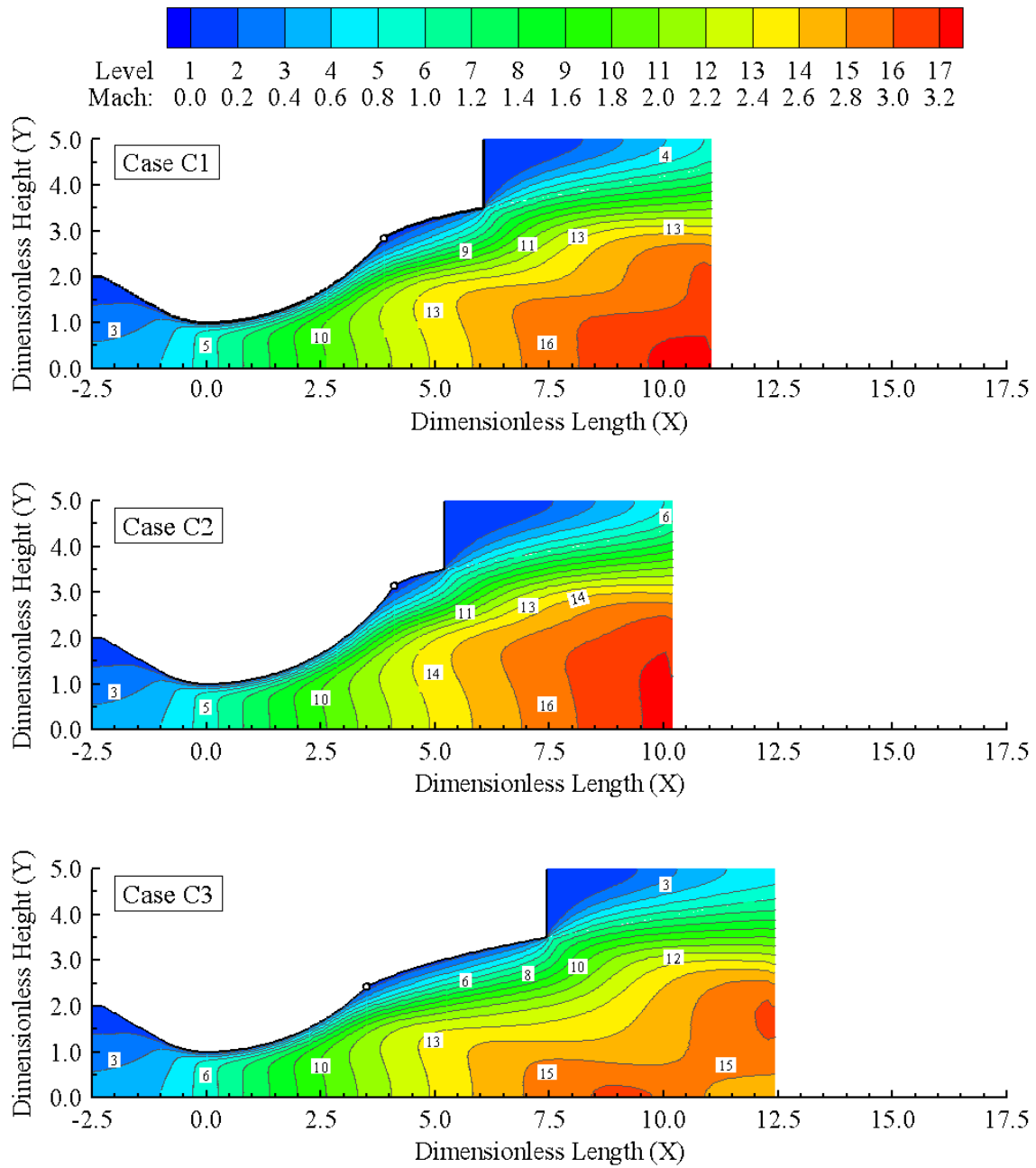


Figure 6.9 - Mach number (M) distribution along the micronozzle for group C cases.

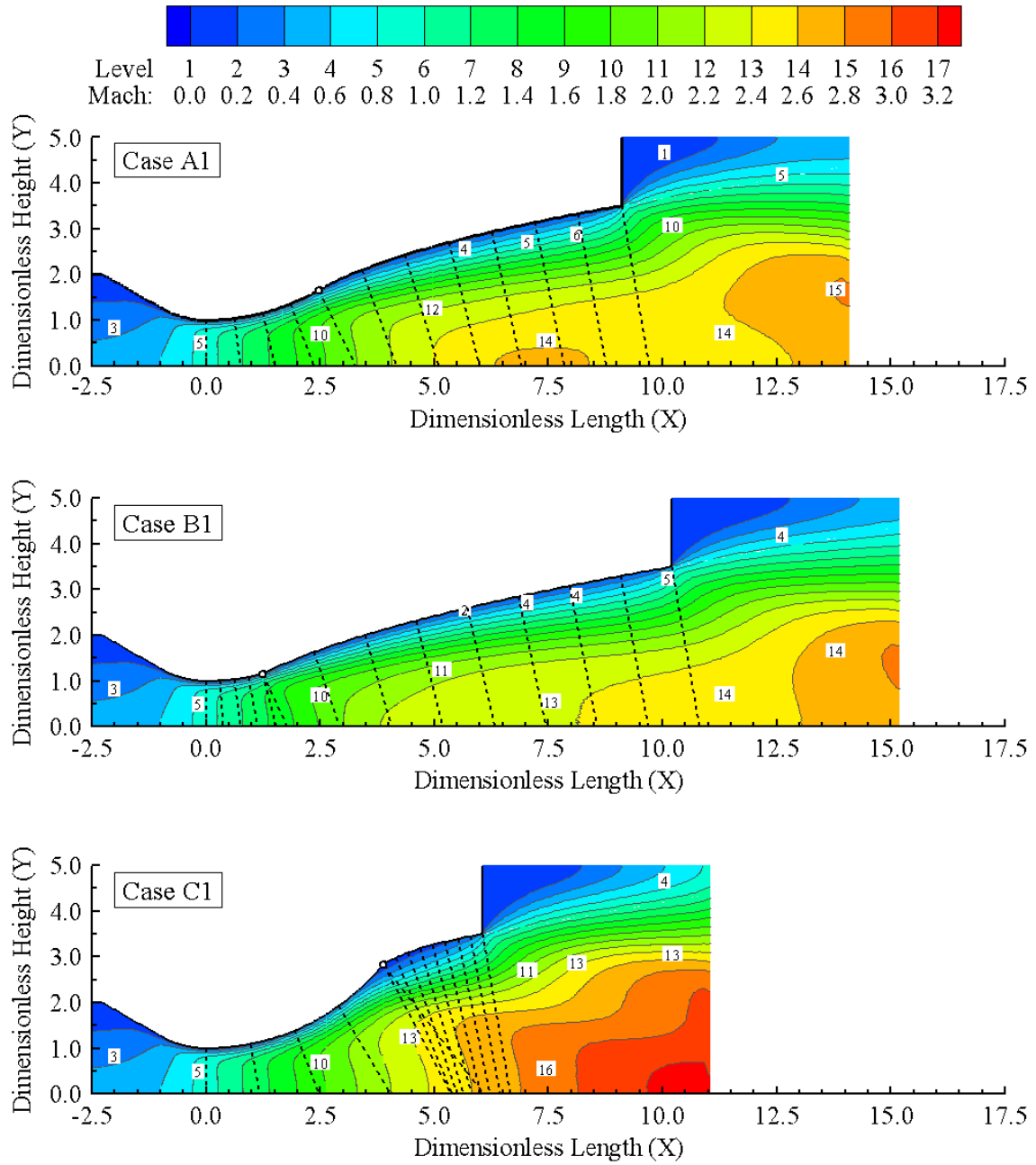


Figure 6.10 - Mach number (M) distribution along the micronozzle for cases A1 (top), B1 (middle) and C1 (bottom), where dashed lines are normal to the divergent surface.

6.1.2 Density Field

The density definition and the numerical expression employed in the DSMC method are given by:

$$\rho = n\bar{m} = \frac{\bar{N}F_N}{V_c} \frac{\sum_{j=1}^N m_j}{N} \quad (6.6)$$

where n is the local number density, m is the molecular mass, and \bar{N} and N are, respectively, the average and total number of simulated molecules computed within a given cell during the simulation. In addition, F_N is the local scaling factor and V_c is the computational cell volume.

The impact of nozzle geometric changes on the density profiles for the same cross-sections investigated in the previous subsection are displayed in Figures 6.11, 6.12 and 6.13 for group A, B and C cases, respectively. In this set of plots, density ρ is normalized by the inlet density ρ_{in} , X and X_{Ld} are the dimensionless lengths and Y is the dimensionless height, as previously defined in Subsection 6.1.1.

According to Figures 6.11, 6.12 and 6.13, the density ratio ρ/ρ_{in} decreases along the downstream direction due to the flow expansion. In general, in the vicinity of the centerline, density gradients in the y -direction are smaller than those ones near the solid surface. Moreover, it is seen that the density ratio ρ/ρ_{in} decreases in the surface direction. Basically, it occurs because the surface temperature T_w is greater than the gas temperature T . Consequently, the temperature increasing promotes a reduction in the density near the wall. In addition, as discussed in Subsection 6.1.3, due to the convex-concave geometry, the centripetal forces produce pressure gradients normal to the surface. Therefore, such gradients may also be related to density changes in the y -direction.

By comparing group A, B and C profiles, a similar qualitative behavior is noted. Due to the geometric complexity and the two-dimensionality of the present flows, only density profiles for some cross-sections may not provide a complete picture of the density pattern. In order to obtain a better insight on such a distribution, it is necessary to examine density contour maps. These results are displayed in Figures 6.14, 6.15 and 6.16 for group A, B and C cases, respectively.

Figure 6.14 indicates that the gas flow experiences a reduction of about two orders of magnitude in the density ratio along the micronozzle. The minimum ρ/ρ_{in}

value occurs near the nozzle lip, where the gas flow expands rapidly because of the abrupt increase in cross-section area. Nevertheless, the present contour maps show small density values in the recirculation region that was previously showed in the streamline traces.

This figure also shows a complex density distribution in the internal microflows, mainly in the divergent regions. It is difficult to relate such patterns to an unique physical mechanism since this simulation takes into account different real processes, such as friction, heating and nonequilibrium effects. It is conjectured here that the present density distributions are due to three main different effects: (i) the surface temperature effect that decreases ρ in the surface direction, since $T_w > T$; (ii) the viscous effects that, due to the diffuse reflection model employed, contributes to an build up of molecules near the wall, i.e., an increasing ρ ; and (iii) the convective effect, caused by the stream gas flow, that results in a number density n reduction in the downstream direction. Evidently, along the micronozzle, the magnitude and preferential direction of each mentioned effect may vary substantially.

Between the inlet and the throat cross-sections, the convective effect overcomes the temperature and viscous effects because $T_w \cong T$ and velocity gradients are small. As a result, density changes are predominant in the flow direction, similar to the quasi-one-dimensional approach. On the other hand, density ratio isolines emanating from the wall near the inflection point are distorted. This is an indication that surface temperature and two-dimensional effects play an important role in this region. Furthermore, between the inflection point and the exit section, the density pattern changes considerably. As mentioned in the Mach number distribution, the subsonic region becomes thicker near the concave surface. Consequently, convective effects should have a minor impact on the density ratio near the concave surface. Therefore, temperature surface effects should be most significant near this surface. This seems a reasonable explanation, since density isolines tend to become parallel to the concave surface. Convective effects become predominant far away from the surface. Essentially, such an effect produces density changes in the streamline direction.

Comparing micronozzle geometric groups in Figures 6.14, 6.15 and 6.16, it is observed that the density patterns of group C cases are somewhat different from the other cases. These differences are probably due to the drastic variation in the divergent shape of group C cases. This indicates that geometric changes may result in different combinations of physical processes – heating, friction, convection, etc – that

cause variations in flow properties. For this reason, the density distribution varies according to the divergent shape.

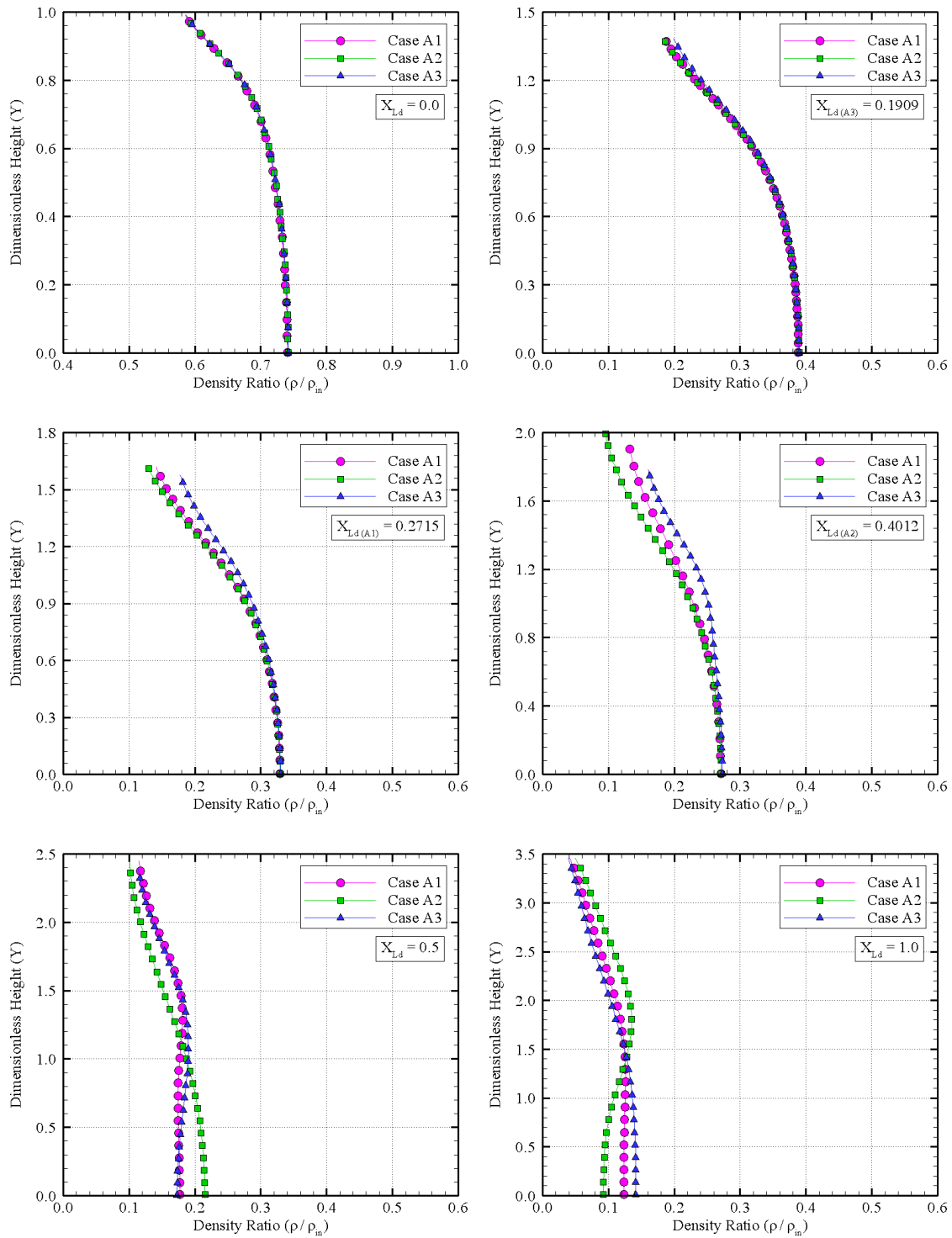


Figure 6.11 - Density ratio (ρ/ρ_{in}) profiles along the micronozzle for group A cases.

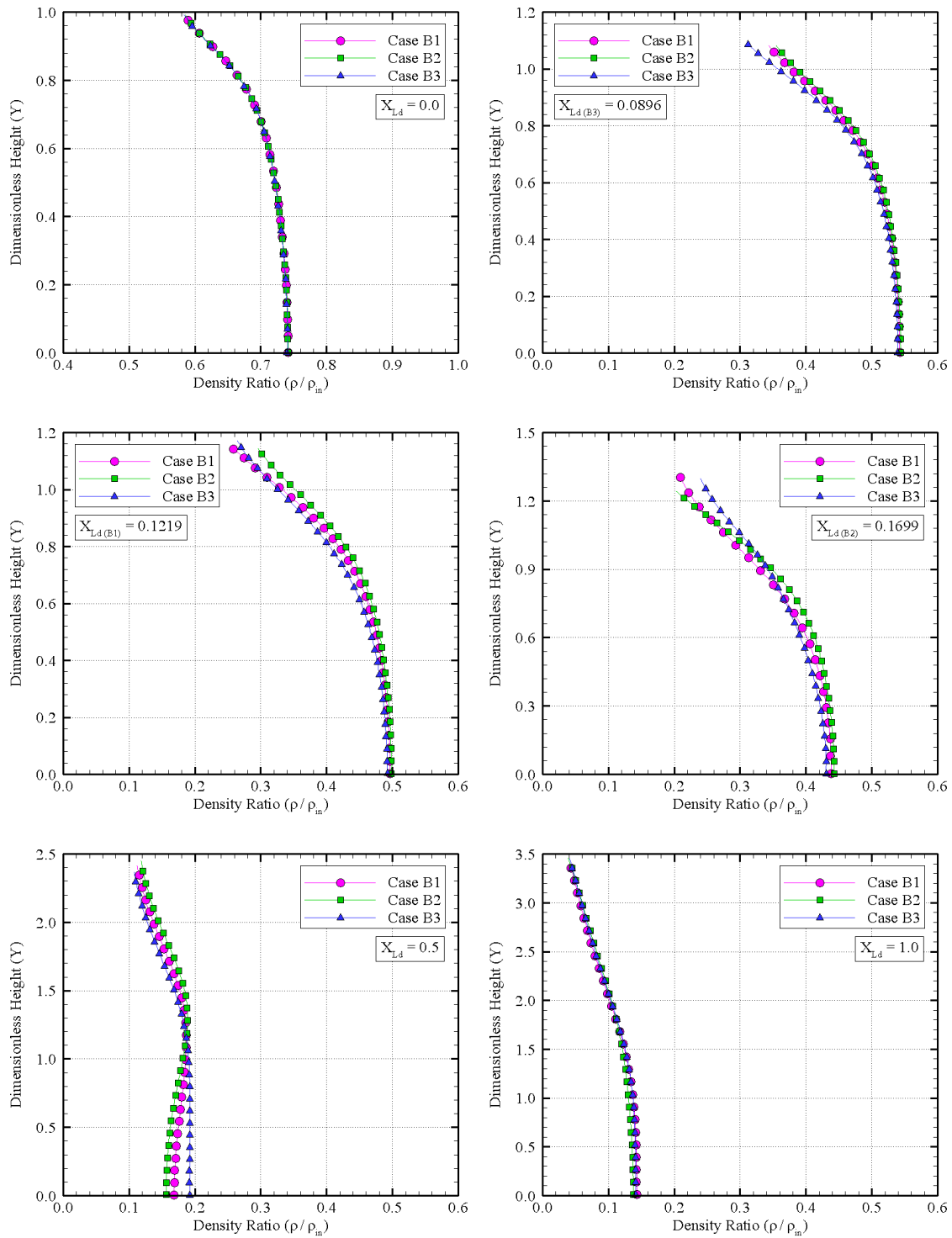


Figure 6.12 - Density ratio (ρ/ρ_{in}) profiles along the micronozzle for group B cases.

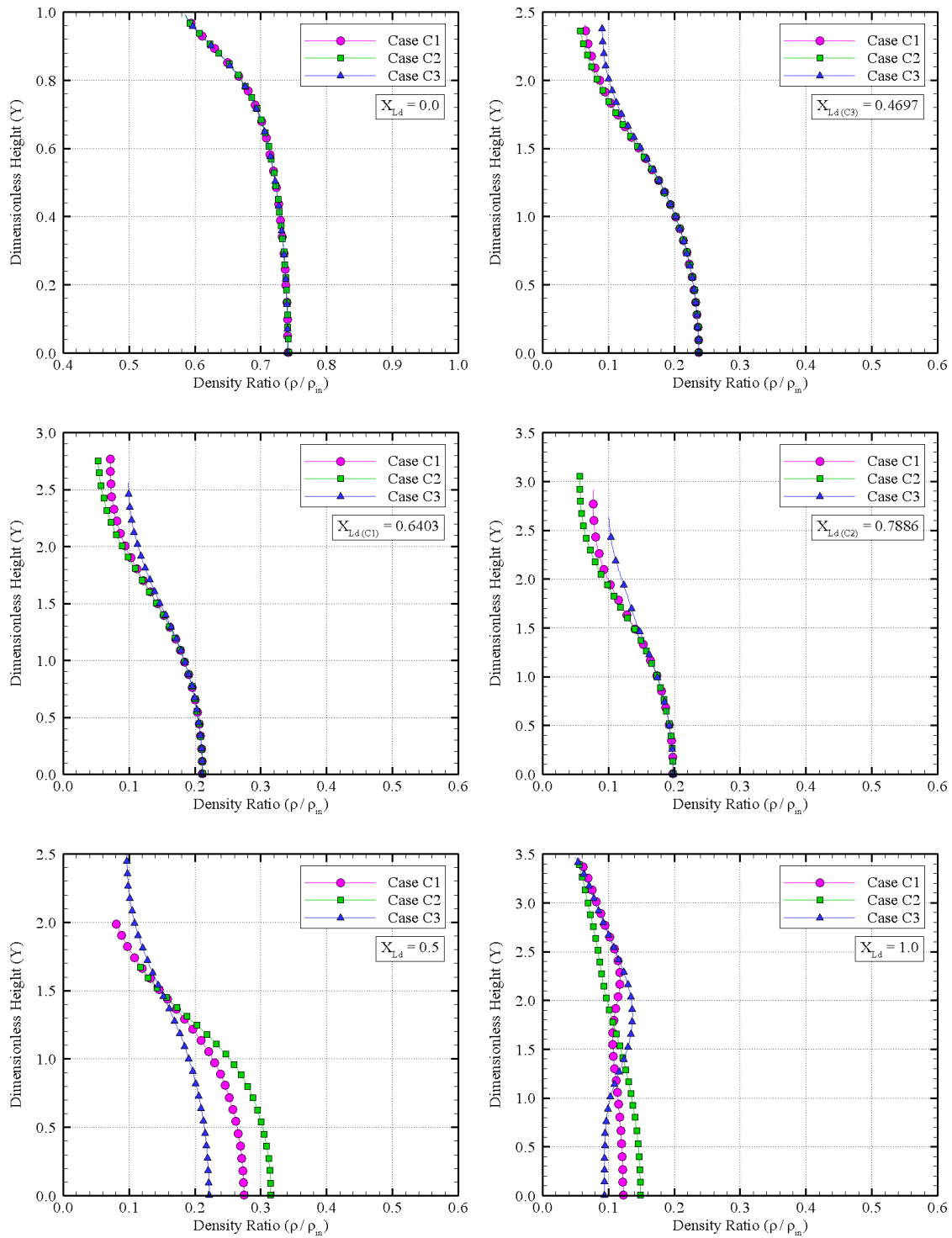


Figure 6.13 - Density ratio (ρ/ρ_{in}) profiles along the micronozzle for group C cases.

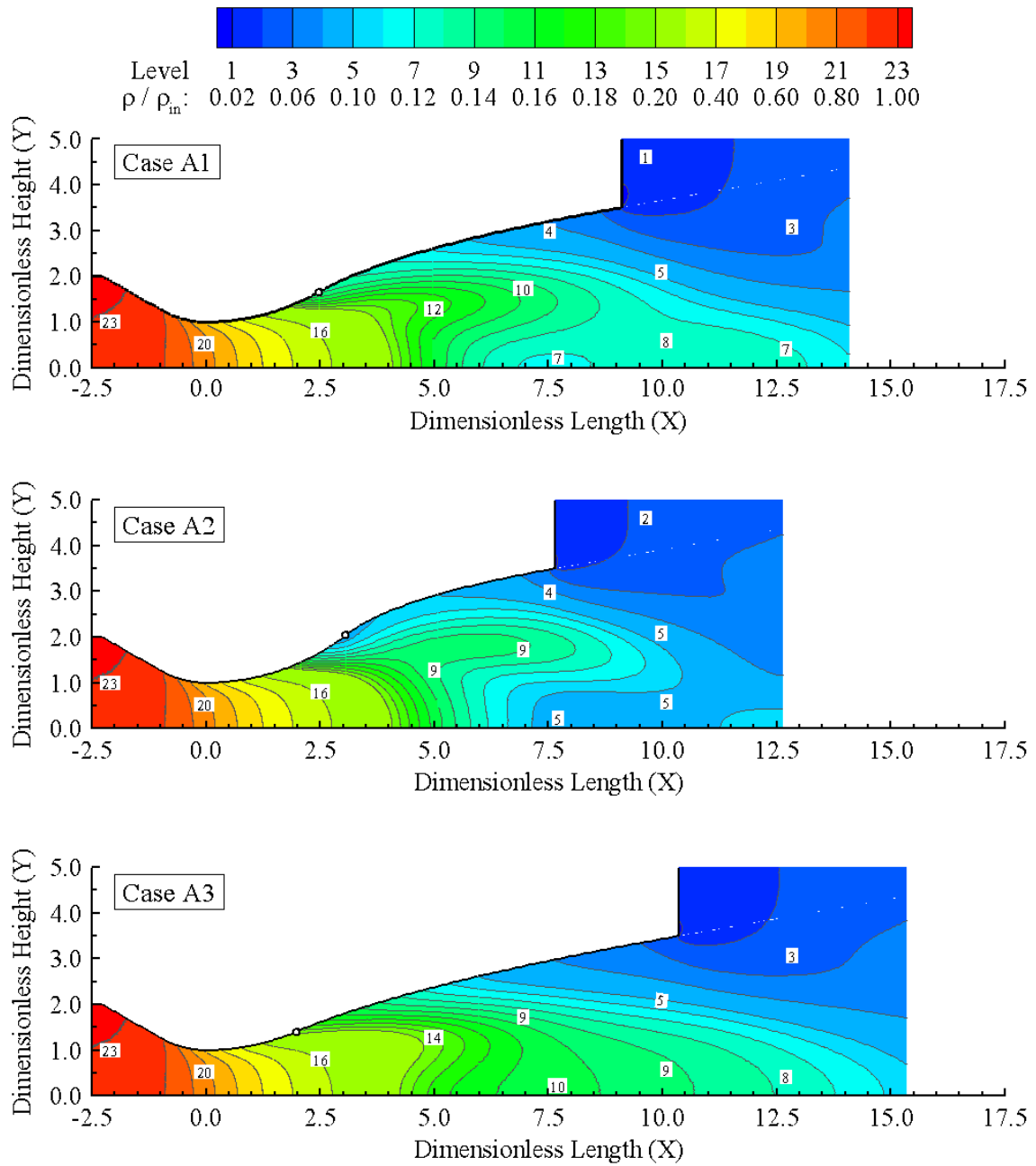


Figure 6.14 - Density ratio (ρ/ρ_{in}) distribution along the micronozzle for group A cases.

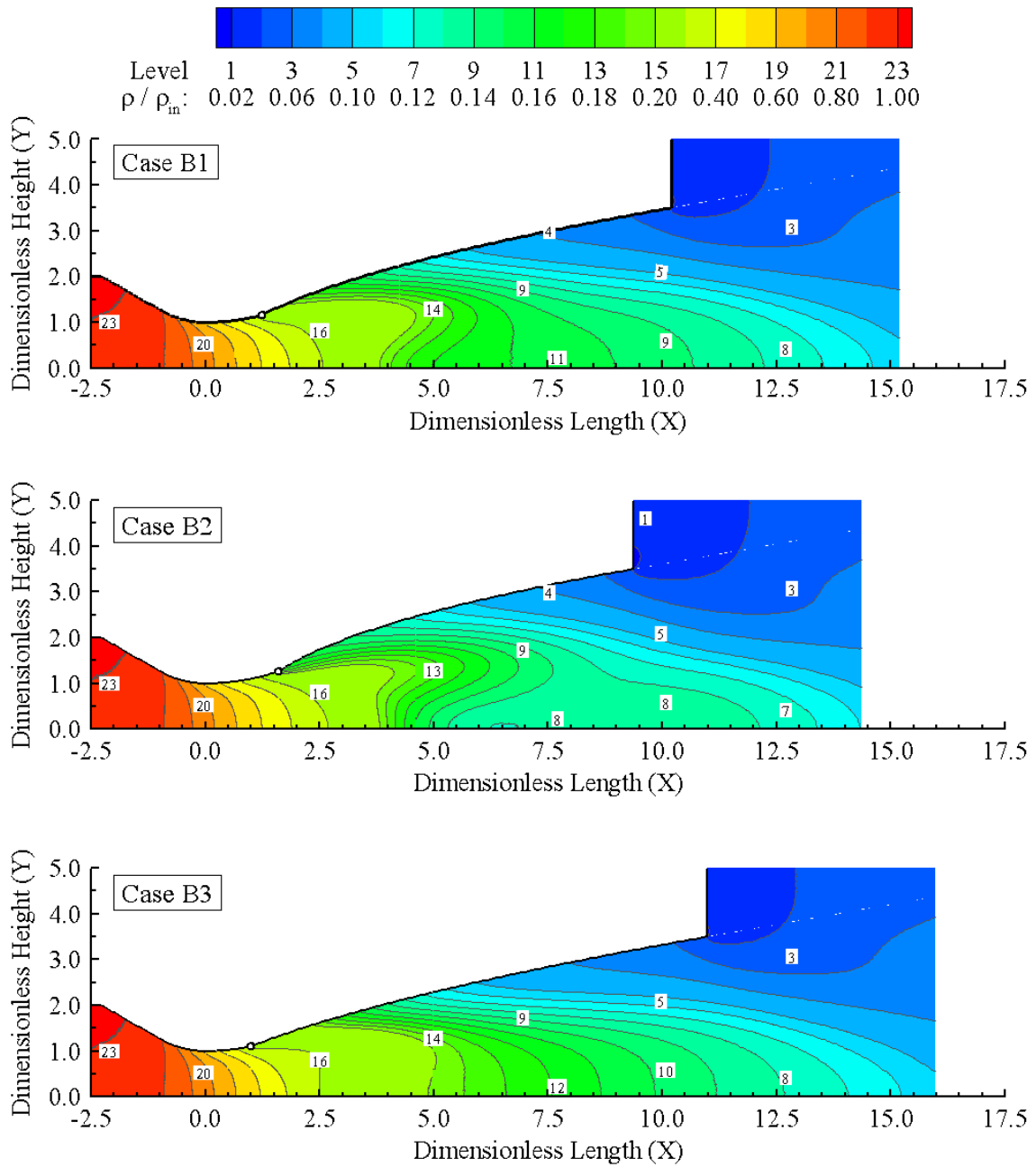


Figure 6.15 - Density ratio (ρ/ρ_{in}) distribution along the micronozzle for group B cases.

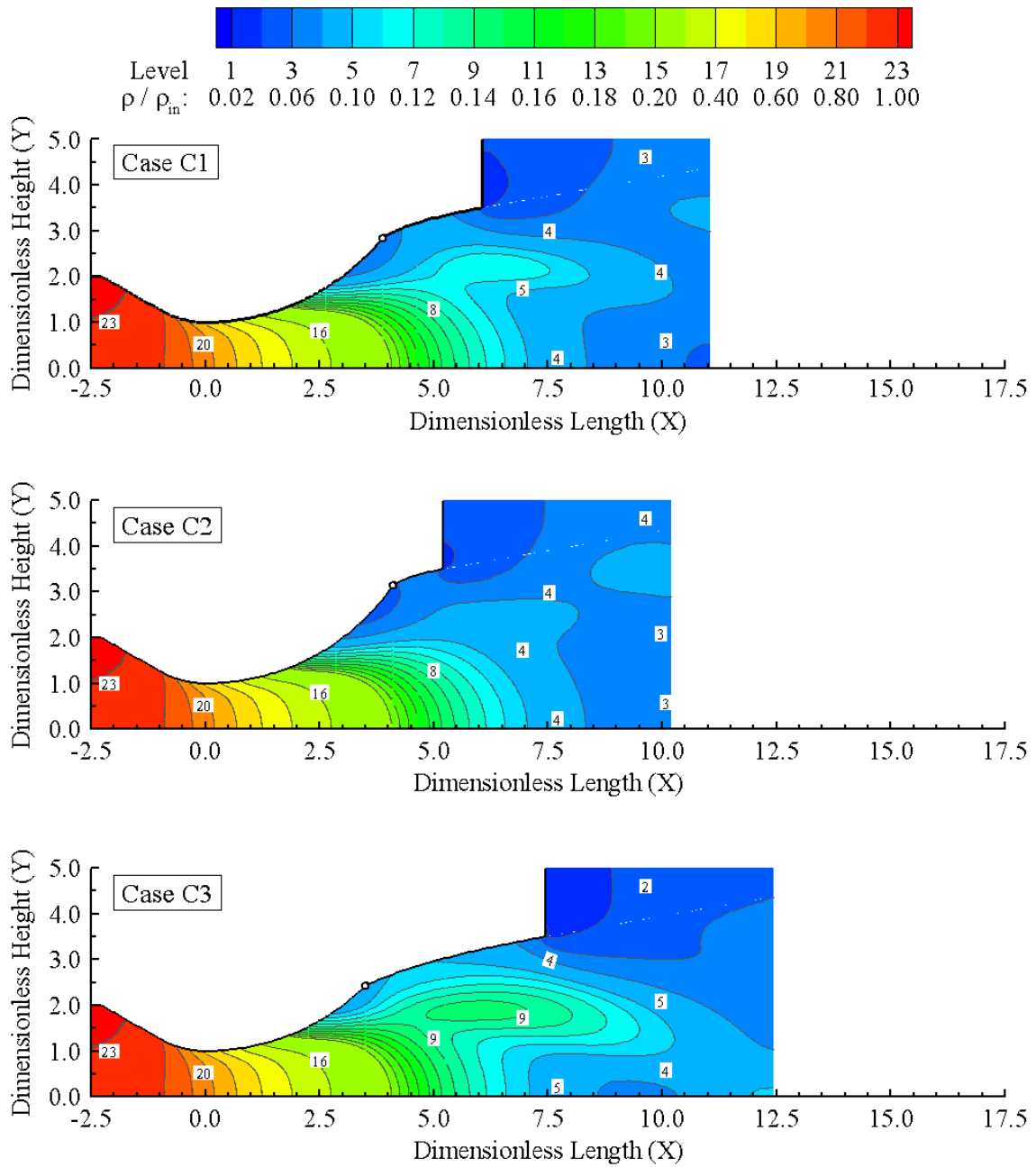


Figure 6.16 - Density ratio (ρ/ρ_{in}) distribution along the micronozzle for group C cases.

6.1.3 Pressure Field

The scalar pressure within each cell of the computational domain is obtained by the following expression:

$$p = \frac{1}{3} n m c'^2 = \frac{1}{3} \frac{\bar{N} F_N}{V_c} \frac{\sum_{j=1}^N m_j c_j'^2}{N} \quad (6.7)$$

where n is the local number density, m is the molecular mass, c' is the thermal velocity speed as well as \bar{N} and N are, respectively, the average and total number of simulated molecules computed within a given cell during the simulation. In addition, F_N is the local scaling factor and V_c is the computational cell volume.

The influence of changing the geometric parameters α_g and β_g on the pressure profiles is exhibited in Figures 6.19, 6.20 and 6.21 for group A, B and C cases, respectively. In these plots, pressure p is normalized by the inlet static pressure p_{in} , X and X_{Ld} are the dimensionless lengths and Y is the dimensionless height, as defined in Subsection 6.1.1.

In flow problems whose the solid surfaces have finite radius of curvature r_c , as in the present case, it proves useful to estimate the influence of centripetal forces. An oversimplified but valuable analysis of such effects can be made by employing Newton's second law along the η -direction normal to the streamlines. Therefore, assuming a steady, two-dimensional, inviscid and continuum flow, without external forces, Equation 6.8 indicates that pressure increases in the opposite direction to the curvature center (MUNSON et al., 2002). An analogous examination can also be carried out by employing Newton's second law along the ξ -direction tangent to the streamlines, as follows in Equation 6.9.

$$\frac{\partial p}{\partial \eta} = -\rho \frac{V^2}{r_c} \quad (6.8)$$

$$\frac{\partial p}{\partial \xi} = -\rho V \frac{\partial V}{\partial \xi} \quad (6.9)$$

Based on these equations and on the present surface temperature effect, the direction of the pressure and temperature gradients are depicted in Figure 6.17 in the vicinity of the convex and concave internal surfaces. This simplified scheme takes into account neither the combination between pressure and temperature effects nor viscous effects. The present idea is just to elucidate the influence of each physical

mechanism separately.

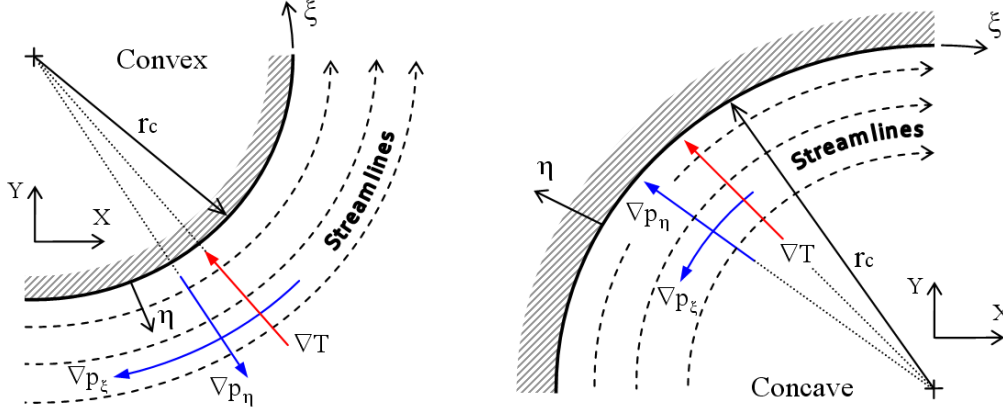


Figure 6.17 - Schematic view of the pressure and temperature gradients near the convex (left) and concave (right) divergent surfaces in present account.

As noted in Figure 6.17, the pressure gradient is composed of two components near the surfaces. The first component acts tangent to the streamline direction while the second component acts perpendicular to the streamline direction. In this context, a local estimative of the most significant component – tangential (∇p_ξ) or normal (∇p_η) – can be made by analyzing the ratio between Equations 6.8 and 6.9. The result is expressed as following:

$$\frac{\partial p / \partial \xi}{\partial p / \partial \eta} = \frac{r_c \partial V}{V \partial \xi} \quad (6.10)$$

For the investigated micronozzles, Equation 6.10 reveals that the tangential component of the pressure gradient essentially overcomes the perpendicular component in the most of the flow. It occurs because, towards the surface, even with a finite r_c value, $V \rightarrow 0$ due to the viscous effects present in the real flow. In the opposite direction, the flow speed increases to a finite value, but the streamlines become straight for the present geometry and hence $r_c \rightarrow \infty$. For both conditions, near to and far away from the surfaces, the term $\partial V / \partial \xi$ is finite, and does not have a significant influence on the previous discussion. It is important to keep in mind that the normal component of the pressure gradient is not zero, it is just smaller than the tangential one.

As noted in Figure 6.19 for group A pressure profiles, pressure decreases in the downstream direction along the micronozzle. This behavior is simply because of the expansion. For the divergent cross-sections located between the throat and inflection point, the pressure ratio p/p_{in} presents a slight decrease in the surface direction. Based on the scheme introduced in Figure 6.17, such a pressure drop is related to the fact that pressure gradients arise in the opposite direction to the curvature center due to the streamline curvature. This pressure difference is caused by the centripetal acceleration. As the flow reaches the concave surface vicinity, centripetal effects promote a pressure increase towards the surface direction, since the curvature direction changes. In this sense, between the inflection point and exit section the pressure ratio tends to increase near the surface. For this reason, profiles are basically uniform at the exit section. Similar behavior is observed in Figure 6.21 for group C cases. On the other hand, in Figure 6.20 for group B cases, it can be noted that the pressure ratio decreases monotonically towards the surface at the inflection point. The curves described by such profiles do not present an inflection point. This behavior occurs due to the abrupt expansion on cases B1, B2 and B3.

In an attempt to bring out the essential features of the pressure distribution in the present micronozzles, Figure 6.22, 6.23 and 6.24 show the pressure ratio contour maps. However, before discussing these maps in detail, it proves worthwhile to point out the main physical mechanisms and flow aspects present in these micronozzles. Ignoring the temperature field for the moment, which will be discussed in Subsection 6.1.4, Figure 6.18 summarizes qualitative flow structures in terms of sub- and supersonic regimes that can be further classified as quasi-inviscid or viscous regions.

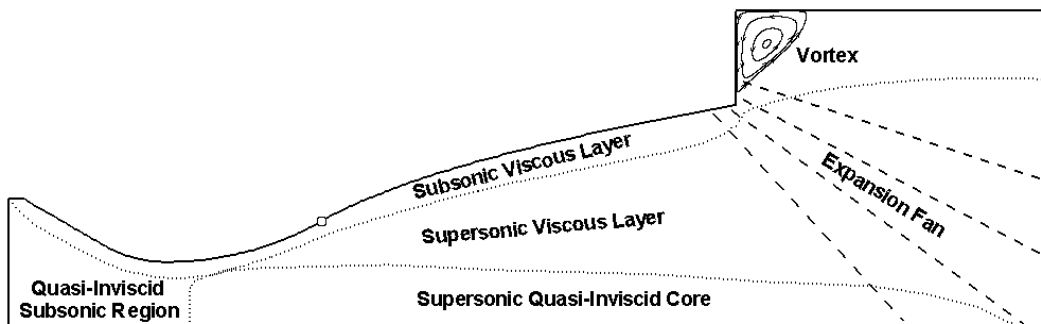


Figure 6.18 - Qualitative flow structure illustrating the main physical mechanisms observed in the present simulations.

As indicated for the convergent part, the flow is essentially inviscid far away from the surface because of the small velocity gradients. The subsonic viscous layer established at the internal leading edge covers the whole micronozzle surface and extends until the external region. Slightly downstream of the throat, the flow becomes supersonic in almost all the micronozzle divergent part. Depending on the viscous layer growth, the supersonic flow may describe a quasi-inviscid and quasi-one-dimensional behavior along the centerline vicinity. In addition, the expansion fan developed at the nozzle lip as well as the vortex confined within the external subsonic region are highlighted.

With an overall qualitative picture of the present micronozzle flow structure, attention is turned to Figures 6.22, 6.23 and 6.24. Classically, at solid surfaces, the fluid velocity must be zero in the normal surface direction. It ensures that no mass flux occurs through such a surface. Similarly, the net flux of any quantity across a symmetry plane must be zero. In this context, within the entire micronozzle, streamlines must deflect appropriately in order to become parallel to the internal surface and symmetry planes. In doing so, the macroscopic flow acquires velocity in the y -direction, i.e., $v_0 \neq 0$. As a consequence of the micronozzle geometries investigated, in general, the convergent and concave regions should present $\partial v_0 / \partial y \leq 0$ while the convex region should present $\partial v_0 / \partial y \geq 0$. Obviously, these velocity gradients are locally related to appropriate pressure gradients. As discussed earlier, near the internal surface and centerline, the tangential component of the pressure gradient overcomes its normal component, which is perpendicular to the streamlines. As a result, the streamlines and pressure isolines tend to be perpendicular to each other in the vicinity of such boundaries. This behavior is clearly recognized in the pressure ratio contour maps. However, somewhere between the concave surface and the centerline, as long as surface temperature effects are significant, pressure isolines tend to align parallel to the surface. Similar effects were previously found in Mach and density patterns. It should also be remarked that the major pressure changes occur between the inlet and the inflection point.

Still referring to the internal micronozzle flow, it is interesting to note that near the wall and centerline, pressure patterns are consistent with the dynamic principle imposed by Newton's second law, i.e., the present pressure patterns satisfy Equations 6.8 and 6.9. Then, between the concave surface and centerline, thermal effect plays the main role on the pressure distribution. Therefore, in order to respect pres-

sure and temperature fields, density patterns must naturally satisfy an adequate thermal equation of state everywhere. Because of the combination of different physical effects, density fields presented in Subsection 6.1.2 demonstrate a complex and less intelligible patterns.

At this point, it is worthwhile to pay attention to the vicinity of the nozzle lip where the supersonic flow develops an expansion fan due to the abrupt increase in cross-section area. For the isentropic case, the two-dimensional continuum approach describes similar expansion waves in terms of the Prandtl-Meyer fan (SHAPIRO, 1954). However, because of the high rarefied nature of the present flow, the fan structure differs substantially from the ideal case one, e.g., the expansion waves are not attached to the sharp corner and they perform a diffuse fashion as long as the distance from the lip increases. The former consequence is also the mechanism that promotes merging between the recirculation region and expansion waves. Such a mixing between these pressure zones is clearly observed in some cases, e.g., in case A1. Finally, beyond the last expansion wave, the pressure level tends to match the pre-defined back pressure p_b value. Hence, for the present account, the pressure ratio p/p_{in} may increase again downstream the expansion fan. Depending on the p_b value, a significant back flow can occur.

A comparison between different geometric groups – A, B and C – shows that case C2 presents a pressure field somewhat different from the other cases in the external region. Based on the streamline traces introduced in Subsection 6.1.1, it seems that even the streamlines nearest to the concave surface are not deflected at the nozzle lip. Consequently, the expansion fan developed along the deflected streamlines is less intense. This effect occurs because the length of the concave surface is substantially shorter in case C2. In this sense, the ability of streamlines far away from the concave surface to fit to such a shape should be reduced. In short, for the present simulations, changes in the length of the concave surface may affect the intensity of the expansion fan and consequently the structure of the external flow.

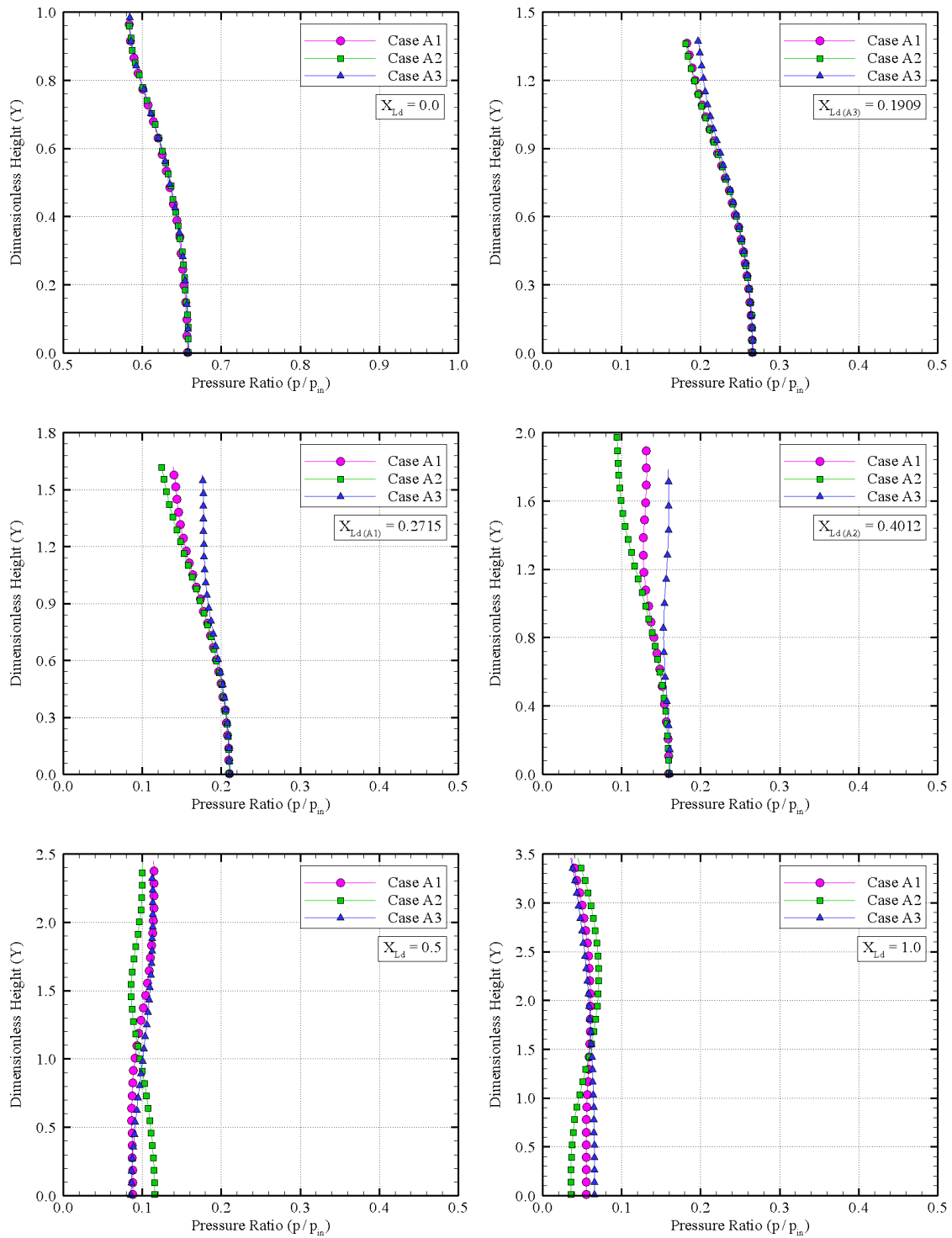


Figure 6.19 - Pressure ratio (p/p_{in}) profiles along the micronozzle for group A cases.

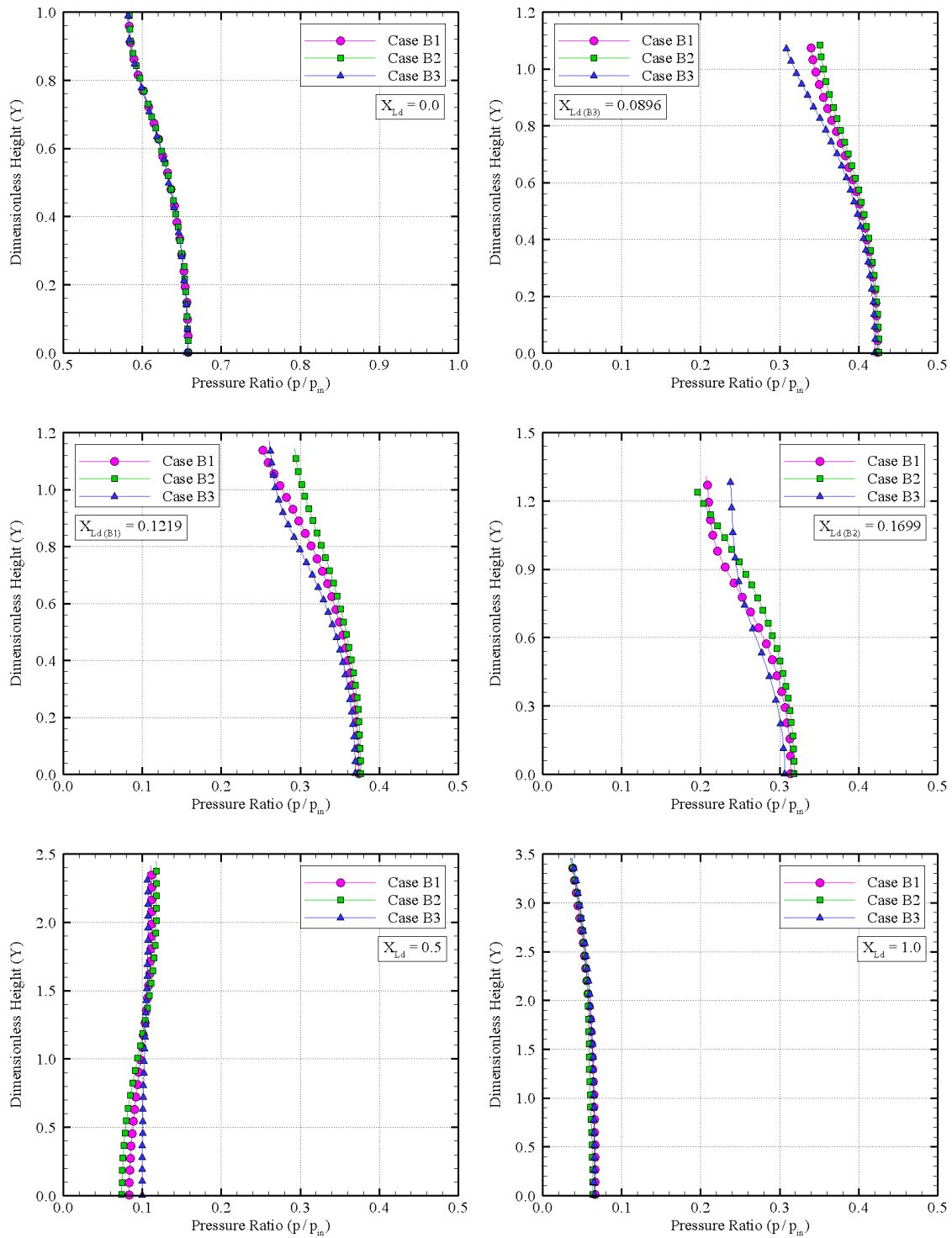


Figure 6.20 - Pressure ratio (p/p_{in}) profiles along the micronozzle for group B cases.

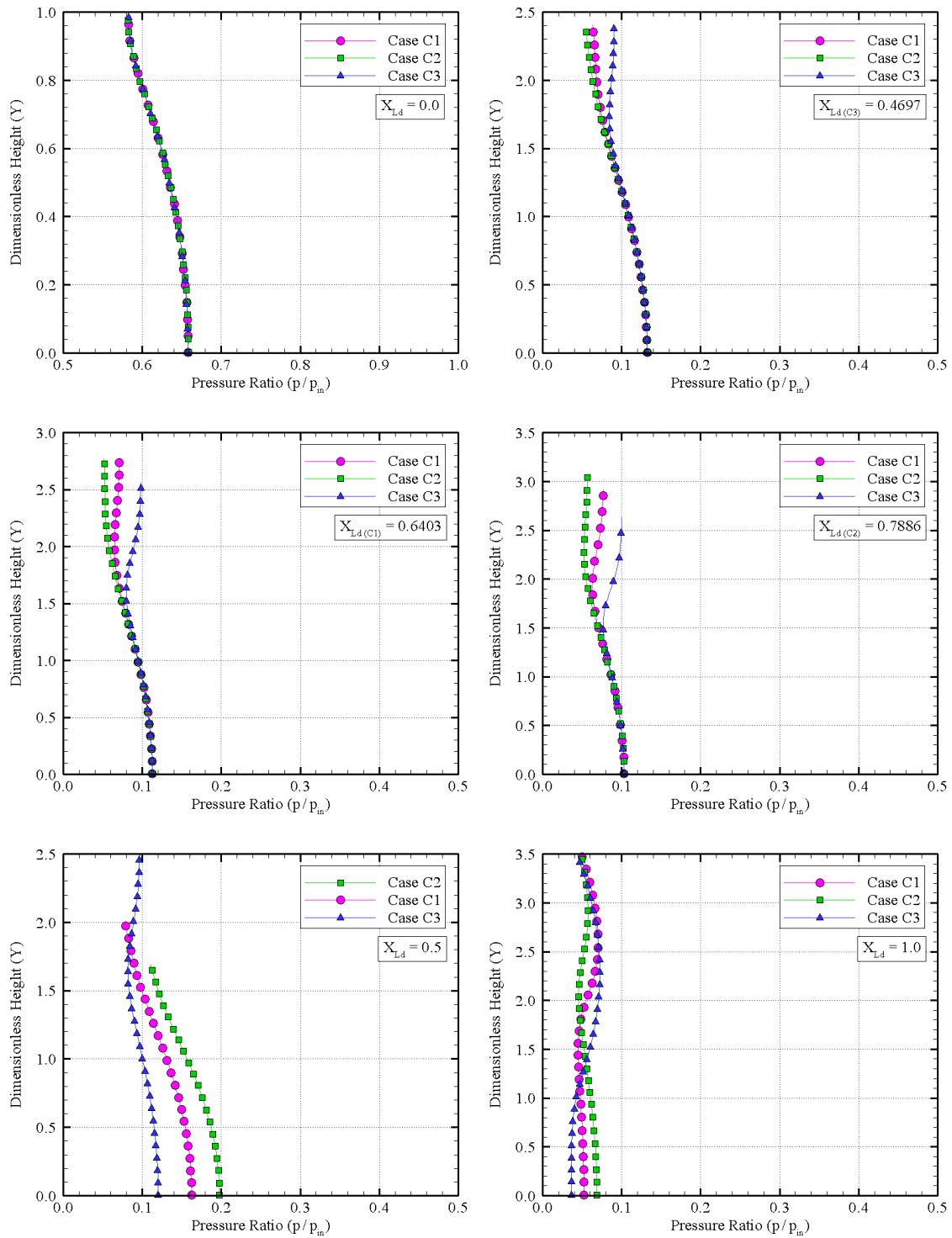


Figure 6.21 - Pressure ratio (p/p_{in}) profiles along the micronozzle for group C cases.

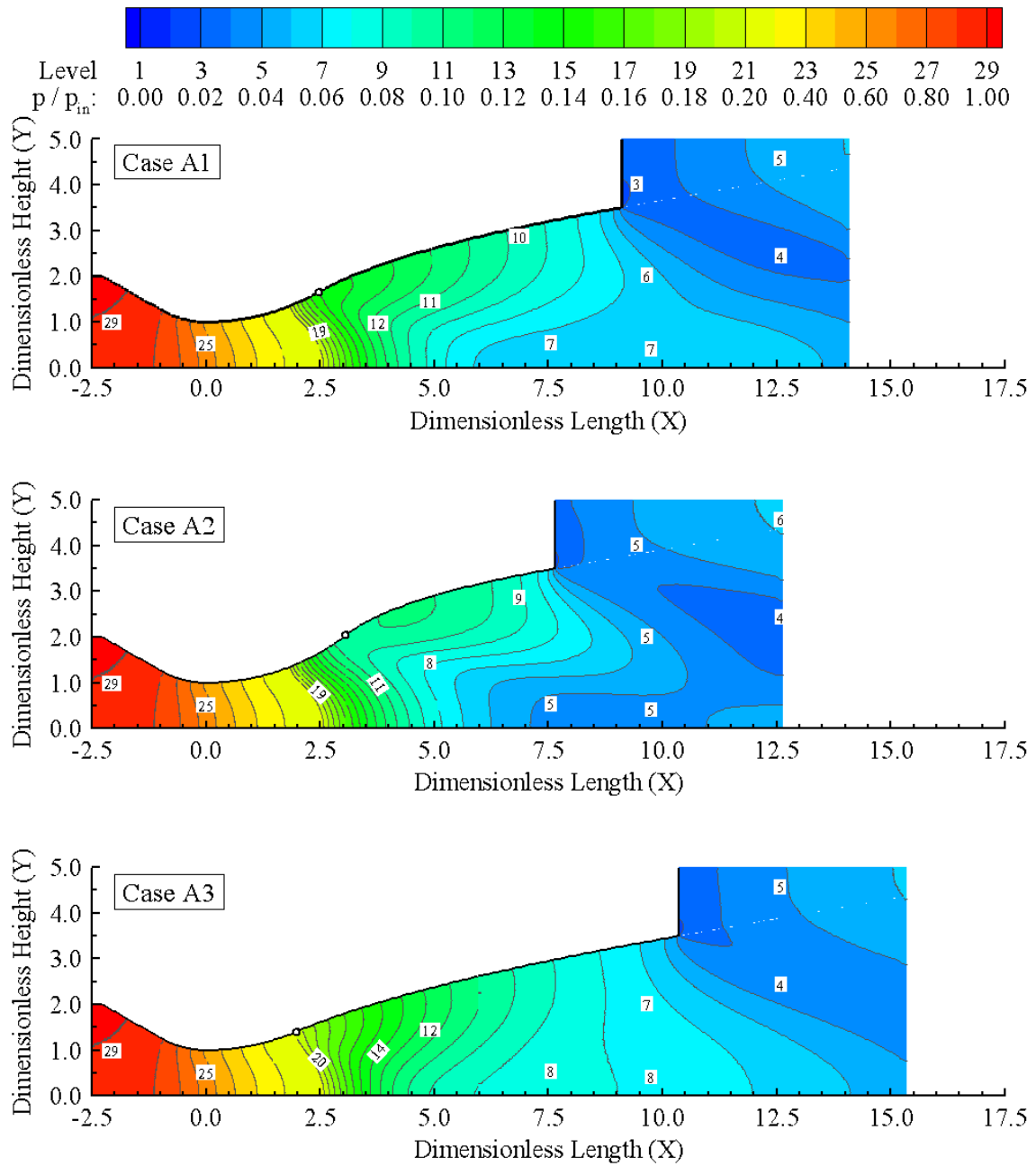


Figure 6.22 - Pressure ratio (p/p_{in}) distribution along the micronozzle for group A cases.

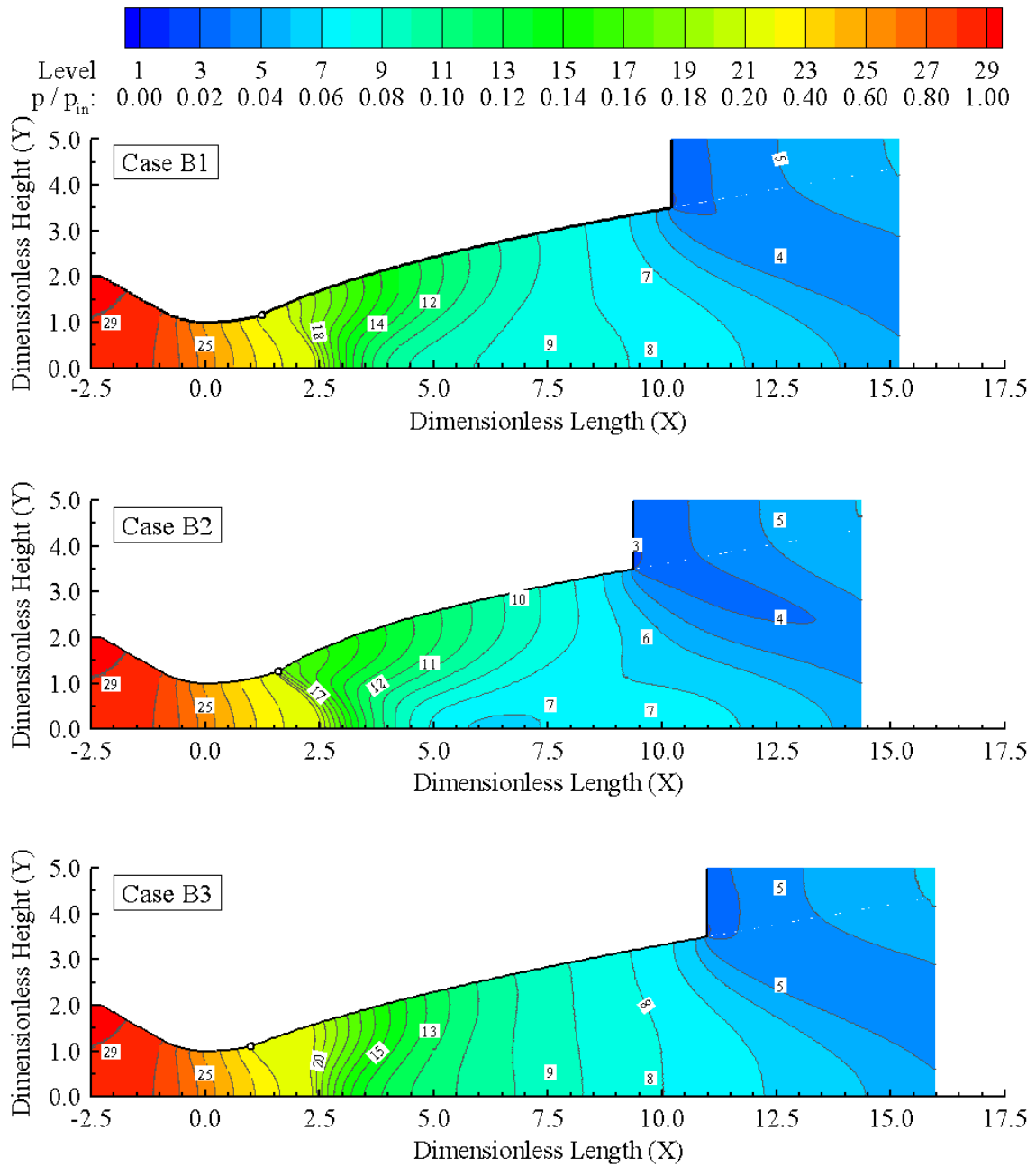


Figure 6.23 - Pressure ratio (p/p_{in}) distribution along the micronozzle for group B cases.

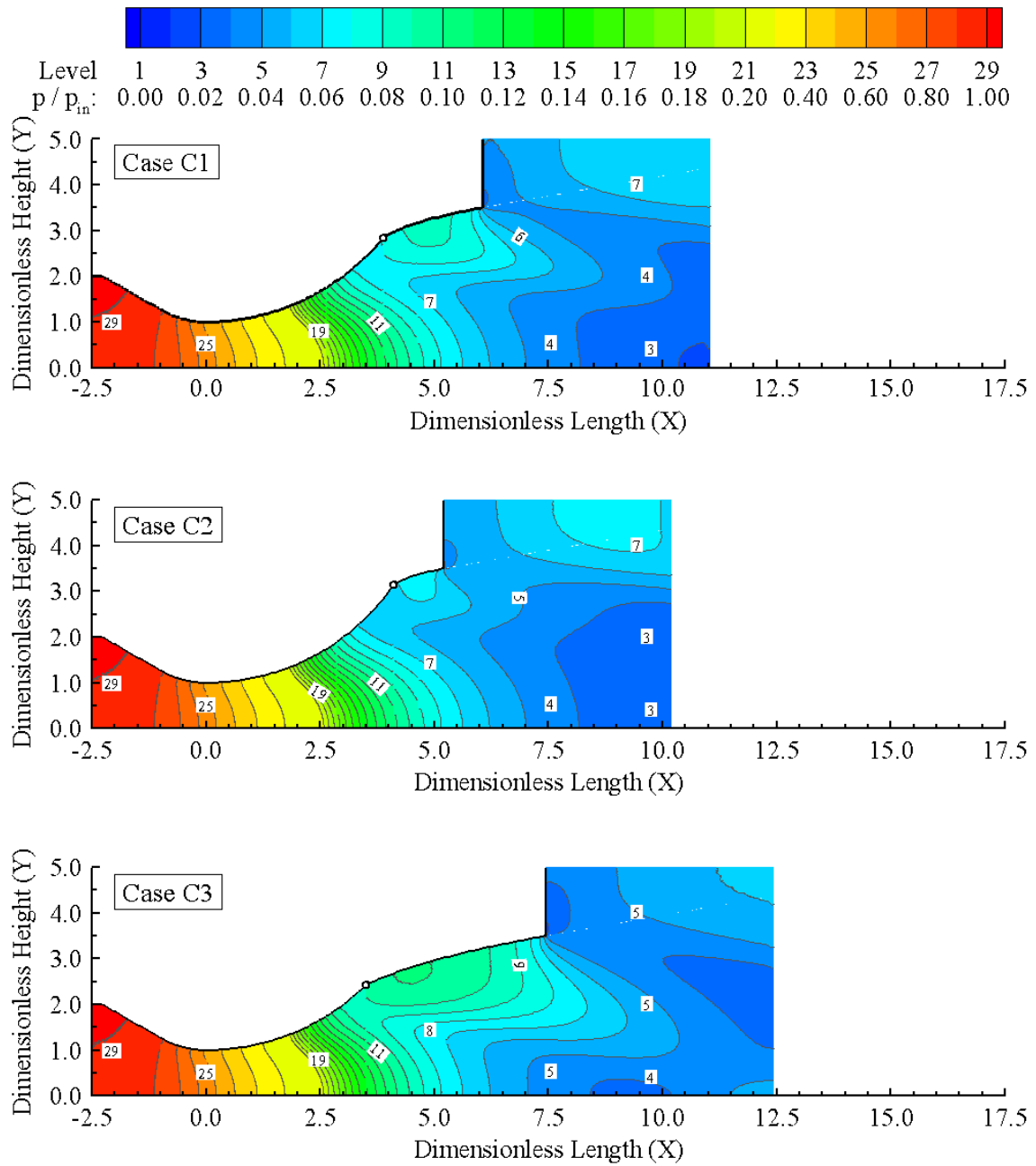


Figure 6.24 - Pressure ratio (p/p_{in}) distribution along the micronozzle for group C cases.

6.1.4 Temperature Field

In the expansion process of a compressible flow, such as that observed in micronozzles, gas temperature and density decrease while the macroscopic stream velocity increases. This behavior is assigned to the conversion of thermal energy¹ to macroscopic kinetic energy². The thermal energy is related to molecular excitation – random translation, rotation, vibration, electronic, etc – and kinetic energy is associated to stream velocity. The opposite physical mechanism is found in shock wave problems. Across shock waves, part of the high kinetic energy present in the supersonic flow is rapidly converted to thermal energy and hence temperature and pressure should increase while the velocity decreases.

As introduced in Section 3.6, the above mentioned thermal-kinetic energy exchange is performed by successive intermolecular interactions. Therefore, a relaxation process between translational and internal modes takes place in order to lead each mode towards the equilibrium state. Thermodynamic equilibrium occurs when there is, statistically, complete energy equipartition between translational and internal modes. In this sense, the thermodynamic temperature is defined when the temperatures based on each energy mode, i.e., translational, rotational, vibrational and electronic temperatures, are equal to each other. However, the relaxation time – commonly expressed in terms of the relaxation collision number (Section 3.6) – differs from one mode to another. Therefore, thermal nonequilibrium arises if the local collision frequency is not sufficient to return the molecules to the total statistical equilibrium. In this context, for a gas in thermodynamic nonequilibrium, as following in Equation 6.11, an overall temperature T_O may be defined as the weighted mean between the translational and internal temperatures (BIRD, 1994).

$$T_O = \frac{\zeta_T T_T + \zeta_R T_R + \zeta_V T_V}{\zeta_T + \zeta_V + \zeta_R} \quad (6.11)$$

In this expression, T and ζ stand for temperature and degrees of freedom, respectively, and the subscripts T , R and V represent the translational, rotational and vibrational modes, respectively. Evidently, ζ_T is always equal to three while the remaining excited internal degrees of freedom may vary according to the thermal state of the gas.

¹Sometimes called as internal energy. However, in the present account the term *internal energy* refers only to the molecular internal modes (rotation, vibration and so on).

²Hereafter referred just as kinetic energy.

Within each cell of the computational domain, translational, rotational and vibrational temperatures are obtained according to Equations 6.12, 6.13 and 6.14 (BIRD, 1994), respectively.

$$T_T = \frac{1}{3k} \frac{\sum_{j=1}^N m_j c_j'^2}{N} \quad (6.12)$$

$$T_R = \frac{2\bar{\varepsilon}_R}{k\zeta_R} = \frac{2}{k\zeta_R} \frac{\sum_{j=1}^N (\varepsilon_R)_j}{N} \quad (6.13)$$

$$T_V = \frac{\Theta_V}{\ln\left(1 + \frac{k\Theta_V}{\bar{\varepsilon}_V}\right)} = \frac{\Theta_V}{\ln\left[1 + \frac{k\Theta_V N}{\sum_{j=1}^N (\varepsilon_V)_j}\right]} \quad (6.14)$$

In these expressions, k is the Boltzmann constant, Θ_V is the vibrational characteristic temperature, and $\bar{\varepsilon}_R$ and $\bar{\varepsilon}_V$ are the rotational and vibrational average energies per molecule computed within the respective cell. The remaining variables are defined in the same sense as presented in the previous sections.

The geometric effects on the translational temperature profiles for the same cross-sections investigated in the previous subsections are displayed in Figures 6.25, 6.26 and 6.27 for group A, B and C cases, respectively. Since for the same group the temperatures related to the internal modes presented similar behavior, for brevity, such temperatures are shown only for cases A1, B1 and C1, respectively, in Figures 6.28, 6.29 and 6.30. In these plots, translational temperature T_T , rotational temperature T_R , vibrational temperature T_V and overall temperature T_O are normalized by the inlet thermodynamic temperature T_{in} . Again, X and X_{Ld} are the dimensionless lengths and Y is the dimensionless height, as defined previously in Subsection 6.1.1.

Figure 6.25 cases for group A shows that the expansion process explained in the beginning of the present subsection decreases the translational temperature T_T in the downstream direction. Moreover, at $X_{Ld} = 0.0$, it is clear that, near the surface, the translational temperature tends to the surface temperature T_w . This is an indication that gas and surface share thermal equilibrium. However, for sections downstream of the throat, the translational temperature T_T near the surface is slightly smaller than surface temperature T_w . This difference, called temperature jump, becomes more significant in the exit section, particularly at the nozzle lip. It occurs because, as the gas expands, density is reduced and, consequently, the mean free path increases and the collision frequency decreases along the downstream direction. Near the surface,

the reduction in collision frequency promotes a local thermal nonequilibrium because molecules that interact with the surface do not perform sufficient collisions in order to reach a state of complete relaxation. At the lip, due to the abrupt increase in cross-section area, the gas expands rapidly and the temperature jump increases substantially.

An examination analogous to that presented for the Mach number in Subsection 6.1.1 can be made here for the temperature field. In the present profiles, the ratio between the Y -range, where the distribution of the translational temperature ratio T_T/T_{in} is nonuniform, to the total Y -range of the same profile, is an indication of the thermal boundary layer. This layer corresponds to the region where translational temperature changes take place normal to the surface. Similar to the viscous boundary layer, these profiles show that the aforementioned ratio increases in the downstream direction. It means that the thermal boundary layer thickness increases and basically occupies most of section at $X_{Ld} = 1.0$. This behavior is caused mostly by two different mechanisms, namely, the viscous dissipation and the heat transfer from the surface. Due to shear stress effects, viscous dissipation converts kinetic energy into thermal energy, i.e., such a dissipation promotes a temperature rise. Evidently, this mechanism becomes more intense near the surface, where there are strong viscous effects and large velocity gradients. On the other hand, with the gas expansion, the difference between the surface and translational temperatures increases. Therefore, the heat transfer from the surface to the gas should become more expressive and, consequently, the temperature rises even more. Finally, Figures 6.26 and 6.27 show, respectively, that group B and C profiles present the same behavior.

Previous discussion provided an overview of the translational temperature distribution along the divergent part as well as the main physical mechanisms that influence such a property. At this point, the idea is to investigate how the translational and internal – rotational and vibrational – temperatures depart from each other along the micronozzle. This analysis should provide a clear indication of the thermal nonequilibrium degree in the gas flow. In this fashion, Figures 6.28, 6.29 and 6.30 show normalized profiles of the translational, internal and overall temperatures for cases A1, B1 and C1, respectively.

Focusing on Figure 6.28, it can be recognized that the thermodynamic nonequilibrium takes place in the entire divergent part as shown by the lack of equilibrium between the translational and internal temperatures. It should also be mentioned

that the overall temperature T_O , defined by Equation 6.11, is equivalent to the thermodynamic temperature only under equilibrium conditions. In addition, the ideal gas law does not apply to nonequilibrium situation.

In the temperature profiles, it is noted that vibrational temperature is quite larger than other temperatures. In the same sense, rotational temperature is slightly larger than translational one. As observed, the overall temperature ratio is essentially equal to the mean value of the translational and vibrational temperatures. Based on Equation 6.11, it can be concluded that, on average, the excited vibrational degrees of freedom ζ_V tend to zero. In this circumstance, $T_V \geq T_R \geq T_T$ occurs because translational and internal modes have different relaxation collision numbers, namely, $Z_V \geq Z_R \geq Z_T$. In other words, a larger number of collisions is necessary to excite molecules vibrationally from a lower to an upper state and vice-versa, as compared to rotational modes. For this reason, T_V/T_{in} decreases much slower than T_R/T_{in} . A similar comparison is also valid between rotational and translational modes. For illustration purposes, in contrast to the rotational mode, it is interesting to mention that Z_T is generally equal to unity, i.e., the translational mode is adjusted by every collision³.

Still referring to Figure 6.28, it is important to point out that the statistical fluctuations observed in the vibrational temperature profiles are explained by the fact that the vibrational energy levels are described by a quantum model, i.e., in a discrete form. Conversely, the translational and rotational modes are based on continuum spectrums of energy. Moreover, at $X_{Ld} = 1.0$, Figure 6.28 reveals clear differences between the temperatures at the surface, that is, ($Y = 3.5$). It confirms the aforementioned reason for the notable temperature jump at the lip. At this point, it proves worthwhile to mention that a translation nonequilibrium may also be found when the local thermal velocity distribution departs from isotropy. In this scenario, a preferential direction may exist for the thermal motion that, in essence, should be equally likely. However, results for the translational nonequilibrium are not shown in the present work. Finally, Figures 6.29 and 6.30 demonstrate that translational and internal temperature profiles for cases A1, B1 and C1 have the same qualitative behavior.

Proceeding in a manner analogous to that for the earlier primary properties, contour maps for the translational temperature ratio in the entire computational domain are

³This concept is valid for interactions between molecules with similar mass.

presented in the following. In this sense, Figure 6.31, 6.32 and 6.33 illustrate how the temperature patterns change along the micronozzle. Figure 6.31 for group A cases shows that temperature changes are similar to those for an one-dimensional model between the inlet and throat sections. This behavior occurs because, upstream of the throat, the difference between surface and translational temperatures ($T_w - T_T$) is small. Thus, the heat flux from the surface does not influence the gas temperature. However, due to the expansion process, heat transfer plays an important role near the surface as the translational temperature decreases. As a consequence, along the micronozzle divergent part, the translational temperature isolines tend to become parallel to the surface. In contrast, near the centerline, where the heat flux from the divergent surface is less intense, temperature changes are essentially due to the expansion process.

As pointed out in the discussion of the Mach number contour maps, near the surface, the subsonic region becomes thicker downstream of the inflection point. Similar to the convex surface, along the concave surface there is a thick layer with a high translational temperature value. Nevertheless, as shown in Figure 6.17, the combination of pressure and temperature gradients takes place in different manners near the convex and concave surfaces. Thus, since pressure is proportional to temperature, pressure and temperature gradients tend to neutralize one to each other along the convex surface, while in the concave surface both pressure and temperature gradients act towards the surface. For this reason, there is a thicker boundary layer with high temperature near the concave surface. Consequently, this mechanism is also responsible for the thick subsonic boundary layer previously mentioned.

Turning the attention to the external flow, around $Y = 3.5$, it is observed that the translational temperature distribution follows the internal flow temperature pattern. On the other hand, the temperature gradient is basically parallel to the X -axis near the centerline. This is an indication that the heat flux from the surface has a minor impact in this part of the flow. Finally, comparing group B and C cases, it is recognized that the translational temperature near the external centerline is reduced as the concave surface becomes shorter. Therefore, because of the aforementioned combination between pressure and temperature gradients, the concave surface is the major contributor for the external gas heating.

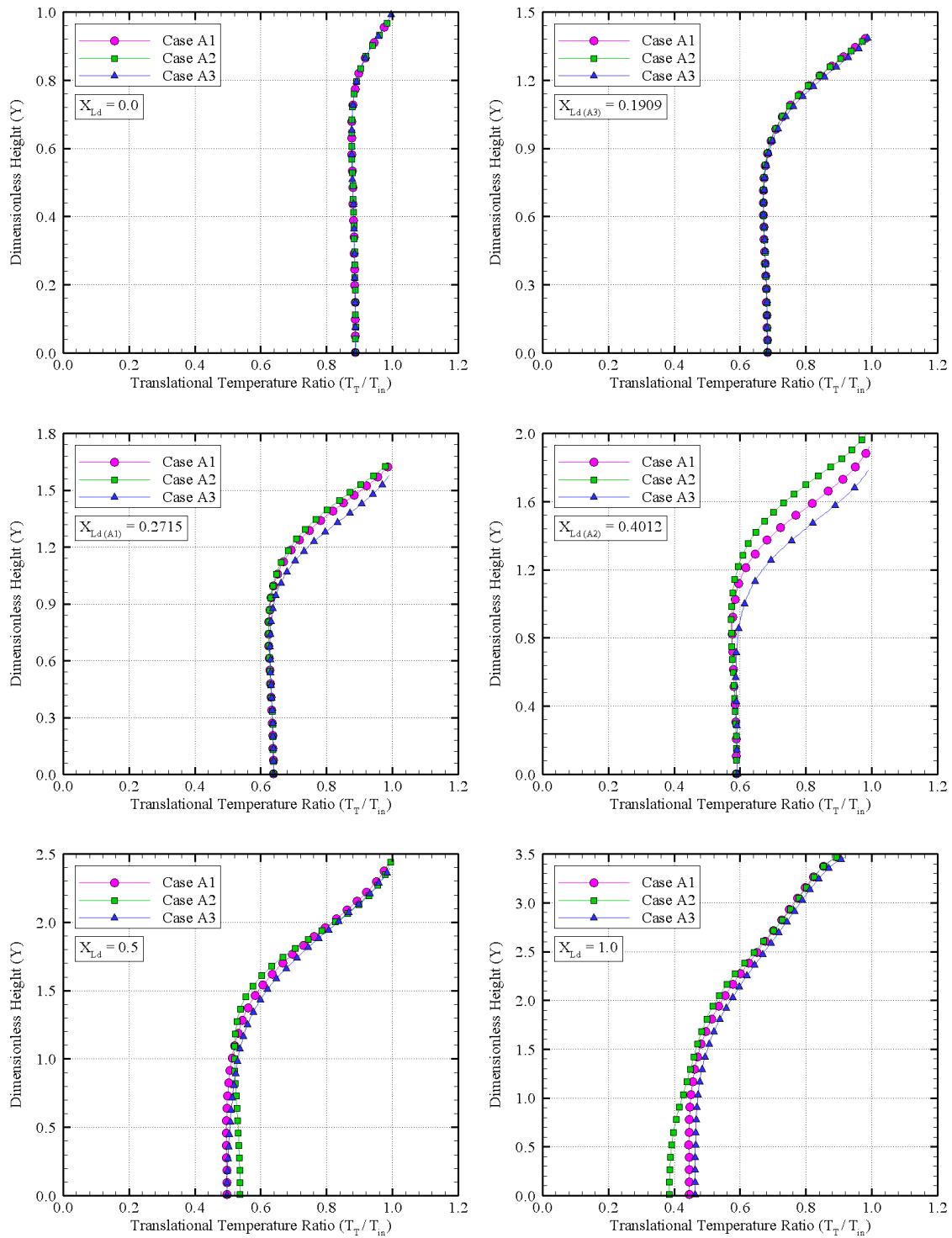


Figure 6.25 - Translational temperature ratio (T_T/T_{in}) profiles along the micronozzle for group A cases.

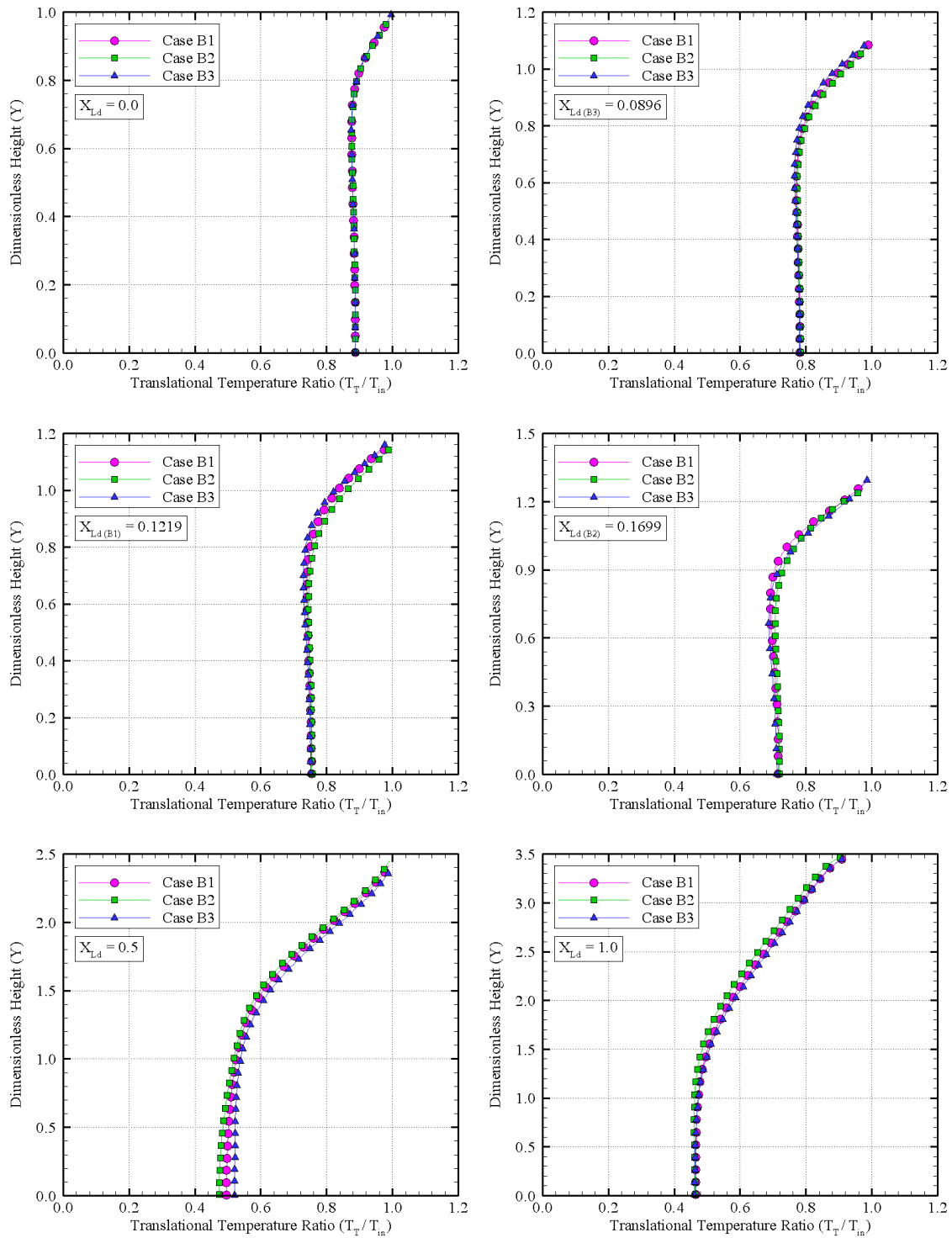


Figure 6.26 - Translational temperature ratio (T_T/T_{in}) profiles along the micronozzle for group B cases.

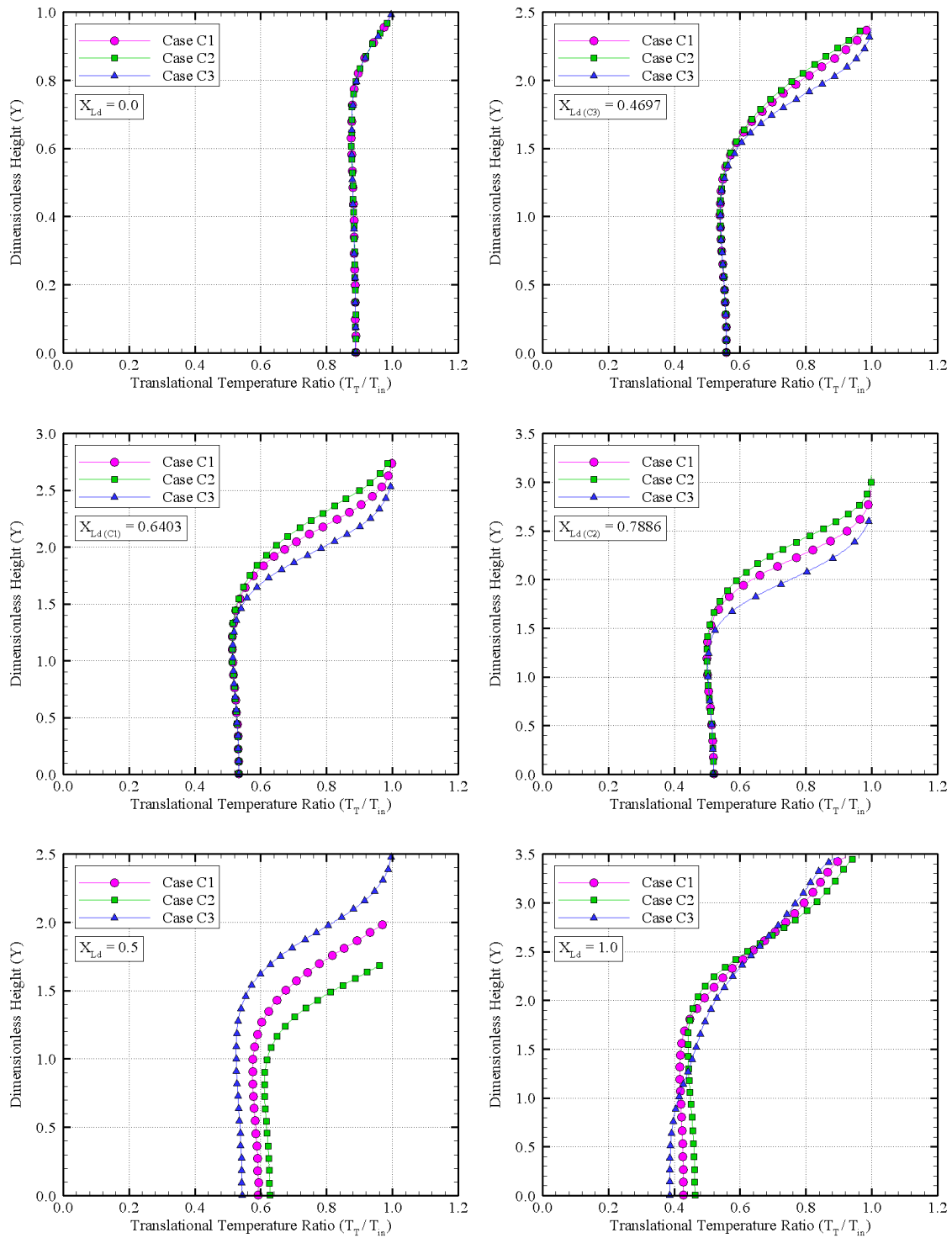


Figure 6.27 - Translational temperature ratio (T_T/T_{in}) profiles along the micronozzle for group B cases.

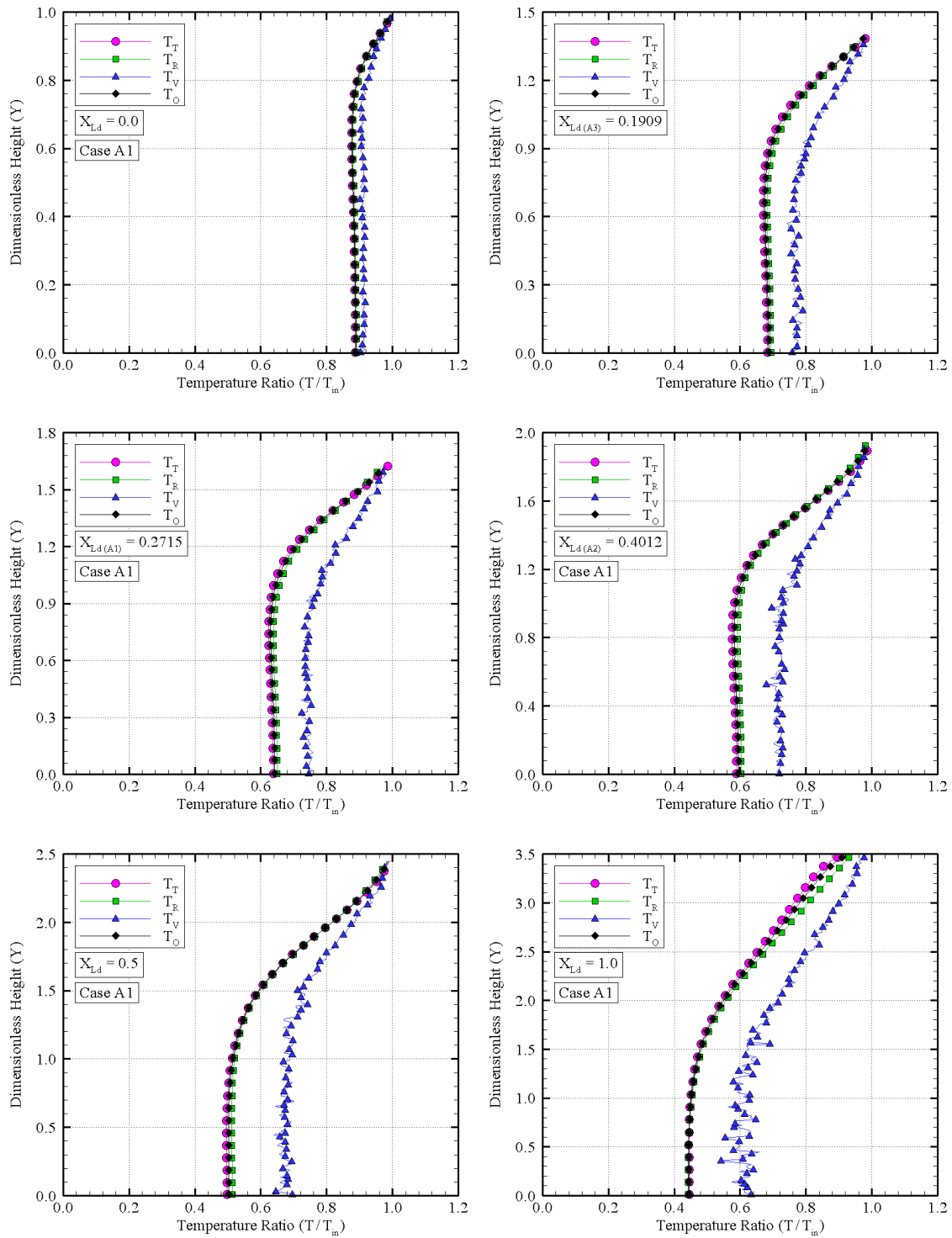


Figure 6.28 - Temperature ratio (T/T_{in}) profiles along the micronozzle for case A1.

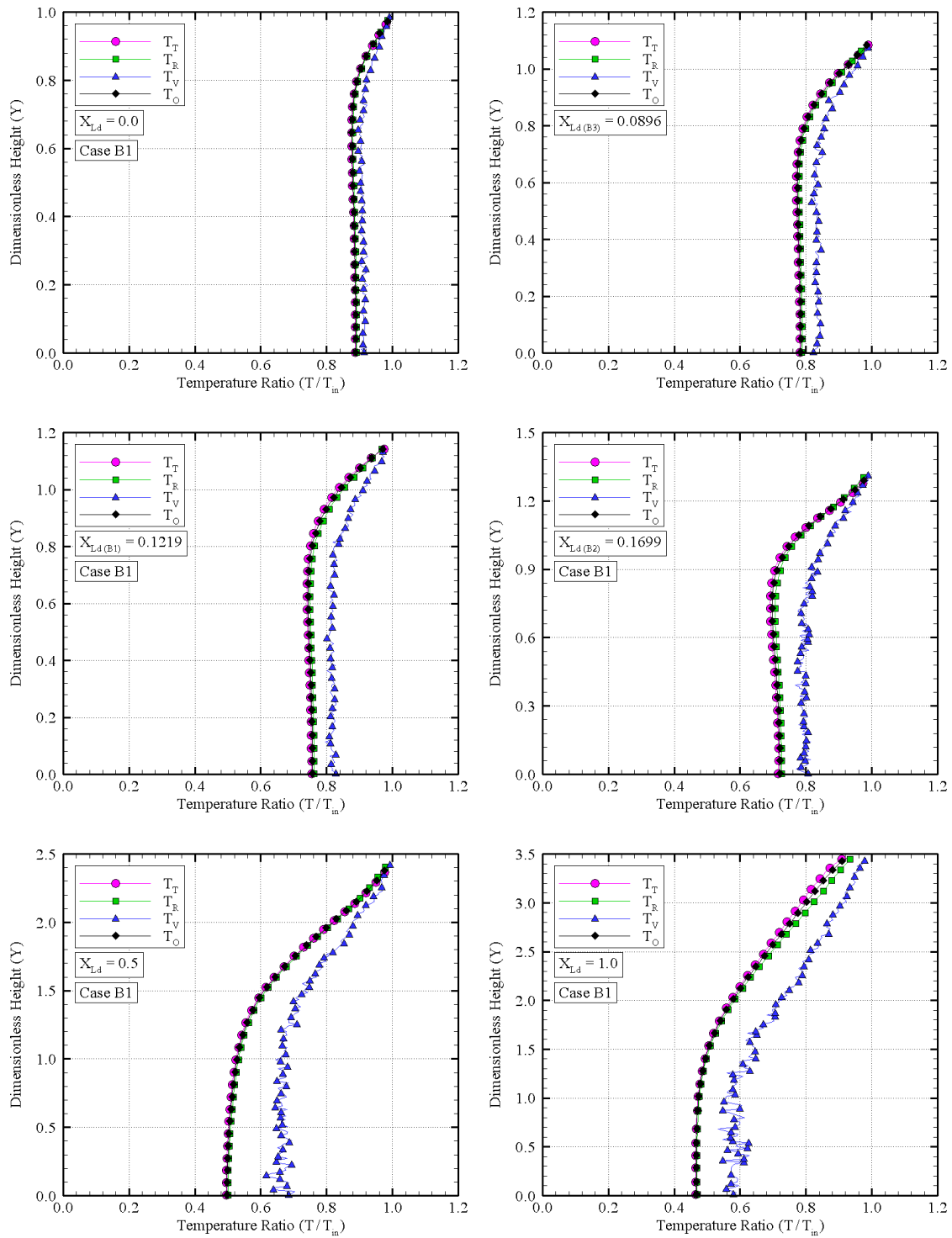


Figure 6.29 - Temperature ratio (T/T_{in}) profiles along the micronozzle for case B1.

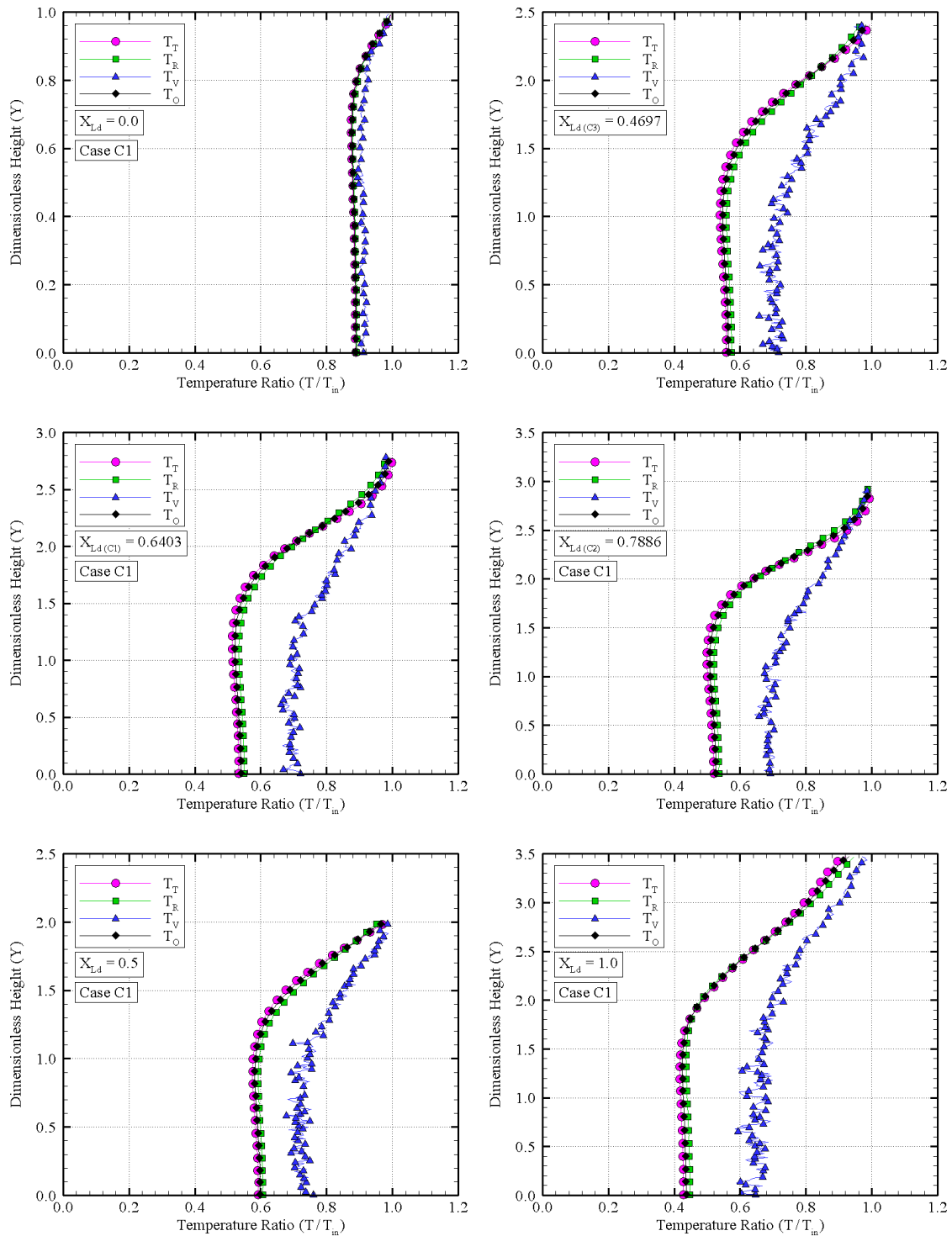


Figure 6.30 - Temperature ratio (T/T_{in}) profiles along the micronozzle for case C1.

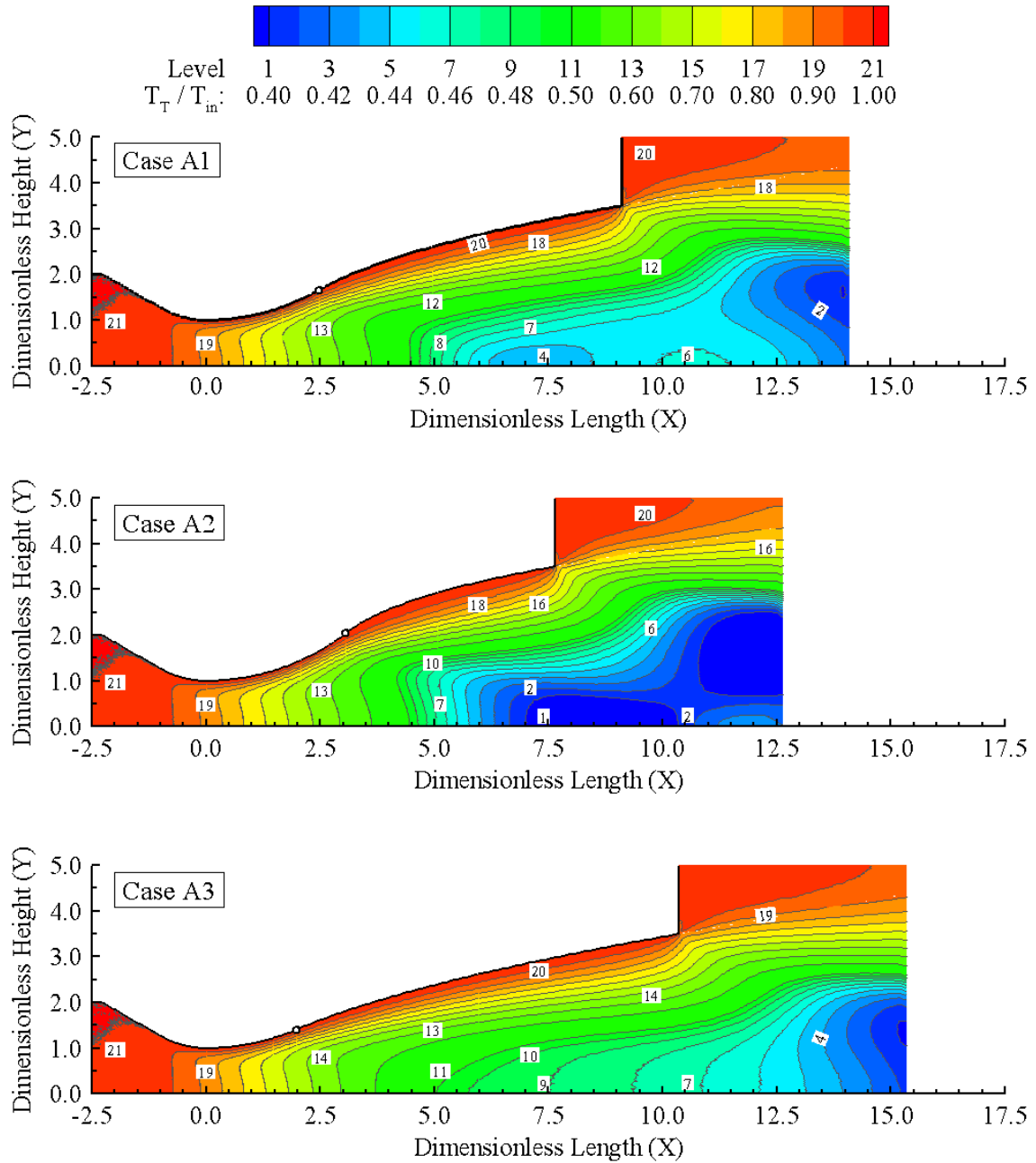


Figure 6.31 - Translational temperature ratio (T_T/T_{in}) distribution along the micronozzle for group A cases.

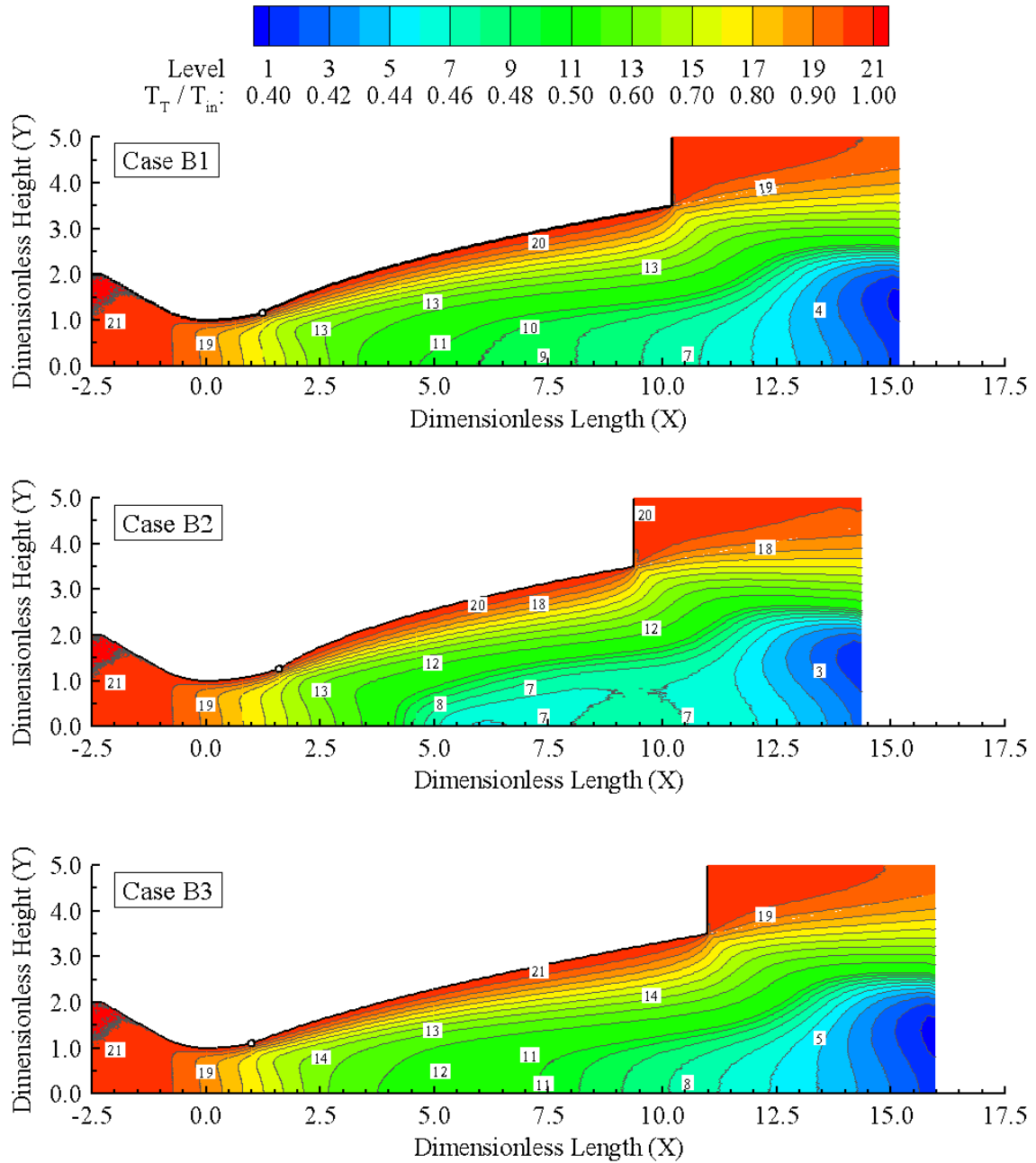


Figure 6.32 - Translational temperature ratio (T_T/T_{in}) distribution along the micronozzle for group B cases.

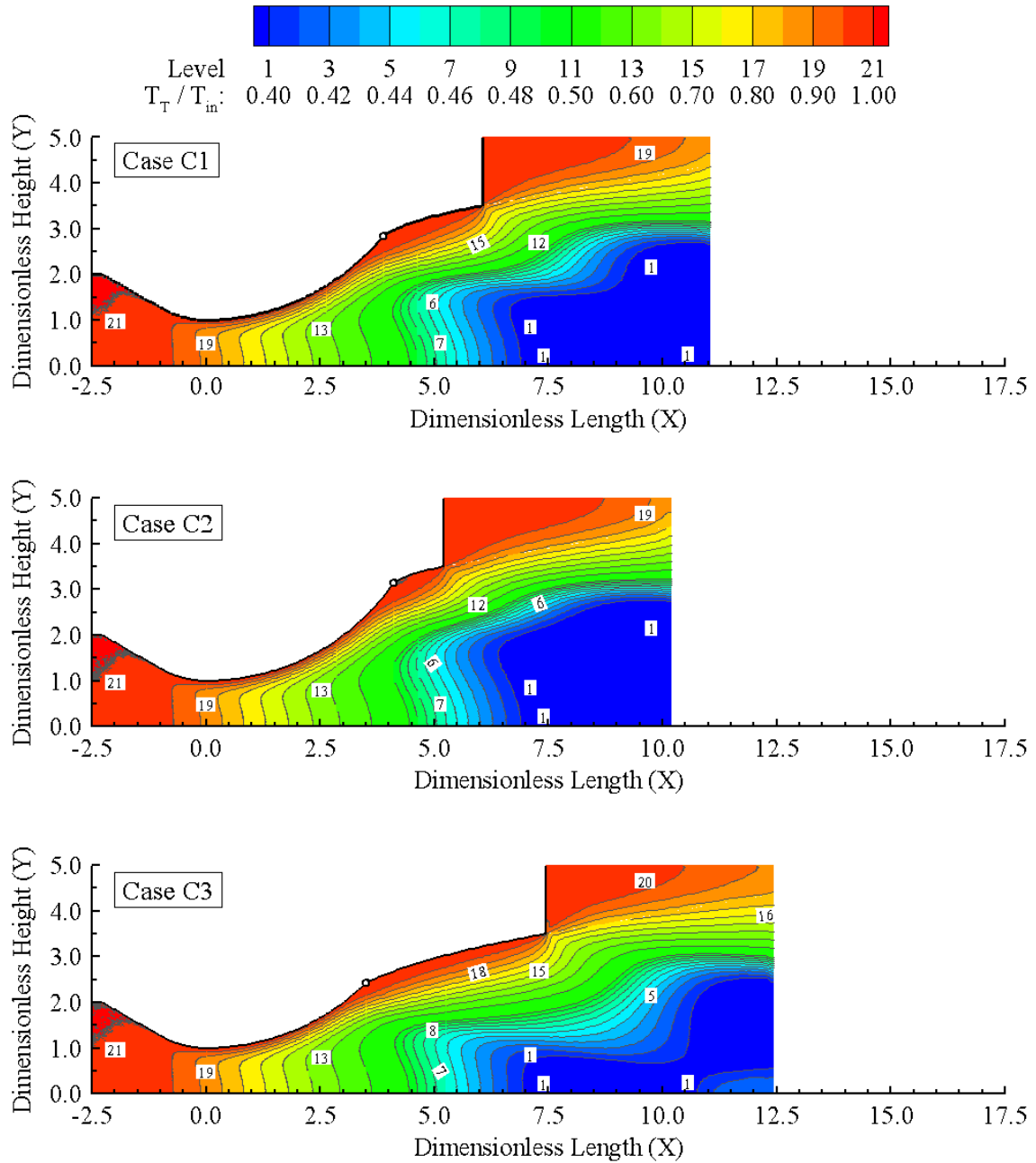


Figure 6.33 - Translational temperature ratio (T_T/T_{in}) distribution along the micronozzle for group C cases.

6.1.5 Knudsen Field

As extensively mentioned in this work, the Knudsen number Kn provides an important measurement of the rarefaction and nonequilibrium degrees of a flow. The Knudsen number is the basic criterion employed to classify the flow in terms of continuum, slip, transitional or free molecular regimes. Thus, based on the Knudsen number, it is possible to define the adequate approach to describe the respective flow problem. For instance, the well known Navier-Stokes (NS) equations are valid for a flow in local equilibrium or slightly disturbed from equilibrium conditions. Therefore, the Knudsen number is generally the appropriate breakdown parameter to predict the validity of the continuum approach.

As reported in Section 2.2, several breakdown parameters have been proposed in the literature. In general, these parameters are strongly based on the traditional definition of the Knudsen number, $Kn = \lambda/L$, which was introduced in Section 1.2. The breakdown of the NS equations is connected to the failure of the constitutive relations: stress tensor and heat flux vector as being linearly proportional to strain and temperature gradient, respectively. As a result, both momentum and energy transport phenomena must be subjected to a complete examination of the Knudsen number as a breakdown parameter. Moreover, if the flow experiences drastic density changes, such as observed across shock waves or at the present nozzle lip, the Knudsen number definition must also take into account density variations.

In this scenario, in order to map the rarefaction and nonequilibrium degrees along the micronozzle, the gradient-length local Knudsen numbers⁴ Kn_ϕ , which are based on different macroscopic properties ϕ , are computed in the present account. According to Boyd (2002), Equations 6.15 to 6.18 define such parameters in terms of the local velocity components u and v , speed sound a , density ρ , translational temperature⁵ T , and mean free path λ . In short, a large Kn value indicates a large nonequilibrium degree. For illustration purposes, in a flow with local Kn equal to 0.05 the relative error between continuum and DSMC approaches is approximately 5% (BOYD, 2002).

$$Kn_u = \frac{\lambda}{\max(|u|, a)} |\nabla u| \quad (6.15)$$

⁴See Equation 1.3.

⁵For brevity, in this subsection the translational temperature is represented just by T .

$$Kn_v = \frac{\lambda}{\max(|v|, a)} |\nabla v| \quad (6.16)$$

$$Kn_\rho = \frac{\lambda}{\rho} |\nabla \rho| \quad (6.17)$$

$$Kn_T = \frac{\lambda}{T} |\nabla T| \quad (6.18)$$

Evidently, each macroscopic property may provide locally different Kn values, i.e., each property may present a different deviation from the equilibrium condition. For this reason, as defined in Equation 6.19, the maximum Kn_{\max} value is considered as the breakdown parameter.

$$Kn_{\max} = \max(Kn_u, Kn_v, Kn_\rho, Kn_T) \quad (6.19)$$

In order to bring out the influence of each property on the thermodynamic nonequilibrium degree, for the same cross-sections investigated previously, Figures 6.34, 6.35 and 6.36 depict the Knudsen profiles – Kn_u , Kn_v , Kn_ρ and Kn_T – for cases A1, B1 and C1, respectively. In this set of plots, X and X_{Ld} are the dimensionless lengths and Y is the dimensionless height, similar to the previous subsections. Since these profiles demonstrate similar behavior for the same geometric group, the other cases are not shown.

Before discussing the results, it is convenient to remind that the continuum no slip flow regime is valid for $Kn \leq 10^{-2}$. Within the Knudsen range $10^{-2} \leq Kn \leq 10^{-1}$, slip boundary conditions should be employed in the continuum approach. In the same sense, $10^{-1} \leq Kn \leq 1$, defines the transitional flow regime, where the molecular structure of the gas must be take into account. In this connection, the present DSMC application is strongly justifiable within every region with $Kn \geq 10^{-2}$. It should also be mentioned that these limits are just indicative values and does not represent a general and precise rule.

According to Figure 6.34, in general, the Knudsen number increases in the downstream direction. This occurs because, as the gas flow expands, the rarefaction degree increases and consequently the collision frequency decreases. It is also interesting to observe that, near the surface, the Knudsen number based on the u velocity component is larger than the other ones. Such a behavior is related to the strong velocity gradients imposed by the surface viscous effects, and it is in agreement with the velocity slip observed in the Mach profiles. The largest Knudsen value occurs at the

nozzle lip, and it is basically caused to two different aspects: the high rarefaction degree and the abrupt changes in flow direction.

As already recognized, changes on the four investigated properties – u , v , ρ and T – at the nozzle lip yield Knudsen numbers slightly greater than 10^{-1} . Similar to the velocity slip, the high Kn_T values at the lip agree with the temperature jump previously reported. Furthermore, Figures 6.35 and 6.36 for cases B1 and C1 show no qualitative differences the in Knudsen profiles. Moreover, it is important to remark that in all three cases – A1, B1 and C1 – the Knudsen number varies by three orders of magnitude.

Finally, in order to provide an overview of the maximum Knudsen value Kn_{\max} in the entire domain, Figures 6.37, 6.38, 6.39 present the contour maps for group A, B and C cases, respectively. These plots show a complex pattern of the Kn_{\max} distribution. According to the present results, near the centerline, the flow experiences $Kn_{\max} \leq 10^{-2}$ and hence a continuum approach may be applied to such regions. On the other hand, in the most part of the domain, mainly near the divergent surface, the flow yields $Kn_{\max} \geq 10^{-2}$. The largest Kn_{\max} value is reached at the external surface of the nozzle lip.

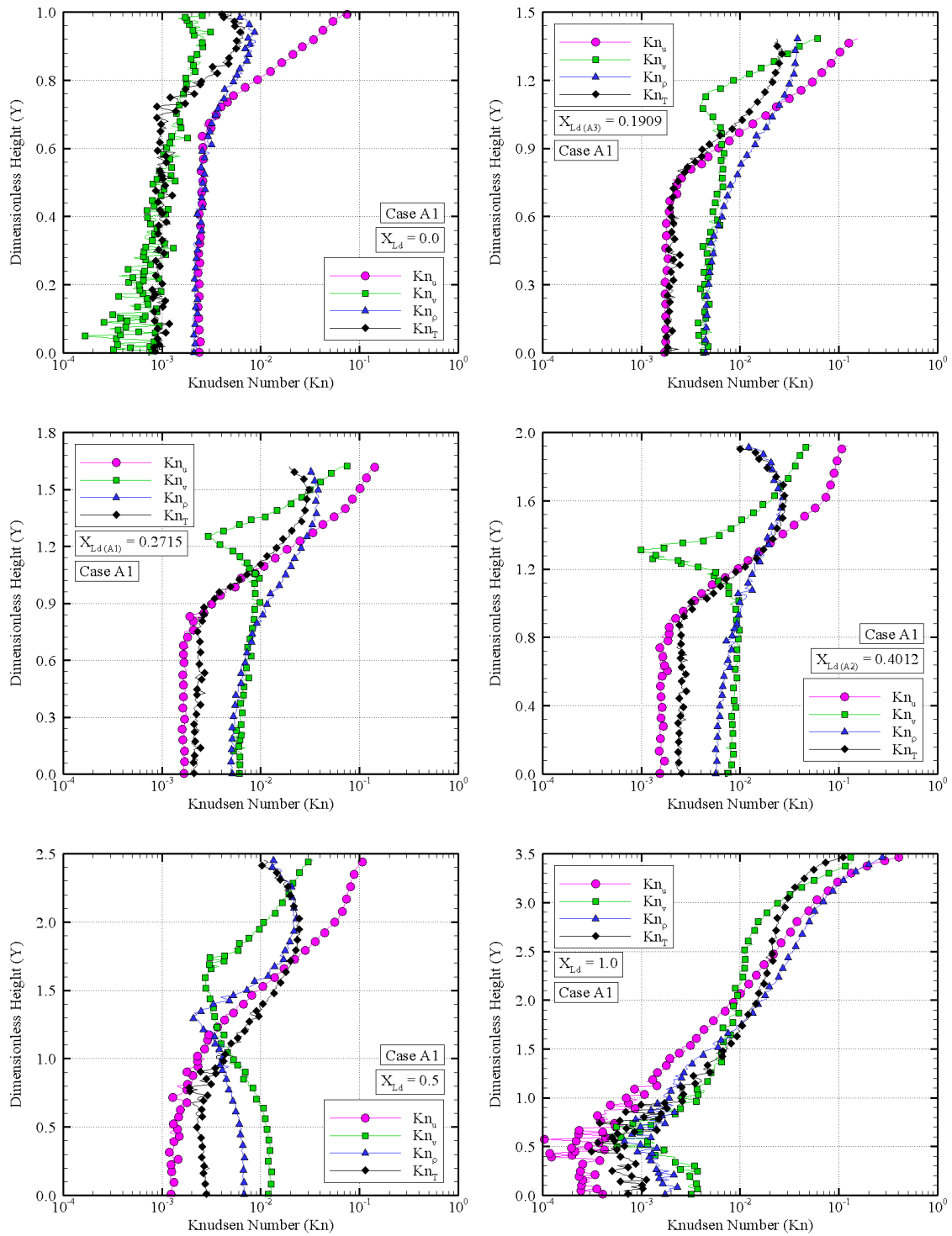


Figure 6.34 - Knudsen number (Kn) profiles along the micronozzle for the case A1.

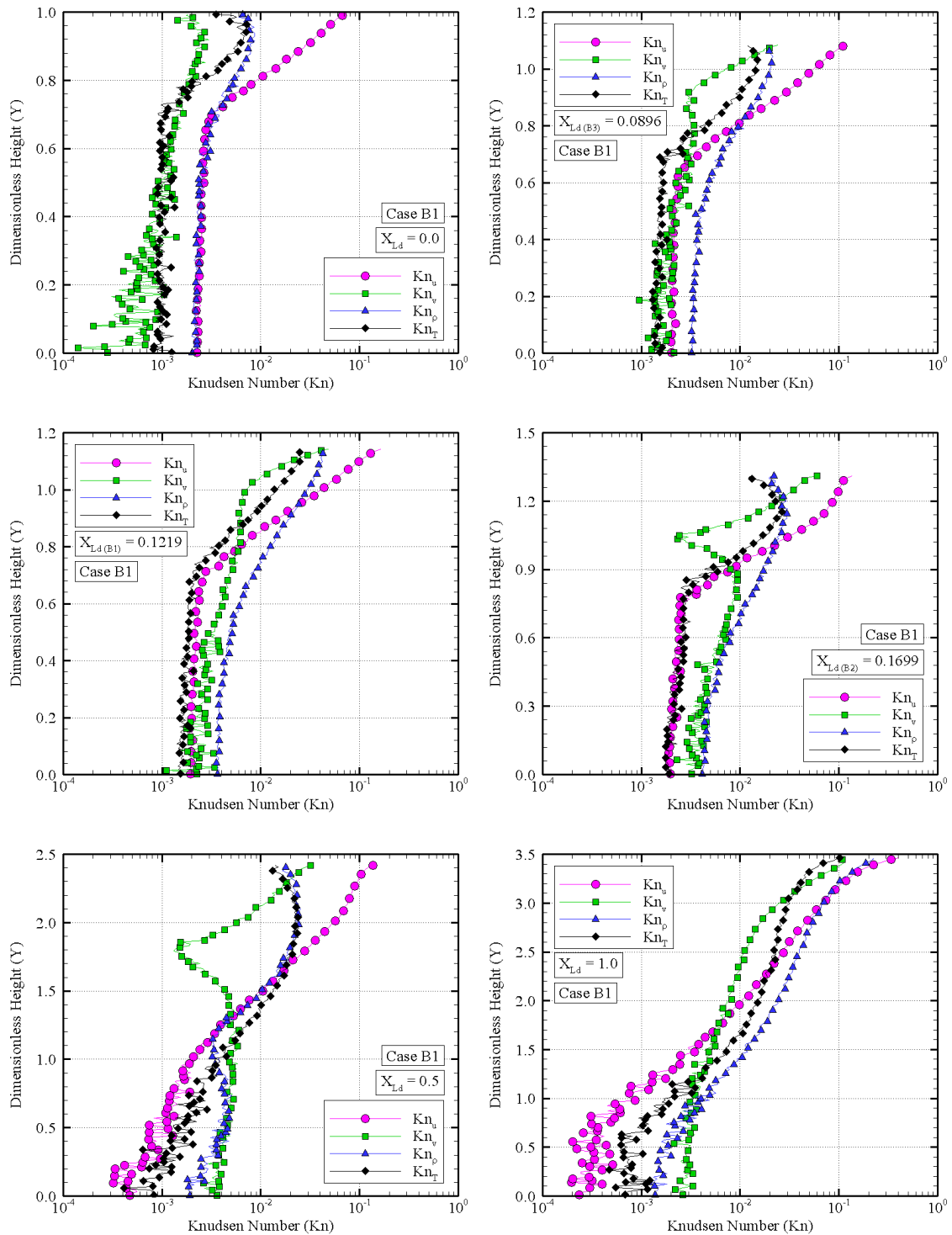


Figure 6.35 - Knudsen number (Kn) profiles along the micronozzle for the case B1.

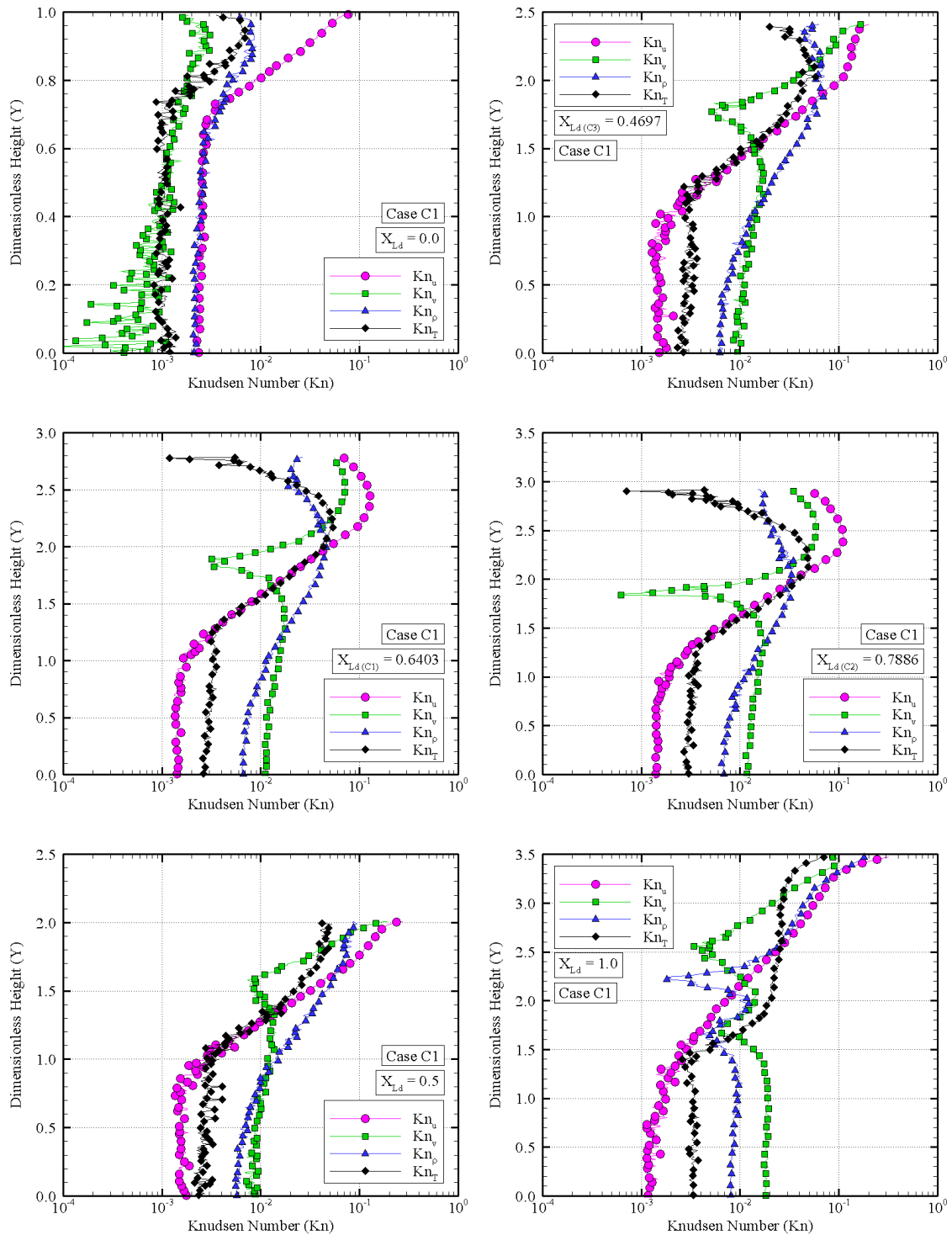


Figure 6.36 - Knudsen number (Kn) profiles along the micronozzle for the case C1.

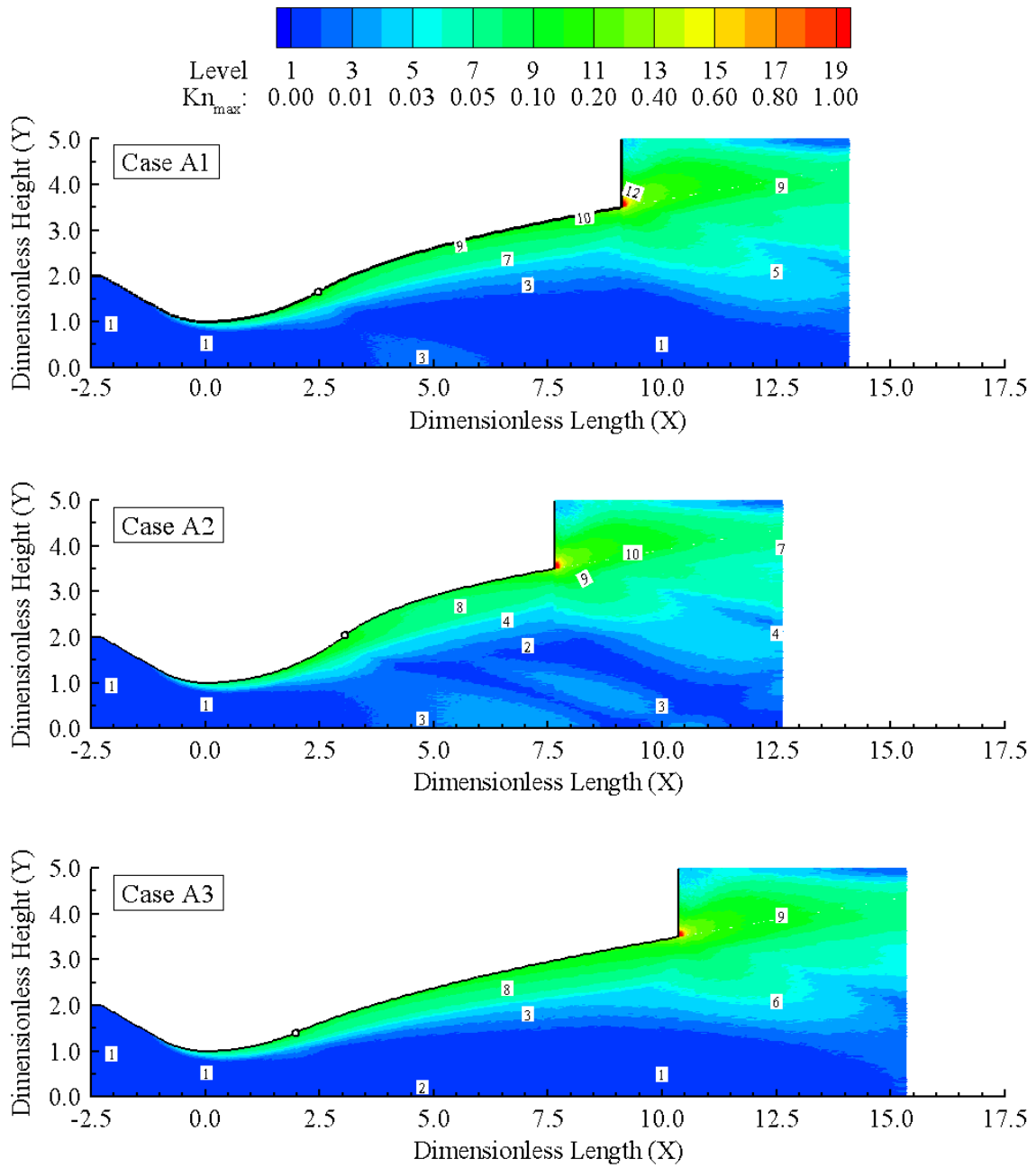


Figure 6.37 - Knudsen number (Kn) distribution along the micronozzle for group A cases.

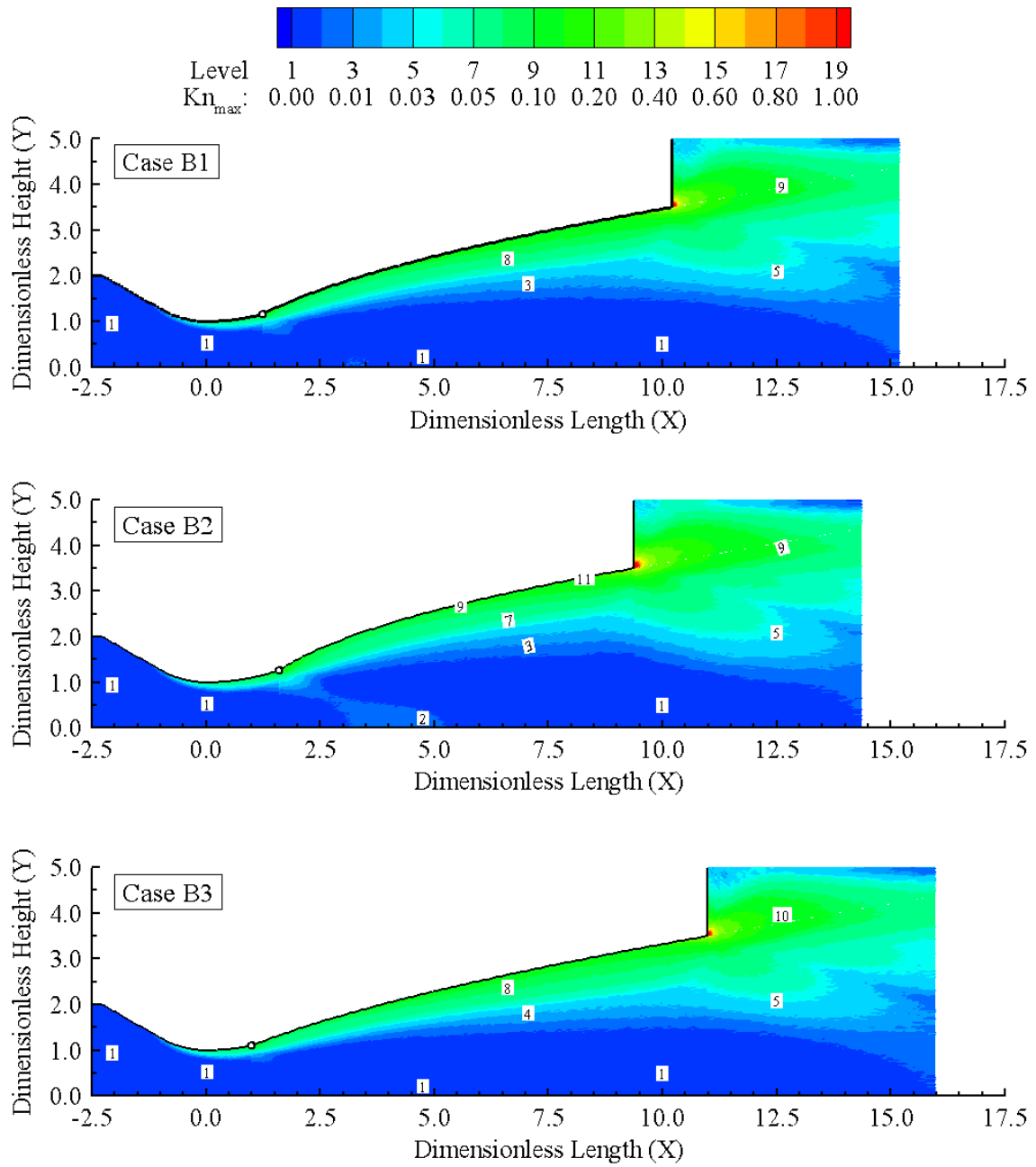


Figure 6.38 - Knudsen number (Kn) distribution along the micronozzle for group B cases.

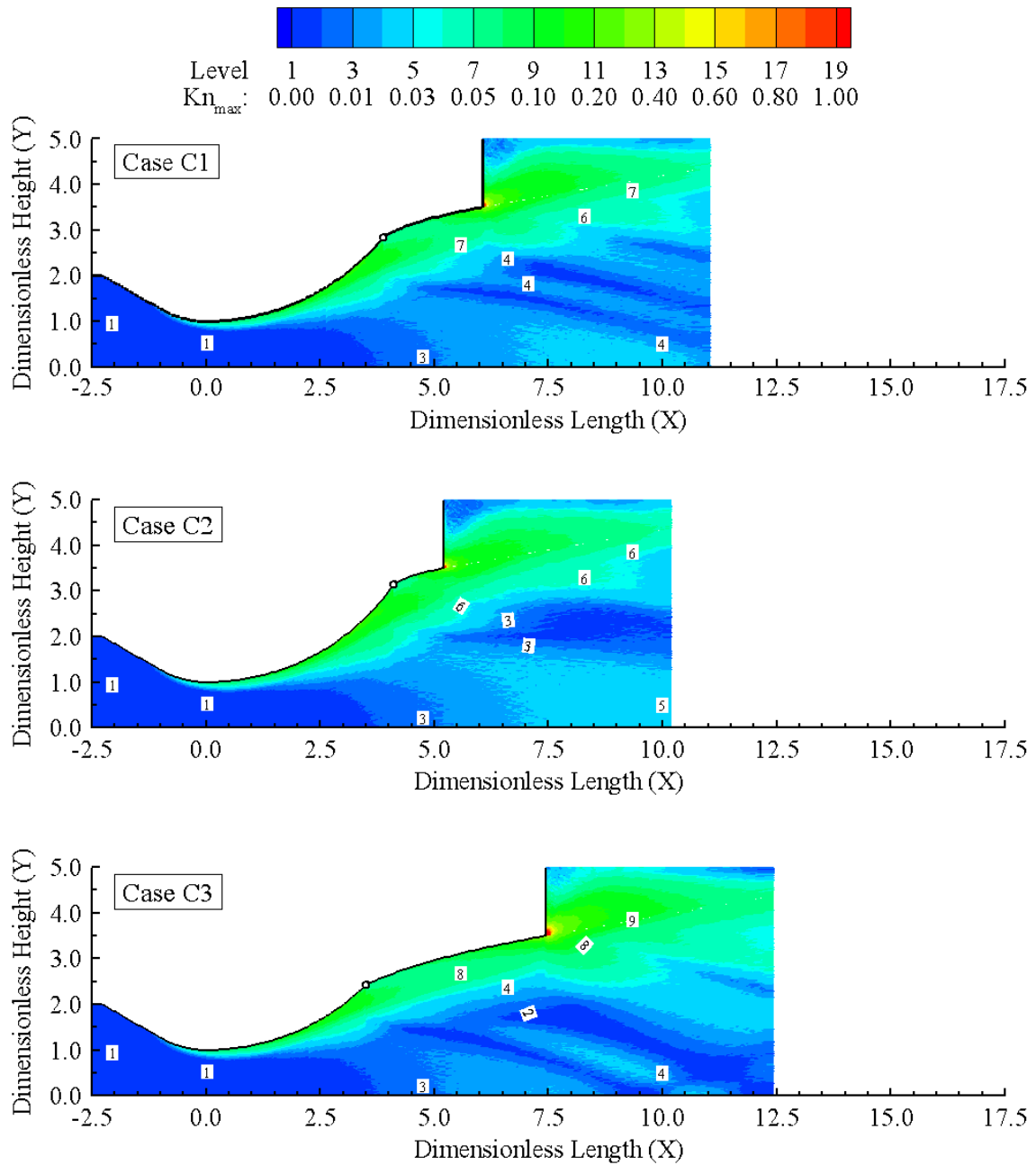


Figure 6.39 - Knudsen number (Kn) distribution along the micronozzle for group C cases.

6.2 Aerodynamic Surface Properties

This section concentrates on variations in the aerodynamic surface quantities due slope and curvature of the divergent surface at the inflection point. Aerodynamic surface quantities of particular interest in the present microflow are the number flux, pressure, skin friction and heat transfer. In other words, the purpose of this section is to present and discuss changes on these quantities, expressed in coefficient form, due to variations on the geometric parameters α_g and β_g .

6.2.1 Dimensionless Number Flux

As the gas flow expands along the micronozzle, neglecting thermal changes, it is expected that the rate of molecules impinging on the solid surface decreases in the downstream direction. Momentum and energy exchanges between molecules and surface are highly dependent on the number of the impinging molecules. For this reason, before discussing pressure, skin friction and heat transfer coefficients, it proves instructive to view the molecular number flux along the internal surface.

The molecular number flux \dot{N} is computed by sampling the number of molecules impinging on the surface by unit time and unit area. According to Equation 6.20, the dimensionless number flux N_f represents the number flux \dot{N} normalized by $n_{in} u_{in}$. In this expression, n_{in} is the inlet number density and u_{in} is the inlet stream velocity.

$$N_f = \frac{\dot{N}}{n_{in} u_{in}} \quad (6.20)$$

In this context, for group A, B and C cases, the impact of the geometric changes on the dimensionless number flux N_f along the micronozzle internal surface is displayed in Figure 6.40. In this group of plots, as defined previously, X represents the length x normalized by the half throat size h_t . Moreover, the vertical dash-dot lines indicate the inflection point X -coordinate of each case. Such an indication aids the identification of surface effects near the inflection point.

In Figure 6.40, focusing first on group A cases, it can be observed that the molecular number flux achieve a maximum at the inlet where the number density is also maximum. As the number density decreases due to the expansion process, N_f drops rapidly up to the inflection point. Downstream of this point, N_f continues to decrease, but at a smaller rate, up to the nozzle lip, where N_f reaches its minimum

value. These different N_f reduction rates are explained by the fact that, downstream of the inflection point, centripetal effects promote a pressure gradient towards the concave surface. Near this surface, centripetal effects minimize the rate at which the number density decreases due to the expansion process. Based on case A1, this explanation also agrees to the fact that, as the radius of curvature of the concave surface increases, e.g., in case A3, centripetal effects become less significant and hence the rate at which N_f decreases tends to rise. An analogous analysis can be employed for cases A1 and A2. Moreover, it is worthwhile to remark that N_f experiences a reduction of about one order of magnitude along the internal surface. In general, the aforementioned explanations are also applied to group B and C cases.

Still referring to Figure 6.40, qualitative differences between group A, B and C cases can be recognized. These differences are strongly related to the fact that the inflection point X -coordinate varies considerably from one group to another. Considering only group A and B cases, it is clear that near the inflection point, the N_f level in group B is larger than the one in group A. This behavior occurs because the inflection point for group B cases is closer to the high pressure regions, as compared to group A cases. A similar situation takes place between group B and C cases. As observed, for group C cases, the reduction in number flux occurs essentially upstream of the inflection point. Further downstream, there is a small jump in the N_f value due to the compression region formed by the convex surface in group C cases ($\alpha_g = 0.5$). In the same sense, in group B cases, due to the abrupt increase in the turning angle ($\alpha_g = 2.0$), a drastic drop in N_f takes place across the inflection point.

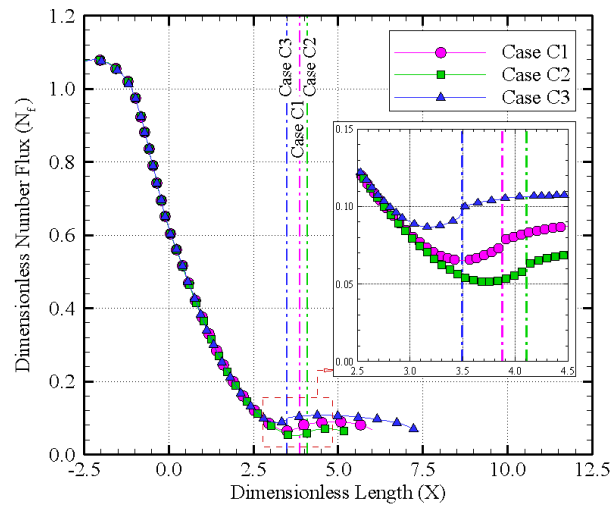
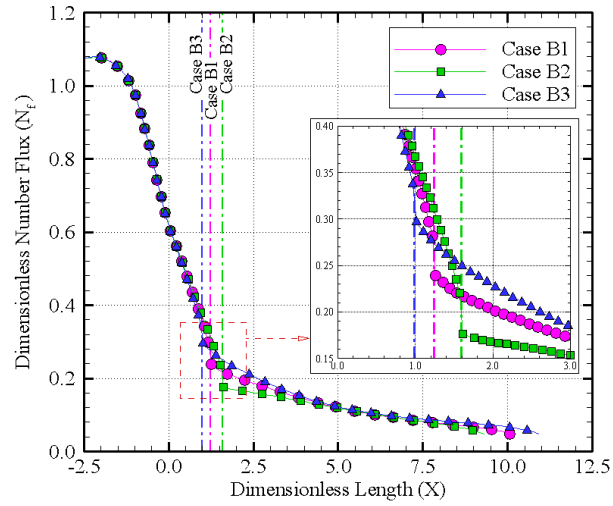
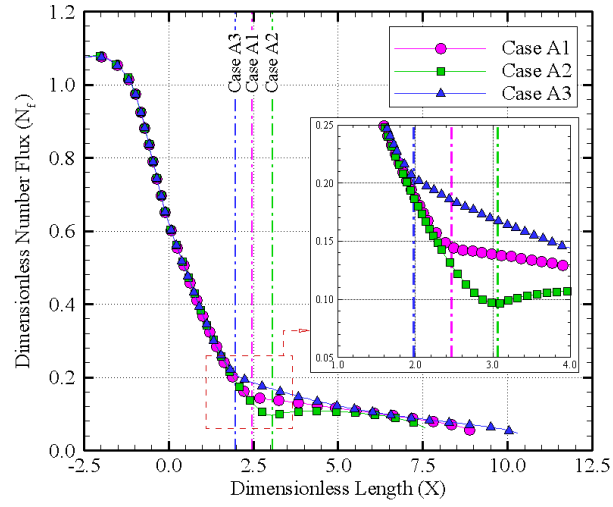


Figure 6.40 - Dimensionless number flux (N_f) distribution along the internal micronozzle surface for group A (top), B (middle) and C (bottom) cases.

6.2.2 Pressure Coefficient

The pressure coefficient is defined by the following equation:

$$C_p = \frac{p_w - p_{in}}{\frac{1}{2} \rho_{in} u_{in}^2} \quad (6.21)$$

In this expression, the pressure p_w on the solid surface is computed by the sum of the normal momentum fluxes of both incident and reflected molecules at each time step as follows:

$$p_w = p_i + p_r = \frac{F_N}{A \Delta t} \sum_{j=1}^N \left\{ \left[(m c_\eta)_j \right]_i + \left[(m c_\eta)_j \right]_r \right\} \quad (6.22)$$

where m is the mass of the molecules, c_η is the normal velocity component of the molecules impinging on the solid surface and N is the total number of simulated molecules that collided on the element of area A over the time interval Δt . In addition, F_N represents the local scaling factor. Subscripts i and r refer to incident and reflected molecules.

Pressure coefficient C_p variations caused by changes on the shape of the divergent surface are displayed in Figure 6.41. According to this set of plots, the pressure coefficient C_p follows the same trend as the dimensionless number flux N_f . As reported previously, the pressure level is reduced because of the expansion process that takes place in the downstream direction. However, centripetal effects impose additional pressure gradients on the surface near the curved surfaces. As a result, these gradients affect the rate at which the pressure coefficient C_p is reduced along the internal surface.

Moreover, abrupt changes on the turning angle presented in group B cases, near the inflection point, results in a drastic drop in the C_p value. In the same sense, a jump in C_p occurs for group C cases after the inflection point due to the flow contraction imposed by the concave surface. By focusing on group A and B cases, somewhere near the half length of the concave surface, the C_p distribution tends to develop the same behavior for the three cases. This is due to the fact that all cases have the same divergent exit angle θ_e at the end of the concave surface. Finally, it can be concluded that no significant changes on the pressure distribution are observed in the present micronozzle flows for the investigated range of α_g and β_g .

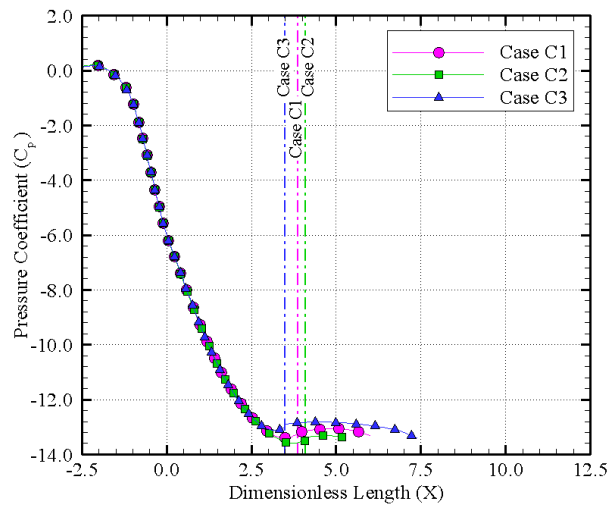
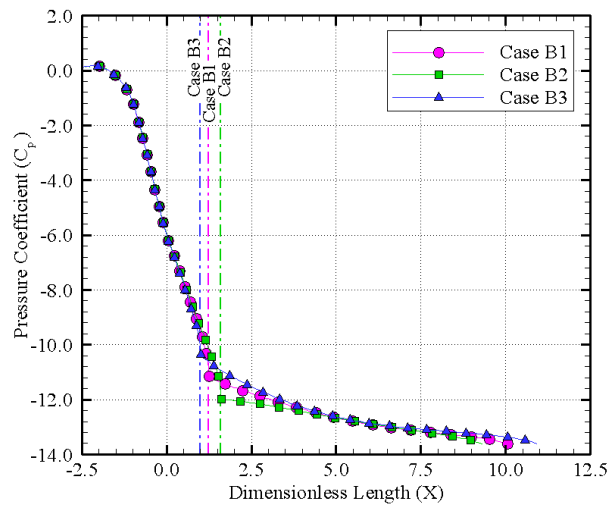
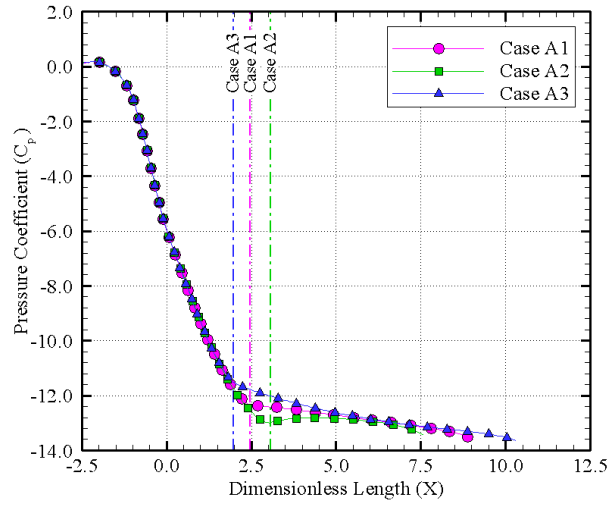


Figure 6.41 - Pressure coefficient (C_p) distribution along the internal micronozzle surface for group A (top), B (middle) and C (bottom) cases.

6.2.3 Skin Friction Coefficient

The skin friction coefficient is defined by the following equation:

$$C_f = \frac{\tau_w}{\frac{1}{2} \rho_{in} u_{in}^2} \quad (6.23)$$

In the microscopic approach, the local shear stress τ_w on the solid surface is calculated by the sum of the tangential momentum fluxes of both incident and reflected molecules at each time step as follows:

$$\tau_w = \tau_i + \tau_r = \frac{F_N}{A \Delta t} \sum_{j=1}^N \left\{ \left[(m c_\xi)_j \right]_i + \left[(m c_\xi)_j \right]_r \right\} \quad (6.24)$$

where c_ξ is the tangential velocity component of the molecules colliding on the solid surface. The remaining variables are defined in the same sense as those presented in the previous subsection.

It proves instructive to mention that, for the limiting case of diffuse reflection employed in this study, the tangential momentum flux of the reflected molecules, on average, should be equal to zero. Under such a circumstance, the net tangential momentum flux at the wall is redefined by:

$$\tau_w = \tau_i = \frac{F_N}{A \Delta t} \sum_{j=1}^N \left\{ \left[(m c_\xi)_j \right]_i \right\} \quad (6.25)$$

The contribution of the skin friction coefficient C_f attributed to changes on the shape of the divergent surface is depicted in Figure 6.42. Data from group A cases shows a rapid increase in skin friction coefficient from the inlet up to the throat vicinity. Downstream of this point, C_f decreases monotonically along the inflection point. Afterwards, centripetal forces associated with concave surface increase its molecule-surface collision rate, causing C_f to decrease slower than it did on the convex surface. At the end of the divergent surface, i.e., near the nozzle lip, C_f experiences a small rise because of the flow acceleration induced by the expansion fan.

In an attempt to clarify the present C_f distribution, one must recall the classical definition of the local shear stress τ_w at the surface:

$$\tau_w = \mu \frac{dc_\xi}{d\eta} \quad (6.26)$$

where c_ξ is the tangential velocity component along the surface and η represents the normal surface direction.

Based on the temperature fields presented in Subsection 6.1.4, it is recognized that the gas temperature matches the surface temperature T_w in practically the entire internal surface. Since $\mu \propto T^\omega$, according to Equation 3.18, it is reasonable to assume that μ is approximately constant along the internal surface. As a result, τ_w is essentially controlled by the velocity gradient $dc_\xi/d\eta$ at the wall. In turn, it is known that the viscous boundary-layer thickness δ increases when the gradient $dc_\xi/d\eta$ decreases and vice-versa.

Using this continuum approach and the fact that δ , in general, decreases for convergent channels and increases for divergent channels (SCHLICHTING, 1968), the present C_f distribution can be explained at least from a qualitative point of view. The velocity gradient $dc_\xi/d\eta$ at the wall increases along the convergent surface and, hence, the body experiences a shear stress rise as depicted in Figure 6.42. As the gas flow reaches the throat vicinity, $dc_\xi/d\eta$ starts dropping in the downstream direction due to a rise in boundary-layer thickness. As a consequence, τ_w decreases along the divergent surface. Finally, as the gas approaches the nozzle lip, flow acceleration increases the skin friction coefficient.

From a microscopic point of view, the present discussion about the viscous boundary-layer thickness δ can be corroborated by computing the component τ_{xy} of the viscous stress tensor τ as follows:

$$\tau_{xy} = \tau_{yx} = -\rho\overline{u'v'} \quad (6.27)$$

The distribution of τ_{xy} normalized by the inlet dynamic pressure p_{din} – defined as $\frac{1}{2}\rho_{in}u_{in}^2$ – is shown in Figures 6.43, 6.44 and 6.45 for group A, B and C cases, respectively. Such a ratio is a measure of shear effects and, hence, indicates a clear pattern of the viscous layer distribution. In general, these results indicate that the viscous boundary-layer thickness δ decreases along the convergent surface and increases considerably along the divergent surface. Such a behavior is in complete agreement with the aforementioned explanation of the skin friction distribution.

Figure 6.42 shows that group B and C cases yield a quite different behavior of C_f near the inflection point. In group B cases the C_f jump at the inflection point is caused by the abrupt increasing of the turning angle from the convex to concave surfaces. In such a circumstance, the sharp corner formed at the inflection point

promotes a flow acceleration in the same sense observed at the nozzle lip. Since the flux of molecules colliding against the surface near the inflection point is larger than the one near the nozzle lip, the acceleration effect developed at the inflection point causes a stronger rise in the skin friction coefficient.

On the other hand, the opposite behavior is observed near the inflection point for group C cases. In these cases, the abrupt reduction of the turning angle from convex to concave surfaces promotes a compression region near the inflection point. Consequently, in the vicinity of this point, the tangential velocity component along the surface is reduced substantially. Due to the high pressure gradients generated, a more intense acceleration process takes place along the concave surface. As a result, the skin friction coefficient rises more rapidly along the concave surface in group C cases.

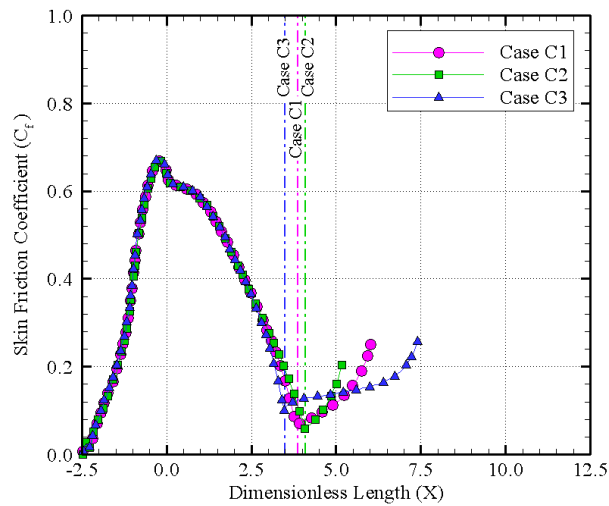
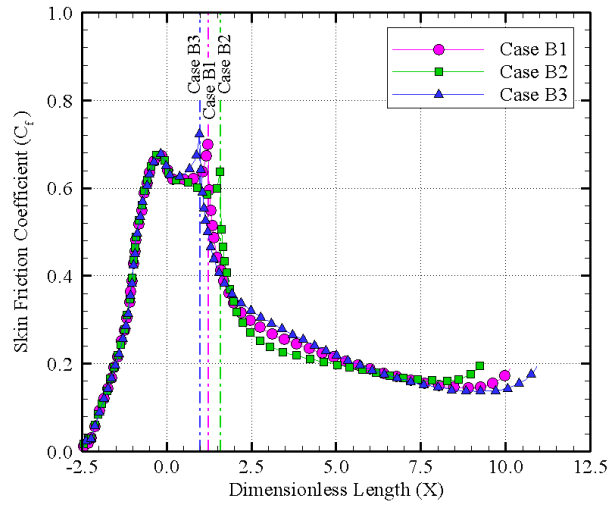
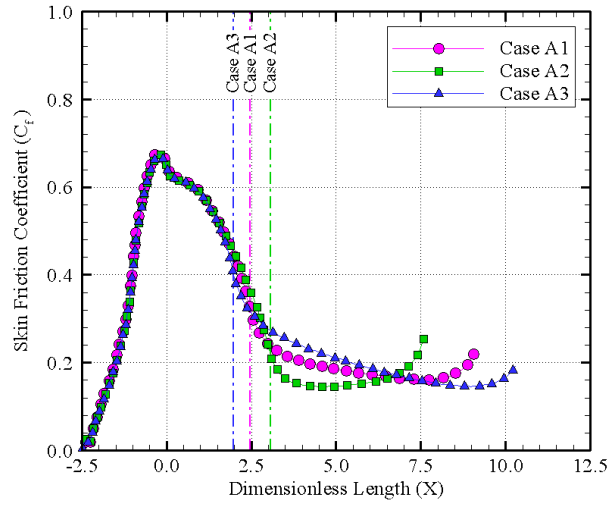


Figure 6.42 - Skin friction coefficient (C_f) distribution along the internal micronozzle surface for group A (top), B (middle) and C (bottom) cases.

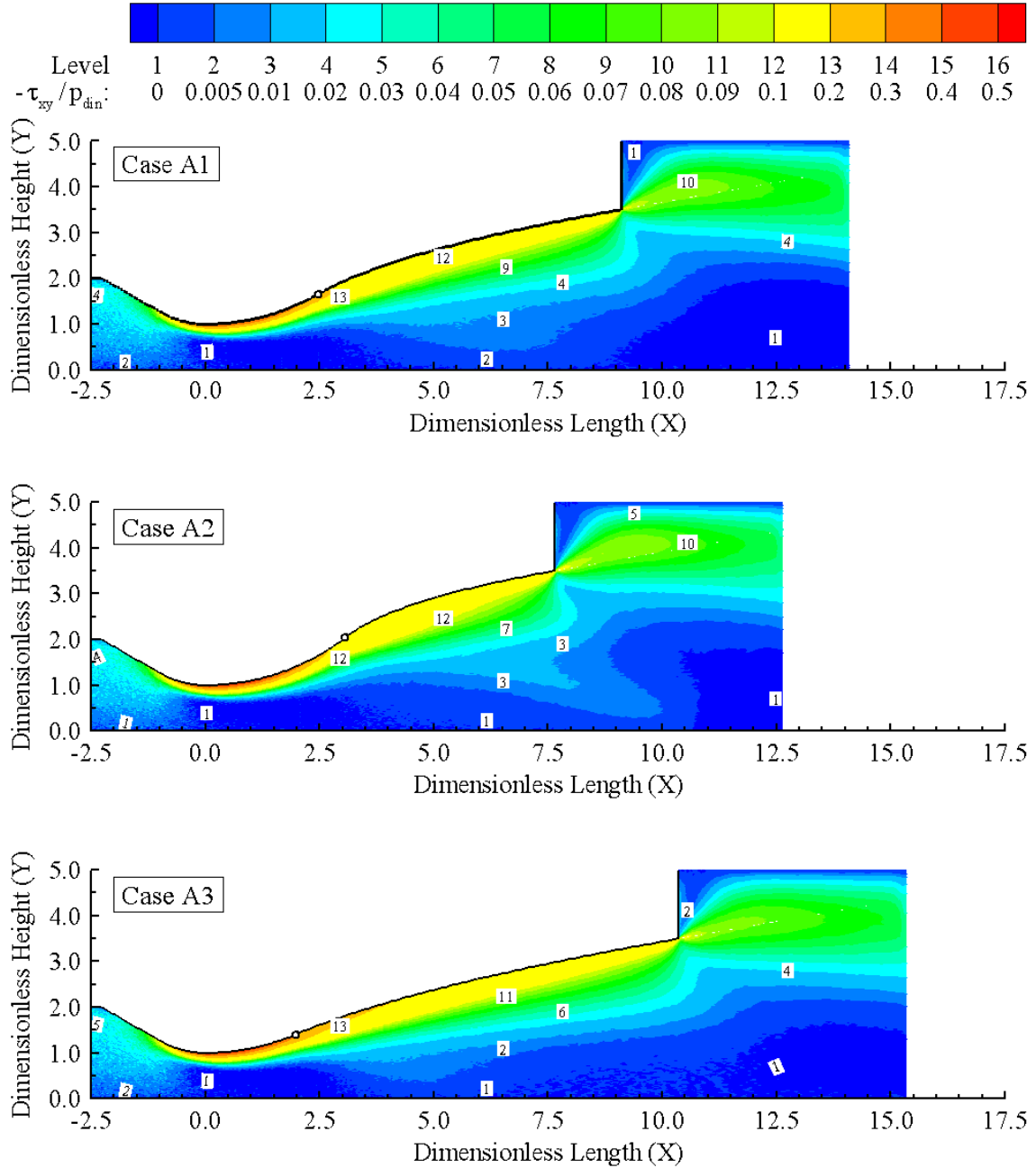


Figure 6.43 - Distribution of the normalized viscous stress tensor component ($-\tau_{xy}/p_{din}$) along the micronozzle for group A cases.

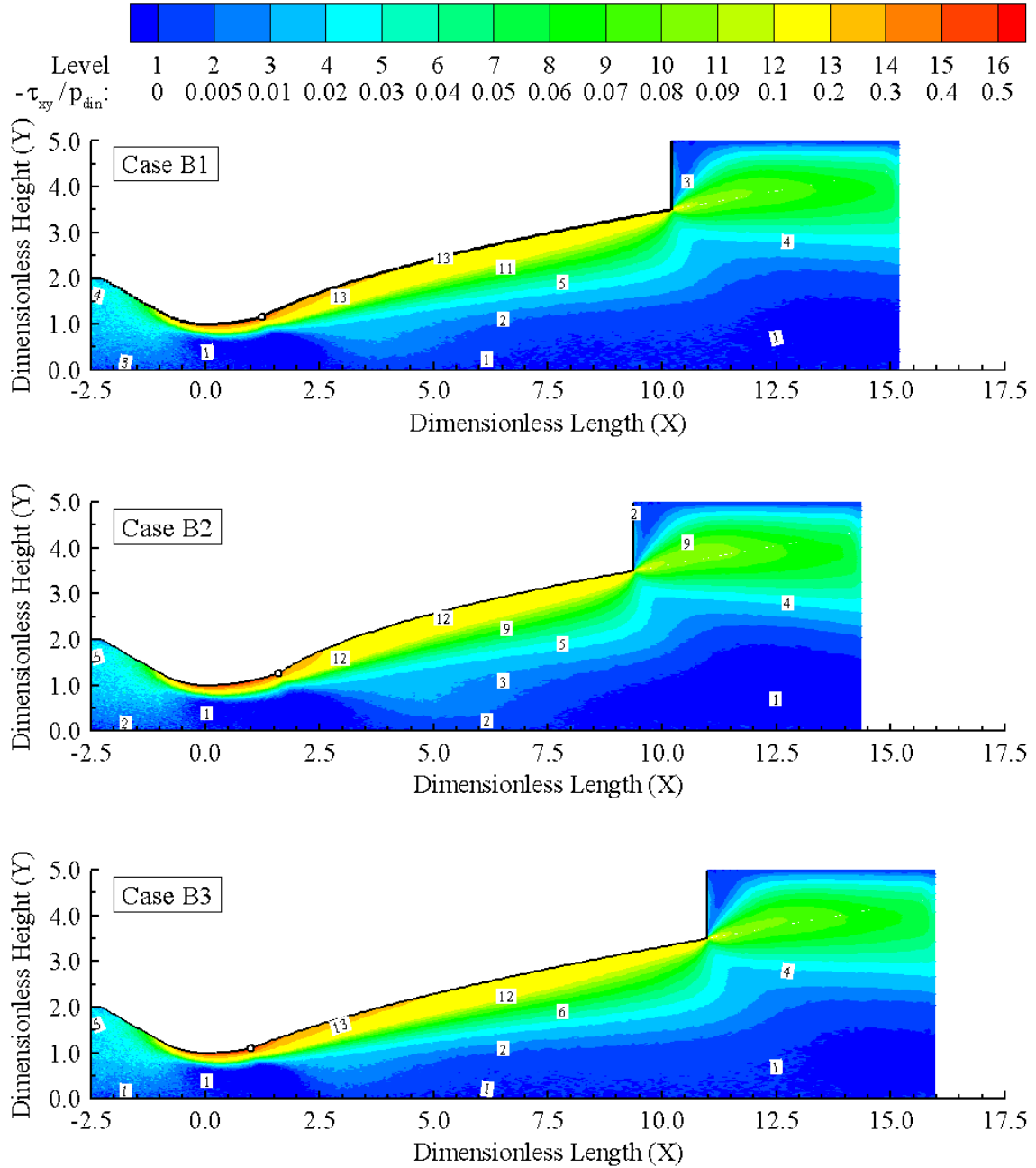


Figure 6.44 - Distribution of the normalized viscous stress tensor component ($-\tau_{xy}/p_{din}$) along the micronozzle for group B cases.

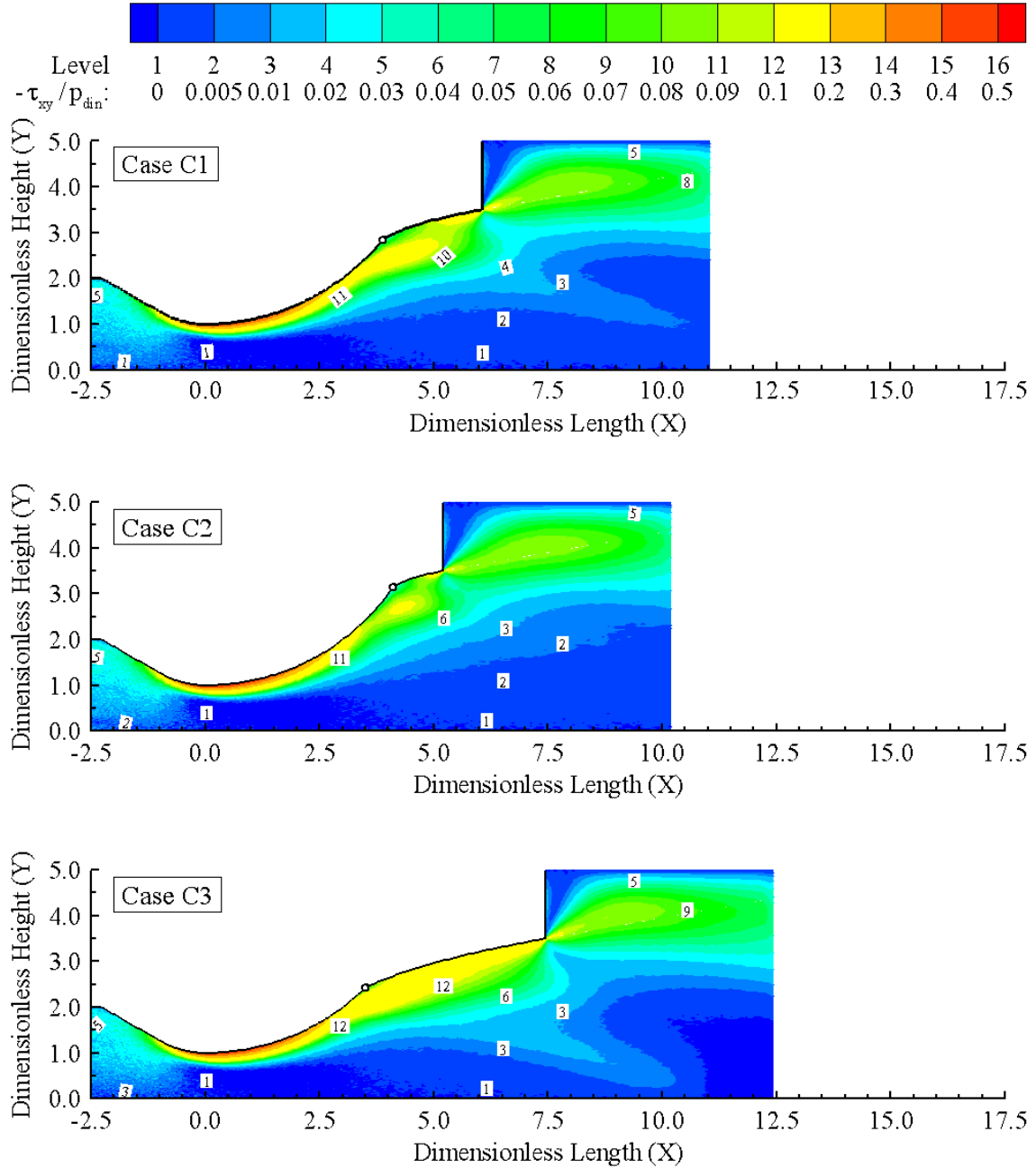


Figure 6.45 - Distribution of the normalized viscous stress tensor component ($-\tau_{xy}/p_{din}$) along the micronozzle for group C cases.

6.2.4 Heat Transfer Coefficient

The heat transfer coefficient is defined by the following equation:

$$C_h = \frac{q_w}{\frac{1}{2} \rho_{in} u_{in}^3} \quad (6.28)$$

The heat flux q_w to the body is calculated by the net energy flux of molecules colliding on the surface. This flux is regarded as positive if it is directed towards the solid surface. In the present account, the net flux q_w is related to the sum of the translational, rotational and vibrational energies of both incident and reflected molecules, defined by:

$$\begin{aligned} q_w &= q_i - q_r \\ &= \frac{F_N}{A \Delta t} \sum_{j=1}^N \left\{ \left[\left(\frac{1}{2} mc^2 + e_R + e_V \right) \right]_{j_i} - \left[\left(\frac{1}{2} mc^2 + e_R + e_V \right) \right]_{j_r} \right\} \end{aligned} \quad (6.29)$$

where e_R and e_V represent the rotational and vibrational energies, respectively, of the molecules colliding on the surface. The remaining variables are defined in the same sense as those presented previously.

Heat transfer coefficient C_h along the internal surface is shown in Figure 6.46 for group A, B and C cases. Group A profiles shows that C_h is slightly positive at the inlet region. Then, it becomes negative as the flow expands along the convergent region. Near the throat, C_h decreases along the surface at a lower rate and then, somewhere upstream of the inflection point, the heat transfer coefficient starts to increase. Finally, in the vicinity of the nozzle lip, the heat transfer from the internal surface increases rapidly. Now, by comparing group A, B and C profiles, a quite different behavior is noted near the inflection point. Such differences are mainly caused by abrupt changes on the turning angle from the convex to the concave surfaces that take place in group B and C cases. On the other hand, no qualitative changes are observed by changing the radius of curvature.

In order to clarify the physical mechanisms responsible by the aforementioned heat transfer distributions, the net heat transfer coefficient C_h defined in Equations 6.28 and 6.29 is expressed in terms of the magnitude of the incident ($|C_h|_i$) and reflected ($|C_h|_r$) parcels. These results are presented only for cases A1, B1 and C1 since for the same geometric group the heat transfer profiles demonstrate similar behavior. In

this connection, as observed in Figure 6.47, the absolute values of the incident and reflected parcels perform a quite similar distribution as that noted in Figure 6.40 for the dimensionless number flux. For the current cases, this indicates a strong relation between the surface heat transfer and the number flux of particles colliding on the surface. In this sense, it is also interesting to point out that near the inflection point C_h follows the number flux distribution. For instance, N_f and C_h drop rapidly at the inflection point for case B1, while for case C1 an opposite behavior is observed. However, a complete understanding of the heat transfer distribution is not clear since $|C_h|_i$ is essentially equal to $|C_h|_r$ along the entire surface.

In this scenario, a further investigation of the heat transfer distribution is carried out by plotting the contribution of each energy mode – translational, rotational and vibrational – to the net heat flux along the surface. Such contributions are depicted in Figure 6.48 for cases A1, B1 and C1. In this set of plots, the subscripts T , R and V stand for the translational, rotational and vibrational contributions, respectively. In this context, it is important to remark that the translational contribution of the heat transfer coefficient is related to the total kinetic energy of the molecules, and not just to the thermal motion since C_h is defined in terms of the molecular speed c . On the other hand, the rotational and vibrational contributions are strictly related to the thermal states of the gas and surface, i.e., they are related to the local temperatures.

According to Figure 6.48, by focusing on case A1, it is observed that C_h is slightly positive at the inlet region due to the translational contribution $(C_h)_T$. This occurs because at the leading edge the inlet flow performs a small, but finite, momentum transfer to the surface. Downstream to this edge, as the viscous effects take place the stream velocity is reduced and then $(C_h)_T$ tends to zero. Nevertheless, as the gas flows along the convergent surface, the gas temperature drops, and $(C_h)_R$ and $(C_h)_V$ also decrease as expected. Somewhere downstream to the throat ($X \approx 1.5$) the temperature difference, $T_w - T_O$, is so large that the heat transfer from the surface becomes more significant than the temperature drop caused by the expansion process. As a result, the rotational and vibrational contributions – $(C_h)_R$ and $(C_h)_V$ – increase along the downstream direction. Further the inflection point, centripetal effects change the flux of particles colliding on the surface and consequently the rate that $(C_h)_R$ and $(C_h)_V$ increases also changes. Finally, near the nozzle lip the strong expansion process causes a flow acceleration and a temperature drop. Consequently, $(C_h)_T$, which is related to $c_i^2 - c_r^2$, jumps while $(C_h)_R$ and $(C_h)_V$ drop at

the nozzle lip. Based on the fact that for the present account the expansion regions provide $c_i^2 \gg c_r^2$, it can be approximated that $(C_h)_T \propto c_i^2$. Because of such a dependence the total heat transfer coefficient C_h is strongly influenced by the translational contribution $(C_h)_T$ in regions with drastic velocity changes.

By turning the attention to cases B1 and C1, it is recognized a discontinuous distribution of the heat transfer coefficient along the inflection point, in contrast to case A1. For case B1, due to the abrupt increasing of the turning angle from the convex to the concave surface, a sharp corner is formed at the inflection point. In this circumstance, similar to the nozzle lip, the temperature drops and the flow accelerates as it approaches to the inflection point. As a consequence, $(C_h)_T$ jumps and $(C_h)_R$ and $(C_h)_V$ drop at this sharper corner. Moreover, as shown in Figure 6.40 for case B1, the molecular number flux drops rapidly along the inflection point. Such behavior is responsible for the drastic drop in $(C_h)_T$ from the convex to the concave surfaces as depicted in Figure 6.48 for case B1. Although the high viscous effects that take place along the surface, the accelerated flow is not able to contour the sharp corner completely, and hence the stream flow does not reach the beginning of the concave surface. Therefore, the combination of this effect with the mechanisms mentioned for case A1 yields the complex distribution of the heat transfer coefficient observed in case B1.

The aforementioned discussions can be also applied to explain the jump in C_h observed in case C1. Near the inflection point the compression region caused by the abrupt reduction in the turning angle promotes a flow deceleration as well as an increasing in the number flux towards the end of the convex surface. Again, the mixture of these effects promotes a discontinuous distribution in the heat transfer coefficient.

An important result obtained from the current profiles is the fact that the sharp corner formed at the inflection point for group B cases holds an absolute value of the heat transfer distribution that is about the double of that observed in the other groups.

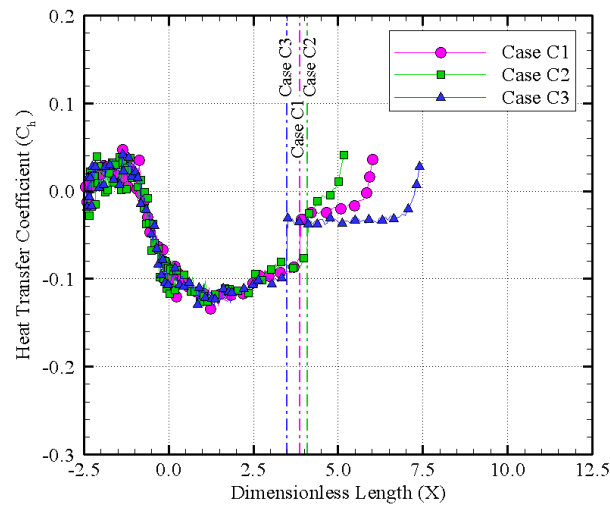
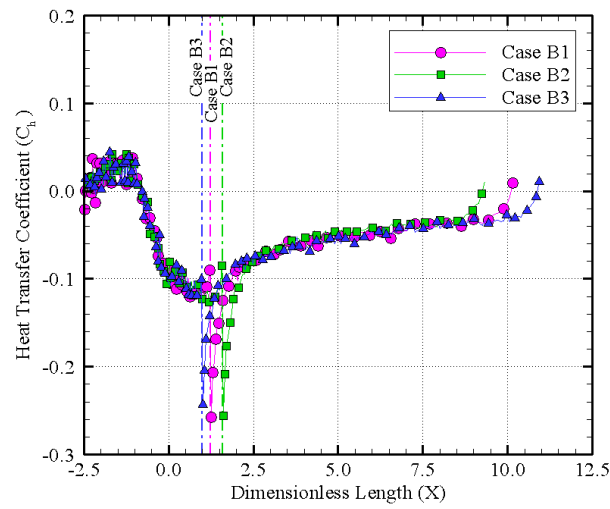
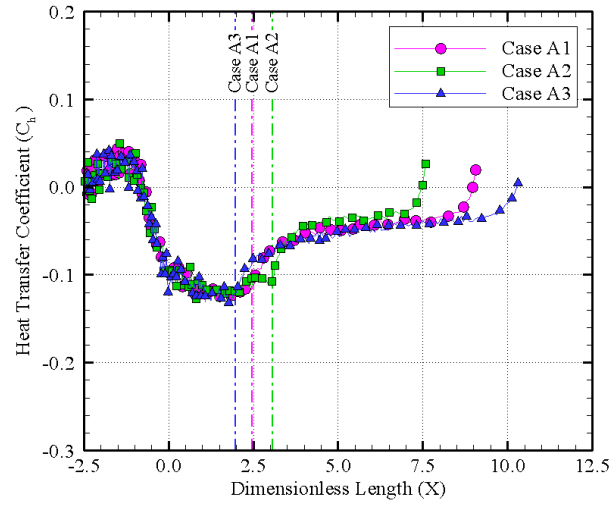


Figure 6.46 - Heat transfer coefficient (C_h) distribution along the internal micronozzle surface for group A (top), B (middle) and C (bottom) cases.

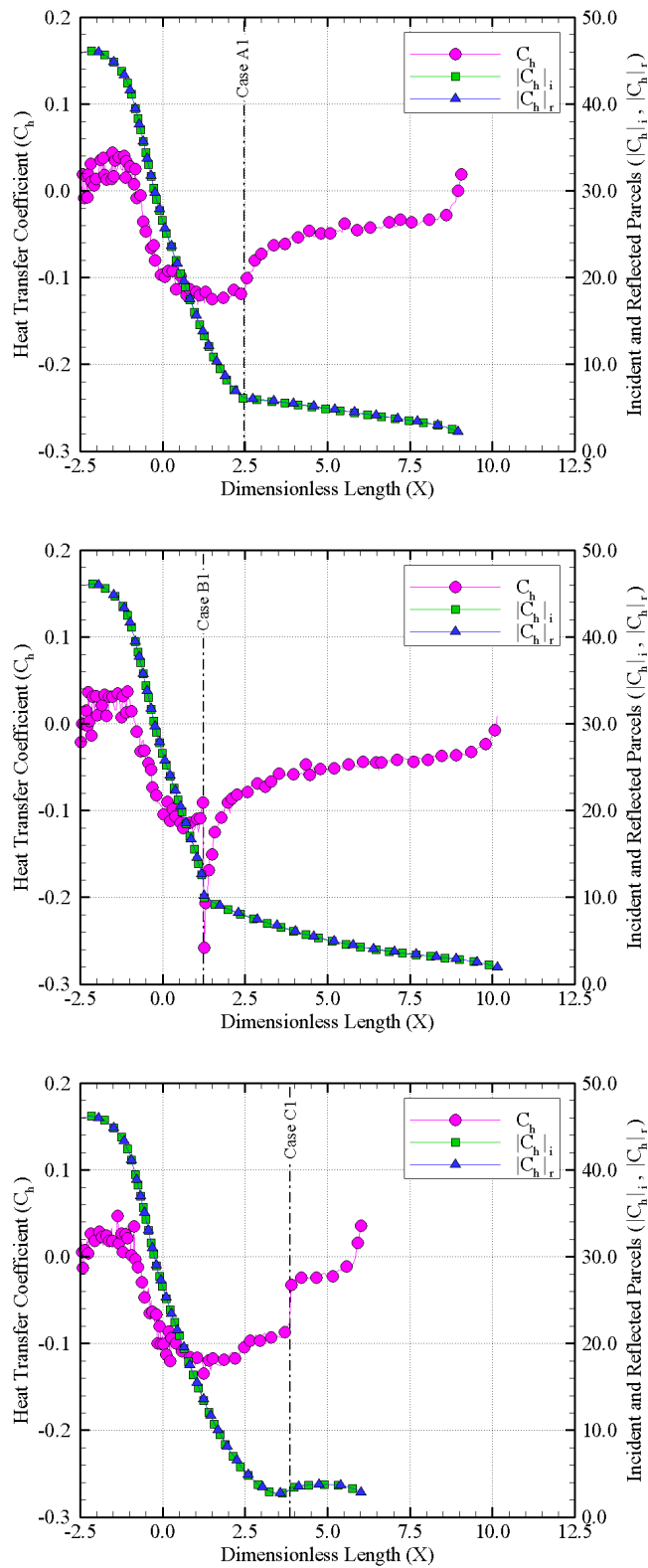


Figure 6.47 - Total, incident and reflected parcels of the heat transfer coefficient (C_h) along the internal micronozzle surface for cases A1 (top), B1 (middle) and C1 (bottom).

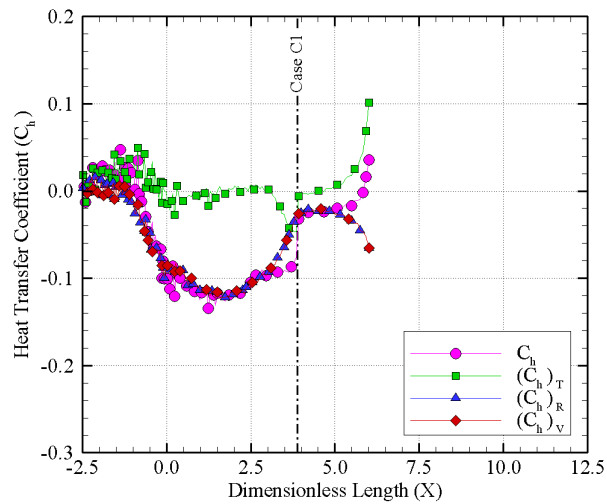
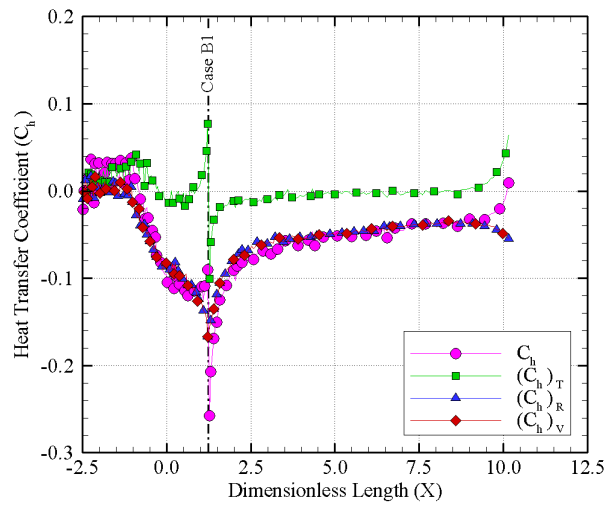
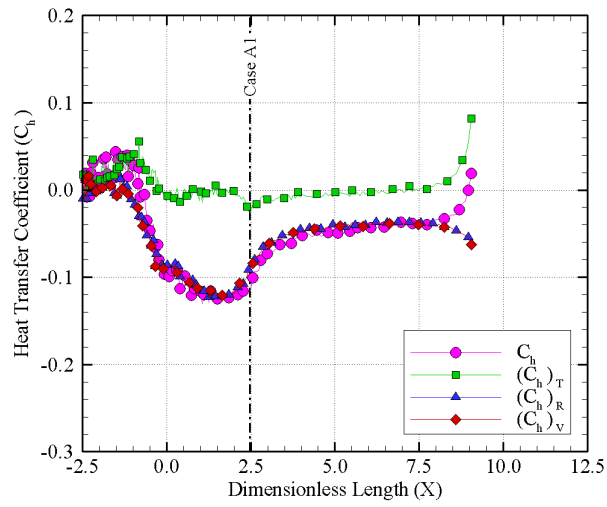


Figure 6.48 - Total, translational, rotational and vibrational contributions of the heat transfer coefficient (C_h) along the internal micronozzle surface for cases A1 (top), B1 (middle) and C1 (bottom).

6.3 Micronozzle Performance

In the previous sections the discussion focused on the physical aspects of the present micronozzle flows as well as how the geometric changes on the divergent surface affected the macroscopic and surface properties. In contrast, this section illustrates the global impact of the current geometric changes on the micronozzle performance. Such an information has primordial importance for engineering applications.

6.3.1 Specific Impulse

The main purpose of micropropulsive systems is to provide sufficient thrust to attain the satellite and mission requirements. The thrust force is composed of two contributions: (i) momentum flux and (ii) pressure thrust (SHAPIRO, 1954). Nevertheless, for the present conditions, the former contribution is at least one order of magnitude greater than the latter one. In this connection, the thrust force F_t is defined according to:

$$F_t = \int \rho u^2 dA \quad (6.30)$$

where ρ and u are the local density and the longitudinal component of the stream velocity as well as $A = A(x)$ stands for the cross-section area at a given x -station.

For practical applications, it is desirable to obtain the maximum level of thrust by means of the minimum propellant consumption, i.e., the minimum mass flow rate \dot{m} through the micronozzle. In this sense, the typical measurement of the nozzle performance is expressed in terms of the specific impulse I_{sp} as follows:

$$I_{sp} = \frac{F_t}{\dot{m}g_0} \quad (6.31)$$

where g_0 is the gravity acceleration.

Figure 6.49 shows the impulse specific I_{sp} normalized by the impulse specific obtained at the throat section I_{sp0} for group A, B and C cases. In this group of plots, X_{Ld} is the length x normalized by the divergent length L_d . In addition, Table 6.1 summarizes the main parameters applied to the calculation of the normalized specific impulse \hat{I}_{sp} , where F_{t_0} stands for the thrust at the throat section. These calculations are based on a micronozzle depth equal to 120 μm that is the same value employed in the validation process (Section 5.5). Moreover, since the present microflows are choked, the following throat values are basically the same for all cases.

Table 6.1 - Common throat section data.

I_{sp0} (s)	F_{t0} (μN)	\dot{m} (kg/s)
28.991	153.163	5.399×10^{-7}

As the flow expands along the divergent region, different effects take place on the specific impulse: (i) density drops; (ii) stream velocity component u increases; (iii) geometric cross-section area A increases, and (iv) viscous layer thickness increases (see Figures 6.43 to 6.45). According to Figure 6.49, the normalized specific impulse \hat{I}_{sp} at the exit section is essentially the same for all cases. For the investigated conditions, these results reveal that even in micronozzles – where surface effects play the main role on the flow structure – the geometric shape of the divergent surface basically does not affect the specific impulse. Such a behavior also indicates that the area ratio h_e/h_t and the divergent exit angle θ_e , kept constant in all cases, may perform the major geometric impact on \hat{I}_{sp} as pointed out in previous studies (BAYT; BREUER, 2001b; KIM, 1994). Notwithstanding, it is important to remark that the thermal and mechanical loads on the divergent surface demonstrated to be affected by the geometric parameters – α_g and β_g – defined in this study. Finally, it can be observed that the presence of the divergent surface provided a specific impulse that is almost two times higher than that one obtained by a micronozzle with only the convergent part operating in the same conditions.

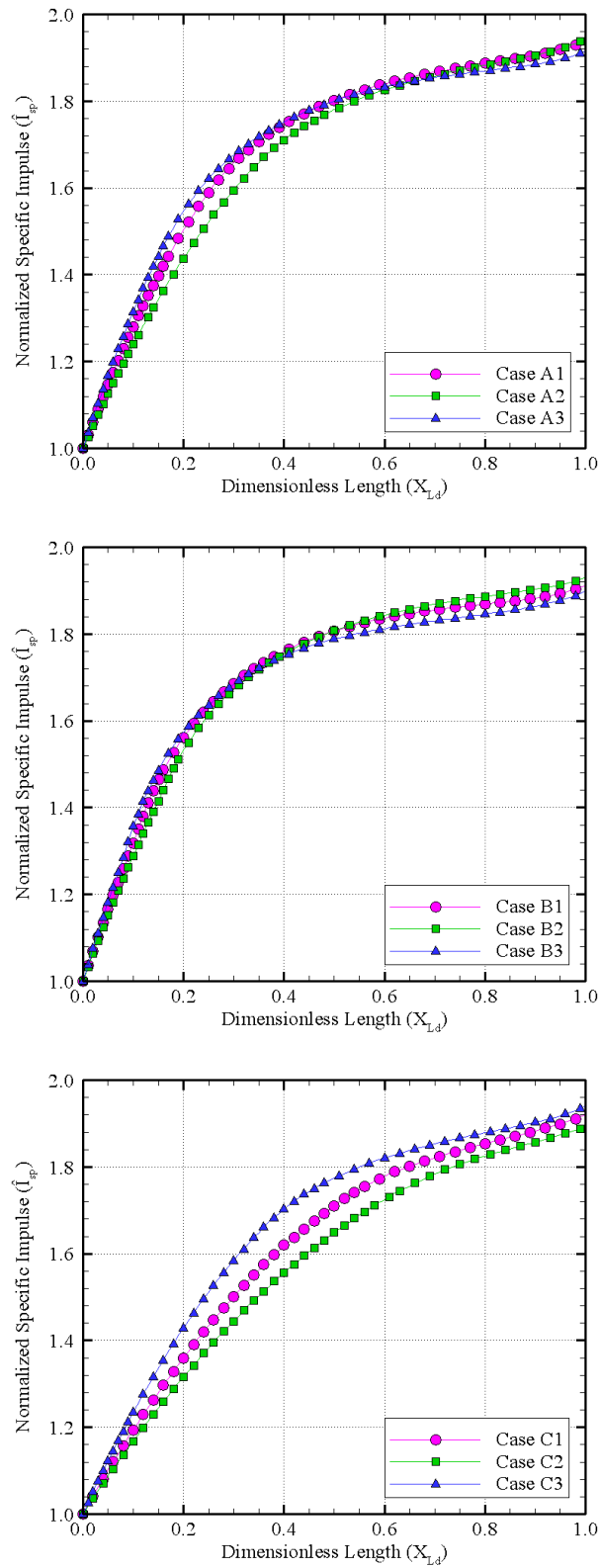


Figure 6.49 - Normalized specific impulse (\hat{I}_{sp}) at different X_{Ld} stations for group A (top), B (middle) and C (bottom) cases.

7 CONCLUSIONS

7.1 Concluding Remarks

In the present account a rarefied gas flow in a convergent-divergent micronozzle array with rectangular cross-section has been investigated by using the Direct Simulation Monte Carlo (DSMC) method. By considering a convex-concave divergent surface, the impact of different divergent shapes on the two-dimensional flowfield structure, aerodynamic surface quantities and micronozzle performance was explored by changing the surface slope and radius of curvature at the inflection point. In order to decouple other geometric influences, the ratio between exit and throat areas as well as the divergent exit angle were kept the same for all cases.

The computational results pointed out a small impact on the primary properties – velocity, density, pressure and temperature – due to variations in the slope and curvature of the divergent surface. These changes in the flowfield structure are mainly assigned to different viscous boundary-layer growth and changes on the magnitude of the internal surface area, which is related to friction and heating processes. Moreover, due to the strong viscous effects present in micronozzle flows, the profiles showed a subsonic condition at the throat section. Near the curved surfaces, centripetal effects promoted different combinations between pressure and temperature gradients. As a result, the subsonic layer was thinner along the convex surface and became thicker along the concave surface. The symmetric assumptions employed in this work resulted in a recirculation region in the external flow. The simulations also showed that thermodynamic nonequilibrium took place in the entire divergent part of the flow. Because of the rapid expansion, the largest rarefaction degree occurred at the nozzle lip. Consequently, in this region the velocity slip, temperature jump and thermal nonequilibrium were more significant.

By concerning to the aerodynamic surface quantities – number flux, pressure, skin friction and heat transfer coefficient – the simulations indicated that the thermal and mechanical loads that take place along the divergent surface are affected by changing the shape of this surface. These coefficients demonstrated to be highly dependent on the smoothness of the surface along the inflection point. For the investigated conditions, a sharp corner at the inflection point yielded a heat transfer to the gas around two times larger than that observed along a continuous surface slope. Conversely, the present aerodynamic coefficients showed only a small sensitivity to

the curvature of the divergent surface.

This study also revealed that even in micronozzles – where surface effects play the main role on the flow structure – the geometric shape of the divergent surface does not perform significant influence on the specific impulse. Anyway, the presence of the divergent surface provided a specific impulse that is almost two times higher than that one obtained by a micronozzle with only the convergent part operating in the same conditions.

7.2 Future Work

In the present dissertation an initial investigation of a micronozzle flow was carried out for different geometric conditions. As mentioned, the main focus was to measure the impact of the shape of the divergent surface on the physical and performance aspects. The major challenges overcome in this research are listed as following: (i) the present DSMC algorithm described an internal flow that covered continuum to transitional flow regimes, (ii) the implementation of boundary conditions expressed in terms of pre-defined pressure values, (iii) a reasonable spatial resolution was obtained at the nozzle lip in the sense that the sonic line merges very near this corner, and (iv) the algorithm was partially rewritten in a parallel architecture in order to improve the computational performance.

In despite of this study has taken into account representative physical assumptions and boundary conditions, a significant number of physical and numerical improvements should also be implemented in future investigations. Among others, it is worthwhile to point out the following extensions:

- 1) The implementation of chemical reaction models, e.g., dissociation and recombination, in order to account high temperature gas flows along the micronozzle.
- 2) The application of gas-surface interaction models that concern with incomplete accommodation. It proves to be more realistic for materials applied to microfabrication.
- 3) Since in microflows the surface effects are predominant, investigations of the surface temperature effect may reveal important features on the flow structure and surface quantities.

- 4) In array patterns, effects of different pitch distances between the micronozzles and different back pressures can also be investigated since these parameters may change drastically the flow behavior.
- 5) The implementation of axisymmetric and three-dimensional versions of the present DSMC algorithm.
- 6) The implementation of a massive and hybrid (OpenMP and MPI) parallel version of the present DSMC algorithm.

Such improvements and additional investigations can provide further insight into the nature of micronozzle gas flows as well as a high computational performance and versatility.

REFERENCES

ABE, T. Generalized scheme of the no-time-counter scheme for the DSMC in rarefied gas flow analysis. **Computers & Fluids**, v. 22, n. 2–3, p. 253–257, 1993. 35

AGARWAL, R. K. Lattice Boltzmann simulations of slip flow in microchannels. In: GAD-EL-HAK, M. (Ed.). **MEMS: introduction and fundamentals**. 2. ed. Boca Raton, FL: Taylor & Francis Group, 2006. chapter 9, p. 9.1–9.10. ISBN 0-8493-9137-7. 23

AGARWAL, R. K.; YUN, K. Y. Burnett simulations of flows in microdevices. In: GAD-EL-HAK, M. (Ed.). **MEMS: introduction and fundamentals**. 2. ed. Boca Raton, FL: Taylor & Francis Group, 2006. chapter 8, p. 8.1–8.35. ISBN 0-8493-9137-7. 27

ALDER, B. J.; WAINWRIGHT, T. E. Studies in molecular dynamics. **Journal of Chemical Physics**, v. 27, p. 1208–1209, 1957. 23

_____. Molecular dynamics by electronic computers. In: PRIGOGINE, I. (Ed.). **Transport processes in statistical mechanics**. New York: Interscience Publishers, Inc., 1958. p. 97–131. 23

ALEXANDER, F. J.; GARCIA, A. L.; ALDER, B. J. Cell size dependence of transport coefficient in stochastic particle algorithm. **Physics of Fluids**, v. 10, n. 6, p. 1540–1542, 1998. 82

_____. Erratum: Cell size dependence of transport coefficient in stochastic particle algorithm. **Physics of Fluids**, v. 12, n. 3, p. 731–731, 2000. 82

ALEXEENKO, A. A.; FEDOSOV, D. A.; GIMELSHEINAND, S. F.; LEVIN, D. A.; COLLINS, R. J. Transient heat transfer and gas flow in a MEMS-based thruster. **Journal of Micromechanical and Microengineering**, v. 15, p. 2069–2073, 2005. 10, 71

ALEXEENKO, A. A.; GIMENLSHEIN, S. F.; LEVIN, D. A.; COLLINS, R. J. Numerical modeling of axisymmetric and three-dimensional flows in MEMS nozzles. **AIAA Journal**, v. 40, n. 5, p. 897–904, 2002a. 10, 12, 76, 77

ALEXEENKO, A. A.; LEVIN, D. A.; GIMELSHEIN, S. F.; COLLINS, R. J.; MARKELOV, G. N. Numerical simulation of high-temperature gas flows in a millimeter-scale thruster. **Journal of Thermophysics and Heat Transfer**, v. 16, p. 10–16, 2002b. 10

ALEXEENKO, A. A.; LEVIN, D. A.; GIMELSHEIN, S. F.; COLLINS, R. J.; REED, B. D. Numerical study of flow structure and thrust performance for 3-D MEMS-based nozzles. In: AIAA FLUID DYNAMICS CONFERENCE AND EXHIBIT, 32., 2002, St. Louis. **Proceedings...** St. Louis, MO: AIAA Paper 2002–3194, 2002c. 10

ANDERSON, J. D. **Modern compressible flow with historical perspective**. 2. ed. New York: McGraw-Hill Inc, 1990. ISBN 0-07-100665-6. 59, 95

ARKILIC, E. B. **Measurement of the mass flow and tangential momentum accommodation coefficient in silicon micromachined channels**. PhD Thesis (PhD) — Massachusetts Institute of Technology, Cambridge, MA, 1997. 64

BACK, L. H.; MASSIER, P. F.; GIER, H. L. Comparison of measured and predicted flows through conical supersonic nozzles, with emphasis on the transonic region. **AIAA Journal**, v. 3, n. 9, p. 1606–1614, 1965. 11

BAGANOFF, D.; MCDONALD, J. D. A collision-selection rule for a particle simulation method suited to vector computers. **Physics of Fluids A**, v. 2, n. 7, p. 1248–1259, 1990. 51

BALAKRISHNAN, R.; AGARWAL, R. K. Entropy consistent formulation and numerical simulation of the BGK-Burnett equations for hypersonic flows in the continuum-transition regime. In: INTERNATIONAL CONFERENCE ON NUMERICAL METHODS IN FLUID DYNAMICS, 15., 1996, Monterey. **Proceedings...** Monterey, CA: AIAA Paper 2001–3331, 1996. 23

BAYT, R. L. **Analysis, fabrication and testing of a MEMS-based micropropulsion system**. 1999. 162 p. PhD Thesis (PhD) — Massachusetts Institute of Technology (MIT), Cambridge, MA, 1999. Available from: http://acdl.mit.edu/Technical_Reports/Bayt_Thesis.pdf. Access in: 16 mar. 2010. 4, 5

BAYT, R. L.; AYON, A. A.; BREUER, K. S. A performance evaluation of MEMS-based micronozzles. In: AIAA/ASME/SAE/ASEE JOINT PROPULSION

CONFERENCE AND EXHIBIT, 33., 1997, Seattle. **Proceedings...** Seattle, WA: AIAA Paper 1997-3169, 1997. Available from: <http://microfluidics.engin.brown.edu/Breuer_Papers/Conferences/AIAA97-3169_MicroNozzles.pdf>. Access in: 16 mar. 2010. 10

BAYT, R. L.; BREUER, K. S. Viscous effects in supersonic MEMS-fabricated micronozzles. In: ASME MICROFLUIDS SYMPOSIUM, 3., 1998, Anaheim. **Proceedings...** Anaheim, CA, 1998. 71

_____. Analysis and testing of a silicon intrinsic-point heater in a micropropulsion application. **Sensors and Actuators A**, v. 91, p. 249-255, 2001a. 10, 11

_____. Systems design and performance of hot and cold supersonic microjets. In: AIAA AEROSPACE SCIENCES MEETING AND EXHIBIT, 39., 2001, Seattle. **Proceedings...** Reno, NV: AIAA Paper 2001-0721, 2001b. Available from: <http://microfluids.engin.brown.edu/Breuer_Papers/Conferences/AIAA01_0721_HotColdMicrojects.pdf>. Access in: 16 mar. 2010. 10, 11, 76, 77, 178

BEEBY, S.; ENSELL, G.; KRAFT, M.; WHITE, N. **MEMS mechanical sensors**. Norwood, MA: Artech House Inc., 2004. ISBN 1-58053-536-4. 5

BERGEMANN, F. A detailed surface chemistry model for the DSMC model. In: HARVEY, J.; LORD, G. (Ed.). **Rarefied gas dynamics**: 19th international symposium. Oxford: Oxford University Press, 1995. v. 2, p. 947-953. 35

BERGEMANN, F.; BOYD, I. D. DSMC simulation of inelastic collisions using the Borgnakke-Larsen method extended to discrete distributions of vibrational energy. In: INTERNATIONAL SYMPOSIUM ON RAREFIED GAS DYNAMICS, 12., 1980, Vancouver. **Proceedings...** Vancouver, Canada, 1992. 52

BESKOK, A. Molecular-based microfluidic simulations models. In: GAD-EL-HAK, M. (Ed.). **MEMS**: introduction and fundamentals. 2. ed. Boca Raton, Fl: Taylor & Francis Group, 2006. chapter 6, p. 6.1-6.27. ISBN 0-8493-9137-7. 8

BIRD, G. A. Approach to translational equilibrium in a rigid sphere gas. **Physics of Fluids**, v. 6, n. 5, p. 1518-1519, 1963. 29

_____. Shock wave structure in a rigid sphere gas. In: de Leeuw, J. H. (Ed.). **Rarefied gas dynamics**. New York: Academic Press, 1965. v. 1, p. 216-222. 29

- _____. Breakdown of translational and rotational equilibrium in gaseous expansions. **AIAA Journal**, v. 8, n. 11, p. 1998–2003, 1970. 20
- _____. **Molecular gas dynamics**. Oxford: Clarendon Press, 1976. 27, 29, 35, 50, 82
- _____. Monte Carlo simulation of gas flows. **Annual Review of Fluid Mechanics**, v. 10, p. 11–31, 1978. 29
- _____. Breakdown of continuum flow in freejets and rocket plumes. In: INTERNATIONAL SYMPOSIUM ON RAREFIED GAS DYNAMICS, 12., 1980, Charlottesville. **Proceedings...** Charlottesville, VA, 1980. 20
- _____. Monte-Carlo simulation in an engineering context. In: FISHER, S. S. (Ed.). **Rarefied gas dynamics: 12nd international symposium**. New York, NY: American Inst. of Physics, 1981. v. 74, p. 239–255. 46, 74
- _____. Definition of mean free path for real gases. **Physics of Fluids**, v. 26, n. 11, p. 3222–3223, 1983. 48, 74
- _____. Direct simulation of high-vorticity gas flows. **Physics of Fluids**, v. 30, n. 2, p. 364–366, 1987. 32
- _____. Perception of numerical method in rarefield gas dynamics. In: MUNTZ, E. P.; WEAVER, D. P.; CAPBELL, D. H. (Ed.). **Rarefied gas dynamics: theoretical and computational techniques**. 1. ed. Washington, DC: AIAA, 1989. v. 118, p. 374–395. 35, 51, 74
- _____. Application of the DSMC method to the full Shuttle geometry. **AIAA Paper 90–1692**, 1990. 29, 80
- _____. **Molecular gas dynamics and the direct simulation of gas flows**. New York: Oxford University Press Inc., 1994. 484 p. ISBN 0198561954. 27, 29, 33, 42, 47, 48, 50, 52, 54, 64, 74, 136, 137
- _____. Monte Carlo simulation of gas flows. **Comput. Math. Appl.**, v. 35, n. 1/2, p. 1–14, 1998. 29
- _____. Forty years of DSMC, and now? In: BARTEL, T. J. (Ed.). **Rarefied gas dynamics: 22nd international symposium**. Melville, NY: American Inst. of Physics, 2001. p. 372–380. 29

- _____. A criterion for breakdown of vibrational equilibrium in expansions. **Physics of Fluids**, v. 14, n. 5, p. 1372–1735, 2002. 20
- _____. The DS2V/3V program suite for DSMC calculations. In: CAPITELLI, M. (Ed.). **Rarefied gas dynamics: 24nd international symposium**. Melville, NY: American Inst. of Physics, 2005. p. 541–546. 32
- _____. **The DS2G program user's guide (version 3.8)**. 2006. Sydney, Australia, G.A.B. Consulting Pty Ltd. Available from: <<http://www.gab.com.au/ds2vman.pdf>>. 82
- BORGNAKKE, C.; LARSEN, P. Statistical collision model for Monte Carlo simulation of polyatomic gas mixture. **Journal of Computational Physics**, v. 18, p. 405–420, 1975. 52, 74
- BOYD, I. D. Direct simulation of rotation and vibration nonequilibrium. **AIAA Paper 89–1880**, 1989. 52, 53
- _____. Analysis of rotational nonequilibrium in standing shock waves of nitrogen. **AIAA Journal**, v. 28, n. 11, p. 1997–1999, 1990. 53
- _____. Monte Carlo study of vibrational relaxation process. In: BEYLICH, A. E. (Ed.). **Proceedings...** Aachen, Germany, 1990. p. 792–799. 53
- _____. Rotational and vibrational nonequilibrium effects in rarefied hypersonic flow. **Journal of Thermophysics and Heat Transfer**, v. 4, n. 4, p. 478–484, 1990. 53
- _____. Analysis of vibrational-translational energy transfer using the direct simulation Monte Carlo method. **Physics of Fluids A**, v. 3, n. 7, p. 1785–1791, 1991. 53
- _____. Monte Carlo simulation of nonequilibrium flow in low power hydrogen arcjets. **Physics of Fluids**, v. 9, p. 3086–3095, 1995. 20
- _____. Predicting breakdown of the continuum equations under rarefied flow condition. In: INTERNATIONAL SYMPOSIUM ON RAREFIED GAS DYNAMICS, 23., 2002, Whistler. **Proceedings...** Whistler, Canada, 2002. 20, 150
- BOYD, I. D.; CHEN, G.; CANDLER, G. V. Predicting failure of the continuum fluid equations in transitional hypersonic flows. **Physics of Fluids**, v. 7, p. 210–219, 1995. 52

Brazilian Space Agency. **National program of space activities (PNAE) 2005-2014**. 2005. Available from:

<http://www.aeb.gov.br/download/PDF/PNAE_INGLES.pdf>. Access in: September 12, 2010. 1

BROADWELL, J. E. Study of rarefied flow by the discrete velocity method. **Journal of Fluid Mechanics**, v. 19, p. 401–141, 1964. 27

BUONI, M.; DIETZ, D.; ASLAM, K.; SUBRAMANIAM, V. V. Simulation of compressible gas flow in a micronozzle: effects of wall on shock structure. In: AIAA THERMOPHYSICS CONFERENCE, 35., 2001, Anaheim. **Proceedings...** Anaheim, CA: AIAA Paper 2001–3169, 2001. Available from: <http://www.cs.ucsb.edu/~buoni/papers/AIAA_paper.pdf>. Access in: 16 mar. 2010. 10

BURNETT, D. The distribution of velocities and mean motion in a slightly non-uniform gas. **Proceedings of the London Mathematical Society**, v. 39, p. 385–430, 1935. 22

CARLSON, A. B.; BIRD, G. A. Implementation of a vibrationally linked chemical reaction model for DSMC. In: HARVEY, J.; LORD, G. (Ed.). **Rarefied gas dynamics**: 19th international symposium. Oxford: Oxford University Press, 1995. v. 1, p. 434. 52

CERCIGNANI, C.; LAMPIS, M. Kinetic models for gas-surface interactions. **Transport Theory and Statistical Physics**, v. 1, n. 2, p. 101–114, 1971. 63

CHAPMAN, S.; COWLING, T. G. **The mathematical theory of non-uniform gases**. 3. ed. Cambridge: Cambridge University Press, 1970. ISBN 0198561954. 23

CHEN, K.; WINTER, M.; HUANG, R. F. Supersonic flow in miniature nozzle of planar configuration. **Journal of Micromechanical and Microengineering**, v. 15, p. 1736–1744, 2005. 10

CHEN, S.; DOOLEN, G. D. Lattice Boltzmann method for fluid flows. **Annual Review of Fluid Mechanics**, v. 30, p. 329–364, 1998. 27

CHEN, X. Q. Efficient particle tracking algorithm for two-phase flows in geometries using curvilinear coordinates. **Numerical Heat Transfer, Part A**, v. 31, p. 337–405, 1997. 33

CHENG, H. K. Perspective on hypersonic viscous flow research. **Annual Review of Fluid Mechanics**, v. 25, p. 455–484, 1993. 29

CHENG, H. K.; EMMANUEL, G. Perspective on hypersonic nonequilibrium flow. **AIAA Journal**, v. 33, p. 385–400, 1995. 29

CHOUDHURI, A. R.; BAIRD, B.; GOLLAHALLI, S. R.; SCHNEIDER, S. J. Effects of geometry and ambient pressure on micronozzle flow. In: AIAA/ASME/SAE/ASEE JOINT PROPULSION CONFERENCE AND EXHIBIT, 37., 2001, Salt Lake City. **Proceedings...** Salt Lake City, UT: AIAA Paper 2001–3331, 2001. 10

COMEAX, K. A.; CHAPMAN, D. R.; MACCORMACK, R. W. An analysis of the Burnett equations based on the Second Law of Thermodynamics. **AIAA Paper 95–0415**, 1995. 23

CURIEL, A. S. **Satellite classification - small satellites home page (SSHP)**. 2004. Available from: http://centaur.sstl.co.uk/SSHP/sshp_classify.html. Access in: September 12, 2010. 1

CYBYK, B. Z.; ORAN, E. S.; ANDERSON, J. D. Combining monotonic lagrangian grid with a directed simulation Monte Carlo. **Journal of Computational Physics**, v. 122, p. 323–334, 1995. 33

DIETRICH, S. Efficient computation of particle movement in 3-D DSMC calculations on structured body-fitted grids. In: INTERNATIONAL SYMPOSIUM ON RAREFIED GAS DYNAMICS, 17., 1990, Aachen. **Proceedings...** Aachen, Germany, 1990. p. 745. 33

DIETRICH, S.; BOYD, I. D. Scalar and parallel optimized implementation of the direct simulation Monte Carlo method. **Journal of Computational Physics**, v. 126, p. 328–342, 1996. 32

EPSTEIN, A. H.; SENTURIA, S. D.; AL-MIDANI, O.; ANATHASURESH, G.; AYON, A.; BREUER, K.; CHEN, K.-S.; ESTEVE, F. E. E. E.; FRECHETTE, L.; GAUBA, G.; GHODSSI, R.; GROSHENRY, C.; JACOBSON, S.; KERREBROCK, J. L.; LANG, J. H.; LIN, C.-C.; LONDON, A.; LOPATA, J.; MEHRA, A.; MIRANDA, J. O. M.; NAGLE, S.; ORR, D. J.; PIEKOS, E.; SCHMIDT, M. A.; SHIRLEY, G.; SPEARING, S. M.; TAN, C. S.; TZENG, Y.-S.;

WAITZ, I. A. Micro-heat engines, gas turbines, and rockets engines - the MIT microengine project. In: AIAA FLUID DYNAMICS CONFERENCE, 28., 1997, Snowmass. **Proceedings...** Snowmass, CO: AIAA Paper 1997-1773, 1997.

Available from: <http://microfluids.engin.brown.edu/Breuer_Papers/Conferences/AIAA97-1773_Microengine.pdf>. Access in: 16 mar. 2010. 5, 11

FALLAVOLLITA, M. A.; BAGANOFF, D.; MCDONALD, J. D. Reduction of simulation cost and error for particle simulations of rarefied flows. **Journal of Computational Physics**, v. 109, p. 30-36, 1993. 82

FAN, J. A generalized soft-sphere model for Monte Carlo simulation. **Physics of Fluids**, v. 14, n. 12, p. 4399-4405, 2002. 49

FAN, J.; SHEN, C. A new algorithm in DSMC method - the randomly sampled frequency method. In: **The theory, methods and applications of CFD**. Beijing, China: Science Press, 1992. p. 127. 35

FISCKO, K. A.; CHAPMAN, D. R. Comparison of Burnett, Super-Burnett and Monte Carlo solutions for hypersonic shock structure. In: INTERNATIONAL SYMPOSIUM ON RAREFIED GAS DYNAMICS, 16., 1988, Pasadena. **Proceedings...** Pasadena, CA, 1988. 23

FROST, R. C.; LIEPMAN, H. P. Supersonic nozzles with continuous wall curvature. **Journal of the Aeronautical Sciences**, v. 19, n. 10, p. 716-716, 1952. 13

GAD-EL-HAK, M. The fluid mechanics of microdevices - the freeman scholar lecture. **Journal of Fluids Engineering**, v. 121, p. 5-33, 1999. 10

Gad-el-Hak, M. Flow physics. In: GAD-EL-HAK, M. (Ed.). **MEMS: introduction and fundamentals**. 2. ed. Boca Raton, Fl: Taylor & Francis Group, 2006. chapter 4, p. 4.1-4.36. ISBN 0-8493-9137-7. 21

_____. Introduction. In: GAD-EL-HAK, M. (Ed.). **MEMS: introduction and fundamentals**. 2. ed. Boca Raton, Fl: Taylor & Francis Group, 2006. chapter 1, p. 1.1-1.5. ISBN 0-8493-9137-7. 17

GARCIA, A. L.; WAGNER, W. Time step truncation error in direct simulation Monte Carlo. **Physics of Fluids**, v. 12, n. 10, p. 2621-2633, 2000. 82

- GATINOL, R. Théorie cinétique d'un gaz à répartition discrète de vitesses. **Z. Fluqwissenschaften**, v. 18, p. 93–97, 1970. 27
- GEORGE, J. D.; BOYD, I. D. Simulation of nozzle plume flows using a combined CFD-DSMC approach. **AIAA Paper 99–3454**, 1999. 20
- HADJICONSTANTINO, N. G. Analysis of discretization in the direct simulation Monte Carlo. **Physics of Fluids**, v. 12, n. 10, p. 2634–2638, 2000. 82
- HAMMERSLEY, J. M.; HANDSCOMB, D. C. **Monte Carlo methods**. New York: John Wiley and Sons Inc., 1964. 29
- HAO, P. F.; DING, Y. T.; YAO, Z. H.; HE, F.; ZHU, K. Q. Size effect on gas flow in micro nozzles. **Journal of Microelectromechanical Systems**, v. 15, p. 181–194, 2005. 10, 71, 76, 77, 93, 98
- HARVEY, J. K. Direct simulation Monte Carlo method and comparison with experiment. In: MOSS, J. N.; SCOTT, C. D. (Ed.). **Rarefied gas dynamics: thermophysical aspect of re-entry flows**. 1. ed. Washington, DC: AIAA, 1986. v. 103, p. 25–43. 29
- HARVEY, J. K.; GALLIS, M. A. Review of code validation studies in high-speed low-density flows. **Journal of Spacecraft and Rockets**, v. 37, n. 1, p. 8–20, 2000. 29
- _____. A review of a validation exercise on the use of the DSMC to compute viscous/inviscid interactions in hypersonic flow. **AIAA Paper 03–3643**, 2003. 29
- HASH, D. B.; HASSAN, H. A. Direct simulation with vibrational-dissociation coupling. **AIAA Paper 92–2875**, 1992. 53
- HASH, D. B.; MOSS, J. N.; HASSAN, H. A. Direct simulation of diatomic gases using the generalized hard sphere model. **Journal of Thermophysics and Heat Transfer**, v. 8, n. 4, p. 758–764, 1994. 49
- HASSAN, H. A.; HASH, D. B. A generalized hard-sphere model for Monte Carlo simulation. **Physics of Fluids A**, v. 5, n. 3, p. 738–744, 1993. 49
- HAVILAND, J. K. The solution of two molecular flow problems by the Monte Carlo method. In: ALDER, B.; FERNBECK, S.; ROTENBERG, M. (Ed.). **Methods in computational physics**. New York: Academic Press, 1965. v. 4, p. 109–209. 27

- HAVILAND, J. K.; LAVIN, M. L. Applications of Monte Carlo method to heat transfer in a rarefied gas. **Physics of Fluids**, v. 5, p. 1399–1405, 1962. 27
- HITT, D. L.; ZAKRZWSKI, C. M.; THOMAS, M. A. MEMS-based satellite micropropulsion via catalyzed hydrogen peroxide decomposition. **Smart Materials and Structures**, v. 10, p. 1163–1175, 2001. 4, 11
- HO, C. M.; TAI, Y. M. MEMS and its applications for flow control. **Journal of Fluids Engineering**, v. 118, p. 437–447, 1996. 10
- _____. Micro-electro-mechanical systems (MEMS) and fluid flows. **Annual Review of Fluid Mechanics**, v. 30, p. 579–612, 1998. 10
- HOFFMANN, K. A.; CHIANG, S. T. **Computational fluid dynamics**. Wichita, Kansas: Engineering Education System, 2000. 83
- HOLDEN, M. S.; WADHAMS, T. P. A review of experimental studies for DSMC and Navier-Stokes code validation in laminar regions of shock/shock and shock/boundary layer interactions including real gas effects in hypersonic flows. **AIAA Paper 03–3641**, 2003. 29
- HORISAWA, H.; SAWADA, F.; ONODERA, K.; FUNAKI, I. Numerical simulation of micro-nozzle and micro-nozzle-array flowfield characteristics. **Vacuum**, v. 83, p. 52–56, 2009. 10, 12, 13, 67
- IKEGAWA, M.; KOBAYASHI, J. Development of a rarefied gas flow simulator using the direct-simulation Monte Carlo method. **JSME International Journal**, v. 33, n. 3, p. 463–467, 1990. 58
- IVANOV, M. S.; GIMELSHEIN, S. F. Current status and prospects of the DSMC modeling of near-continuum flows of nonreacting and reacting gases. In: INTERNATIONAL SYMPOSIUM ON RAREFIED GAS DYNAMICS, 23., 2003, Whistler. **Proceedings...** Whistler, Canada, 2003. v. 663, p. 339–348. 81
- IVANOV, M. S.; MARKELOV, G. N.; GIMELSHEIN, S. F. Statistical simulation of reactive rarefied flows: numerical approach and applications. **AIAA Paper 98–2669**, 1998. 32, 54
- IVANOV, M. S.; MARKELOV, G. N.; KETSDVER, A. D.; WADSWORTH, D. C. Numerical study of cold gas micronozzle flows. **AIAA Paper 99–0166**, 1999. 67

IVANOV, M. S.; ROGASINSKY, S. V.; RUDYAK, Y. Y. Direct simulation method and master kinetic equation. In: INTERNATIONAL SYMPOSIUM ON RAREFIED GAS DYNAMICS, 16., 1989, Pasadena. **Proceedings...** Pasadena, CA, 1989. v. 118, p. 171–181. 81

IVANOV, M. S.; ROGAZINSKII, S. V. Comparative analysis of algorithms of DSMC in rarefied gas dynamics. **Comput. Math. and Math. Phys.**, v. 23, n. 7, p. 1058, 1988. 35

JANSON, S. W.; HELVAJIAN, H.; BREUER, K. MEMS, microengineering and aerospace systems. **AIAA Paper 99–3802**, 1999. 5

JEANS, J. H. **The dynamical theory of gases**. London: Cambridge University Press, 1916. 53

JONES, J. R.; MATTICK, A. T. MEMS micronozzle flow analysis of a high-temperature chemical propulsion system. In: SPACE 2003 (AIAA), 2003, Long Beach. **Proceedings...** Long Beach, CA: AIAA, 2003. p. 62–70. 10

KANNENBERG, K. C.; BOYD, I. D. Strategies for efficient particle resolution in the direct simulation Monte Carlo method. **Journal of Computational Physics**, v. 157, p. 727–745, 2000. 81

KARNIADAKIS, G. E.; BESKOK, A.; ALURU, N. **Microflows and nanoflows, fundamentals and simulation**. 1. ed. New York: Springer, 2005. 10

KETSDEVER, A. D. Microfluidics research in MEMS propulsion systems. In: AIAA AEROSPACE SCIENCES MEETING AND EXHIBIT, 41., 2003, Reno. **Proceedings...** Reno, NV: AIAA Paper 2003–0783, 2003. 5

KETSDEVER, A. D.; CLABOUGH, M. T.; GIMELSHEIN, S. F.; ALEXEEKO, A. A. Experimental and numerical determination of micropropulsion device efficiencies at low Reynolds numbers. **AIAA Journal**, v. 43, n. 3, p. 633–641, 2005. 10

KIM, S. C. Calculations of low-Reynolds-number resistojet nozzles. **Journal of Spacecraft and Rockets**, v. 31, n. 2, p. 259–264, 1994. 178

KLAF, A. A. **Calculus refresher**. New York: Dover Publications, 1956. (Dover books on mathematics). ISBN 9780486203706. 69

KNUDSEN, M. The law of molecular flow and viscosity of gases moving through tubes (in germany). **Ann Physik**, v. 28, p. 75, 1909. 17

KNUDSEN, M.; WEBER, S. Air resistance for slow motion of small spheres. **Ann Physik**, v. 36, p. 981–994, 1911. 17

KOGAN, M. N. **Rarefied gas dynamics**. 2. ed. New York: Plenum Press, 1969. 25, 27

KOHLER, J.; BEJHED, J.; KRATZ, H.; BRUHN, F.; LINDBERG, U.; HJORT, K.; STENMARK, L. A hybrid cold gas microthruster system for spacecraft. **Sensors and Actuators A**, v. 97–98, p. 587–598, 2002. 4

KONECNY, G. Small satellites - a tool for Earth observation? **International Archives of Photogrammetry Remote Sensing and Spatial Information Sciences**, v. 35, n. 4, p. 580–582, 2004. 1, 3

KOURA, K.; MATSUMOTO, H. Variable soft sphere molecular model for inverse-power-law of Lennard-Jones potential. **Physics of Fluids A**, v. 3, n. 10, p. 2459–2465, 1991. 35, 48

_____. Variable soft sphere molecular model for air species. **Physics of Fluids A**, v. 4, n. 5, p. 1083–1085, 1992. 48

KUNC, J. A.; HASSAN, H. A.; HASH, D. B. The GHS interaction model for strong attractive potentials. **Physics of Fluids**, v. 7, n. 3, p. 1173–1175, 1995. 49

LAN, X. A modified relaxation time Monte Carlo method with a multiple translational temperature model for micronozzle gas flows. **Journal of Micromechanics and Microengineering**, v. 19, n. 3, p. 35007, 2009. 93

LANDAU, L.; TELLER, E. Theory of sound dispersion. **Phys. Z. Sowjetunion**, v. 10, n. 34, p. 1, 1936. 53

LAUX, M. Optimization and parallelization of the DSMC method on unstructured grids. **AIAA Paper 97–2515**, 1997. 33

LEBEAU, G. B. A parallel implementation of the direct simulation Monte Carlo method. **Computer Methods in Applied Mechanics and Engineering**, v. 174, p. 319–337, 1999. 32

LEE, C. J. Unique determination of solutions to the Burnett equations. **AIAA Journal**, v. 32, n. 5, p. 985–990, 1994. 23

LIU, W. W.; FANG, Y. C. Implicit boundary conditions for direct simulation Monte Carlo method in mems flow predictions. **Computer Modeling in Engineering and Science**, v. 4, p. 119–128, 2000. 58

LIU, M.; ZHANG, X.; ZHANG, G.; CHEN, Y. Study on micronozzle flow and propulsion performance using DSMC and continuous methods. **Acta Mechanica Sinica**, v. 22, p. 409–416, 2006. 10, 71

LORD, R. G. Application of the Cercignani-Lampis scattering kernel to direct simulation monte Carlo Method. In: INTERNATIONAL SYMPOSIUM ON RAREFIED GAS DYNAMICS, 17., 1990, Aachen. **Proceedings...** Aachen, Germany, 1991. p. 1427–1433. 63

_____. Some extensions to the Cercignani-Lampis gas-surface interactions. **Physics of Fluids A**, v. 3, n. 4, p. 706–710, 1991. 63

_____. Some further extensions of the Cercignani-Lampis gas-surface interactions. **Physics of Fluids**, v. 7, n. 5, p. 1159–1161, 1995. 64

LUMPKIN, F. E.; HAAS, B. L.; BOYD, I. D. Resolution of differences between collision number definitions in particle and continuum simulations. **Physics of Fluids A**, v. 3, n. 9, p. 2282–2284, 1991. 54

MACPHERSON, G. B.; NORDIN, N.; WELLER, H. G. Particle tracking unstructured, arbitrary polyhedral meshes for use in CFD and molecular dynamics. **Communications in Numerical Methods in Engineering**, v. 25, p. 263–273, 2009. 33

MALUF, N.; WILLIAMS, K. **An introduction to microelectromechanical systems engineering**. 2. ed. Norwood, MA: Artech House Inc., 2000. ISBN 1-58053-590-9. 5

MANSON, M. L.; PUTNAM, L. E.; RE, R. J. **The effect of throat contouring on two-dimensional converging-diverging nozzles at static conditions**. Hampton, Virginia: NASA, 1980. 67 p. (NASA TP-1704). 11

MANZONI, G. Design of a highly integrated micropropulsion system for microsatellites attitude control. In: AIAA/ASME/SAE/ASEE JOINT

PROPULSION CONFERENCE AND EXHIBIT, 36., 2000, Huntsville.

Proceedings... Huntsville, AL: AIAA Paper 2000–3476, 2000. 4

MARGOTTINI, L. **Microsatellites “pose global threat”**. 2007. Available from: <<http://news.bbc.co.uk/2/hi/technology/6902800.stm>>. Access in: September 12, 2010. 1

MAXWELL, J. C. On stresses on rarefied gases arising from inequalities of temperature. **Philosophical Transactions of the Royal Society of London**, v. 170, p. 231–256, 1879. Reprinted in *The Scientific Papers of J. C. Maxwell*, Dover, New York, 1965. 62

MEIBURG, E. Comparison of the molecular dynamics method and the direct simulation Monte Carlo technique for flows around simple geometries. **Physics of Fluids**, v. 29, n. 10, p. 3107–3113, 1986. 32

MENZIES, R. D. D.; RICHARDS, B. E.; BADCOCK, K. J. Computational investigation of three-dimensional flow effects on micronozzles. **Journal of Spacecraft and Rockets**, v. 39, n. 4, p. 642–644, 2002. 10

MILLIKAN, R. A. The isolation of an ion, a precision measurement of its charge, and the correction of Stokes' law. **Physics Review**, v. 32, p. 349, 1911. 17

_____. The general law of a small spherical body through a gas, and is bearing upon the nature of molecular reflection from surfaces. **Physics Review**, v. 22, p. 1, 1923. 17

MO, H.; LIN, C.; GOKATUN, S.; SKUDARNOV, P. V. Numerical study of axisymmetric gas flow in conical micronozzles by DSMC and continuum methods. In: AIAA AEROSPACE SCIENCES MEETING AND EXHIBIT, 44., 2006, Reno. **Proceedings...** Reno, NV: AIAA Paper 2006–0991, 2006. 10

MOSER, R.; COLLINS, D.; DAS, A.; FERBER, R.; JAIVIN, G.; MADISON, R.; SMITH, J.; STALLARD, M. Novel missions for next generation microsatellites: the results of a joint AFRL-JPL study. In: ANNUAL AIAA/USU CONFERENCE ON SMALL SATELLITES, 13., 1999, Logan. **Proceedings...** Logan, UT: AIAA, 1999. 2, 3

MUNSON, B. R.; YOUNG, D. F.; OKIISHI, T. H. **Fundamentals of fluid mechanics**. 4. ed. New York: John Wiley & Son, 2002. 125

- MUNTZ, E. P. Rarefied gas dynamics. **Annual Review of Fluid Mechanics**, v. 21, p. 387–417, 1989. 29
- NAMBU, K. Rarefied gas dynamics: theoretical basis of the direct simulation Monte Carlo methods. In: INTERNATIONAL SYMPOSIUM ON RAREFIED GAS DYNAMICS, 15., 1986, Grado. **Proceedings...** Grado, Italy, 1986. 35
- NAMBU, K.; WATANABE, Y.; IGARASHI, S. Conservation of angular momentum in the direct simulation Monte Carlo method. **Journal of the Physical Society of Japan**, v. 57, n. 9, p. 2877–2880, 1988. 32
- NANCE, R. P.; HASH, D. B.; HASSAN, H. A. Role of boundary conditions in Monte Carlo simulation of microelectromechanical system. **Journal of Thermophysics and Heat Transfer**, v. 12, n. 3, p. 447–449, 1998. 58
- NANCE, R. P.; WILMOTH, R. G.; HASSAN, H. A. Comparison of grid-definition schemes for Monte Carlo simulations. **Journal of Thermophysics and Heat Transfer**, v. 11, n. 2, p. 296–303, 1997. 33, 80
- NARASHIMA, R. Collisionless expansion of gases into vacuum. **Journal of Fluid Mechanics**, v. 12, p. 294–308, 1962. 29
- NERI, J. A. C. F. Microsatélite do INPE e o programa espacial brasileiro. In: PIRES, T. (Ed.). **Revista parcerias estratégicas**. Brasília, DF: Centro de Gestão e Estudos Estratégicos, 1999. v. 7, p. 227–233. 2, 3
- NORDSIECK, A.; HYCKS, B. L. Monte Carlo evaluation of the Boltzmann collision integral. In: BRUNDIN, C. L. (Ed.). **Rarefied gas dynamics**. New York: Academic Press, 1967. v. 1. ISBN 0-8493-9137-7. 27
- OBERKAMPF, W. L.; TRUCANO, T. G. Verification and validation in computational fluid dynamics. **Progress in Aerospace Sciences**, v. 38, p. 209–272, 2002. 79
- O'CONNOR, L. MEMS: microelectromechanical systems. **Mechanical Engineering**, Aachen, Germany, v. 114, p. 40–47, 1992. 10
- O'LEARY, R. A.; BECK, J. E. Nozzle design. **Threshold Journal**, 1992.
Available from:
<<http://www.pwengineering.com/articles/nozzledesign.htm>>. Access in: September 12, 2010. 6

OLYNICK, D. P.; MOSS, J. N.; HASSAN, H. A. Grid generation and adaptation for the direct simulation Monte Carlo method. **Journal of Thermophysics**, v. 3, n. 4, p. 368–373, 1989. 80, 82

ORAN, E. S.; OH, C. K.; CYBYK, B. Z. Direct simulation Monte Carlo: recent advances and applications. **Annual Review of Fluid Mechanics**, v. 30, p. 403–441, 1998. 29

PHAM-VAN-DIEP, E. D.; MUNTZ, E. P. Nonequilibrium molecular motion in a hypersonic shock wave. **Science**, v. 245, p. 624, 1989. 29

PIEKOS, E. S.; BREUER, K. S. Numerical modeling of micromechanical devices using the direct simulation Monte Carlo method. **Transaction of the ASME**, v. 118, p. 464–469, 1996. 71

PRASANTH, P. S.; KAKKASSERY, J. K. Direct simulation Monte Carlo (DSMC): a numerical method for transition regime flows - a review. **J. Indian Inst. Sci.**, v. 86, p. 169–192, 2006. 29

_____. Molecular models for simulation of rarefied gas flows using direct simulation Monte Carlo method. **Fluid Dynamics Research**, v. 40, p. 233–252, 2008. 46

RAJASANOW, S.; WAGNER, W. Stochastic weighed particle method for the Boltzmann equation. **Journal of Computational Physics**, v. 124, p. 243–253, 1996. 33

RAO, G. V. R. Recent developments in rocket nozzle configurations. **ARS Journal**, v. 31, n. 11, p. 1488–1494, 1961. 13

RAULT, D. F. G. Efficient 3-D DSMC for complex geometry problems. **Progress in Astro. and Aero.**, v. 159, p. 137, 1994. 80

RIEFFEL, M. A. A method for estimating the computaional requirements of DSMC simulations. **Journal of Computational Physics**, v. 149, p. 95–113, 1999. 82

ROSSI, C.; DOCONTO, T.; ESTEVE, D.; LARANGOT, B. Design, fabrication and modelling of MEMS-based microthrusters for space application. **Smart Materials and Structures**, v. 10, p. 1156–1162, 2001. 4

SAAD, M. A. **Compressible fluid flow**. 2. ed. Upper Saddle River, NJ: Prentice Hall, 1993. ISBN 0-07-100665-6. 19, 95, 106

SAN, O.; BAYRAKTAR, I.; BAYRAKTAR, T. Size and expansion ratio analysis of micro nozzle gas flow. **International Communications in Heat and Mass Transfer**, v. 36, p. 402–401, 2009. 93

SANTOS, W. F. N. Gas-surface interaction effect on round leading edge aerothermodynamics. **Brazilian Journal of Physics**, v. 37, n. 2A, p. 337–348, 2007. 64, 65

SCHAFF, S.; CHAMBRE, P. **Fundamentals of gas dynamics**. Princeton, NJ: Princeton University Press, 1958. 63

SCHLICHTING, H. **Boundary layer theory**. 6. ed. New York: McGraw-Hill Inc, 1968. 165

SEBASTIÃO, I. B.; SANTOS, W. F. N. Gas-surface interaction effects on the flowfield structure of high speed microchannel flow. In: BRAZILIAN CONGRESS OF THERMAL SCIENCES AND ENGINEERING, 13., 2010, Uberlândia. **Proceedings...** Uberlândia, Brazil, 2010. 65

_____. Gas-surface interaction impact on heat transfer and pressure distribution of high speed microchannel flow. In: SOUTHERN CONFERENCE ON COMPUTATIONAL MODELING, 4., 2010, Rio Grande. **Proceedings...** Rio Grande, Brazil, 2010. 65

SEN, M.; WAJERSKI, D.; GAD-EL-HAK, M. A novel pump for MEMS applications. **Journal of Fluids Engineering**, v. 118, p. 624–627, 1996. 10

SHAPIRO, A. H. **The dynamics and thermodynamics of compressible fluid flow**. New York, NI: Ronald Press, 1954. ISBN 0-07-100665-6. 10, 95, 104, 106, 107, 129, 177

SHEA, H. R. MEMS for pico- to micro-satellites. In: DICKENSHEETS, D. L.; SCHENK, H.; PIYAWATTANAMETHA, W. (Ed.). SPIE, 2009. v. 7208, n. 1, p. 72080M. Available from: <<http://link.aip.org/link/?PSI/7208/72080M/1>>. 2, 3

SHEN, C. **Rarefied gas dynamics: fundamentals, simulations and micro flows**. Germany: Springer, 2000. 32, 36, 40, 42, 52, 62

- SHEVYRIN, A. A.; BONDAR, Y. A.; IVANOV, M. S. Analysis of repeated collisions in DSMC method. In: CAPITELLI, M. (Ed.). **Rarefied Gas Dynamics**: 24th international symposium. Melville, NY: American Inst. of Physics, 2005. p. 565–570. 81
- SHU, C.; MAO, H. M.; CHEW, Y. T. Particle number per cell and scaling effect on accuracy of DSMC simulation of micro flows. **International Journal of Numerical Methods for Heat and Fluid Flow**, v. 15, n. 8, p. 827–841, 2005. 32, 82
- SIMMONS, R. S.; LORD, R. G. DSMC simulation of hypersonic metal catalysis in a rarefied hypersonic nitrogen/oxygen flow. In: SHEN, C. (Ed.). **Rarefied Gas Dynamics**: 20th international symposium. Beijing: Peking U.P., 1997. p. 416. 35
- SIVELLS, J. C. Design of two-dimensional continuous-curvature supersonic nozzles. **Journal of the Aeronautical Sciences**, v. 22, p. 685–691, 1955. 10, 13
- SUCCESSOS E INSUCCESSOS DO PROGRAMA ESPACIAL BRASILEIRO. 2009. Available from: <<http://brazilianspace.blogspot.com/2009/05/successos-e-insuccessos-do-programa.html>>. Access in: September 12, 2010. 2
- TAN, Z.; CHEN, Y. K.; VARGHESE, P. L.; HOWELL, J. R. New numerical strategy to evaluate the collision integral of the Boltzmann equation. **Progress in Astro. and Aero.**, v. 118, p. 359–373, 1989. 27
- TITOV, E.; GALLAGHER-ROGERS, A. R.; LEVIN, D.; REED, R. Examination of a collision-limiter direct simulation Monte Carlo method for micropropulsion applications. **Journal of Propulsion and Power**, v. 24, n. 2, p. 311–321, 2008. 12, 76, 77
- TITOV, E.; LEVIN, D.; ROGAZINSKY, S. V. Analyses of numerical errors in the kinetic modeling of microthruster devices. **Journal of Thermophysics and Heat Transfer**, v. 21, p. 616–622, 2007. 10
- TITOV, E.; ZEIFMAN, M. I.; LEVIN, D. A. Application of the kinetic and continuum techniques to the multi-scale flows in MEMS devices. In: AIAA AEROSPACE SCIENCES MEETING AND EXHIBIT, 43., 2005, Reno. **Proceedings...** Reno, NV: AIAA Paper 2005–1399, 2005. 10

TORRE, F. L.; KENJERES, S.; KLEIJN, C. R.; MOEREL, J. L. P. A. Effects of wavy surface roughness on the performance of micronozzles. **Journal of Propulsion and Power**, v. 26, n. 4, p. 655–662, July-August 2010. 9

TRIMMER, W.; STROUD, R. H. Scaling of micromechanical devices. In: GAD-EL-HAK, M. (Ed.). **MEMS: introduction and fundamentals**. 2. ed. Boca Raton, FL: Taylor & Francis Group, 2006. chapter 2, p. 2.1–2.7. ISBN 0-8493-9137-7. 9

VARADAN, V. K.; VINOY, K. J.; JOSE, K. A. **RF MEMS and their applications**. England: John Wiley and Sons Inc., 2003. 5

VINCENTI, W. G.; KRUGER, C. H. **Introduction to physical gas dynamics**. New York: John Wiley and Sons Inc., 1965. 25, 42, 44, 100

WANG, M.; LI, Z. Simulations for gas flows in microgeometries using the direct simulation Monte Carlo method. **International Journal of Heat and Fluid Flow**, v. 25, p. 975–985, 2004. 10

WANG, M. R.; LI, Z. X. Numerical simulations on performance of MEMS-based nozzles at moderate or low temperatures. **Microfluid and Nanofluid**, v. 1, p. 62–70, 2004. 58, 59

WANG, W. L.; BOYD, I. D. Predicting continuum breakdown in hypersonic viscous flows. **Physics of Fluids**, v. 15, n. 1, p. 91–100, 2003. 20

WELDER, W. T.; CHAPMAN, D. R.; MACCORMACK, R. W. Evaluation of various forms of the Burnett equations. **AIAA Paper 93–3094**, 1993. 23

WICK, R. S. The effect of boundary layer on sonic flow through an abrupt cross-sectional area change. **Journal of the Aeronautical Sciences**, v. 20, p. 675–682, 1953. 105

WILMOTH, R. G.; LEBEAU, G. J.; CARLSON, A. B. DSMC grid methodologies for computing low-density, hypersonic flows about reusable launch vehicles. In: AIAA THERMOPHYSICS CONFERENCE, 31., 1996, Louisiana. **Proceedings...** Louisiana, NO: AIAA Paper 1996–1812, 1996. 33, 80

WU, J.; LEE, F.; WONG, S. Pressure boundary treatment in micromechanical devices using the direct simulation Monte Carlo. **JSME International Journal**, v. 44, n. 3, p. 439–450, 2001. 58

- WU, J. S.; TSENG, K. C.; LEE, U. M.; LEE, Y. Y.; LIAN, Y. Y. Development of a general parallel three-dimensional direct simulation Monte Carlo code. In: CAPITELLI, M. (Ed.). **Rarefied Gas Dynamics: 24th international symposium**. Melville, NY: American Inst. of Physics, 2005. p. 559–564. 33
- XIE, C. Characteristics of micronozzle gas flows. **Physics of Fluids**, v. 19, p. 037102, 2007. 10, 93
- YANG, J.; YE, J. J.; ZHENG, J. Y.; WONG, I.; LAM, C. K.; XU, P.; CHEN, R. X.; ZHU, Z. H. Using direct simulation Monte Carlo with improved boundary conditions for heat and mass transfer in microchannels. **Journal of Heat Transfer**, v. 135, p. 041008–1, 2010. 59
- YANG, Z.; WEI, Y. H. Gas flow simulation in a micro nozzle. **Aircraft Engineering and Aerospace Technology: An International Journal**, v. 78, p. 387–390, 2006. 10
- YEN, S. M. Monte Carlo solutions of nonlinear Boltzmann equation for problems of heat transfer in rarefied gases. **International Journal of Heat and Mass Transfer**, v. 14, p. 1865–1869, 1970. 27
- ZAKIROV, V.; GIBBON, D.; SWEETING, M.; REINICKE, B.; BZIBZIAK, R.; LAWRENCE, T. Specifics of small satellite propulsion: part 2. In: AIAA/ASME/SAE/ASEE JOINT PROPULSION CONFERENCE AND EXHIBIT, 37., 2001, Salt Lake City. **Proceedings...** Salt Lake City, UT: AIAA Paper 2001–3834, 2001. 4
- ZHAN, K.; CHOU, S. K.; ANG, S. S. MEMS-based solid propellant microthruster design, simulation, fabrication, and testing. **Journal of Microelectromechanical Systems**, v. 13, n. 2, p. 165–175, 2004. 67
- ZHONG, X. **Development and computation of continuum higher order constitutive relations for high-altitude hypersonic flow**. PhD Thesis (PhD) — Stanford University, Stanford, CA, 1991. 23

PUBLICAÇÕES TÉCNICO-CIENTÍFICAS EDITADAS PELO INPE

Teses e Dissertações (TDI)

Teses e Dissertações apresentadas nos Cursos de Pós-Graduação do INPE.

Manuais Técnicos (MAN)

São publicações de caráter técnico que incluem normas, procedimentos, instruções e orientações.

Notas Técnico-Científicas (NTC)

Incluem resultados preliminares de pesquisa, descrição de equipamentos, descrição e ou documentação de programas de computador, descrição de sistemas e experimentos, apresentação de testes, dados, atlas, e documentação de projetos de engenharia.

Relatórios de Pesquisa (RPQ)

Reportam resultados ou progressos de pesquisas tanto de natureza técnica quanto científica, cujo nível seja compatível com o de uma publicação em periódico nacional ou internacional.

Propostas e Relatórios de Projetos (PRP)

São propostas de projetos técnico-científicos e relatórios de acompanhamento de projetos, atividades e convênios.

Publicações Didáticas (PUD)

Incluem apostilas, notas de aula e manuais didáticos.

Publicações Seriadas

São os seriados técnico-científicos: boletins, periódicos, anuários e anais de eventos (simpósios e congressos). Constam destas publicações o Internacional Standard Serial Number (ISSN), que é um código único e definitivo para identificação de títulos de seriados.

Programas de Computador (PDC)

São a seqüência de instruções ou códigos, expressos em uma linguagem de programação compilada ou interpretada, a ser executada por um computador para alcançar um determinado objetivo. Aceitam-se tanto programas fonte quanto os executáveis.

Pré-publicações (PRE)

Todos os artigos publicados em periódicos, anais e como capítulos de livros.